Modelling invasion, migration and cellular networks in Glioblastoma stem cells

Bronwyn Kate Irving

Submitted in accordance with the requirements for the degree of
Doctor of Philosophy

The University of Leeds
School of Medicine

October 2020

The candidate confirms that the work submitted is his/her own and that appropriate credit has been given where reference has been made to the work of others.

Work described in Chapter 3 made a significant contribution to the revision of the following publication:

da Silva, B., Irving, B.K., Polson, E.S., Droop, A., Griffiths, H.B., Mathew, R.K., Stead, L.F., Marrison, J., Williams, C., Williams, J. and Short, S.C., 2019. Chemically induced neurite-like outgrowth reveals a multicellular network function in patient-derived glioblastoma cells. Journal of Cell Science, 132(19), p.jcs228452.

Below is the figure within the thesis followed by (figure from the paper):

- Figure 3.1A (Fig S1B)
- Figure 3.1B (Fig 1B)
- Figure 3.1C (Fig S1D)
- Figure 3.2B (Fig S1A)
- Figure 3.2C (Fig 1E)
- Figure 3.4A (Fig 1F)
- Figure 3.5A (Fig 3H)
- Figure 3.5B (Fig 3I)

Acknowledgements

Firstly, I would like to say thanks to Heiko for his support, enthusiasm, and supervision, pushing me to be a more independent researcher. I would also like to say thanks to Anestis for all his support and supervision.

To past members of the Stem Cells and Brain Tumour group, especially Barbara and Jenny, whose help I couldn't have done without.

To the members of the Tsakiridis group, specifically Tom, who helped teach me all things stem cells, and to the everyone at KCL's CSCRM who accepted me into their team and taught me so much in a small amount of time.

This wouldn't have been possible without the massive amounts of help from many members of Level 5, either in the lab or at coffee mornings, and in particular to Fiona and Rhiannon who have provided endless amounts of support.

This whole experience has been made better by being a DiMeN student, being supported by being part of cohort 2, as well as from Emily specifically, who without I could not still be here.

To the genetic gals Dimitra, Anna and Ruth who started my science journey with me and remain both Greek and British rays of sunshine in my life.

Thank you to my family and Jack for the constant support, listening ear and for making me strive to push myself.

Thanks to my Pop who throughout has encouraged me to remember, even when things went wrong, “well, what is the learning?” and to whom without I could not have got to completion.

This work is dedicated to Luke.

Abstract

Glioblastoma (GBM) is the most common and aggressive brain tumour in adults. The prognosis for the average patient is very poor with median survival times of only 12-15 months. Despite treatment (surgical debulking and adjuvant chemoradiotherapy), glioblastoma tumours inevitably recur, which is attributed to the existence of cancer stem cell subpopulations, known as glioma stem cells (GSC). GSCs are highly infiltrative and have been shown to significantly contribute to tumour growth and recurrence. However, GSCs remain moving targets in terms of their adaptive molecular phenotype which hampers targeted treatment strategies against GSCs. Here we have developed model systems to investigate aspects of adaptive GSC phenotypic behaviour including invasion, epithelial-mesenchymal transition (EMT) and cellular networks, which all contribute to the overall aggressiveness of GBM tumours.

Specifically, we have developed a human-human assembloid assay, whereby patient derived GSC spheroids spontaneously fuse and infiltrate human cerebral organoids (hCOs). This enabled us to dynamically model and quantify the GSC tissue invasion process. Importantly, the assay differentiates between the invasive behaviour of malignant and non-malignant control cell types, also indicating different invasion timelines across different patient-derived GSC models.

Additionally, we have explored conditions that promote the transcriptional upregulation of an EMT profile in GSC subpopulations derived from GBM tumour specimens. These GSCs have characteristics of a mesenchymal GSC subpopulation that warrants further functional investigation. We propose that this previously unidentified cell population may contribute to a more infiltrative tumour phenotype through the EMT pathway.

We have also further validated an inducible cellular network in GSCs using chemical inhibition of Rho associated protein kinase (ROCK). Such an *in vitro* system recapitulates features of cellular networks discovered *in vivo* in an accessible manner for the study of functional cell co-operation mechanisms. Specifically, we have determined the ability of networked cells to transfer mitochondria intercellularly and propose this as a mechanism that critically contributes to a radioresistant GSC phenotype.

By modelling the phenotypic plasticity of GSCs, with the ability of cells to invade and infiltrate, demonstrate EMT transcriptional upregulation as well as the formation of cellular networks, we have paved a way for the interrogation of GSC functional biology ex vivo. This is expected to complement time and resource-intense in vivo experimentation in rodents, hence aiding the identification of GSC-directed therapeutic strategies that target key adaptive GSC phenotypes in the treatment of GBM.

Table of Contents

List of Tables

List of Figures

Chapter i. Introduction

i.1 Glioblastoma multiforme (GBM)

i.1.1 Classification

Globally, the incidence of tumours of the brain and central nervous system account for around 250,000 new cancer cases annually and are the cause of 189,000 deaths [1]. Although there are over 100 types of brain tumours, glioma is an umbrella classification for malignant brain tumours of glial origin. Gliomas are classified based on shared histological and morphological features of glial lineages (astrocytomas, ependymomas, oligodendrogliomas) and they are graded based on World Health Organisation (WHO) classification [2]. There are 4 glioma grades with an increasing degree of aggressiveness: low grade gliomas (LGG) are graded I & II and high grade gliomas (HGG) III & IV. Glioblastoma multiforme (GBM) is the most common and aggressive primary brain tumour (45% of all gliomas) [3] and classified as a grade IV astrocytoma [2]. GBM tumours are diffusely infiltrative neoplasms which exhibit hypercellularity, nuclear atypia and microvascular proliferation and/or necrosis [2].

i.1.2 Incidence and prognosis

Globally the incidence of GBM is 3-5 per 100,000 people [4], with approximately 2,100 new cases diagnosed in England annually [5]. Through multistep mutational gain, grade III anaplastic astrocytomas can progress to grade IV, making up 40% of GBM incidences, whereas 60% of GBMs arise de novo [6].

Patients often present with a range of symptoms, attributed to rapid expansion and displacement of brain structures, such as progressive headaches, focal neurological signs and, in 23% of patients, seizures [7], and are diagnosed at a median age of 65 years [8]. Diagnosis is performed using contrast enhanced magnetic resource imaging (MRI) with GBM tumours typically appearing as an enhancing, necrotic mass which is surrounded by non-enhancing abnormalities consisting of edema and infiltrative tissue. This is also sometimes observed with hemorrhage, cystic changes or multicentric enhancement [9]. Diagnosis can be further confirmed with differentiation from other tumour types based on perfusion-weighted imaging. Dynamic susceptibility contrast MRI measures cerebral blood volume, thus providing information regarding microvessel density and area [10, 11], which can further identify GBM from other tumours due to its hallmark feature of microvascular proliferation [12].

Following MRI diagnosis, patients often undergo neurosurgery for tumour debulking and biopsies for pathology confirmation of diagnosis and subclassification. While historically classification has been based solely on histological resemblance to cells of the glial lineage, the 2016 WHO release for CNS tumours classification included molecular parameters including isocitrate dehydrogenase (IDH) mutational status and detection of a 1p/19q chromosomal co-deletion [2]. These new IDH based classifications, IDH-wildtype, IDH-mutant or 'not otherwise specified' (NOS), now allows for prediction of prognosis [13, 14]. IDH-wildtype tumours indicate a de novo or primary tumour, whereas a IDH-mutant status indicates progression from a lower grade (often previously undetected) gliomas [15, 16]. NOS tumours were classified before the WHO 2016 update and therefore did not take into account IDH classification or IDH status could not be determined [2].

The overall global 5-year survival for GBM is only 6.8% [8], which drops to 3.4% for 5-year survival in England [5]. Patients up to the age of 69 have a medial survival of 14.9 months, with maximal treatment of debulking neurosurgery with chemo- and radiotherapy [17, 18]. However, this prognosis significantly drops with increases in age, with patients over the age of 70 unlikely to receive maximal treatment [5].

i.1.3 Current treatments and challenges

GBM tumours are notoriously difficult to treat and with little advancement in treatment options or prognosis in the last 30 years, standard of care remains to be maximal safe surgical resection of the tumour mass followed by radiotherapy and chemotherapy [19–21]. However, the existence of tumour heterogeneity fuelled by populations of glioma stem cells (GSCs) and contribute to treatment resistance provide a great challenge for the treatment of GBM.

i.1.3.1 Primary GBM

GBM had a highly diffuse and infiltrative growth pattern with dissemination throughout the brain along white matter tracts significantly decreasing the likelihood of complete surgical resection [17, 22, 23]. Only gross total resection is associated with improved outcome in both newly-diagnosed and recurrent GBM, despite the indication in some studies of gradual improvements in outcome with resections increasing over 78% [24–31]. Although resection aims to leave as little tumour as possible as this correlates with survival [32], only maximal safe resection is performed to prevent new postoperative neurological deficits as this is a negative prognostic factor [33, 34].

However, advancements in imaging techniques such as functional MRI and positron emission tomography (PET) provide better delineation of tumours to aid surgical planning and optimum surgical trajectories to help ensure maximal safe resection is achieved [25, 35–37]. Additionally, intraoperative imaging such as ultrasound, stereotactic navigation systems using anatomical and functional MRI datasets with intraoperative MRI, along with the fluorescent dye 5-aminolevulinic acid (5-ALA) which visualised tumour tissue and, in some cases, functional monitoring, maximise the chance of achieving maximal safe resection while further reducing the chance for new neurological deficits [24, 38, 39].

Following maximal safe surgical resection patients most commonly undergo radiotherapy with concomitant chemotherapeutic agent temozolomide (TMZ) followed by six 28 cycles of adjuvant TMZ [40, 41]. Patients follow the Stupp regime [40] for radiotherapy treatment, often between 50-60 Gy, which has been shown to improve overall survival by 2.5 months, and progression-free survival by 1.9 months [41, 42]. Higher doses of radiotherapy have not been associated with any additional survival benefit, but an increased incidence of injury to the normal brain. Patients also receive TMZ, a DNA alkylating agent, which triggers apoptosis through the induction of DNA damage and cytotoxicity synergistic with the mechanisms of radiotherapy induced apoptosis [43–45]. Despite combined treatments of radio- and chemotherapy, 2 year survival only increased from 10.4% to 26.1% [41] this still remains a poor prognosis and many elderly patients over the age of 70 do not receive maximal treatment due to increased toxicities and therefore do not benefit from this increased survival [46].

i.1.3.2 Recurrent GBM

One of the major challenges when treating GBM is that tumours invariably recur after a median interval of less than 7 months [40] at which time median overall survival is 22-24 weeks [47–49]. Recurring tumours are highly resistant to treatment [50] and thus the National Comprehensive Cancer Network guidelines recommend clinical trials for those patients who are eligible [51]. Although some patients may be offered temozolomide rechallenge, vascular endothelial growth factor (VEGF) targeted therapy bevacizumab or re-irradiation, these have not shown a survival benefit in either randomised trials or in palliative care [52–54]. The only treatment option with survival benefit for recurrent GBM tumours is complete resection which is not appropriate in every case [31], and due to the diffuse growth pattern of the tumours is unlikely to be achieved.

i.1.3.3 GBM heterogeneity

The failure to effectively treat GBM has been attributed to the presence of one of its hallmark features heterogeneity. Intertumoural heterogeneity, differences exhibited between patients, has led to the subtyping of tumours for prognostic value. However, this is significantly complicated in GBM with high levels of intratumoural heterogeneity whereby cells across the same tumour can differ with respect to mutational load, histology, and/or transcriptional and epigenetic landscape.

i.1.3.3.1 Intertumoural heterogeneity: genetic subtypes

As previously described tumours are molecularly diagnosed with IDH status indicating whether the tumour is de novo (IDH-wildtype) or a secondary (IDH-mutant) [15, 16]. Subgrouping based on IDH is therefore routinely performed in clinics due to the prognostic implications for patients in either category.

Bulk sequencing of tumours has since determined three GBM subtypes based on genetic alteration patterns, DNA copy number and transcriptional signatures: classical (TGCA-classical), proneural (TCGA-proneural) and mesenchymal (TCGA-mesenchymal) [55–57].

TCGA-classical subtype is characterised by the amplification of chromosome 7 and consequently high expression of EGFR. Deletion of CDKNA2A and loss of chromosome 10 were also associated with the TCGA-classical subtype. High expression of neural stem cells marker NESTIN as well as members of the NOTCH (NOTCH3, JAG1, and LFNG) and Sonic hedgehog (SMO, GAS1, and GLI2) pathways were also frequently detected.

TCGA-proneural tumours showed frequent loss of TP53 and loss of heterozygosity as well as features such as PDGFRA alterations along with point mutations in IDH1. The TCGA-proneural subtype was also associated with high expression of oligodendrocytic developmental genes such as PDGFRA, NKX2-2, and OLIG2.

TCGA-mesenchymal tumours displayed activated pathways such as PI3K/Akt, as a result of mutations in NF1 and PTEN, and NF-κB. Upregulation of mesenchymal markers such as YKL40 and MET indicate features of epithelial-mesenchymal-transition (EMT).

In the first instance there were suggested to be four subtypes including neural (TCGA-neural), however subsequent analysis revealed this expression signature to be non-tumour specific [58, 59]. TCGA-neural was previously associated with the tumour margin and therefore may have resulted from normal tissue contamination. This perhaps explains the lack of characteristic gene abnormalities in the TCGA-neural subtype compared to the other remaining subtypes [60, 61] and as a result TCGA-neural is no longer considered and was removed as a GBM subtype [56].

Although there is suggestion of prognostic value of the three established subgroupings, with classical or mesenchymal GBM showing reduced mortality with more intensive therapy [55, 57], this stratification is not currently routinely performed in clinic. The clinical adoption of this stratification may come following the development of therapies targeting the specific genetic subtypes.

i.1.3.3.2 Intratumoural heterogeneity: histological subtypes

Differences within the same tumour, evidence of intratumoural heterogeneity, can be identified histologically.

Gliosarcoma (GS) tumours, a rare histologic variant seen in 2.8% of GBM, [62] exhibits both neural compartments as well as a sarcomatous compartment [63–74]. Sarcomatous components of GS are often positive for reticulin, a marker of connective tissue, but not GFAP, a marker of astrocytes [66]. The mesenchymal component is often similar to fibrosarcoma and may also exhibit mesodermal-like morphologies resembling cartilage, osseous, adipocytic, and smooth and skeletal muscle entities [67, 68, 72, 74–77]. Clinical presentation of GS, in relation to diagnosis age and tumour location, is similar to GBM and therefore follows the same treatment course. However, GS has a poorer prognosis with median overall survival 9.8 months [78], for reasons that are yet to be elucidated. Originally it was proposed sarcomatous compartments arose due to infiltration of transformed cells, such as vascular smooth muscle or histiocytic cells originating from outside of the tumour. Genetic analysis however determined both neural and sarcomatous compartments within the same tumour harbour the same genetic alterations, suggesting they arose from a monoclonal cell of origin [65, 66, 71]. This suggests that intratumoural heterogeneity, not only on the basis of genetic abnormalities but also histologically, may carry clinical implications influencing patient treatment response and survival. Despite the presence of a sarcomatous compartment being the major difference between GBM and GS, the contribution of mesodermal-like entities to tumour growth and a decrease in survival, is currently unknown.

i.1.3.3.3 Intratumoural heterogeneity: genetic subtypes

Although patients can be separated and subtyped based on genetic mutations (TCGA-classical/mesenchymal/proneural) multi-region sampling and single cell-RNA sequencing (scRNA-seq) revealed intratumoural heterogeneity with the coexistence of multiple TCGA- subtypes within the same tumour [79, 80]. Additionally, the composition of subtypes within one tumour has also been shown to change over time and following therapy in longitudinal analysis [56, 81]. The existence of multiple subtypes within one tumour has been associated with poorer prognosis indicating the heterogenous nature of GBM tumours influencing aggressiveness and a challenge for effective treatment [79].

i.1.3.3.4 Intratumoural heterogeneity: cellular states

The intratumoural heterogeneity exhibited in GBM patients is not only thought to be governed by genetic mutations, but also transcriptional and epigenetic abrogations. Recent scRNA-seq has determined malignant cells, within IDH-wildtype GBM tumours, exist in four cellular states. which mimic developmental cell types: oligodendrocyte progenitor cell-like (NEFTEL-OPC), neural progenitor cell-like (NEFTEL-NPC), mesenchymal-like (NEFTEL-MES) and astrocyte cell-like (NEFTEL-AP) [82, 83].

NEFTEL-OPC state was associated with markers of the oligodendroglial lineage such as OLIG1, OMG, PLP1, PLLP, TNR and ALCAM and influenced by copy number amplifications in PDGFRA

NEFTEL-NPC was further subdivided into NEFTL-NPC1, which included association with OPC related genes such as OLIG1 and TNR, and NEFTL-NPC2 which was associated with neuronal lineage genes such as STMN1, STMN2, STMN4, DLX5-AS1 and DLX6-AS1. Both subdivisions are influenced overall with copy number amplifications in CDK4.

NEFTEL-MES state is associated with genes involved in stress (e.g. DDIT3), glycolysis (e.g ENO2, LDHA) and response to hypoxia (e.g. HILPDA). This is also subdivided on the basis of association with hypoxia signatures with NEFTL-MES1 independent of hypoxia and NEFTL-MES2 dependent. Both subdivisions are influenced with point mutations at the NF1 loci.

NEFTEL-AC cells were associated with astrocytic markers S100B, GFAP, SLC1A3, GLAST and MLC1 and are influenced by copy number amplifications in EGFR.

Although these states were associated with signatures relating to neural developmental cell types, these states were shown to be influenced by abrogations in key genetic drivers. The background genetic drivers within a particular patient may therefore sustain the predominance of a particular cellular state and therefore explain tumour subgroupings based on bulk RNA sequencing [55]. Following Patal et al showing individual GBM cells able to harbour TGCA- genetic subgroup signatures [79], ~15% of cells were also shown by Neftal et al to exist as a hybrid of two cellular states. The existence of cells of transcriptionally intermediate states and lineage tracing experiments show the plasticity of cell states within GBM tumours with the ability for transition between the states [83]. The influence of these cellular states on prognosis and treatment response have yet to be determined, but the cellular plasticity exhibited by GBM cells exemplifies why a pan therapeutic agent has not previously succeeded in the treatment of this disease.

How GBM tumours arise and then sustain these highly heterogeneous and plastic cells populations have been attributed to the existence of cancerous GSCs.

Intertumoural heterogeneity	
Variety between different patient's tumours	

Genetic
• IDH status
• TCGA subtypes
  ○ TCGA-classical- chromosome 7 amplification, high EGFR expression
  ○ TCGA-proneural- TP53 loss, PFGFRA alternations
  ○ TCGA-mesenchymal- NF1, PTEN and NF-κB
	Histological
	• Gliosarcoma
	  ○ Rare histological subtype
	  ○ Evidence of both neural and sarcomatous compartments
	  ○ Poor prognosis of 9.8 months median survival

Intratumoural heterogeneity	
Variety within the same patient's tumour	

Genetic
• More than one TCGA subtype found to exist within one tumour
  ○ Multi-region sampling
  ○ Single cell RNA sequencing
	Transcriptional
	• Single cell RNA sequencing revealed cells within one tumour exists in one of four cellular states
	  ○ NEFTEL-OPC- associated with oligodendroglia markers and copy number amplifications of PDGFRA
	  ○ NEFTEL-NPC- associated with copy number amplifications in CDK4, subdivided based on association with oligodendroglia markers (NEFTEL-NPC1) or neural lineage markers (NEFTEL-NPC2)
	  ○ NEFTEL-MES- associated with NF1 mutations, subdivided based on association with hypoxia dependent (NEFTEL-MES1) or independent signatures (NEFTEL-MES2)
	  ○ NEFTEL-AP- EGFR copy number amplification with association of astrocytic markers

Table i.1 Summary of heterogeneity in GBM tumours.

i.2 Cancer stem cells

Cancer stem cells (CSC) are subpopulations of cells, within tumours, with capabilities of self-renewal, differentiation and tumourigenicity when transplanted into an animal host [84]. Consequently, CSCs are implicated both in cancer initiation and treatment resistance.

Due to tumours containing heterogeneous neoplastic cell populations with influences from the tumour microenvironment led to the postulation of similarity between tumourigenicity and normal development healing processes where sustained stem cell populations are present within tissues. The CSC hypothesis was underpinned following the ability of a single leukaemic cell into mice exhibited the ability of producing a lethal tumour within 2 weeks [85]. Subsequent investigations showed the ability of a subset of leukemic cells to sustain proliferation with self renewal properties, and differentiate maintaining original tumour cell phenotypes [86, 87]. Following the identification of a CSC population within leukaemia a similar population was sought in other tumour types such as breast [88], prostate [89], colorectal [90, 91], and pancreatic cancer [92].

i.2.1 Glioma stem cells (GSCs)

i.2.1.1 GBM’s cell of origin

Despite many efforts to characterise GBM tumours at the genomic level, GBM’s cell of origin is still not determined and is an area of great debate. Some argue transformation of differentiated astrocytes give rise to GBM tumours, whereas others suggest tumours form as a result of transformation of a neural stem cell (NSC) to a GSC population [93]. Although some studies were able to show genetic alterations in differentiated astrocytes was sufficient to form GBM in mouse models [94], others could not replicate this and only determined alterations in NSCs were capable of generating GBM tumours [95–98]. Many recent studies focus on the notion that NSCs residing in the adult subventricular zone (SVZ) may be the GBM cell of origin, notably following the determination of transcriptional similarity in immature cells of the SVZ with GBM cells [98, 99]. Overexpression of mutant IDH, known to drive progression of lower grade gliomas to GBM, in SVZ NSCs was shown in mouse models to induce hyperplasia and early indications of GBM formation [100]. Following the detection of shared mutations in matched human GBM tissue and normal SVZ tissue in half of the sequenced patients further indicates GBMs arise from a malignant NSC cell of origin [98]. Recent single cell RNA-sequencing (scRNA-seq) suggests that tumours then recapitulate normal neurodevelopmental cell types and therefore hierarchy as they develop and progress [80].

i.2.1.2 GSCs support tumour growth and recurrence

GSC populations have been shown to not only initiate tumours but also recapitulate tumour heterogeneity following orthotopic injection into mice [101, 102], and have been identified functionally, [101, 103] and through primary tumour sequencing [79, 83, 104]. These GSC populations are marked with stemness markers similar to that which are indicative of NSCs, such as SOX2 [105, 106], NESTIN [107, 108], OLIG2 [109], vimentin (VIM) [110] and MYC [111], indicating a sustaining neoplastic NSC-like GSC population within GBM tumours, not just an initiation cell of origin.

Due to the highly infiltrative nature of GBM, populations of GSCs can invade surrounding healthy brain parenchyma far enough for total surgical resection to be impossible [112]. These self-renewing GSC populations, following invasion, reside throughout the brain therefore evading treatment allowing formation of another tumour at a secondary site and promote its growth by supporting angiogenesis [113]. GSCs are characteristically radio- and chemotherapy resistant [114–116], and therefore support the growth of secondary tumours. These secondary tumours forming from already highly infiltrative and treatment resistant populations consequently mean recurrent tumours are more aggressive [116]. Despite high levels of mutational load being rarely detected in primary GBM tumours, hypermutation signatures are frequently detected in recurrent tumours [117-122]. Hypermutation signatures are associated with defective mismatch repair (MMR) genes, with potential implications for response to immunotherapy [117–119, 121–123]. Hypermutations are thought to arise either de novo, with fundamental defects in DNA polymerase and MMR genes, or associated with acquired treatment resistance driven by MMR defects following treatment with alkylating agent TMZ [122]. Despite the mechanism by which hypermutational signatures arise, resulting tumours are highly treatment resistant and are associated with poor patient survival [122].

i.2.1.3 GSCs are regulated by intrinsic and extrinsic factors

GSCs are thought to be sustained and regulated within GBM tumours with influence from intrinsic mechanisms such as genetics, epigenetics and metabolism as well as extrinsic factors such as the microenvironment, niche factors and the immune system (Fig i.1).

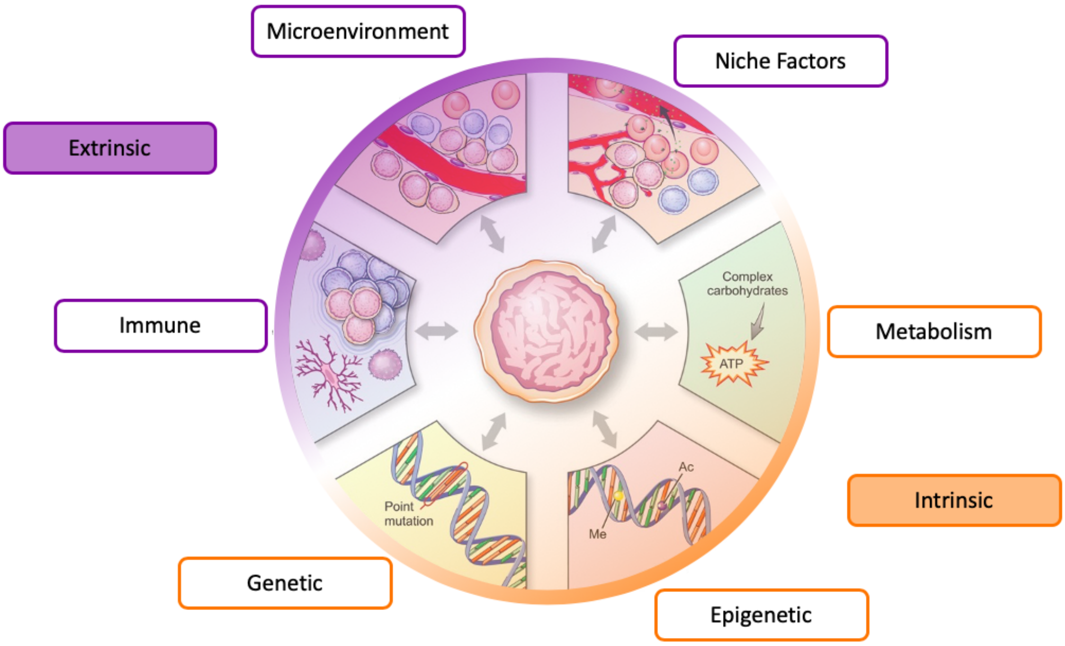

Figure i.1 Extrinsic and intrinsic factors regulating GSCs. Extrinsic factors include microenvironment, immune system and niche factors in combination with intrinsic factors such as metabolism, genetics and epigenetics. Adapted from Lathia et al [124].

i.2.1.3.1 Intrinsic mechanisms

Advances in sequencing technology has allowed interrogation of the genomic landscape of GBM tumours [55, 60, 83]. Alterations of EGFR, IDH1, PDGFRA, HDM2, PI3KCA and the TERT promoter through gain of function mutations or amplifications are frequently detected. Mutations or deletions are also detected in PTEN, TP53, CDKN2A, NF1, ATRX and RB1 tumour suppressors [124]. The role of genetics is complicated by the frequency of specific alterations differing between samples from different locations of the same tumour and between patients further indicating the high levels of heterogeneity within GBM [55, 104]. This makes it more complicated when trying to understand the driving mutations between clones during tumour evolution.

Heterogeneity is also evident with respect to epigenetic regulation throughout GBM tumours. Epigenome wide mapping of cellular chromatin states found SOX2, POU3F2, SALL2 and OLIG2 to be master transcriptional regulators of specifically the TCGA-proneural GBM subtype [125]. However, many other factors have also been shown to recruit chromatin remodelers to promote maintenance of GSC stem cell state, such as STAT3 [126], FOXM1 [127], GLI1 [128], ASCL1 [129], ZFX [130], NANOG [131] and ZFHX4 [132]. Additionally, the epigenetic methylation status of the O-6-methylguanine-DNA methyltransferase (MGMT) gene within GBM tumours influences therapeutic response to TMZ chemotherapy [133]. TMZ has been shown to only be efficacious with MGMT methylation and consequently TMZ is often withheld from patients with unmethylated MGMT tumours where the benefit of TMZ is minimal [133, 134]. However, there is a decrease in MGMT methylation in recurrent GBM tumours [135, 136]. As a result, this epigenetic change from primary to recurrent tumour eliminates TMZ for rechallenge as a secondary treatment option in these tumours. Although it is clear there is a role and influence of both genetics and epigenetics on GSC population’s stem cell state and susceptibility to treatment, this relationship still needs clarifying and further interrogation required.

GSCs reside in microenvironments which have limited access to nutrients such as glucose and oxygen and as a result demonstrate metabolic shift to aerobic glycolysis, demonstrating the Warburg effect [137]. The hypoxic conditions within GBM tumours results in the upregulation of HIF-2α promoting the maintenance of self-renewal, proliferation and survival of GSCs [138]. Additionally, to outcompete other tumour components, specifically GSCs have been shown to upregulate the GLUT3 transporter for glucose uptake [139]. GSCs exploit the production of reactive oxygen species, generated as a consequence of their altered metabolic programmes, becoming dependent on NOS2 activity to promote tumour growth [140]. GSCs metabolic programmes are not only plastic, responding to the tumour microenvironment but are exploited by recurrent tumours through IDH mutations. Mutations are thought to induce a loss of differentiation potential of GSCs, maintaining their stem cell state and promote genetic instability through aberrant hypermethylation of DNA and histones [141]. There have been efforts to exploit GSC altered metabolic programmes with the use of compounds such as KHS101 which can cause GSC specific apoptosis, a consequence not observed in treatment on normal neural progenitors (NPs) [142].

More interrogation of the relationship between genetics, epigenetics and metabolism is needed to understand how their interplay regulates a stem cell state of GSCs and how this contributes to tumour growth and recurrence in an effort to exploit for treatment.

i.2.1.3.2 Extrinsic factors

GSCs are not only maintained as a result of intrinsic mechanisms but are also influenced by extrinsic factors.

GSCs hijack developmental processes within the brain niche as a means to increase survival and maintain their undifferentiated state and thus show up-regulation of pathways such as Notch, BMP, NF-kB and Wnt [129, 143–145]. These niche factors provide survival advantage as GSCs acquire features of normal stem and progenitor populations. For example, the canonical Wnt signalling cascade is known to be a key regulator in both adult and embryonic stem cells [146, 147] and plays a pivotal role in normal brain development [148]. Upregulation of the Wnt pathway is evident in a subset of GBM tumours and aberrant Wnt signalling is implicated in not only GSC maintenance but tumour invasiveness and therapeutic resistance [149, 150]. Additionally, amplification of factors such as PLAGL2 are shown to suppress terminal differentiation of not only NSCs but also GSCs through modulation of the Wnt/β-catenin pathway [151]. Widespread activation of the Wnt pathway is evident at the chromatin level with loss of Polycomb-mediated repression and through activation of chromatin remodeller ASCL1 [129]. Therefore, GSCs are indicated to reside in Wnt specific niches within GBM tumours as a means to maintain their stem cell state [149].

Immune suppression is a well-established feature and hallmark of many tumours [152]. Despite it being known that immune surveillance is activated when the brain is in a pathogenic state [153], immunosuppression has been characterised as a feature of GBM [154] through GSC mediated modulation of T-cells and tumour associated microglia/macrophage function. GSCs have been shown to evade attenuation by T-cell through the secretion of T-cell checkpoint molecule PD-L1 contained in extracellular vesicles [155]. Additionally, the secretion of TGFβ and IL-10 by GSCs have shown to favour the immunosuppressive (M2) phenotype of tumour associated microglia and macrophages [156–158]. GSCs attenuation of the immune system in an effort to evade detection and immune mediated apoptosis has thus sparked interest in immunotherapies targeting GBM tumours. Through reversal of the immunosuppressive microenvironment it is hoped the brain's endogenous immune surveillance could contribute to the targeting of neoplastic cells.

Due to their highly infiltrative behaviour, GSCs are remarkably adaptive to new environments. To sustain and repopulate tumours in distant locations throughout the brain from the original tumour GSCs interact with the angiogenic environment to help supply nutrients. By using an Olig2-Wnt7 signalling axis GSCs are able to invade along blood vessels [159]. This ensures expanding primary tumours, and secondary site tumours are in close contact to existing vasculature to promote neoangiogenesis using vessel angioproteins and tumour derived VEGF [113, 160, 161]. There are also interactions between many components of stroma which support tumours and maintain GSC stemness characteristics. High levels of extracellular matrix (ECM) components, such as extracellular matrix glycoprotein tenascin C (TNC), contributes to matrix stiffness which in turn activates integrin mechanosignalling pathways [162]. Subsequent upregulation of integrins, such as integrin-α7, promotes GSC proliferation, invasiveness and stemness through activation of pathways such as NOTCH [163, 164]. NOTCH is also activated, maintaining GSCs self renewal, through the engagement of NOTCH ligands on endothelial cells by GSCs at the perivascular niche [165, 166].

To determine more effective ways of treating GBM disease, with a focus on targeting GSCs, it is imperative to accurately isolate and model GSCs. Investigation of the extrinsic and intrinsic factors that play a role in the maintenance of the GSC state, will increase our understanding of their influence on tumour heterogeneity, invasion, treatment resistance and contribution to recurrence.

i.2.1.4 Isolation and modelling of GSCs

GSCs are often identified and isolated using methodologies based on surface cellular markers as well as exploiting similarities to NSC and promote growth through the use of medium supporting NSC growth: glioma NSC (gNSC) conditions. GSC behaviour can be further modelled using a variety of *in vitro* and *in vivo* models such as neurosphere and adherent cultures, organoid generation as well as engineered and xenograft murine models, each with both advantages and limitations discussed in Table i.2.

GSC model	Advantages	Limitations	References
Sorting based on surface cellular markers (such as CD133 and CD15)	Can enrich for a stem cell population from tumour samples.	The use of individual marks has been disputed with currently no evidence of individual marker reproducibly isolating cells that meet functional GSC criteria. Isolation of these populations using one marker may be problematic with worries of the integrity of surface markers following single cell dissociation. Additionally, selecting for a specific marker may also reduce heterogeneity in the stem cell fraction of these GBM tumours.	[101, 167–171]
In vitro neurosphere culture	Utilises functional assay for self-renewal capability of isolated population and maintains 3D interactions in population. High throughput system.	Does not determine tumour formation capability. Loss of interactions with microenvironment factors. Percentage of enriched GSCs will vary sphere to sphere as well as depending on passage and length of time in culture. Not suitable for assays which require homogeneity.	[102, 171, 172]
Adherent culture on poly-lysine/laminin	May reduce spontaneous differentiation compared to neurosphere culture. Provides more homogeneity which is more suitable for some assays. High throughput system.	Does not determine tumour formation capability. Loss of tumour heterogeneity with a dependency on selected culture medium whereby all GSC fractions may not be isolated and sustained. May reduce heterogeneity with serial passaging.	[102, 173, 174]
Three-dimensional GSC ‘organoid-spheroids’ and biomaterial scaffolds	Allows for interactions with multicellular compartments. Able to model hypoxic and other biological gradients.	Reduction in throughput compared to adherent culture with complex establishment and maintenance. Does not contain all tumour interactions such as vasculature and microglia. Is often only one tumour compartment.	[175–178]
Genetically engineered and syngeneic mouse models	Allows the following of tumour initiation as well as progression. Also, able to integrate influences from microenvironment including tumour stroma and immune system.	Initiation processes are not fully mimicked compared to the human disease. Resultant tumours do not fully recapitulate human disease. Murine models also have a lower throughput as there are high costs and are labour intensive.	[95, 100, 179–181]
Patient-derived xenograft models	Allows the study of human tumours with cellular interactions within a more physiological environment.	Does not allow interrogation of tumour initiation events. Either requires immediate generation following surgery or subsequent implantation of GSCs following isolation and maintenance by one of the other modelling techniques, thus adding additional limitations.	[101, 182–185]

Table i.2 Various models used within GBM research for investigation of invasion. Advantages and disadvantages of each model is noted.

i.2.1.4.1 Previously derived patient GSC cell lines used within this study

Within this study we utilise a variety of previously isolated GSC lines. Lines were derived using NSC based culture conditions, with a dependency on FGF and EGF, serum free as cells continually cultured in serum conditions were shown to no longer reflect patient heterogeneity and disease [102]. Cells were isolated from freshly resected dissociated tumour specimens and grown adherently with the use of poly-ornithine and laminin [173, 174]. The GSC lines used within this study were derived from a variety of patients and reflect different subtypes of GBM [142], as described in Table i3.

Model	Disease	IDH1	Notes
GBM1	Primary GBM	wt	Subtypes: TCGA-classical, TCGA-proneural
GBM4	Primary GBM	wt	Subtype: TCGA-mesenchymal, TCGA-classical, TCGA-proneural
GBM11	GS	wt	Subtype: TCGA-mesenchymal
GBM13	Primary GBM	wt	Subtype: TCGA-proneural
GBM20	Recurrent GBM	wt	Subtypes: TCGA-proneural, TCGA-mesenchymal
OX2 E	Primary GBM	wt	Derived from tumour edge
OX2 CE	Primary GBM	wt	Derived from mix of tumour core and edge
GBM30P	Primary GBM	wt	-
GBM30RC	Recurrent GBM	unknown	Derived from tumour core
GBM30RE	Recurrent GBM	unknown	Derived from tumour edge
GBM40C	GBM	unknown	Derived from tumour core
GBM40E	GBM	unknown	Derived from tumour edge

Table i.3 Patient tumour characteristics from which patient cell lines were derived and used within this study. Disease, IDH1 status and notes regarding either tumour subtype or region of specimen used to derive line is noted. Wildtype= wt.

i.3 GBM invasion

One of the greatest challenges when trying to treat GBM is its highly invasive behaviour. GSCs have been shown to have an elevated invasive potential compared to other tumour compartments [186] indicating these to be the cells which invade up to several centimetres away from the tumour mass [187, 188]. As a result, GSC populations that have migrated from the tumour mass remain following maximal safe surgery and can consequently drive proximal and distant tumour recurrence within 2 years of first line treatment [116, 187, 189]. However, unlike many other solid tumours, GBM rarely metastasises outside of the brain indicating unique invasion mechanisms [190–192].

i.3.1 Invasion routes

Cancer cells have been shown to invade either in groups, as mesenchymal chains, clusters or multicellular sheets or as single cells in a blebbing amoeboid or elongation mesenchymal mode [193]. Although other cancers that metastasise to the brain, such as carcinoma, have been shown to invade within the brain as groups of cells, GBM exhibits single cell invasion primarily as a result of mesenchymal movement [194–196].

In mesenchymal single cell invasion cells develop polarized cytoskeletal extensions with integrin mediated focal adhesion points at the leading edge indicating migration direction [193, 197]. Movement is then mediated via Rho-pathway mediated adhesion, and cellular contractility [198]. Therefore, cells undergo cytoskeleton remodelling, becoming elongated and spindle-like as they move [199, 200]. Subsequently, to allow for movement cells secrete proteases such as matrix-metalloproteinases 2, 9 and 14, serine proteases uPA and cell surface proteases [201, 202] for proteolytic degradation of surrounding ECM components [203].

GBM has been described to hijack migratory routes, using pre-existing structures within the brain, adopted by immature neurons and NPs [202]. These structures include white matter tracts, brain parenchyma, perivascular space and the leptomeningeal space [204]. Some are used as migratory routes such as perivascular space surrounding blood vessels [205] and white matter tracts such as the corpus callosum as a means to invade the contralateral hemisphere [188, 206–208]. However, the brain parenchyma provides higher physical resistance with tight spaces for invading cells due to the high proportion of neuronal and glial cell bodies [202, 209, 210]. As a result, GBM tumours remodel surrounding ECM with the dysregulation of components such as upregulation of hyaluronan, vitronectin and collagens and downregulation of thrombospondin and versican to aid invasion [194, 211–213]. On the other hand, in the perivascular space GBM cells have been shown to upregulate components such as thrombospondin and SPARC indicating the adaptation of GBM invasion mechanisms with respect to invading microenvironment [214, 215].

i.3.2 Invasion networks

i.3.2.1 *In vivo* cellular network formation

Cellular networks have recently been implicated as another invasion mechanism within GBM. Tunnelling microtubule-like structures within GBM have been detected in xenograft [216, 217] and genetic GBM murine models [218] and described as tumour microtubules (TMs). These ultra-long, long-lived TMs with thick extensions interconnected, forming multicellular networks of glioma cells. TMs were found at the invasive front of tumours and within cell populations which have invaded the contralateral brain hemisphere, indicating their role in tumour dissemination [216]. TMs of cells at the invasive front of GBM tumours were found to resemble neurite growth cone-like structures [216], which function by leading and steering axons during outgrowth [219], furthering the indicating the role of TMs in dissemination.

Interconnected GBM cells were not only shown to use TMs as a means of dissemination but formation of multicellular networks permitting cell-cell communication and radioresistance. Osswald et al demonstrated the ability of GBM networks to communicate via calcium signalling using TMs [216]. Additionally, TM connected networked demonstrated resistance to radiation with less cell death than unconnected cells not involved in the network [216], indicating a survival advantage for interconnected networked cells.

Jung et al described that glioma TMs could be categorised into interconnecting or invasive subtypes [220]. Although the conversion between the two subtypes has not yet been explicitly shown, the ability to convert may allow cells to disseminate, invading over long distances and then interconnecting cells would be able to be protected from radiation therapy.

i.3.2.2 *In vitro* cellular network formation

The phenomenon of cellular networking has not only been described *in vivo* but also able to be modelled in *in vitro* conditions.

The RhoA pathway is known to be a regulator of actin cytoskeletal dynamics with downstream effectors such as LIM domain kinases (LIMK1/2) and RHO-associated serine/threonine kinase proteins (ROCK1/2) [221–223]. Pan inhibition of ROCK1/2 proteins, via chemical Y-27632 treatment for 24 hours, demonstrates long neurite extensions with interconnectivity inducing a cellular network of GSCs in 2D *in vitro* conditions [224]. As shown *in vivo* [216], GSCs within ROCK inhibitor induced (ROCKi) networks demonstrated multicellular cooperation with transmission of calcium waves as well an increase in number of organelles (lysosomes and mitochondria) within cellular projections. Additionally, *in vitro* ROCKi GSC networks also demonstrated resistance to radiation with increased cell viability and increased oxygen consumption in response to high doses of radiation (20 Gy). ROCKi networks via Y-27632 treatment were indicated to not induce cellular differentiation, with no increased expression of neural differentiation markers NEUROD1 and NTRK2 [225, 226] as determined by RNA-seq. ROCKi networked cells demonstrated similar proliferation as control GSCs, as determined by Ki67 staining, no upregulation of neuronal differentiation pathways as determined by mRNA-seq, and the reversal of the cellular projection phenotype within 8 hours of ROCK inhibitor washout [224]. However, some questions remained regarding the demonstration whether Y-27632 directly inhibits the kinase activity of ROCK and whether inhibition is still observed with upstream pathway activation. Additionally, although neurite length is shown to extend it is unclear whether these extensions are formed using existing neurofilaments or are formed de novo. Although the trafficking of organelles is alluded to both *in vitro* [224] and *in vivo* [216] currently there is a lack of demonstrating regarding movement of organelles from one cell to another through cellular networks. Although Y-27632 successfully demonstrated the induction of a cellular network phenotype, how this phenotype compares to phenotypes induced as a result of exposure to other network inducers, such as Matrigel [227], is not yet known.

Modelling of GSC cellular networks using ROCK inhibition enabled more mechanistic insight to the behaviour of cells within cellular networks [224]. Also modelling in 2D allowed live cell tracking, simple cell harvesting for mRNA sequencing and direct comparisons of networked and non-networked phenotypes. Although this work was conducted in 2D Y-27632 inhibition of ROCK was found to induce cellular networked outgrowths in spheroid conditions [217].

i.3.3 Models for GBM invasion

Traditionally 2D models, often the scratch wound assay, were used to investigate migration and invasion mechanisms. However, this lacked many factors and cell types to represent the complexity of tumour cells invading within the brain. Although the scratch wound assay allows interrogation of the influence of simple factors, other models which gain in physiologically relevance have been developed and adopted. Each of these models have their own advantages and disadvantages when studying invasion in GBM. These are discussed in Table i4.

	Model	**Advantages**	**Disadvantages**	**References**
2D *in vitro*	Scratch wound assay	Relatively simple and low-cost assay with high throughput. Allows the real time tracking of single cells in real time.	Simple 2D environment is not very physiologically relevant. Actually, only shows migration, not invasion. Requires suppression of the cell cycle otherwise cannot separate the migratory behaviour from proliferation. Simple variables such as wound width and ECM coating can greatly affect migration velocity of cells.	[210, 228–230]
3D *in vitro*	Boyden chamber	Relatively simple and low cost with high throughput/ Allows study interactions of matrix components.	Difficult to distinguish migration or invasion. Not all components commonly used to create 3D matrix are brain ECM components. These matrices and their percentage composition is also static which is not the case within the brain.	[230–232]
	Bioscaffolds	More complex matrices better repopulate the brain ECM with relevant components. More of the properties of different brain components can be tested with control over features such as elasticity, density or stiffness. Allows real time cell tracking in a 3D environment with high throughput. Does model invasion.	Are often unable to sustain more than one cell type which are shown to have an influence on invasion capability therefore lacks tumour-stroma complexity and brain structures.	[194, 233–237]
	Microfluidic co-culture	Co-culture systems allow the use of gel scaffolds and therefore the control over physical scaffold properties. Can determine the influence of different cells in co-culture with GBM cells and the effect of shear force, mimicking blood flow, on invasion.	Still cannot get full cellular complexity or native brain environment which together influences invasion. More technically complex and expensive therefore reducing throughput.	[238–240]

		Allows real time cell tracking in a 3D environment.		
Ex vivo	Organotypic brain slice	Preserves complex cell interactions and brain structure, therefore allows for the study of the different invasion routes. Allows from more than one slice per animal helping to increase throughput/ use of less animals. Higher resolution imaging than *in vitro*.	However, there is limited tissue stability not allowing for long term study. Also lacks blood flow and immune compartment. Although blood vessels and endothelial cells are present there is lack shear force due to no flow. No immune compartment if GSCs are patient derived.	[214, 241–246]
In vivo	Orthotopic xenograft	Cellular complexity with a physiological environment allowing for study of the different invasion routes. Allows study of the effect of blood flow. Tumours can be tracked *in vivo*.	Lacks immune compartment and therefore influence. Although tumours often recapitulate invasion patterns still need to consider murine context being different. Technically difficult with higher costs and therefore limited throughput. Limited *in vivo* imaging resolutions may require end point analysis. Associated ethical issues with the use of animal models.	[247–254]

Table i.4 Various models used within GBM research for investigation of invasion. Advantages and disadvantages of each model is noted.

i.4 Organoids

Organoids are defined as “3D structures grown from stem cells and consisting of multiple organ specific cell types that self-organises with spatially restricted lineage commitment and some organ specific function” [255–257]. Simply, they resemble an organ *in vitro*. Organoid methodology is based on classical developmental investigations involving cell dissociation and reaggregation [258–261]. Organoid methodologies describe formation with the use of either pluripotent stem cells (PSCs) ((embryonic stem cells (ESC) or induced pluripotent stem cells (iPSC)) or organ restricted adult stem cells (aSCs) [262, 263].

Organoids have potential uses in uncovering developmental processes or disease mechanisms, as well as organ replacement therapy, drug screens and personalised therapy [256]. Genetic manipulation of cells from healthy individuals, or disease affected individuals, either PSC or aSC, can give an indication of how subsequent organ development is affected, in direct comparison to normal controls [264]. Organoids have also been employed in studying the effect infectious disease has on particular organs, such as in the case of Zika virus infection [265–268].

PSC-organoids often recapitulate *in vivo* developmental processes with structures forming as cells undergo multi-step differentiation as a consequence of specifically timed exposure to particular growth factors. PSC-derived organoids are usually structurally complex containing multicellular compartments containing mesenchymal, epithelial and/or endothelial cell types [263]. Following the development of PSC-derived organoids for the brain [269], methodology was developed for the stomach [270], liver [271], intestine [272], lung [273] and kidney [274].

Contrasting to PSC-derived organoids which can recapitulate developmental processes, aSC-dervied organoid model processes involved in adult tissue repair. As a result, aSC-derived organoids can only be established from tissue compartments with regenerative capacity and therefore currently only represent epithelial compartments of organs [263]. Consequently aSC-derived organoids lack complexity due to lacking compartments such as stroma, nerves and vasculature [275], however they do recapitulate the architecture and functional features of original epithelium [276–279]. Additionally, aSC-organoids can be directly derived from both normal and diseased [280] or malignant tissue [281], and if done so from the same patient can allow direct comparison and potential application in personalised medicine. aSC-derived organoid protocols were first developed for the intestine [276, 282] and then for normal and cancerous organoids including for the stomach [277], esophagus [276], salivary gland [283], fallopian tube [284], ovary [285], liver [279, 286, 287], prostate [288], pancreas [278], breast [289], airway [290], colon [281], taste buds [291], endometrium [292], kidney [293] and brain [175].

i.4.1 Cerebral organoids (COs)

Due to the inaccessibility to normal brain tissue, brain-like cerebral organoids are often PSC-derived. Lancaster et al developed methodology for self-assembling PSC-derived COs using either ESCs or iPSCs [256, 294]. From the generation of embryoid bodies (EBs), allowing for differentiation of the three germ layers (mesoderm, ectoderm and endoderm), cells are directed towards a neural lineage, based on initial work by Xia et al [295]. Following embedding of resulting neuroectodermal tissue in Matrigel scaffolds Lancaster et al describe the expansion and growth of COs was enabled by increased nutrient absorption after transfer to spinning bioreactors. Resulting COs form complex structures, with rosette-like neuroepithelia surrounding cavities reminiscent of ventricles as well as display markers of discrete brain regions [256, 294].

Since the establishment of Lancaster et al's CO protocol there has been many adaptations such as the use of photostimuli to investigate the maturation of retinoid-like photoreceptors within COs [296], the development of brain-region specific COs [297–299], the use of stackable mini-bioreactors to increase throughput [265] and for the investigation of vascular flow microfluidic chips [300], or *in vivo* intracerebral *in vivo* grafting [301]. Development of methodology has allowed CO technology to be applied to the investigation of various aspects affecting development and disease such as foetal brain development [302, 303], evolutionary diversion of human specific brain development mechanisms [304], autism [305] and exposure to Zika virus [265–268].

i.4.1.1 Cerebral organoids as a model for GBM

Following the development of CO methodology, they have subsequently been used as a model to study many aspects of GBM disease. GBM COs largely separate into two groups, tumour organoids and multicompartment organoids.

i.4.1.1.1 GBM tumour organoids

GBM tumour organoids, whereby all tissue within the CO is malignant, can be derived using both PSC or aSC starting material.

PSC-derived GBM COs are used primarily for the study of tumour formation through oncogenic initiation events. Genetic engineering techniques, such as CRISPR-Cas9, can be employed to facilitate oncogenic gene expression in PSCs. This has been shown to be successful with the delivering of plasmids either before the EBs are embedded in Matrigel [176], or following full CO formation [177]. Resulting COs showed to contain GBM-like cells which transcriptionally categorised into the TCGA-GBM subtypes which were immunopositive for GSC markers and exhibited an invasive phenotype when orthotopically xenografted [177]. Although mutations within the TP53 gene region were sufficient to produce GBM resembling cells within it may be difficult to model multi-step mutational abrogations, also it is still unclear how closely these tumourigenic trajectories resemble the process of tumour initiation within patients.

ASC-derived GBM tumour COs are able to be derived using patient derived GSCs. These tumour COs are able to recapitulate some architecture characteristics of GBM tumours with a gradient of GSC density, with a highly proliferative outer region and a hypoxic core with slower cycling GSCs [175]. When orthotopically transplanted or frozen and recovered in a biobank, aSC-GBM COs were shown to be able to retain histological and invasive features of parental tumours [175, 306]. aSC-GBM COs provide the possibility of personalised treatments for patient’s, although they lack vital interactions with the normal brain which will have implications for treatment and biological disease understanding.

i.4.1.1.2 Multicompartment GBM organoids

To model long term behaviour, many studies co-culture GBM cells with normal PSC-derived COs to mimic conditions with interactions between GBM and normal cells [177, 307–311]. Through monitoring via immunofluorescence microscopy successful tumour formation within COs can be determined qualitatively in real time, and tumour patterns detected as a result of invasion throughout the CO. Resulting GBM tumours reflect, histologically and transcriptionally, parental tumours even following long term culture [177, 308–311]. However as patient derived GSCs were isolated from established tumours, subsequent formation of tumours within COs may not reflect incipient cancer initiation. Although the isolation of cells from aSC-derived GBM tumours and then co-culture with normal COs may provide more insight into this aspect.

Many of these studies described the co-culture of healthy COs with single cell solutions of GBM cells [177, 308–311], therefore the single cell invasive behaviour is replicated as the cells are already singular. As a result, this does not replicate how cells at the edge of GBM dissociate from the tumour mass to invade the normal brain. Additionally, although some studies describe different invasion patterns between different GBM patient derived lines, these studies fail to fully interrogate specifically this invasive behaviour and the mechanisms which govern this.

However, da Silva et al describe an assembloid system, whereby spheroids of patient derived GSCs spontaneously invade normal early stage

COs following uninfluenced co-culture [307]. They focus on the invasion behaviour of GSCs as the spheroids attach, fuse and infiltrate across the CO. Additionally they uncovered major differences in invasive potential between malignant GSCs and non-malignant NPs. Although this assembloid assay provided a model to interrogate invasion mechanisms that specifically govern GSC malignant invasion, the COs were derived from mouse ESCs. Therefore, with adaptations, with the use of human PSC-derived COs, a human-human system may provide an insight into more translatable mechanisms of GBM invasion within the brain.

i.5 Neuromesodermal Progenitors (NMPs)

During early development a bipotent progenitor population, NMPs, contribute to both the posterior spinal cord and adjacent paraxial mesoderm.

i.5.1 Discovery

Morphological observations in 1884 first led to the proposition that the posterior spinal cord was mesoderm-derived, rather than ectoderm, in second neurulation [312]. Following grafting of GFP embryonic tissues into wildtype embryos to investigate the elongation of the body axis, at E8.5 the node-streak border (NSB) was identified to contain cells which provided long term contribution to both the neural tube and paraxial mesoderm within the mouse [313, 314]. Fate-mapping experiments in both mouse and chick embryos revealed cells residing in the NSB, primitive streak (PS) and caudal lateral epiblast (CLE) contributed to cells of both neural and mesodermal lineage (Fig i.2) [315–318].

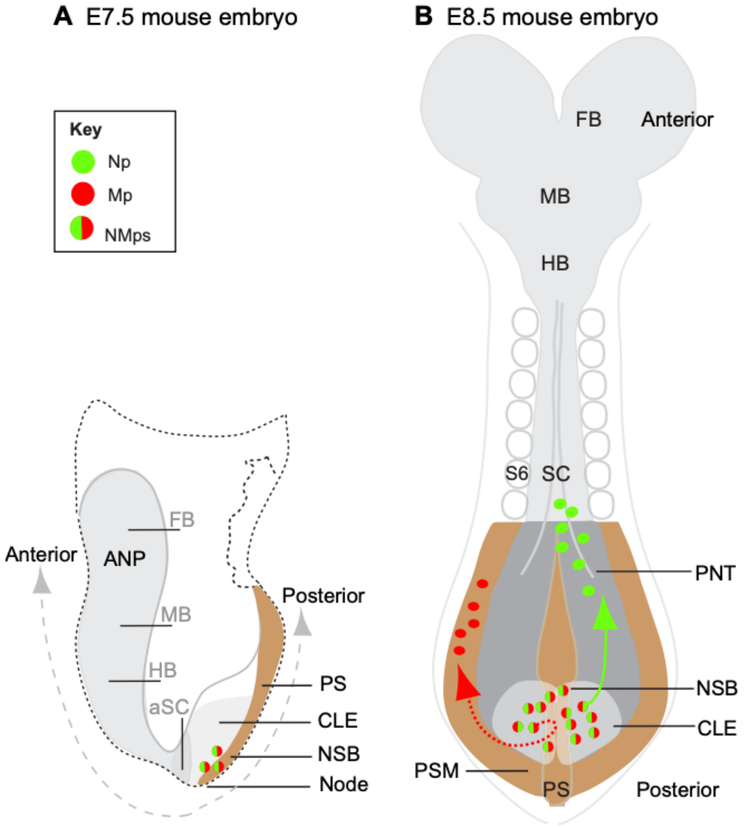

Figure i.2 NMPs within posterior of elongating body axis contribute to both neural and mesodermal lineages. Schematics of E7.5 **(A)** and E8.5 **(B)** mouse embryos indicating NMP (green/red) cell populations found in regions of node-streak border (NSB), caudal lateral epiblast (CLE) and primitive streak (PS). At E8.5 these NMPs give rise to new neural (green) and mesoderm progenitors (red). Adapted from Henrique et al [319].

i.5.2 Defining NMPs

Currently there are no unique markers defining NMPs. Within the CLE and PS, correlating to the determined position of NMPs, immunostainings and fate mapping mouse embryos revealed cells co-expressing early neural marker sex determining region Y-box 2 (Sox2) and early mesoderm marker brachyury (T) [320]. Additionally, T/SOX2 co-expressing cells within chick and human embryos were found within these regions, and in the chick these T/SOX2 cells were found to contribute to the neural tube and paraxial mesoderm [318]. As a result, NMPs have been defined by the co-expression of T and SOX2.

Sox2 is a member of the SOX (sex determining region Y box) gene family of transcription factors [321, 322]. Despite sharing 80% homology, and therefore redundancy, with other SoxB1 subfamily members Sox1 and Sox3 [323, 324], failure of Sox2-deficient embryos to form epiblast and therefore die around implantation [325], the specific roles of Sox2 in embryonic development are indispensable.

T is a member of the T-box transcription box family and is required for mesoderm and body axis formation [326]. It was first described in 1927 with mutant traits affecting tail length in mice and hence is often referred to as 'T' [327]. Expression of T is found to coincide with primitive streak formation and is maintained in the mesoderm of tail bud during axis elongation with later restriction to the notochord [326]. As a result, homozygous mouse embryos result in early body axis truncation and absence of mesoderm derived structures with embryos consequently dying in early stages of development [328] [329–332].

Post developmentally the expression of T dramatically reduces with low expression restricted to the testis and in some thyroid tissues [326, 333, 334]. However, the overexpression of T has been detected in a selection of epithelial tumours and is associated with poor prognosis with the activation of the EMT pathway, increased cell proliferation and resistance to radio- and chemotherapy [334–357]. Gene duplications of *T* is a hallmark of central nervous system (CNS) tumour chordomas [334] and the consequential amplified expression is attributed to the highly aggressive and stemness characteristics of these tumours [351, 358, 359].

i.5.3 *In vitro* derivation

Following the determination of signals that govern NMP generation and maintenance, *in vitro* NMP models were generated using FGF and Wnt signalling [320, 360–365]. Although using slightly different protocols, ESCs, epiblast stem cells or iPSCs, both mouse and human, have been used to produce *in vitro* differentiated NMPs (dNMPs) using FGF2 and a Wnt agonist (GSK3β inhibitor CHIR99021) [319]. Following 3-7 days of FGF/CHIR99021 exposure results in cells co-expressing T and SOX2 indicating an NMP state. Resulting dNMPs can then be further differentiated along neural or mesodermal lineages [320, 360, 366]. *In vitro* dNMPs, when grafted into chick and mouse embryos, have also been shown to contribute to the neural tube and paraxial mesoderm [360]. Additionally, clones derived from a single dNMP have been shown to possess dual fate potential [366], and transcriptomic data indicating sufficient similarity to post-gastrulation isolated

NMPs, indicating *in vitro* dNMPs appear to model their *in vivo* counterparts [365, 367].

i.5.4 Applications of *in vitro* NMPs

Identification of an NMP population and development of protocols for the derivation of dNMPs has allowed the opportunity of many applications. Following the ability of dNMP derived to generate progenitors which colonise the enteric nervous system in mice, indicating ability to functionally rescue disorders such as Hirschsprung, presents dNMP as a possible cell based therapy [368]. Low passaging and therefore a lower tumour potential further supports the use of dNMPs as a cell based therapy. *In vitro* modelling may provide new insights into development, such as of the spinal cord, as well as study disease pathology in addition to small molecule screening.

Chapter ii

Materials and Methods

ii.1 Brain tumour patient sample collection

Brain tumour stem cells were isolated from surgically resected tumour tissue from either Sheffield Teaching Hospital (SHF_ cells, Ref: 16/WA/0380), or Leeds General Infirmary Teaching Hospital (BM_ cells, Ref: 18/EM/0159) as previously described [174].

ii.2 Cell Culture

ii.2.1 Glioma neural stem cell culture (gNSC)

Glioma stem cell lines (GBM-N, SHF-N, BM-N) were cultured as monolayers in Neurobasal medium (Gibco, 21103-049) supplemented with B-27 (0.5x, Invitrogen, 17504-044), N-2 (0.5x, Invitrogen, 17502-048), recombinant human basic fibroblast growth factor (bFGF, 40ng/ml, Gibco, PHG0026) and epidermal growth factor (EGF, 40ng/ml, R&D Systems, 236-EG). Cells were maintained in a humidified incubator with 5% CO_2 at 37°C on poly-L-ornithin (5µg/ml, Sigma, P3655) and laminin (5µg/ml, Invitrogen, 23017-015) coated cell culture flasks/plates, and split using TrypLE (Gibco, 12604-013).

ii.2.2 Glioma NMP stem cell culture (NMP_)

Wnt dependent lines (CHIR99021:SHF-C, Wnt3a: SHF-W, BM-W) were cultured as monolayers in 50:50 Dulbecco’s modified eagle medium (DMEM)/F-12 (Gibco, 31330-038) and Neurobasal medium. In the first isolation (SHF001N) medium was supplemented with B-27 (0.5x), N-2 (0.5x), minimum essential medium non-essential amino acids solution (MEM-NEAA, 1%, Gibco, 11140-035), L-glutamine (2mM, Gibco, 21051040), β-mercaptoethanol (0.1mM, Sigma, M3148), bFGF (20ng/ml) and CHIR99021, 3µM, Tocris, 4423). In the remaining isolations and lines culture medium was supplemented with B-27 (0.5x), N-2 (0.5x), bFGF (20ng/ml) and Wnt3a (150ng/ml, R&D Systems, 5036-WN-010).

All cells were maintained in a humidified incubator with 5% CO_2 at 37°C on vitronectin (5µg/ml, Gibco, A14700) coated cell culture flasks/plates and split using TrypLE.

ii.2.3 Neural progenitor cell culture

Human NP cells were derived from non-tumour brain surgical tissues obtained from epilepsy surgery at Stanford University Medical Centre as previously described [174]. Cells were cultured in DMEM/F12 (Gibco, 2133-020) supplemented with B-27 (0.5x), N-2 (0.5x), GlutaMAX (1x, Gibco, 35050-038), bFGF (20ng/ml, Gibco, PHG0026), EGF (20ng/ml) and fetal bovine serum (FBS, 5% (v/v), Gibco, 10270) at 37°C with 5% CO_2 and split using TrypLE.

ii.2.4 Human stem cell (HSC) culture

H9 ESCs were cultured in either Essential 8 (E8, Gibco, A1517001) or modified Tenneille special recipe plus (mTeSR Plus, Stem Cell Technologies, 05825) and Hoik_1 iPSCs were cultured in mTeSR Plus. Both H9 and Hoik_1 cells were maintained in a humidified incubator with 5% CO_2 at 37°C on vitronectin (5µg/ml, Gibco, A14700) coated cell culture flasks/plates and split using ethylenediaminetetraacetic acid (EDTA, 0.5mM, Invitrogen, 15575020).

ii.3 Stem cell differentiation

ii.3.1 Differentiated neuromesodermal progenitors (dNMP)

H9 cells were plated at approximately 20,000 cells/cm^2 on vitronectin coated plates in normal growth medium supplemented with CHIR99021 (3µM) and Y-27632 (10 µM, Sigma, Y0503). The medium was replaced the following day minus Y-27632 and maintained for 2 further days until the end of differentiation.

ii.3.2 Early stage cerebral organoid (hCO) differentiation

H9 or Hoik_1 cells were differentiated using a whole cerebral organoid protocol [256] with minor modifications. Cells were dissociated using treatment with EDTA (0.5mM) followed by accutase (Thermofisher, A1110501). Subsequently 9000 cells/well were plated into ultra-low attachment (ULA) 96-well plates (Corning, CLS7007).

In stage 1 of differentiation for the generation of embryoid bodies (EBs) cell suspensions were cultured in human stem cell media (HSC), DMEM/F12 (Gibco, 31330-038) supplemented with knockout serum replacement (KSR, 20% (v/v), Gibco, 10828-028), MEM-NEAA (1%), GlutaMAX (1%), β-mercaptoethanol (55µM), bFGF (4ng/ml, Gibco, PHG0026), unless use of mTeSR is stated, and supplemented with Y-27632 (50µM). Medium was replaced every other day but Y-27632 only supplemented for the first 4 days.

At day 7 the resulting EBs were advanced to stage 2 of differentiation. EBs are transferred to ULA 24-well plates (Corning, CLS3473) in neural induction (NI) medium consisting of DMEM/F12 (Gibco, 31330-038) supplemented with N-2 (1%), GlutaMAX (1%), MEM-NEAA (1%) and heparin (1µg/ml). NI medium was replenished each day until the end of hCO differentiation.

ii.3.3 hCO Growth analysis

During stage 1 of differentiation EBs were imaged following media replenishment on days 2, 4 and 7 using a Nikon A1R confocal microscope. Area and diameter measurements were calculated using a bespoke Nikon NIS-Elements imaging software module using a threshold-based method to automate the imaging and analysis of 3D objects.

ii.4 Germ layer differentiation

Hoik_1 cells were differentiated along ectoderm, mesoderm and endoderm lineages using STEMdiff™ Trilineage Differentiation Kit (StemCell Technologies, #05230) according to manufacturer’s instructions.

ii.5 Neural lineage differentiation

Hoik_1 cells were plated on Matrigel (Corning, 365234, Lot# 9238002) at a density of 100,000 cells/ 24 well, in mTeSR plus Y-27632 (10µM). Following 24 hours cell adhesion media was replaced with the organoid NI media and cells differentiated for either 5 (Neural 5) or 7 (Neural 7) days with daily media changes.

ii.6 Cell imaging

ii.6.1 Live cell imaging

Real-time phase contrast images were acquired using an IncuCyte ZOOM live imaging system (Essen Bioscience) every 30 min over a period of 48 hours using a 10x objective and confluency determined using IncuCyte software.

ii.6.2 Freshly isolated cell line growth quantification

Following acquisition of 15 phase contrast images per cell line growth condition daily, cells were manually counted using ImageJ (standard settings). Data were analysed by a two-sided paired Student’s t-test on matched samples, performed using samples using GraphPad Prism software (version 7.05).

ii.7 Immunofluorescence

ii.7.1 Sample preparation

ii.7.1.1 Whole cell

Plated live cells were fixed with paraformaldehyde (PFA, 4% (w/v), Sigma, P6148) for 10 minutes then incubated in permeabilization solution (0.5M glycine in PBS pH 7-8,) supplemented with Triton X-100 (0.5% (v/v), Sigma, T8787).

ii.7.1.2 Patient tissue

Paraffin embedded patient slides were prepared by a process of dewaxing with washes in xylene and ethanol, followed by antigen retrieval by incubation in EDTA (1mM) at 95°C for 20 minutes.

ii.7.1.3 OCT embedded organoids

Organoids were fixed with PFA (4% (w/v)) for 15 minutes at 4°C. Following three PBS washes, the organoids were re-suspended in sucrose solution (30% (w/v)) and left at 4°C until the organoids had sunk. Organoids were then embedded in Optimum Cutting Temperature solution (OCT, VWR, 36160E) in cryo-moulds and sectioned on a cryostat (20mm thickness). Sections were then equilibrated in PBS for 10 minutes.

ii.7.2 Staining

Blocking was carried out at room temperature for 2 hours with staining buffer (10% FBS in PBS) supplemented with Triton X-100 (0.04% (v/v)). Samples were then incubated at 4°C overnight in staining buffer with primary antibodies and subsequently incubated in staining buffer with secondary antibodies for 1 hour in the dark at room temperature. Cell nuclei were counterstained using 4',6-diamidino-2-phenylindole (DAPI, 1μM/ml, Sigma) and the fluorescence signal detected using an EVOS digital inverted fluorescence microscope (Life Technologies).

ii.7.3 Antibodies

Antigen	**Host**	**Supplier**	**CAT no.**	**Dilution**
Primary				
Vimentin	Mouse	Dako	M0725	1:200
Ki67	Rabbit	Abcam	ab16667	1:200
SOX2	Rabbit	Abcam	ab92494	1:200
T	Chicken	R&D	AF2085	1:100
PAX6	Mouse	Developmental Studies Hybridoma Bank	PAX6	1:200
SOX17	Goat	R&D	AF1924	1:200
MAP2	Chicken	Abcam	ab5392	1:1000
T	Rabbit	Abcam	ab209665	1:200
TuJ1	Mouse	Biolegend	801202	1:300
Secondary				
α-mouse 488	Goat	Life Technologies	A11029	1:200
α-chicken 647	Goat	Life Technologies	A21449	1:200
α-goat 647	Donkey	Invitrogen	A21447	1:200
α-rabbit Cy3	Donkey	Jackson ImmunoResearch	711-165-152	1:400

Table ii.1 List of antibodies used in immunofluorescence.

ii.8 Gene expression analysis

ii.8.1 Quantitative reverse transcription polymerase chain reaction (qRT-PCR)

Total RNA was extracted using the RNeasy mini kit (Qiagen, 74106) according to manufacturer’s instructions. Synthesis of cDNA was performed using SuperScript II Reverse Transcriptase (Invitrogen; 18064-014) according to the manufacturer’s instructions for cDNA synthesis using Oligo(dT) primer (Invitrogen; 18418012) using the following conditions:

For the qPCR using TaqMan Gene Expression Assays (Applied Biosystems) the following 15 µL reaction mixtures were prepared in triplicates:

Component	Volume for one reaction:
20x TaqMan Gene Expression Assay	0.75 µl
2x TaqMan Universal PCR Master Mix II, no UNG	7.5 µl
cDNA	3.0 µl
Nuclease-free H_2O	3.75 µl
Total reaction volume:	15 µl

Step	Temperature	Time
Hold	95°C	10 min
Cycle x40	95°C	15 sec
	60°C	1 min

Table ii.2 Reaction mixture compositions and qRT-PCR conditions.

The qPCR reaction was performed using Fluidigm BioMarkTM HD System and data was analysed using the 2-ΔΔCt method or 2-ΔCt for relative expression, using GAPDH as housekeeping control.

Gene	Assay ID
POU5F1	Hs04260367_gH
NANOG	Hs02387400_g1
PAX6	Hs01088114_m1
EGR2	Hs00166165_m1
T	Hs00610080_m1
NESTIN	Hs04187831_g1
TBX6	Hs00365539_m1

SOX2	Hs0105349_s1
GAPDH	Hs02758991_g1

Table ii.3 List of TaqMan probes (Thermofisher) used for qRT-PCR.

ii.8.2 mRNA Sequencing

ii.8.2.1 Sample preparation

Matched gNSC and NMP_Wnt3a GBM patient derived lines (BM005N/BM005W, BM007N/BM007W, BM009N/BM009W) were grown to confluency at passage 1 and RNA extracted using the RNeasy mini kit according to manufacturer's instructions. The integrity and concentration of RNA were determined using the Qubit RNA Integrity and Quality assay (Thermofisher). Sequencing was carried out by Novogene using Illumina NovaSeq 6000.

ii.8.2.2 Analysis

All data was analysed by Bioinformatics Support Unit at Newcastle University.

ii.8.2.2.1 Quality Control

Quality of FASTQ files were assessed with FastQC (version 11.8, https://www.bioinformatics.babraham.ac.uk/projects/fastqc/) then passed to MultiQC (https://multiqc.info) to aggregate results. Quality was very high in all samples with only reported errors confined to first ~ten bases and no read trimming necessary.

ii.8.2.2.2 Read Quantification

Reads were quantified against transcripts using Salmon [369] against Gencode Release 32 (https://www.gencodegenes.org/human/) with gene level counts obtained using R package 'tximport' (http://bioconductor.org/packages/release/bioc/html/tximport.html).

ii.8.2.2.3 Differential gene expression analysis

Differential expression between groups was calculated for NMP_Wnt3a samples against gNSC samples and genes classified as significant with <0.01 (>2 -log10) p-value using DEseq2.

ii.8.2.2.4 Gene set enrichment analysis (GSEA)

GSEA was carried out with the R package clusterProfiler (https://bioconductor.org/packages/release/bioc/html/clusterProfiler.html) and GSEA calculated for all genes comparing NMP_Wnt3a to gNSC with an absolute log2FoldChange greater than 1 using the Hallmark Gene Set from MSigDB [370–372].

ii.8.3 Survival analysis

ii.8.3.1 Gene signatures

Gene signature survival analysis was conducted using standard settings interrogating TCGA_GBM and TCGA _LGG [http://cancergenome.nih.gov/] datasets using GEPIA2 [373].

ii.8.3.2 Individual gene

Overall survival interrogated using [374] of RNA-sequencing TCGA_GBM_LGG [http://cancergenome.nih.gov/] and CCGA_GBM_LGG datasets [375].

ii.9 Assembloid assay

ii.9.1 Assay set up

ii.9.2 hCO assembloid assay

Spheroids of GBM or NP lines were formed in ULA 96-well plates, 1000 cells/well (unless otherwise stated), in normal growth media for 24 hours. For non GFP- expressing lines, following formation, spheroids or tissue pieces were labelled by incubation with ViaFluor® SE Cell Proliferation 488 Kit (Biotium, 30086) or CellTracker Green (1μM, Thermofisher, C7025) for 1 hour. Subsequently, hCO (following 9 days of differentiation) were placed in co-culture with spheroids, in ULA 96-well plates, for 48 hours.

ii.9.3 LBsph (Lineage biased spheroid) assembloid assay

Spheroids of GBM or NP lines were formed in ULA 96-well plates, 1000 cells/well (unless otherwise stated), in normal growth media for 24 hours.

Hoik_1 cells were differentiated along ectoderm, mesoderm and endoderm lineages using STEMdiff™ Trilineage Differentiation Kit (StemCell Technologies, #05230) according to manufacturer’s instructions. For neural differentiation Hoik_1 cells were plated on Matrigel (Corning, 365234, Lot# 9238002) at a density of 100,000 cells/ 24 well, in mTeSR plus Y-27632 (10µM). Following 24 hours cell adhesion media was replaced with the organoid NI media and cells differentiated for either 5 (Neural 5) or 7 (Neural 7) days with daily media changes.

LBsphs of lineage differentiated cells were formed in ULA 96-well plates, 50,000 cells/well in their respective media supplemented with Y-27632 (50µM) for 24 hours. Subsequently LBsph were placed in co-culture with GBM/NP spheroids, in ULA 96-well plates, for 48 hours.

ii.9.4 ImageJ invasion image analysis

Images were collected at various time points using an EVOS digital inverted fluorescence microscope, analysis conducted using ImageJ (Fiji) (standard settings) [376], and data analysed using one/two way ANVOA using GraphPad Prism (version 8.42).

ii.9.4.1 Percentage infiltration

Total GFP area was detected using colour thresholding of the GFP-positive pixels in each field and calculating area using the measure function. Infiltrated GFP area was detected by tracing the borders of the cerebral organoid using freehand tool and identifying it as a region of interest (ROI). By clearing the area outside of the ROI of the GFP-pixels within the organoid can be thresholded and area calculated. Percentage infiltration calculated as infiltrated GFP area divided by total GFP area.

ii.9.4.2 Disseminated cells

Number of disseminated cells was calculated using colour thresholding of GFP-positive pixels. Using the analyse particles functions, using parameters of 0-infinity for pixel size and 0.00-1.00 for circularity, number of particles was measured.

ii.9.4.3 Migration distances

Migration distances were measured using freehand straight line tool. Distances were measured from estimated entry point to edge of spheroid within organoid (spheroid leading edge) and to outermost detected GFP pixel (single outermost cell).

ii.9.5 CellProfiler automated image analysis

Images were collected at various time points using an EVOS digital inverted fluorescence microscope, analysis conducted using CellProfiler (3.1.8) [377].

Module	**Function**	**Settings**
LoadImages	Identify image files	Any file ending in .tif. Upload images already split into TRANS and GFP channels.
NamesAndTypes	Assign meaningful names to images	GFP images identified as Sph and TRANS images identifies as Org
ColorToGray	Convert GFP images to grayscale	Split channel 2
EnhanceEdges	Enhance the edges of GFP to help identify individual cells with lower intensity	Use Canny as edge-finding method calculating automatically Gaussian’s sigma, threshold and value for low threshold with threshold adjustment factor 2
IdentifyPrimaryObject	Identifies GFP as biological object of interest	Use of advanced settings identifying objects with diameter 5-100 pixels but do not discard objects outside of the diameter range. However, discard objects which touch the border of the image. For thresholding use the global strategy with Otsu method, 1.3488 smoothing scale, 1.0 correction factor and 0.0-1.0 bounds on threshold. Use intensity to distinguish clumped objects and draw dividing lines between clumped objects. Automatically calculate size of smoothing filter for declumping and minimum allowed distance between local maxima. Never fill holes in identified objects and continue handling of objects if excessive number of objects identified.
SplitOrMergeObjects	Merge all of GFP to one object	Use identified GFP primary objects and merge using distance at a maximum of 1000.
MeasureObjectIntensity	Measure intensity	Measure intensity of grayscale image using merged

	features for identified object	GFP image
SpitOrMergeObjects	Merge only cells that are touching to try and identify 'core'	Merge objects using 0 maximum distance
MeasureObjectSizeShape	Measures several area and shape features of merged GFP objects after merging touching objects allowing for subsequent filtering	Measure GFP merged objects
FilterObjects	Remove other objects leaving just the 'core' of merged objects	Filter on the GFP merged image. Filter using 1000 minimum value limit for area measurement only.
MaskObject	Removes objects outside of a specified region or regions to help identify just the core as object	Mask using objects identified following filtering. Do not invert mask, keep overlapping region in objects that are partially masks and renumber resulting objects
IdentifySecondaryObjects	Identify the 'core' as secondary object having identifying it by previous module	Identify secondary object by propagation method, thresholding by global strategy with Otsu method. Two classes thresholding to be performed with 0.0 smoothing scale, 1.0 correction factor, 0.0-1.0 bounds on thresholding with 0.02 regularization factor. Holes should be filled in identified objects with no discarding of objects touching the border of the image.
IdentifyTertiaryObjects	Identifies 'infiltrates' as tertiary object by removing 'core' objects from total GFP objects	Smaller 'core' secondary object subtracted from larger total GFP primary object. No shrinking of smaller object prior to subtraction.
SplitOrMergeObjects	Merge all of 'infiltrates' to identify as one object	Use identified 'infiltrates' and merge using distance at a maximum of 1000.
MeasureObjectSizeShape	Measures several area and shape features	Measure size and shape of total GFP objects, 'infiltrates' (merged and unmerged) and 'core'
ImageMath	Inverts Org image by subtracting image intensities from 1.	Invert Org image, multiplying first image by 1.0, raising the power of the result by 1.0, multiply the rest by 1.0 and add to result 0.0. Values set less than 0 equal to 0 and greater than 1 equal to 1, with image masks not ignored.
IdentifySecondaryObject	Identify Org as a secondary object	Identify secondary object by propagation method, thresholding by global strategy with Otsu method. Two classes thresholding to be performed with 0.0 smoothing scale, 1.0 correction factor, 0.0-1.0 bounds on thresholding with 0.02 regularization factor. Holes should be filled in identified objects with no discarding of objects touching the border of the image.
SplitOrMergeObjects	Merge organoid to create one Org object	Use Org secondary object and merge using distance at a maximum of 0.
MeasureObjectSizeShape	Measures several area and shape features of merged Org object allowing for subsequent filtering	Measure Merged Org objects
FilterObjects	Filter out background objects leaving just one Org	Filtered Merged Org using area limits measurements with a minimum value of 50000.

MeasureObjectSizeShape	Measures several area and shape features of objects allowing for subsequent filtering	Measure filtered Org and Merged total GFP objects
ExportToSpreadsheet	Export all measurements	Do not select measurements to export and export all measurement types. Do calculate per-image mean values for object measurement. Do not calculate per-image median, standard deviation values for object measurements or create a GenePattern GCT file.

Table ii.4 CellProfiler pipeline components Indicated is the function of each module with specific settings used.

Infiltrate Behaviour Parameter	Object	Exported Measurement
Area	Merged GFP primary object	Area
RFU	GFP greyscale	Mean intensity
Number of objects	Infiltrates tertiary object	Number of objects
x, y Co-ordinates	Merged GFP primary object and filtered Org object	Location centre X and Y

Table ii.5 Measurement used for particular invasion behaviour parameters. Indicates what object was used for each infiltrate behaviour parameter, and what the exported measurement was.

ii.10 Protein interaction networks

Protein interaction networks were determined by the STRING database v.11 [378] and visualised by Cytoscape [379].

ii.11 Cellular network treatments

ii.11.1 ROCK inhibition treatment

Cells were seeded at a density of 10,000 cells/cm^2 and treatment started post cell adhesion. Network phenotype cells were established with Y-27632 (20μM) treatment and control phenotype cells with vehicle (H_2O) treatment for 24 hours.

ii.11.2 Network cellular projection length (CPL) quantification

Images of neurite-like projection formation were obtained and subject to image analysis using the NeuriteTrace plugin for ImageJ (Fiji) [380]. The

TuJ1-stained CPL (µm) was calculated as follows: total projection length (all cells) divided by the number of (DAPI-stained) nuclei. For CPL quantification, at least 5 different images (technical replicates) were analysed per treatment for each independent experiment.

ii.11.3 LPA treatment

Control and network phenotypes were established for 24 hours with treatment of vehicle (H_2O) or Y-27632 (20µM) in cells seeded at a density of 10,000 per cm^2. Established control cells continued to be treated with vehicle (H_2O) or treated with Oleoyl-L-α-Lysophosphatidic acid sodium salt (LPA, 1 µM, Sigma, 22556-62-3). Established network cells were subsequently treated with vehicle or LPA with and without Y-27632 (20µM). After 8 hours cells were fixed for 15 minutes with 4% (w/v) PFA. Cells underwent staining for TuJ1 and CPL quantification was performed for each experiment on 5 images per condition using the NeuriteTracer ImageJ plugin.

ii.11.4 Matrigel network formation

GFP-expressing GBM1 cells were incubated in matrigel droplets (10,000 cells per droplet) with the addition of vehicle (H_2O) or Y27632 (20µM). After 16 hours images were acquired using an EVOS digital inverted fluorescence microscope and cellular projection lengths quantified from 4 images per condition in each biological replicate using NeuriteTracer ImageJ plugin.

ii.11.5 TGFβ treatment

GFP expressing cells were seeded at a density of 10,000 cells/cm^2 on matrigel coating (lot dilution factor) or on cell lines's normal growth coating conditions. Cells were treated for 72 hours with Y-27632 (20µM), transforming growth factor beta (TGF-β, 10ng/ml, Miltenyi, 130-095-067), Y-27632 (20µM) and TGF-β, 10ng/ml, or vehicle (H_2O). CPL quantification was performed on 5 images per condition using the NeuriteTracer ImageJ plugin.

ii.12 Immunoblotting

Whole-cell extracts were prepared by harvesting cells either in Laemmli sample buffer supplemented with 10 mM sodium fluoride, 1mM sodium vanadate, 10 mM sodium β-glycerophosphate, 0.5 mM PMSF and Complete-EDTA free protease inhibitor (Roche, Diagnostics GmbH), or in cell lysis buffer (Cell Signalling, 98035) supplemented with 1mM PMSF (Cell Signalling, 8553). Samples were sonicated for 15 seconds prior to centrifugation. Lysates were then loaded onto Mini-Protean TGX precast gels (4-15%, Biorad, 4561085 or 4561083) and resolved proteins transferred onto nitrocellulose membrane (0.45 µm, Biorad, 9004-70-0). Fluorescence was detected using ChemiDoc MP Imaging System (BioRad) and HRP detected using ECL prime detection reagent (Amersham, RPN2232), with quantification performed using ImageJ (Fiji) (standard settings).

Antigen	**Host**	**Supplier**	**CAT no.**	**Dilution**
Primary				
MAP2	Chicken	Abcam	ab5392	1:1000
TuJ1	Mouse	Biolegend	801202	1:1000
p-MYPT1 (Thr853)	Rabbit	Cell Signalling	4156	1:1000
MYPT1	Rabbit	Cell Signalling	2634	1:1000
β-actin	Mouse	Sigma	A1978	1:10000
Secondary				
α-chicken 647	Goat	Life Technologies	A21449	1:5000
α-mouse 488	Goat	Life Technologies	A11029	1:5000
α-mouse HRP	Goat	Sigma	A4416	1:5000
α-rabbit HRP	Goat	Sigma	A6154	1:5000

Table ii.6 List of antibodies used in immunoblotting

ii.13 Mitochondrial transfer assay

Mitochondria of donor cells were fluorescently labelled by incubating cells for 2 hours with MitoTracker Red (25 nM, Thermofisher, M7512) before washout and seeding in a 1:1 co-culture with GFP-expressing recipient cells (harbouring unlabelled mitochondria) at a total cell density of 10,000, per cm^2 unless otherwise stated. Control and network phenotypes were established using vehicle (H_2O) or Y-27632 (20µM) for 24 hours. Cells were subsequently fixed with 4% (w/v) PFA for 15 minutes. Images were taken using an EVOS digital inverted fluorescence microscope. By defining the area of GFP labelled cells by colour threshold using ImageJ (default setting, colour space, HSB), the percentage area of MitoTracker positive mitochondria could be determined per cell. For analysis 5 images per condition were quantified, with >90 cells analysed per condition. Confocal images were also taken using a Nikon A1R confocal microscope following staining with Alexa Fluor 647 Phalloidin (1:100, Invitrogen, A22287).

Chapter 1

Establishment of human-human assembloid assay allows detection of GBM invasive behaviour

1.1 Results

1.1.1 Establishing assembloid formation using human derived eCOs

The assembloid assay was previously developed and described using mouse ESCs generating early stage mouse derived-CO (mCO) [307]. Although in some CO literature ‘assembloid’ refers to the fusion of spheroids resembling different brain regions in the development of a CO by directed differentiation [299], here assembloid refers to the fusion of an invading patient derived spheroid compartment and a PSC-derived hCO. While the previously developed mouse assembloid assay overcame limitations in other GBM invasion studies by introducing a 2-compartment tissue self-assembly system [381], the use of mCOs could limit the potential for clinical translation. As with xenograft models, there are concerns with regards to human cells artificially adapting to the murine microenvironmental context [382], and an entirely human-based cellular system may be of advantage. To this end, we sought to establish the use of human PSC-derived cerebral organoids (hCO) for the assembloid assay.

We first sought to qualitatively assess whether the assembloid formation could be achieved with early hCO differentiation stages, which would be expected to be throughput-compatible and more homogeneous compared to prolonged differentiation protocols [256] [307] [303]. Full differentiation of hCOs takes 1-2 months, however initial lineage commitment and maturation occurs within around 3-4 weeks in 4 stages utilizing different growth media (Fig 1.1A). Advancement to next stages is based on EB or spheroid size as previously defined [256]. Following the formation of self-organising EBs both mCOs and hCO subsequently follow through the same CO differentiation stage, but with variance in the number of days in each stage as a consequence of hCOs growing to larger sizes than mCOs.

Previously, hCOs at similar stages were compared, previously used for mCO (stage 4) and at an earlier time point for hCOs (stage 2) (Fig 1.1B, data from Barbara da Silva). After co-culture, these observations suggested that a larger number of stage 2 hCOs were invaded by GBM1 cells (Fig 1.1B) compared to stage 4 hCOs leading to assembloids at every investigated time point: 2, 4 and 6 days (Fig 1.1C).

Within differentiation stage 2 of hCOs, we further investigated the optimal period of neural induction hCOs for use in the assembloid assay. A differentiation period of 9 days was associated with 100% of hCOs being invaded fully compared to 83% of ‘day 10 hCOs’, already 1 day after co-culture with GBM spheroids (Fig 1.1D). Henceforth the human-human standard-assembloid assay was enabled by a ‘stage 2, day-9-hCO-differentiation period’ (Fig 1.1E).

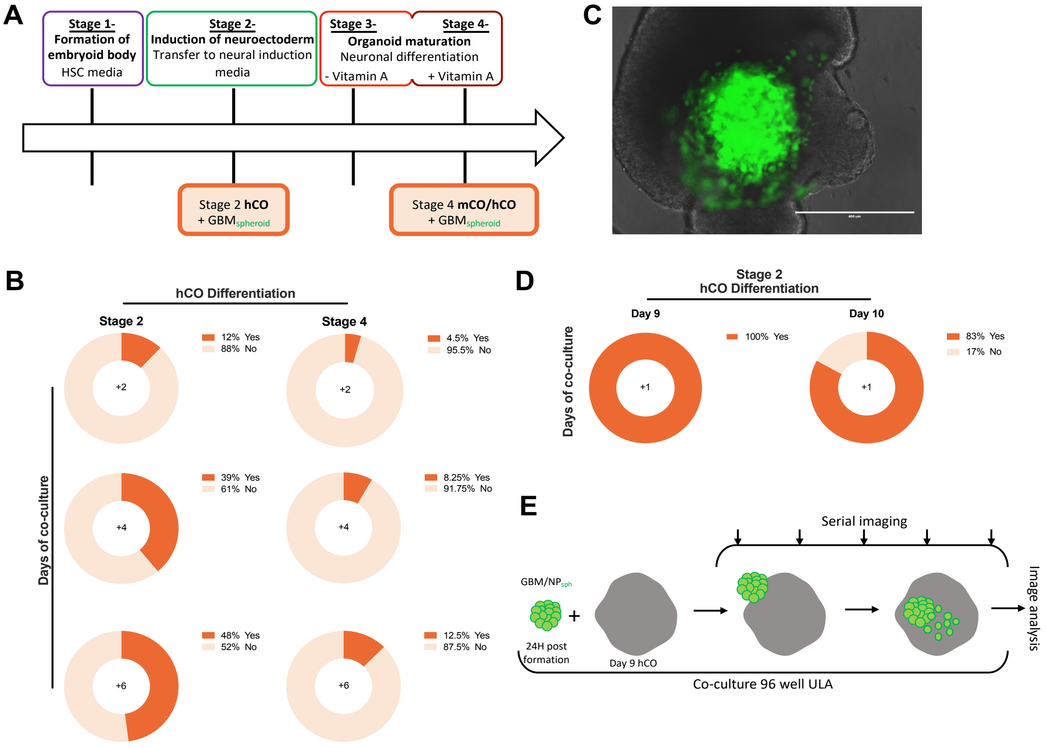

Figure 1.1 Development of GBM assembloid assay using early stage human derived cerebral organoids (hCO). (A) Schematic describing stages mCO and hCO are taken for assembloid assay in the whole organoid differentiation timeline. **(B)** Percentage of stage 2 and 4 hCO successfully infiltrated by GFP-GBM1 spheroids by days 2, 4, and 6 following co-culture. Data obtained from Bárbara da Silva. **(C)** Representative image of assembloid 2 days post co-culture of stage 2 hCO and GFP-GBM1. Scale bar 400µm. **(D)** Percentage of stage 2 hCO (days 9 and 10) successfully infiltrated by GFP-GBM1 spheroids 1 day post co-culture, n=5. **(E)** Standard-assembloid assay schematic overview describing co-culture of hCO and GFP spheroids with serial imaging throughout assay with image analysis and immunofluorescent staining final readouts. HSC= human stem cell, ULA= ultra low attachment, mCO= mouse cerebral organoid, hCO= human cerebral organoid.

1.1.2 Brain identity is dynamic in early stages of CO differentiation and sustained during assembloid formation

As our results suggested the use of hCOs at the earlier differentiation stage 2 than previously used for mCO assemoloid formation (stage 4), we investigated whether stage 2 hCOs displayed brain lineage identity.

At days 9 and 10 post EB formation, we isolated total RNA from hCOs and carried out qRT-PCR to detect marker gene expression. Results indicated a reduction of pluripotency capability with a decrease in gene expression of POU5F1 and NANOG [383]. There was also evidence of neural lineage identity with upregulation of forebrain marker PAX6 [384] and hindbrain marker EGR2 [385]. Significant fluctuations in neural marker expression at different days of the same differentiation stage (Fig 1.2A) suggest that lineage specification cues and cellular organisation are dynamic in the early stages of differentiation, before sustained cell maturation in the later stages of differentiation.

Following 48 hours post co-culture of early stage hCO with GBM (Fig 1.2B), we confirmed the presence of neural and GBM markers VIM and SOX2 [105, 110]. We also quantitatively confirmed assembloid expansion capability with Ki67 immunopositivity which was found to co-localise with VIM but not SOX2 (Fig 1.2B). Although tumour and neural assembloid compartments cannot be distinguished using human specific antibodies, it is possible that VIM/Ki67 co-staining indicates a proportion of the invading GBM1 cellular compartment.

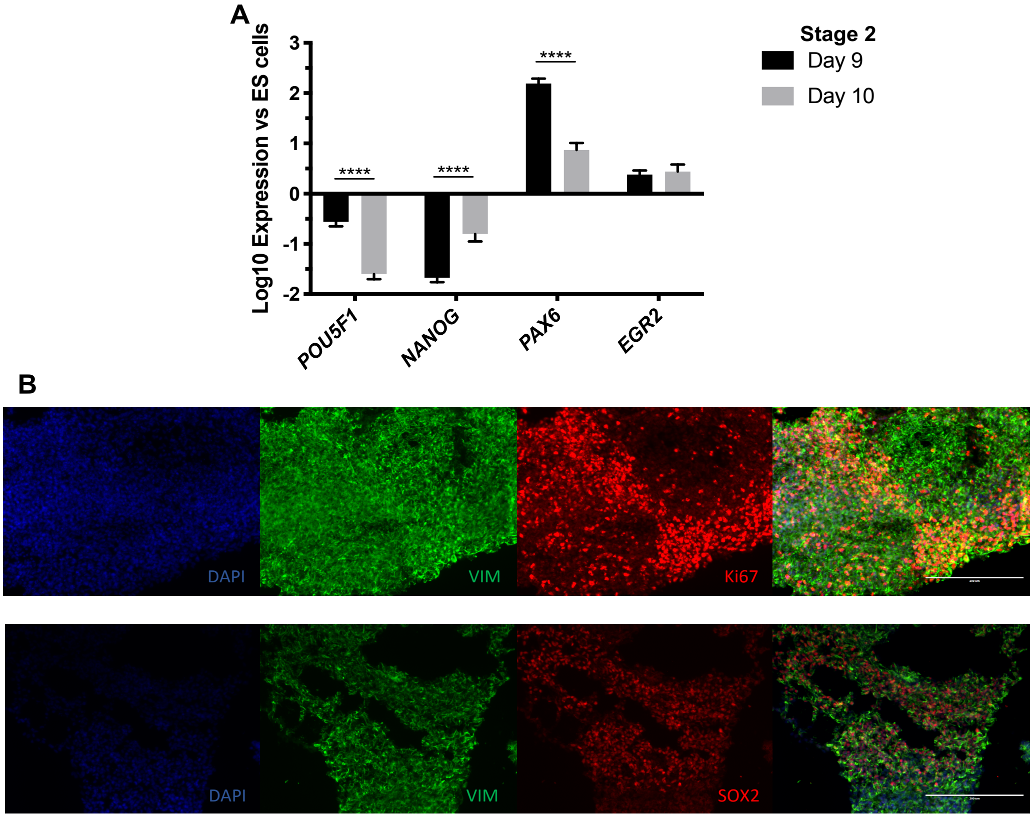

Figure 1.2 hCOs express brain markers. (A) At stage 2 differentiation hCOs show downregulation of pluripotency markers (POU5F1, NANOG) with upregulation of forebrain (PAX6) and hindbrain (EGR2) markers. Mean (± SD) shown for hCOs (n=3) at both day 9 and 10 of differentiation. P-values obtained by two-way ANOVA are shown as *(<0.05), **(<0.005), ***(<0.0005), and ****(<0.0001). **(B)** Representative immunofluorescence images of assembloids, 48 hours following co-culture with GBM1 showing positivity for VIMENTIN, SOX2, and MKI67 (Ki67). Scale bar 200 μm.

1.1.3 Infiltration of hCO is a cancer specific phenotype

The assembloid assay previously revealed differences in invasive capability of GBM and noncancerous NP cells into mCOs [307]. We thus qualitatively confirmed that the use of hCOs in the assembloid assay could still discriminate invasive behaviour of GBM1 compared with NP1 cells. We tested GBM1 and NP1 spheroid aggregates containing 500, 1000, 2000 and 5000 cells.

Across all of the spheroid sizes we observed that GBM spheroids were able to infiltrate hCOs, whereas their NP counterparts did not show an invasion phenotype. (Fig 1.3A). The use of 1000 rather than 500 cells per

GBM/NP spheroids appeared to be most appropriate with regards to mimicking the published protocol [307]; however, accounting for the larger size of hCOs compared with mCOs. The 1000 cells containing spheroids showed individual and patches of cells migrating from the main core of the spheroid, which suggested that our human-human assembloid system can indicate differences of different cellular infiltration behaviours.

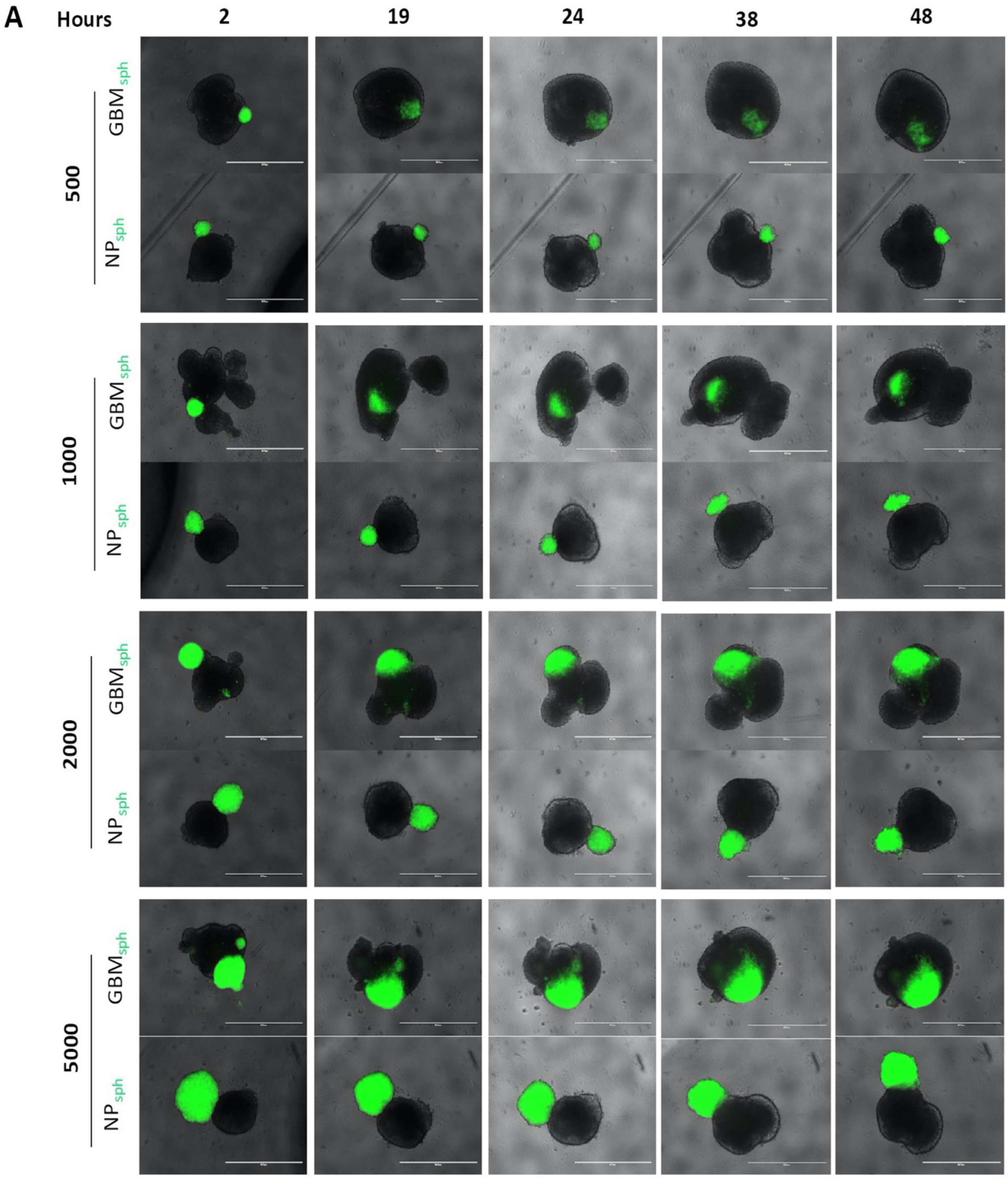

Figure 1.3 Infiltration of hCO is a cancer specific phenotype. (A) GFP-GBM1 and GFP-NP1 spheroid infiltration into hCOs at the indicated cell numbers per spheroid Scale bar 1mM.

1.1.4 Establishing image-based parameters revealing significant differences in invasion behaviour of GBM and NP cells

For interrogating cellular mechanisms of invasion beyond binary (yes versus no) observations, we tested several parameters reflecting different aspects of cell migration during and after assembloid formation. We first quantified the percentage of signal (pixels) emitted from GFP-positive GBM1 and NP1 spheroids that had invaded the assembloids beyond the hCO border (Fig 1.4A). At 24 hours post assembloid formation, GBM1 cells infiltrated the assembloids by 91%, whereas NP1 cells displayed an 18% invasion capacity (Fig 1.4B). We also quantified cellular spread/migration from the parental spheroid within the hCO. This was based on the number of ‘patches’ or ‘objects’ that the GBM1 spheroid cells segregated into during hCO infiltration (Fig 1.4C). This revealed a marked spread of GBM1 spheroids over time with an increase from on average 97 to 194 disseminated GFP-positive signals (defined as objects) at 24 and 48 hours post assembloid formation respectively. In contrast, NP1 spheroids exhibited a lower spread with an average of 11 and 17 disseminated objects at the 24- and 48-hours time points, respectively (Fig 1.4D). We further determined the distance between the cells/patches that had migrated farthest in the assembloid (defined as ‘outermost cell’; Fig 1.4E right) and edge of remaining spheroid core compared to the point of docking and entry into the hCO (defined as ‘leading edge’ cell population; Fig 1.4E left). This revealed that GBM1 cells showed a marked increase in both outermost cell and leading edge migration distance compared to NP1 cells at the 24-hour and 48-hour time points post assembloid formation (Fig 1.4F). Quantifying infiltrative behaviour has therefore enabled the elucidation of differences between different cellular invasive capabilities in the GBM1 and NP1 cell models.

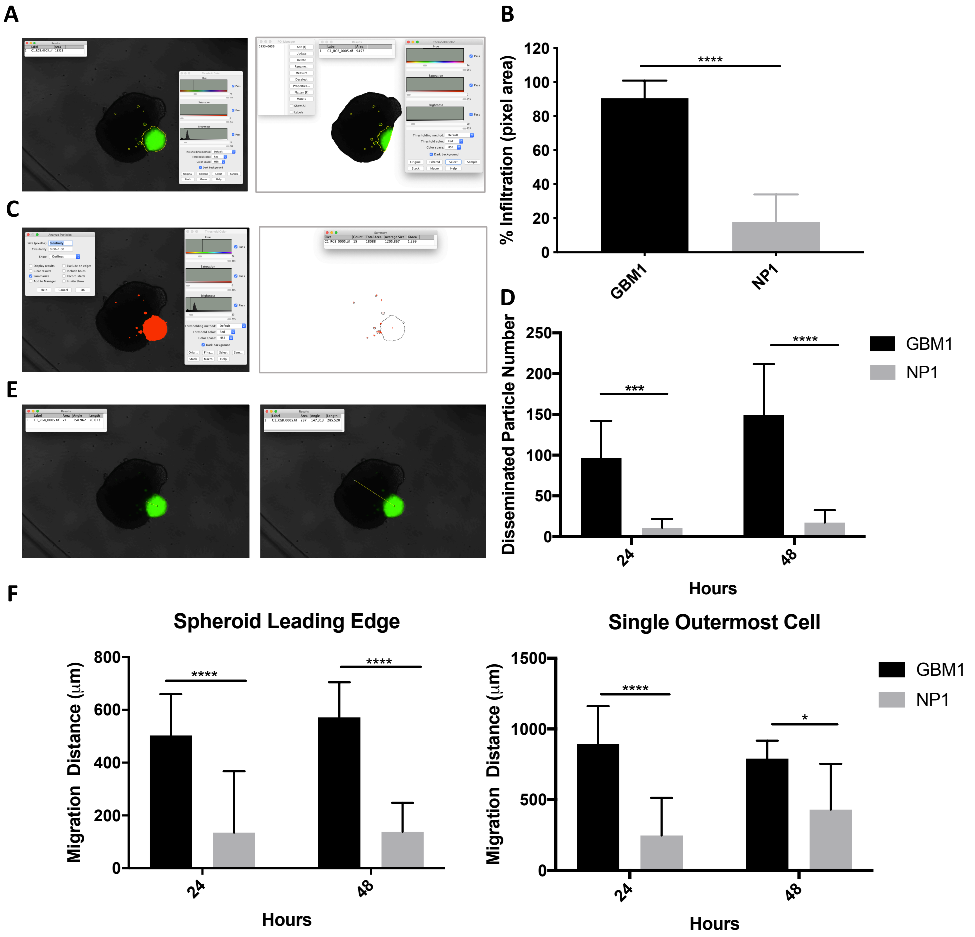

Figure 1.4 Invasion behaviour of 1000 cell GBM spheroids, following co-culture with hCO, is significantly different to controls. (A) Total GFP signal thresholded area measured in the entire imaging field (left) and infiltrated GFP signal within the ROI organoid (right). **(B)** Percentage infiltration of GFP-GBM1 compared to GFP-NP1 area after 24 hours of hCO co-culture. (**C**) Following GFP colour thresholding (left), number of particles are calculated (right). **(D)** Number of GFP-GBM1 particles compared to GFP-NP1 at 24- and 48-hour time points. **(E)** Distance measured from organoid border (at estimated entry point) to spheroid edge (left) and from same entry point to outermost GFP particle (right). **(F)** The leading edge of GFP-GBM1 spheroids (left) and single outermost cell (right) compared to GFP-NP1 spheroids infiltrating hCOs at the 24- and 48-hour time points. Data are mean (± SD) shown using 9 independent assembloids per condition. P-values are based on unpaired t-test (B) or two-way ANOVA (D, F) and shown as *(< 0.05), **(<0.005), ***(<0.0005), and ****(<0.0001).

1.1.5 Automated image analysis parameters describe significant differences between GBM and NP invasion

The percentage of GBM1/NP1 spheroid infiltration into hCOs, the number of disseminated cells, and migration distances discriminated between two discrete invasion behaviours (GBM1 versus NP1), as determined using ImageJ software, provided a basis for developing automated image analysis. To this end, a CellProfiler [377] pipeline (Table ii.4) was established with the goal of automatically detecting the difference in invasive assembloid behaviours of the GBM1 and NP1 models.

For the image analysis pipeline training, one set of GBM1 images was used featuring assembloid images at the 2-, 19-, 24-, 36- and 48-hour timepoints that were chosen for representing the dynamic cellular behaviours. We set out to evaluate whether spheroid infiltration, disseminated cells and migration distances could be determined through a dedicated image analysis workflow that analysed image properties such as identifying objects of interest and measuring characteristics based on size and shape. Once this pipeline was established (Table ii.4), it was further trained on one NP1 image set, and subsequently, analysis was completed for one full experimental set of images including 3 assembloids per condition for the 5 time points (2-, 19-, 24-, 36- and 48-hours).

To determine the percentages of GBM1/NP1 spheroid infiltration within hCOs, the GFP signal was identified and merged to consider as one region of interest and the total GFP area was determined for this merged primary object. Next, we identified the hCO as a separate object to allow quantification of the GFP area within it. However, as thresholding is traditionally performed using different fluorescence-based labels, the unlabelled hCOs could not be segmented as a separate object to spheroids within brightfield images (Fig 1.5A). Alternatively, in an effort to load pre-segmented objects into our CellProfiler pipeline, RGB images were attempted to be processed using Ilastik [386] and Cellari [https://cellari.io]. Both softwares allow signal segmentation without explicitly requiring fluorescence labelling following training with manual object/signal segmentation on a small subset of images. Despite training using >15 images, both softwares did not efficiently segment hCO and GFP compartments (Fig A.1). Training the programmes using this manual segmentation successfully identified the main core of GFP spheroids but was inadequate for tracing cells at the hCO-invading spheroid edge as well as distally migrated GFP ‘patches’ throughout the hCO. Hence, we did not continue efforts to automate quantification of these parameters for the existing image data and omitted them from the pipeline (therefore not included in Table ii4).

Despite being unable to uncouple spheroid objects from hCO we sought to determine parameters that would describe differences in invasive behaviour based solely on GFP objects, whose behaviour would be determined by assembloid invasion, or lack thereof. The ‘measure total area module’ of CellProfiler highlighted the total GFP signal of GBM in the initial image set, which increased throughout the assay. When applying this analysis to the GBM1 and NP1 images sets, it showed a consistent and significant (>2 fold) increase in the GBM1 GFP-positive area over 48 hours, as compared to the NP1 GFP counterpart (Fig 1.5B). Subsequently, we used a module to measure the intensity of the GFP green signal. We determined that the increase in GFP signal area in the assembloid, was coupled with a decrease in GFP signal intensity as a consequence of the GBM1 cell spread (Fig 1.5C). In contrast, the GFP signal intensity of the NP1 GFP-positive signal was not altered, hence remaining significantly higher by between 1.0-1.8 fold over time compared with the GBM1 GFP signal (Fig 1.5C). At ~48 hours of assembloid culture, the GBM1 GFP-positive signal intensity showed a drop of 40% compared to NP1 GFP-positive signal.

Additional CellProfiler software functions allowed us to identify closely related objects that define the GFP spheroid ‘core’ in a semi-supervised fashion. By filtering the resulting objects based on their pixel size (cutoff = >1000), the spheroid ‘core’ was able to be removed, enabling the quantification of the remaining GFP-positive ‘disseminated’ objects which had migrated into the assembloid (Fig 1.5D, right). Throughout the assay the number of GBM1 ‘disseminated objects’ increased by >2 fold, whereas NP1 numbers remained unaltered over a 48-hour culture period (Fig 1.5D, left). The significant difference between the number GBM1 and NP1 ‘disseminated objects’ indicates a selective ability of GBM1 cells to migrate from the spheroid post assembloid formation.

To automatically measure migration distance, we utilised the x- y- coordinates of the total merged GFP-positive centre position, tracking the movement of objects over time. To take the effects of hCO movement in suspension into account, all coordinates were normalised to the hCO ‘centre coordinate’ at each time point using relative to t_0. We observed a smaller radius of the GBM1 object movement around the ‘centre coordinate’ compared to the NP1 trajectory (Fig 1.5E). This indicates GBM infiltration of hCOs, whereas, due to lack of invasion, NP1 spheroids rotate at the hCO periphery (Fig 1.5E).

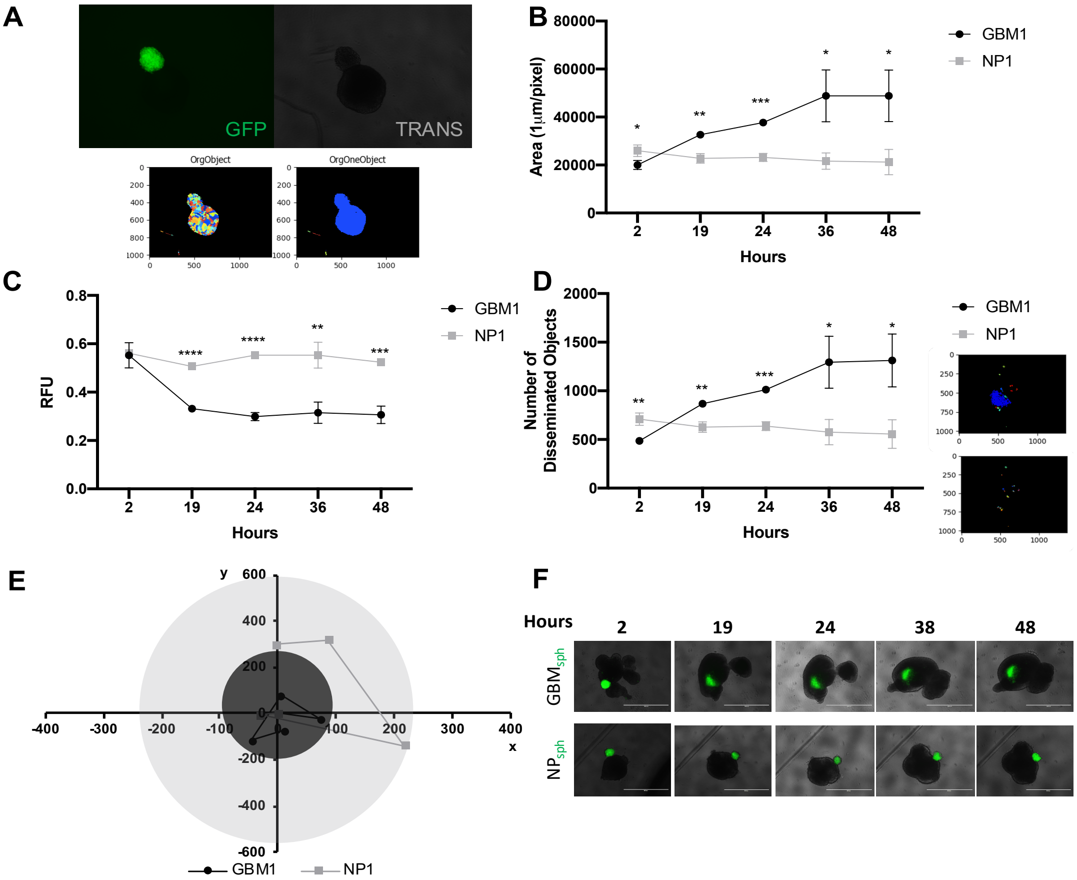

Figure 1.5 Several automated analysis parameters identify significant differences between GBM and controls within assembloids. (A) Due to lack of organoid fluorescent labelling (top) cell profiler analysis did not segment spheroids and organoids as separate objects (bottom). Area **(B)** of GBM GFP positive pixels increases over time, whereas GFP signal intensity **(C)** in GBM compared to NP assembloids. Number of GFP-GBM1 objects outside of core increased during assembloid formation **(D)** as determined by CellProfiler analysis after removal of GFP 'core' leaving 'infiltrates' (right). Data are mean (± SD) shown for 3 assembloids per condition. P-values are based on multiple t-tests and shown as *(< 0.05), **(<0.005), ***(<0.0005), and ****(<0.0001). **(E)** Radius of GFP-GBM1 movement is smaller than GFP-NP1, where data points are x, y position coordinates of GFP centre at 2, 19, 24, 36, 48 hours post assembloid formation. All tracks aligned to hCO and then origin. **(F)** GFP-GBM1 movement is restricted once intermingled within assembloid, whereas GFP-NP1 rotates together with hCO. Scale bar 1 mM.

1.1.6 Assembloid invasion dynamics vary across GBM specimens

GBM is a highly heterogeneous malignancy characterized by inter-tumoural variability. Therefore, we endeavoured to investigate if the assay could determine differences in invasive capability across GBM models. To this end, in addition to the previously used GBM1 and NP1 models, we employed a range of established patient lines, including a gliosarcoma model (GBM11), the recurrent GBM line GBM20, the GBM model GSC001, and the OX2 E line, which was isolated from the surgical ‘edge’ of a GBM tumour. After 2 hours of co-culture with hCOs, differences in the invasive behaviour between the lines were detected. GBM20 and OX2 E spheroids exhibited 92% and 52% percent infiltration. For the GBM1, GBM11, and SHF001N spheroids, infiltration was 22, 19 and 21 percent respectively (Fig 1.6A, left). Furthermore, we observed that all lines were able to almost fully infiltrate at the 24-hour time point (Fig 1.6A right). The average percentage of infiltration ranged from 93 to 100% across the models and was significantly (p=<0.0001) higher in the GBM lines compared to the NP1 control.

As the assay detected differences in invasive potential between different lines, and specifically, an increased invasive potential of a tumour edge-derived model during the early stage of the assay, we elucidated the invasive potential of matched ‘core’ and ‘edge’ GBM models derived from the same patient. The additional models were: GBM 30 with primary and matched recurrent ‘core’ and ‘edge’ lines, GBM40 ‘core’ and edge’, GBM52 ‘core’ and ‘edge’ and OX2 with ‘edge’ and mixed ‘core and edge’ lines. We captured more time points during the earlier dynamic stage of assembloid formation (0.5, 2, 4, 6 and 8 hours) to improve the quantification of invasion differences between lines. Between the 0.5 and 8 hour timepoints, the tumour-edge-derived models GBM40 and GBM52 showed a tendency for an increase (>1.6 and >1.1-fold) in hCO infiltration by compared to their matched ‘core’ models (Fig 1.6B). Also ‘edge’ OX2 model showed an increase in hCO infiltration by <1.2-fold compared to it’s matched ‘core and edge’. GBM30 ‘recurrent edge’ spheroids exhibited a 2.4-fold higher infiltration compared to ‘primary spheroids’ within the first 2 hours of assembloid formation. However, after 4 hours of assembloid culture, we observed little difference in percentage infiltration between the ‘recurrent core’ and ‘primary’ models (fold changes between 0.3-1.0) indicating that assembloid infiltration entered a more static phase.

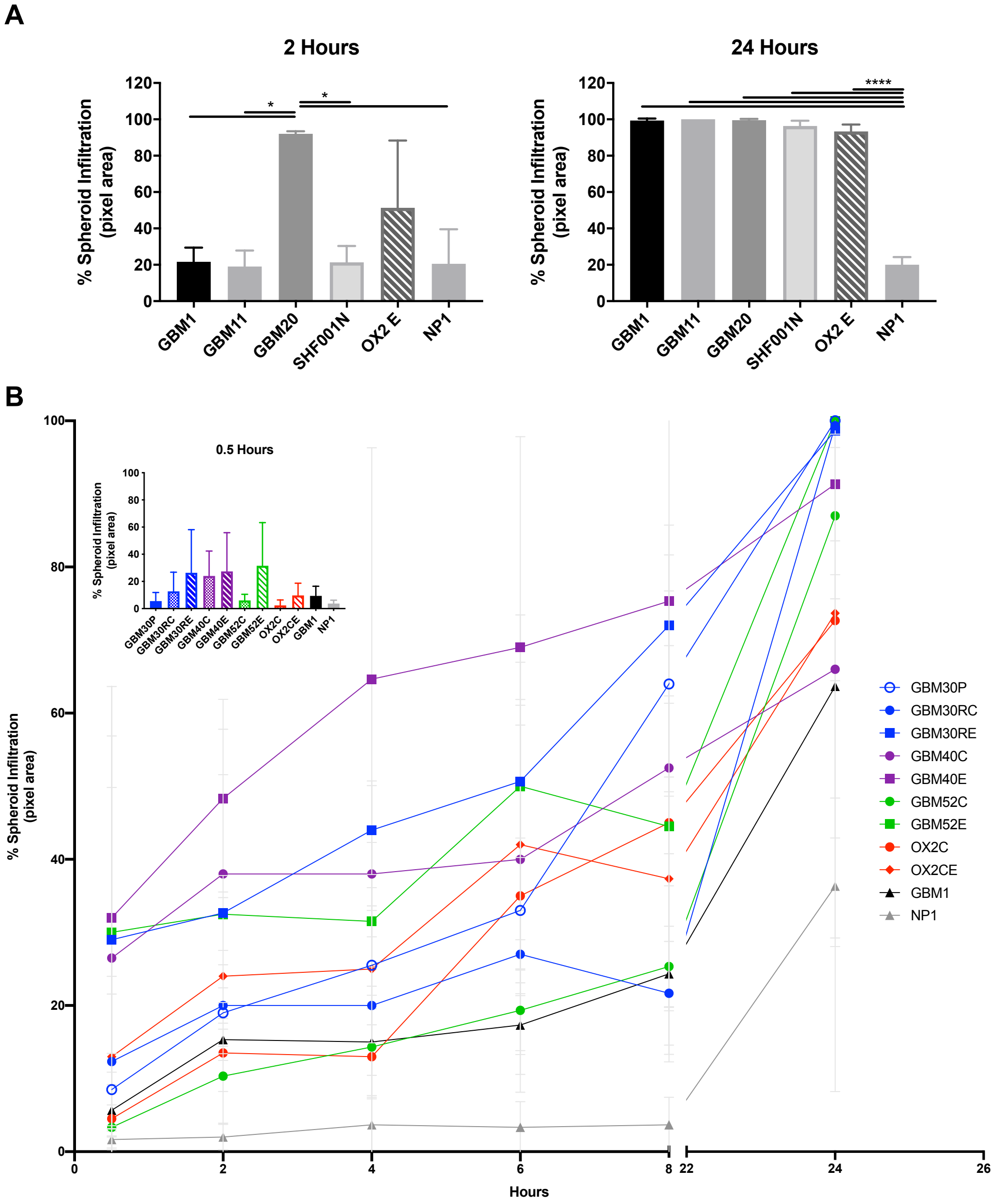

Figure 1.6 Different GBM models show differences in early infiltration in hCO. (A) Differences in percentage spheroid infiltration between GBM models seen at 2 hours (left) rather than 24 hours (right) following co-culture. Spheroids were labelled using CellTracker Green (Invitrogen). **(B)** Percentage spheroid infiltration of matched GBM models over time following co-culture with hCO, where P=primary, R=recurrent, core= core and E=edge. Inset shows spheroid infiltration after 0.5 hours of co-culture with hCO. Spheroids were labelled using ViaFluor 488 (Biotium). Data are mean (± SD) is shown for 3 independent assembloids per condition. P-values are based on one-way ANOVA and shown as *(< 0.05), **(<0.005), ***(<0.0005), and ****(<0.0001).

1.1.7 Freshly resected tumour pieces infiltrate hCOs

To test whether freshly resected tumour tissue could be used for hCO infiltration in the assembloid assay, we fluorescently labelled tumour samples with live cell dye.

Within 24 hours of surgical resection, samples (~200-600 µM in diameter) were placed into co-culture with day 9 hCOs. Over a period of 48 hours all three SHF003N tumour pieces exhibited infiltration behaviour into and within hCOs (Fig 1.7A). After 48 hours SHF003N pieces infiltrated hCOs by 88% (Fig 1.7B). The number of disseminated particles increased over the assay period resulting in ~40 fold more than NP1 at 48 hours (Fig 1.7C). SHF001N pieces demonstrated further migration distances from docking point on hCO compared to NP1 spheroids. At 48 hours the distances of SHF001N 'spheroid edge' and 'outermost cell' were 735 µM and 495 µM compared to NP1 300 µM and 225 µM respectively (Fig 1.D).

Detection of SHF003N invasive behaviour was dynamic between hours 2 and 24 as observed by large increases in percentage infiltration (~10 fold) and particle number (~4 fold). From 24 hours onward SHF003N cells were more static with regards to migration within the assembloid as observed by smaller differences between distances for 24 and 48 hours for both 'leading edge' and 'outermost cell' (1.6 and 1.1 fold respectively). Additionally, differences in percentage infiltration and disseminated cells between 24 and 48 hours are also more slight (both 1.2 fold). Although preliminary, these results are encouraging in terms of using freshly resected tumour samples in the assembloid assay.

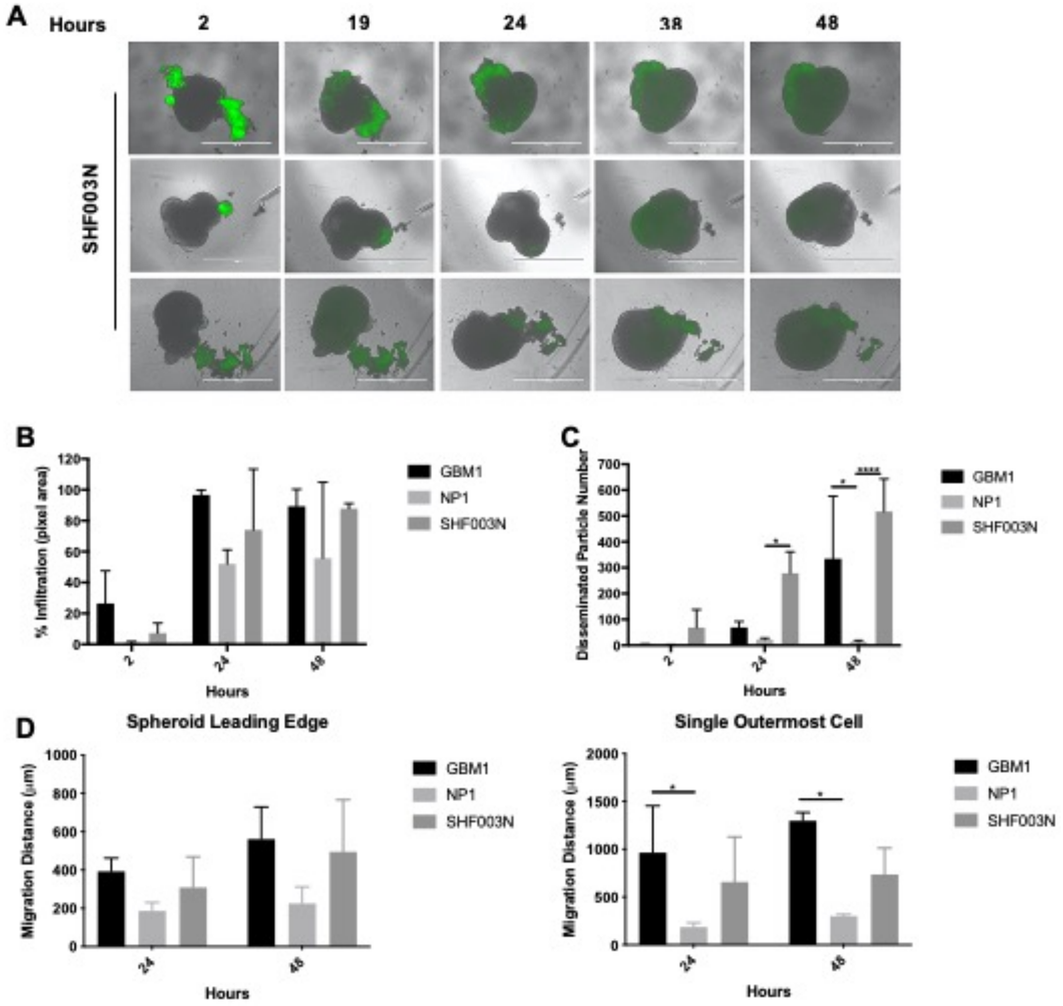

Figure 1.7 Successful infiltration of freshly isolated GBM tumour pieces. **(A)** Infiltration of freshly isolated tumour pieces into hCO over a period of 48 hours following co-culture. Scale bar 1mM. **(B)** Increased percentage of GBM1 and GSC GFP pixels within hCO over time following co-culture with hCO, compared to NP1. **(C)** Increased number of GFP GBM1 and SHF003N particle numbers compared to NP1. **(D)** The distance of leading edge (left) and single outermost pixel (right) of GFP spheroid within hCO from entrance point. Spheroids and tissue pieces were labelled using CellTracker (Invitrogen). Data are mean (± SD) shown for 3 independent assembloids per condition. P-values are based on two-way ANOVA and shown as *(< 0.05), **(<0.005), ***(<0.0005), and ****(<0.0001).

1.1.8 Human iPSCs derived hCOs are suitable in assembloid assay

It has been previously shown that both ESC and iPSC can be used to derive hCOs [256]. We compared the expansion of both ESC H9 and iPSC Hoik_1 derived hCOs at stage 2 of our hCO derivation protocol (Fig 1.1A). In addition, we tested both H9 and Hoik_1 early stage hCOs in co-culture with GBM1 and NP1 to determine if both would be suitable for use in the assembloid assay.

As EB diameter is the determining factor for proceeding from stage 1 to 2 [256], we tracked the area and diameter of both H9 and Hoik_1 EBs throughout stage 1 of differentiation. Measurements were carried out following media replenishment to reduce cell debris. On both days 2 and 4 Hoik_1 EBs showed >110% increase in area and diameter compared to H9. However, by day 7 there is no significant difference in either area or diameter between H9 and Hoik_1 (Fig 1.8A).

Advancement to stage 2 of differentiation is determined partly on the basis of EBs reaching ~500 µM. As Hoik_1 EBs exhibited diameters of above 500 µM from day 2 we sought to investigate whether the differentiation timeline would need adaptation, with advancement to stage 2 earlier than the established day 7 for H9s. Therefore, we compared both H9 and Hoik_1 derived EBs advancing to NI stage 2 early at day 4 or late at day 7 before their use in the assembloid assay (Fig 1.8B). Since the establishment of the Lancaster protocol, many adapted methodologies now describe the use of mTeSR for EB plating, formation and growth during stage 1 of differentiation [302, 304]. To ascertain that these culture conditions make a difference to hCO differentiation, we tested both H9 and Hoik_1 EBs derived with HSC or mTeSR during the EB growth phase. Resulting EBs were then transitioned to stage 2 NI conditions in either early or late timelines (at day 4 or 7 respectively) (Fig 1.8B).

We determined the level of invasion of spheroids at 48 hours post co-culture, describing the phenotypic invasion pattern exhibited by GBM1 and NP1 (Fig 1.8C). Full invasion was indicated by encapsulation of GFP-positive spheroids within hCO borders and spread of cells or patches within hCOs. Partial invasion was defined as cell migration from the spheroid core but with not all spheroid encapsulated into the hCO. Non-invasion was defined as lack of spread of cells or patches with docking of compact spheroids remaining outside of hCO borders.

Both H9- and Hoik_1 hCO-cultured assembloids showed the established difference in GBM1 and NP1 behaviour (Fig 1.8D). However, GBM1 spheroids were able to infiltrate deeper into Hoik_1-derived hCOs with 94% of the assembloids exhibiting full tumour cell infiltration compared to 12% of H9 assembloids. NP1 spheroids showed no infiltration across all H9 hCOs. There was partial infiltration of NP1 in 38% of the Hoik_1-cultured hCOs.

The use of HSC EB media conditions either in early or late NI for H9 and mTeSR in the late NI for Hoik_1 were observed to be the optimum timelines for discrimination of invasive potential between GBM and NP. This indicates the requirement for slight alterations of establishing NI, depending on iPSC or ESC model used for deriving hCO.

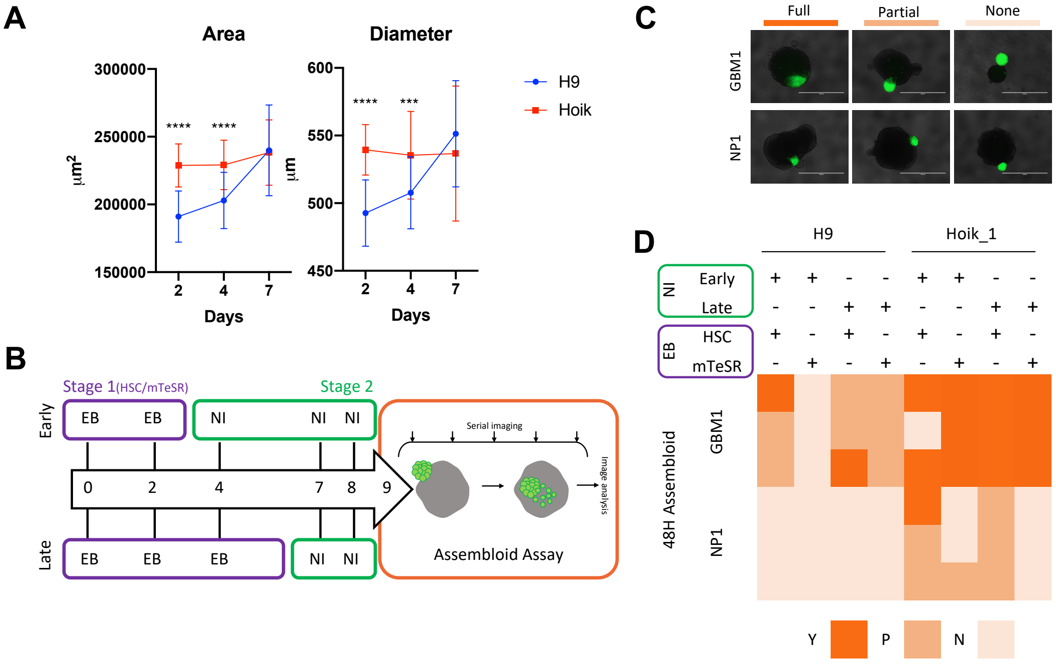

Figure 1.8 hCOs differentiated from iPSC or ESC sees differences in growth and assembloid invasion. (A) Growth of hCO, area (left) and diameter (right), while differentiating in HSC media over 7 days. Data are mean (± SD) is shown for 48 individual EBs per condition. P-values are based on two-way ANOVA and shown as ***(<0.0005), and ****(<0.0001). **(B)** Schematic overview for hCO differentiation with early and late timelines for transfer into neural induction (NI) media before use in assembloid assay at day 9. **(C)** Representative images indicating level of invasion, (Y=yes, P=partial or N=none), of GFP-GBM1 or GFP-NP1 spheroids into hCO after 48 hours of co-culture. Scale bar 1000µM. **(D)** Heat map showing level of invasion of GFP-GBM1 and GFP-NP1 within assembloids after 48 hours of co-culture, with hCO differentiated with either HSC or mTeSR at EB stage and placed into neural induction media (NI) in early or late timeline. Each square indicates one assembloid.

1.1.9 Lineage identity of normal assembloid compartment influences infiltration patterns

The effect of the microenvironment on tumour cell migration and invasion has been long established, especially during metastasis [387]. Although the tumour microenvironment is known to be important for maintaining the cellular state in GBM [93], conserved within GBM organoids [310] the effect of the microenvironment on the invasive potential of GBM remains unknown. Alterations in hCO differentiation protocol resulted in assembloids showing different levels of invasion (Fig 1.8D), which we hypothesize may be due to slightly different microenvironmental signalling cues within the assembloids. We sought to test whether the differentiation of iPSCs along neural, ectodermal, mesodermal, and endodermal lineages affects assembloid formation of GBM1 versus NP1 cells. To this end, we modified our hCO derivation protocol. Firstly, we differentiated Hoik_1 iPSC in 2D which allowed for a more homogeneous differentiation and rapid detection of lineage specific markers. Each directed lineage exhibited positive immunostaining for hallmark markers of mesoderm (T) ectoderm (PAX6), endoderm (SOX17) and neural (MAP2) cell fates (Fig 1.9A). We induced Hoik_1 differentiation using a 'staggered' approach, hence allowing for the same experimental endpoint for assessment of all lineage-biased spheroids (LBsphs).

At the differentiation endpoint, Hoik_1 cells were seeded into ULA 96 well plates to form spheroids overnight using 50,000 cells/well, a similar cell number was determined for day 9 hCOs (Fig 1.9B). Resulting LBsph: ectodermal (ECTsph), endodermal (ENDsph) and mesodermal (MESsph), were placed in co-culture with GBM1 or NP1 spheroids (Fig 1.9C). The following LBsphs were used as controls; neural whereby Hoik_1 cells were differentiated for 5 (NEUsph5) or 7 (NEUsph7) days in hCO NI media and undifferentiated (iPSCsph).

48 hours post assembloid formation full and deep invasion of GBM1 cells was observed in ECTsph, ENDsph, MESOsph as well as NEUsph5, NEUsph7 and iPSCsph controls. (Fig 1.9D). In respect to NP1 invasion there was full invasion observed within ECTsphs and MESsphs, with a spectrum of full to partial invasion within ENDsph, NEUsph5 and NEUsph7. NP1 invasion was not observed in iPSCsphs (Fig 1.9D). Across both GBM1 and NP1 assembloids the depth of invasion was observed to present in varying invasion patterns (Fig 1.9, middle).

The separation of GBM1 and NP1 invasive behaviour was only detected with the use of NEUsph5, NEUsph7 and iPSCsphs, with respect to the level of invasion within the assembloid assay (Fig 1.9D, left). However, when you consider the depth of invasion, this behaviour does discriminate with GBM1 invading more deeply, and NP1 remaining peripheral (Fig 1.9D, right).

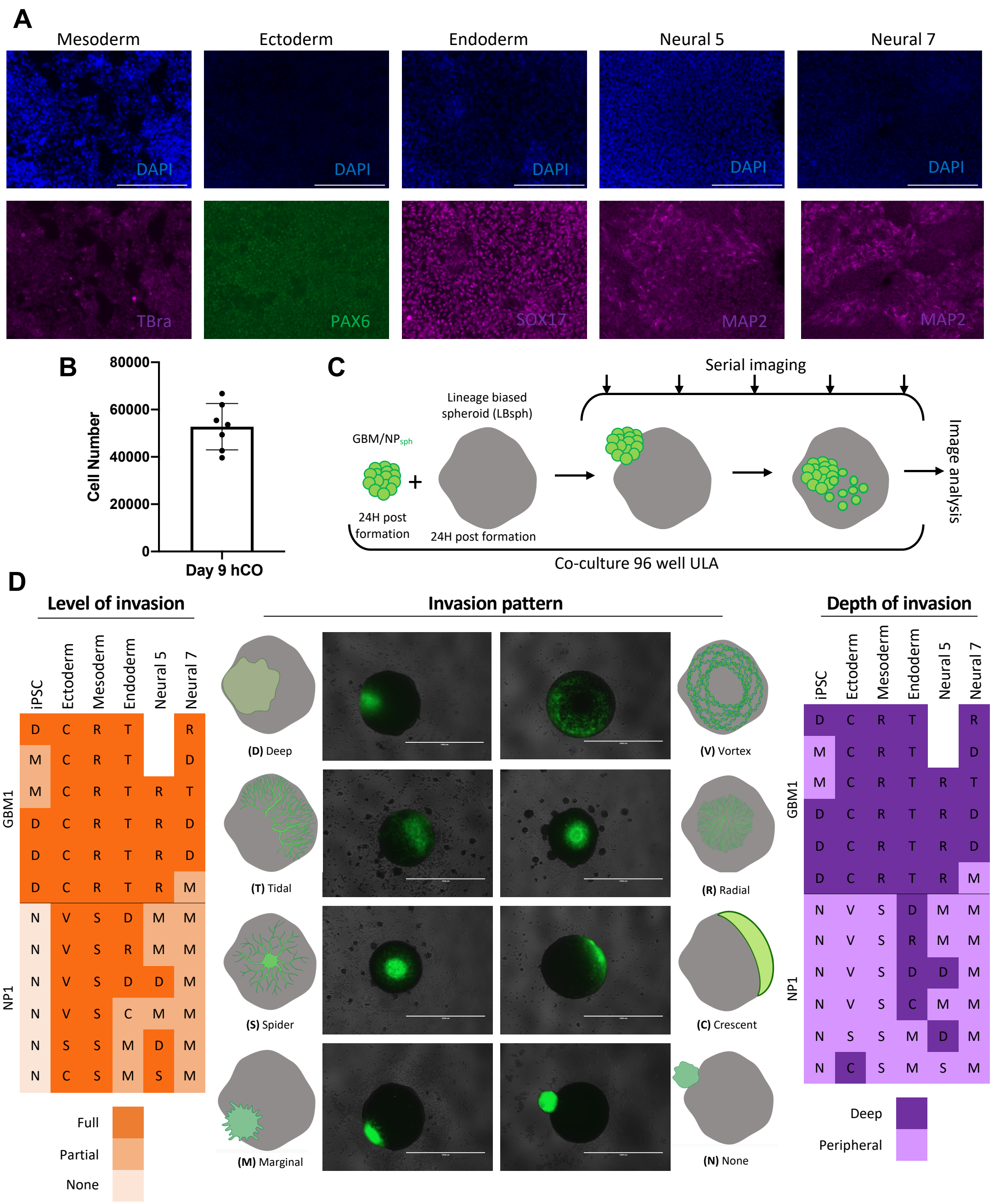

Level of invasion

	iPSC	Ectoderm	Mesoderm	Endoderm	Neural 5	Neural 7
GBM1	D	C	R	T		R
	M	C	R	T		D
	M	C	R	T	R	T
	D	C	R	T	R	D
	D	C	R	T	R	D
	D	C	R	T	R	M
NP1	N	V	S	D	M	M
	N	V	S	R	M	M
	N	V	S	D	D	M
	N	V	S	C	M	M
	N	S	S	M	D	M
	N	C	S	M	S	M

Depth of invasion

	iPSC	Ectoderm	Mesoderm	Endoderm	Neural 5	Neural 7
GBM1	D	C	R	T		R
	M	C	R	T		D
	M	C	R	T	R	T
	D	C	R	T	R	D
	D	C	R	T	R	D
	D	C	R	T	R	M
NP1	N	V	S	D	M	M
	N	V	S	R	M	M
	N	V	S	D	D	M
	N	V	S	C	M	M
	N	S	S	M	D	M
	N	C	S	M	S	M

Figure 1.9 Invasion spacial behaviour differs with microenvironment cell lineage. (A) Representative images indicating successful differentiation along cell lineages from iPSC. Where neural 5 was differentiated for 5 days whereas neural 7 was differentiated for 7 days. Scale bar 200µM. **(B)** Cell number of hCOs following 9 days of differentiation. Mean shown (±SD), each dot represents one hCO). **(C)** Schematic overview of assembloid assay with co-culture of GBM/NP spheroids and various lineage spheroids. **(D)** Heatmaps showing level of invasion (left, full, partial and none) and depth of invasion (right, deep and partial), within assembloids 48 hours after co-culture of GFP-GBM1 or GFP-NP1 with spheroids of different lineages. Each square indicates one assembloid and invasion pattern corresponding to representative images (middle). Scale bar 1mM.

1.2 Discussion

GBM is a highly aggressive tumour. Subpopulations of GSCs are highly migratory and invade across the normal brain, evading physical removal in surgical resections. Chemo- and radioresistant properties of GSCs allow the evasion of therapy and the regrowth of tumours at secondary sites, and or recurrent tumours typically 2-3 cm from the original tumour within the margin zone [388, 389]. Being able to understand and effectively target the invasive behaviour of GBM would increase the likelihood of maximal resection, improving the prognosis for patients. However, modelling of GBM invasive behaviour has previously lacked complexity in 2D. It is thought that multiple cell types contribute to the microenvironmental cues involved in an invasive phenotype, and therefore model systems that incorporate additional cell types could more accurately mimic the invasive cues tumour cells encounter within the brain [390].

The fairly recent development of COs has allowed adaptations for the study of GBM. COs are promising in interrogating aspects of GBM modelling such as phenotypic and genotypic complexity of patient tumours. Firstly, the use of COs for GBM modelling entailed the formation of aSC-derived COs using patient tissue allowing the observation of structures mimicking tumour architecture [175]. This was followed by genetic manipulation of PSC-derived COs allowing for the study of tumour initiation events [176, 177]. However, modelling in a one compartment system does not take into consideration the effect of interactions of GBM cells with normal components of the brain. As a result, multicompartmental systems placing GBM cells into PSC-derived normal COs, were more recently developed with the aim of modelling GBM in a more physiologically relevant microenvironment [177, 307–311]. This approach largely utilizes the ability of GBM cellular compartments to be sustained and maintained within COs while retaining the parental tumour transcriptional landscapes. Although these models are able to observe invasion patterns following entry and migration across COs, the dynamics and mechanisms of invasion have yet to be fully explored. Initial studies began to study the differences in invasive behaviour between malignant GSCs and normal NPs, however using PSC-derived mCO [307]. Although this assembloid system described a short term assay to compare specifically the invasive behaviour of GSCs, differences between mouse and human PSC [391, 392] may result in variance between the resulting microenvironments. This may affect how translatable mechanisms governing invasion dynamic, or features of tumour growth, are between species.

Differences between mouse and human derived organoids have been previously discussed and identified, with specific advantages and disadvantages as discussed below in Table 1.1. Such interspecies variance has previously hindered extrapolation of mechanisms or therapeutic success from xenograft models to patients [390].

Organoids	Advantages	Disadvantages
Mouse	• Less expensive • Well suited to protocol optimisation • Extensive *in vivo* data to compare to • Fast growth rate, short time scale	• Shows variability • Lack of vascularisation • Lack of human features
Human	• Contains human specific cell types • Growing literature with increasing number of protocols • Best for modelling human specific disease and development	• Shows variability • Slow growth rate, long time scales • Expensive reagents • Little *in vivo* data to compared to, so usually compared to mouse studies

Table 1.1 Advantages and disadvantages of organoids derived from mouse and human stem cells. Adapted from Marshall et al [539].

To interrogate invasion potential of GSCs, with adaptations to the mouse-assembloid assay [307], we aimed to develop a more physiologically relevant and translatable human-human system. Specifically, this work focused on:

1. GBM spheroid invasion into human COs
2. Determination of invasion behaviour of malignant and non-cancerous cells
3. Interrogation of factors influencing glioma invasive behaviour

1.2.1 GBM spheroid invasion occurs in human COs

Initially, we found that invasion of patient derived GSCs within the mouse-assembloid assay was not as efficient as using hCOs that were differentiated to the same stage 4 as mCOs (Fig 1.1A). This may be due to differences between mouse and human stem cell-derived microenvironments; however, this highlighted the need for adaptation of the original published protocol. Preliminary experiments, previously conducted by Barbara da Silva, indicated more efficient invasion of GSCs into hCOs at stage 2 of differentiation (Fig 1.1B). It was determined that the use of hCOs within stage 2 of differentiation, 9 days of overall differentiation, was the most efficient for the invasion of GSCs (Fig 1.1D). Therefore, the standard-assembloid assay timeline included the co-culture of GSC spheroids, with a day 9 hCO, with serial imaging as the assay progressed (Fig 1.1E). Despite the use of hCOs at the early stage 2 of differentiation, day 9 hCOs showed expression of forebrain marker PAX6 and hindbrain marker EGR2 (Fig 1.2A) indicating a brain-like microenvironment. Following co-culture resulting assembloids still appeared healthy with regions of proliferation, independent of the expression of GSC markers VIM and SOX2 (Fig 1.2B).

Although other studies have observed the ability of GBM cells to invade later stage hCOs, many of these studies cultured hCOs in single cells solutions of GBM cells, which may allow for easier penetration and invasion though the outer envelope of the hCOs [177, 308–311]. However, both Goranci-Buzhala et al and Ogawa et al described the co-culture of GBM spheroids with mature hCOs and observed a longer GBM spheroid infiltration period, around 7 days, until hCOs were observed as ‘invaded’ [177, 393]. This indicates that hCOs are adaptable for invasion assays along various differentiation timelines and levels of maturity. However, the previously developed mCO assembloid assay described invasion timelines of GSC spheroids within mCO in ~48 hours. Therefore, here when developing a human-human assembloid assay, using human derived tumour cells with hCOs, it was vital to maintain this aspect of a short term, medium throughput assay. By using an earlier stage, day 9 hCOs we were able to observe invasion within hCO within 24 hours.

It is accepted that differentiated hCOs mimic a foetal brain identity [302, 303], however GBM is more commonly in elderly adults with diagnosis at a median age of 65 years [8]. Therefore, current differentiation protocols can only suboptimally model the mature microenvironment within an aged brain, a current limitation of the use of hCOs within GBM research. Some studies have increased the differentiation time of hCOs in order to create a more mature brain-like environment. Consequently, they have observed a longer time till full infiltration of GBM cells. Although there was evidence that these later stage hCOs exhibited more mature neural markers [308, 393], variability in cell types between organoids increases as organoids mature [296]. With increased variability this may require an increase in the number of organoids used to draw accurate conclusions from results, reducing throughput. However, by differentiating hCOs to an earlier stage maintains less variability between organoids and batches of organoids, meaning large numbers of hCOs are not required, maintaining the medium throughput of the assembloid assay.

For the herein described assembloid platform, we had considered ageing the initial PSC cultures before hCO differentiation. This would allow for variability between hCOs to remain low as all ‘aged’ PSCs would be subsequently differentiated to the same early hCO stage, whilst theoretically mimicking an ‘aged’ phenotype. We performed preliminary experiments aiming to age PSCs (data not included into thesis), before hCO differentiation. To this end, we carried out preliminary experiments based on small molecule inhibitors of telomerase leading to telomerase shortening, which has been previously shown to promote ageing-like phenotypes in iPSC cultures [394]. However, ‘ageing’ using this particular protocol overtly caused cell death/toxicity in our treated cultures, and therefore, chemical telomerase inhibition was not carried forward. Negative data was not included here as we cannot exclude that more extensive optimisation of treatment concentrations and timelines may allow aged hCOs for use in an aged-assembloid assay. In the future, other ageing techniques may also be investigated for incorporation into our assembloid platform, for example the overexpression of progerin [395]. Overexpression of progerin, a laminin A splicing variant which accumulates with age and induces early cellular senescence associated with increased DNA-damage signalling [396], in iPSCs has also been shown to induce ageing-related markers in neurons [395]. Developing robust PSC ‘ageing’ methodology to produce an aged hCO could maintain lower levels of variability between hCOs with the elimination of long-term culture for hCO maturity.

PSC ageing techniques are known to be difficult to replicate with aged phenotypes as these have been described to be often unstable [397]. Therefore, the successful ‘ageing’ of PSCs for the differentiation of an ‘aged’ hCO for use within the assembloid assay, may require extensive study and optimisation. For these reasons we didn’t take PSC ‘ageing’ forward for further investigation as we wished to concentrate on first quantifying invasive behaviour before investing significant time in developing an aged-assembloid assay, although this does represent one of many potential developments for the assembloid assay in the future (Fig 1.10).

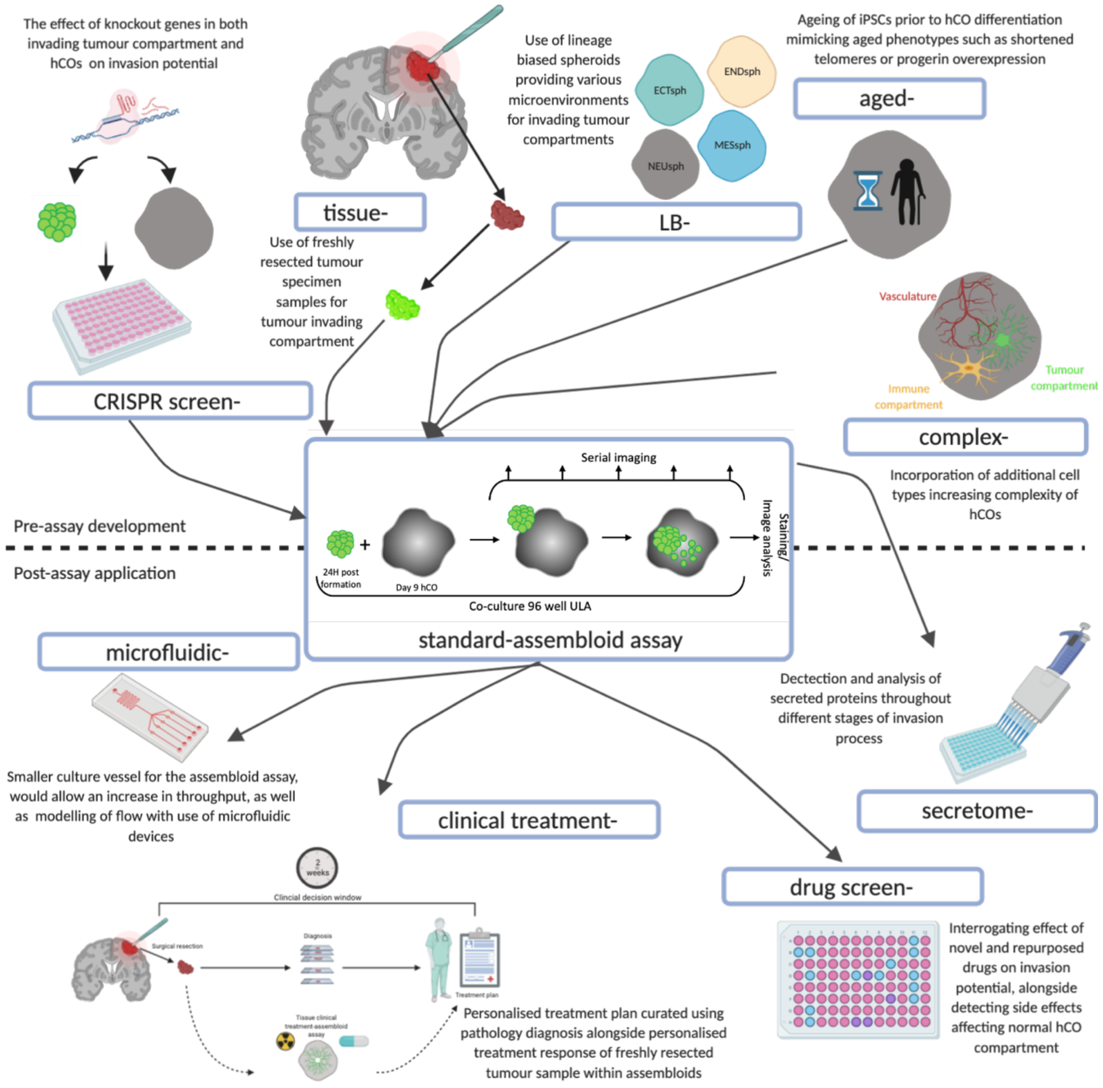

Figure 1.10 Potential developments and applications of assembloid assay. The standard-assembloid assay involves the co-culture of human tumour or control cell spheroids with a day 9 hCO with serial imaging over the 48 duration of the assay. Adaptations of hCO compartment could be through increasing complexity (complex-), inducing an aged phenotype (aged-), screening effect of gene knockouts using CRISPR (CRISPR screen-) or replacing with lineage biased spheroids (LB-), whereas invasion compartment spheroids could be replaced with freshly resected tumour specimens (tissue-). Detection of invasion capability in the standard-assembloid assay can be applied to detect the secretome profile (secretome-), treatment response to standard clinical treatments (clinical treatment-) or novel (drug screen-) and with a smaller well system increase throughput with use of microfluidic device (microfluidic-). Created with BioRender.com

1.2.2 Determination of invasion behaviour of malignant and non-cancerous cells

1.2.2.1 Difference between invasive behaviour of GSCs and NPs

Many of the studies using a multicompartment system of GSCs and COs, compare invasive behaviour between different GSC models, different CO ages or following treatment [308, 393]. However, the ability to determine non-invasive behaviour would aid to delineate invasive potential of specifically GSCs. Previously da Silva et al described the ability of non-invasive potential of NPs to be demonstrated through lack of invasion into mCO in the mouse-assembloid assay [307]. Here, we were also able to demonstrate discrimination of GSC invasive behaviour from non-invasive potential of NPs in the human-human assembloid system, irrespective of spheroid cell number (Fig 1.3). Although these observations are based on 2D images, preliminary light sheet microscopy (data not shown) indicates as GSCs invade, they do so into the core of hCOs and are not just spreading across the periphery of the hCO envelope. However, the resolution of the light sheet microscopy images was poor due to hCOs not being fluorescently labelled. In 3D reconstruction images GSC spheroids were located within the core of the space occupied by the hCO. Fluorescent labelling of the hCO prior to light sheet microscopy in the future would allow better observation of the invasion process of GSC spheroids within hCOs.

The ability of the assembloid assay to discriminate invasive capabilities of different cellular contexts over time was highlighted with the use of ‘non cancerous’ control brain cells. However, many of the other hCO GBM modelling systems fail to include controls to compare malignant to normal neural invasive behaviour. What the most appropriate controls to use within GBM research is greatly debated [398]. Here NPs isolated from epilepsy patient cortical resection specimens [174, 399], are used to compare normal to malignant stem cell behaviour. Some studies suggest the use of peritumoral brain zone tissue which surrounds the tumour resection cavity as controls [398]. However, firstly this is difficult to obtain as safety is paramount during surgical resection, therefore removal of ‘normal’ tissue is unlikely due to the potential of postoperative neurological deficits [33, 34]. Additionally, due to GBM’s highly infiltrative nature, malignant cells have often already spread into the adjacent tissue and therefore cannot be used as matching control regions for brain tumours. Due to the implications of NP cells as a potential cell of origin for GBMs, NPs from excess epilepsy surgery tissue can provide an appropriate non-malignant cellular control. NP lines have been utilised in many GBM studies comparing NP cells to GBM cells, investigating differential Cytomegalovirus infection [400], differential gene expression [174, 401] and for differential drug responses [142]. Within the assembloid assay the observation of lack of invasive behaviour of NPs provided a suitable control to compare to the highly infiltrative malignant behaviour specific to GBM. We have only to date employed one NP cell line (NP1) within the assay but do have access to others and therefore additional control experiments would demonstrate the robustness of NPs as a non-invasive control within the assembloid assay.

In previous studies, invasive behaviour has been described as the binary ability to invade versus inability to invade, or as descriptions of resulting patterns following invasion [308, 393]. However, this categorization neither fully describes different aspects of invasive behaviour, nor does it allow for the detection of subtle differences in invasive potential. Therefore, we endeavoured to quantify different aspects of invasive behaviour over time, capturing differences in the ability of GSC spheroids to infiltrate and disseminate across hCOs, with lack of this behaviour demonstrated by NPs.

1.2.2.2 Image analysis parameters quantify different aspects of invasive behaviour

By considering the percentage of spheroid within the hCO gives an indication of infiltration progress at a particular time, and then how this change and develops as the assay progresses (Fig 1.4B). This furthers the information gained from previous binary yes or no invasion observations. No invasion may indicate no entry of GSCs into the hCO, but if there is a small amount of invasion it is unclear whether that is defined as yes or no invasion. Invasion is a dynamic process over time and describing infiltration as a percentage of how much is enclosed within the hCO gives a better indication of how the spheroid is invading, and at what rate.

Further to describing whether invasion has taken place, other parameters are able to describe other aspects of invasive behaviour. Following fusion with hCOs, GSCs were able to spread and migrate through the hCO body. GSCs were observed to spread from one main spheroid to migration of patches and single cells throughout the hCO, similar to the way in which we know cells disseminate from tumour bulk across the brain within patients as smaller patches or single cells [194–196]. This behaviour is not replicated by NPs which remain as a main spheroid body, even if a small percentage has entered the hCO. Quantifying the number particles at each time point indicates whether there is a smaller number of cells remaining within the main spheroid body with little spread, as observed with NP cells, or an increase in particle number over time indicating spreading out from the spheroid body, as observed with GSCs (Fig 1.4D).

We were also able to detect migration distance from the point of spheroid docking on hCO to either the outermost detectable cell (single outermost cell), or to the edge of the main spheroid body (spheroid leading edge). Across timepoints GSCs were shown to migrate further than NP cells with respect to both leading edge and outermost cells (Fig 1.4F). We are aware the measurement assumes a linear trajectory, which is unlikely to represent how the cells or patches will have migrated across the hCO. Therefore, more timepoints and live single cell tracking would be required to indicate trajectory and exact distance measurements. However, these linear measurements allow an indication of migration distance and can still differentiate invasive behaviour differences between invasive GSCs and non-invasive NP cells.

All of the above quantifications were performed non-automated using ImageJ, meaning they are labour and time intensive. The design of the assembloid assay was for a medium throughput system, and although the wet lab aspect of the assay is amenable for upscale, with higher throughput, analysis of increased image data by hand is not. Therefore, by developing image analysis pipelines to automatically quantify invasion behaviour, this would allow for the upscale of the assay as a whole, removing data analysis timelines as a bottleneck in throughput. We employed high content screening concepts [402], whereby image based parameters are analysed from large data sets and have been previously employed in applications such as image-based high throughput chemical screens [403].

Initially, through the development of pipelines, using CellProfiler as a tool, we efforted to replicate the same parameters that we established previously using ImageJ. As with the nature of image analysis automation allowing analysis of large datasets, the subsequent analysis included more time points, allowing us to observe behaviour more closely throughout time; something that we were unable to do due to labour time previously.

We first aimed to build modules within the pipeline to quantify the total area of GFP within images, and then the GFP specifically within the hCO region to determine the percentage infiltrated at any specific time point. This required identification of the GFP spheroids as one object and the hCO as a separate object. This would allow us to determine the GFP area within the hCO area and consequently indicate what percentage of total GFP area this was. However due to only the infiltrating spheroid compartment being fluorescently labelled, and the hCO compartment not, segmentation of the two as two different objects was unachievable, even despite manual training using additional various segmentation tools (Fig 1.4A, A.1A). This led us to investigate long term labelling of hCOs using fluorescent dyes, which was observed to be successful for the ~2 week time from hCO initial differentiation to assembloid assay endpoint (data not shown). However, this has yet to be incorporated into further runs of the assembloid assay. However, when experiments are completed with fluorescence labelling of hCO with GFP spheroids, the modules to determine the area of GFP within the hCO have already been developed. Therefore, analysis to determine GFP percentage infiltration would be easily adapted and built into the latest version of the analysis pipeline.

We were, however, able to replicate the parameter describing how cells disseminate from a main spheroid body. We were able to identify the main spheroid body with tightly compacted objects identified as one core object on the basis of very small distance from each other. By then removing this identified ‘core’ object, the remaining objects which had disseminated from the spheroid core could be quantified. Despite the slight difference in sensitivity of CellProlifer analysis compared to ImageJ producing different raw numbers of CellProfiler disseminated objects (Fig 1.5D) compared to ImageJ particles (Fig 1.4D), the trend detected was still the same. The number of GSC objects increased over time, as they exhibited the ability to disseminate and spread across the hCO, whereas NP cells remained within a main core spheroid, with no increase in disseminated objects.

Additional CellProfiler measurement functions revealed other parameters that discriminated between GSC and NP invasive behaviour not previously analysed using ImageJ. Increases in GFP area mimicked the trend as seen with the number of disseminated objects (Fig 1.5D), with GSC increasing whereas NP remained steady (Fig 5.5B). This was unsurprising, as more cells disseminate from the spheroid core, the area of GFP detected would therefore also increase.

We attempted to measure the distance of GFP migration by identifying a starting coordinate at t_0 of the centre of identified GFP, which would define the position of the spheroid when initially docked onto the hCO. We would then identify the centre of GFP coordinate at each timepoint as the spheroid invaded into the hCO, as well as the coordinates for disseminated objects. By using t_0 and t_x coordinates the overall distance between the two points could be calculated for how far the main spheroid body had migrated, or the outermost cells. However, we observed that between time points even if the spheroid had not migrated into the hCO, in the cases of NP cells, there was a movement of coordinate position. On interrogation, we found that due to suspension culture the hCOs were rotating and thus the position of the GFP object did so too. Therefore, the distance migrated between t_0 and t_x points could not be accurately determined. This was not an issue encountered previously with the ImageJ as the docking point was assumed for each individual time point rather than attempting to define the same starting coordinate to use in the later time points as in the CellProfiler pipeline. For automatic migration distance analysis live cell tracking should be adopted allowing a single GFP object to be traced over time. This would require much smaller gaps between timepoints to ensure the same object is identified and tracked and allowing for the distance between each time point to be calculated and then cumulated for the overall migration distance. This may indicate between which time frames the most migration distance, perhaps allowing the dynamic phase of invasion to be narrowed down. Additionally, this would also not only provide information regarding distance but also trajectory which we have not previously been able to identify.

Although rotation in suspension culture made quantifying migration distance problematic, observation of GFP coordinates indicated that NP spheroids had more movement than GSC spheroids (Fig 1.5F). Due to lack of invasion NP spheroids move the circumference of hCOs as it rotates in suspension. On the other hand, as GSC spheroids invade their movement is then restricted within the hCO envelope, meaning movement is more constricted and irrespective of hCO rotation. This highlighted the radius of movement is able to discriminate between invasive and non-invasive behaviour, exemplified by GSC and NP cells (Fig 1.5E).

The development of CellProfiler pipelines facilitates future potential upscaling of the assembloid assay, with automation of image analysis alongside increased timepoints, which has been previously unachievable. In fact, due to using slightly different parameters it has widened the amount of information we can extract from existing image datasets. In addition, it identified parameters we had not previously considered which also describe aspects of invasive behaviour.

The overall development of quantitative parameters discriminating invasive behaviour, goes beyond the binary yes or no invasive behaviour that studies have previously described. By employing quantitative parameters, the detection of more subtle changes in invasive behaviour may be detected rather than only a drastic increase or decrease. This may also reveal how different aspects of invasive behaviour may be governed by different mechanisms and may be able to be abrogated independently.

1.2.2.3 Invasive behaviour of multiple GSC models reveal a dynamic then static phase of invasion

Although other studies describe the use of multiple GSC models in their hCO systems [177, 307–311], previously the assembloid assay, both mouse and human, had only been used to interrogate the GSC model GBM1.

To test the ability of the assembloid assay to detect the invasive capability of multiple GSC models, we tested a panel of models which represented various GBM TCGA-subtypes, historic and more recent isolations, as well as isolations from primary and recurrent tumours. We also wanted to determine if the assembloid assay was able to detect differences in invasive potential between different GSC models. This was determined using the parameter analysing percentage infiltration at various time points, across the different lines. At 24 hours all models were determined to almost fully infiltrate and exhibited significantly higher infiltration than control non-invasive NP cells (Fig 1.6A, right). This validated the assembloid assay as a system to determine infiltrative behaviour of various GSC models. Although at 24 hours there was no significant difference between the models (Fig 1.6A), at the earlier time point of 2 hours there was an indication of some models exhibiting a higher invasive potential with increased percentage infiltration (Fig 1.6A, left). Recurrent tumour model GBM20 and tumour edge derived model OX2 E were shown to have invaded more than the other tested models by 2 hours post co-culture with hCO. Cells with highly infiltrative potential at the edge of GBM tumours disseminate throughout the brain, consequently forming a recurrent tumour [388, 389]. Therefore, the assembloid assay has succeeded in identifying cells with an elevated invasive potential, as indicated in patient tumour biology.

The ability of all GSC models to infiltrate within 24 hours, indicates that significant infiltration took place within the first portion of the assay, with more stable invasion in the latter. When considering the previous quantitative analysis of GBM1 and NP1, between 24 and 48 hour timepoints, the behaviour of GSCs also did not drastically alter (Fig 1.4B, 1.4D, 1.4F, 1.5B-D). In fact, the major changes in behaviour occur between 2-19 hours (Fig 1.5B-D). This indicates invasion occurs in an initial rapid and dynamic phase whereby the spheroids attach, fuse, and infiltrate, resulting in enclosure by the hCO envelope. This is then followed by a more static phase which includes more subtle spreading within the hCO.

Due to the indication that the assembloid assay could detect elevated invasive potential of models derived from the edge of tumour specimens we endeavoured to see if it could elucidate differences between cells isolated from the edge or core of matched tumour specimens. As the dynamic phase of infiltration, where differences between models can be detected, was shown to be within the early stages of the assembloid assay, we took earlier and more frequent timepoints to capture this. A trend of increased invasive potential of edge and recurrent models was detected when compared to matched core and primary lines (Fig 1.6B). Although this particular experimental run did not result in statistically significant differences, the trends indicate the expected higher invasive capability of recurrent and tumour edge samples due to their highly infiltrative biology. The highly dynamic initial phase is evidenced with large error bars for each model, which may indicate when focusing on the dynamic phase of invasion more assembloids per condition may be required. However, by the 24 hour time point there was less spread of percentages of infiltration between the GSC lines, indicating a slowing to the end of the dynamic phase of invasion. Across all time points however, there remained more infiltration of GSC models than NP controls.

The GBM1 model does not appear to reach the same infiltration level in this experimental run (Fig 1.6B), as seen in previously described experiments (Fig 1.1-5, 1.6A). However, this particular experiment labelled the spheroid models using a proliferation dye, compared to a cell tracking dye (Fig 1.6A) and lentiviral labelling (Fig 1.1-5) previously used. Hence as cells proliferate the fluorescence signal decreases. As a result, we may not have been able to fully detect all GBM patches and single cells if the fluorescence decreased beyond detectable levels. Consequently, at this time comparison between GSCs models can only be made within each individual experiment. The use of the same more stable cell tracker labelling of cells will allow comparisons from intra-experimental results.

Observing two different phases of invasion indicates there may be different mechanisms governing invasive processes during each phase. The sensitivity of the assembloid assay provides a system to interrogate the various mechanisms involved in each phase across time. This may elucidate the requirement for abrogation of both phases when wanting to truly target the invasion process therapeutically.

To investigate factors involved in these phases CRISPR screens could be performed in the GSC models. The lines could then be tested in an assembloid assay, indicating how the knockout of genes would subsequently affect invasive behaviour. Herein such a system, performing CRISPR screen to one of the compartments prior to co-culture and observing subsequent invasion into hCOs is termed a CRISPR screen-assembloid assay (Fig 1.10). The medium throughput, with short assay length, allows the assembloid assay to be developed for such molecular screens. This may allow us to uncover particular factors which affect overall invasion capability, or if there are factors involved in governing either the dynamic or static phases. These CRISPR screens could be performed in various GSC lines, indicating if there are common mechanisms and factors involved in invasive behaviour across subtypes. Additionally, the use of a CRISPR screen-assembloid assay could be applied to involve CRISPR screens within NP cells. GSCs are thought to hijack and exploit invasive mechanisms used by normal NSC populations in non-diseased brains [202]. Therefore, the screen may uncover factors which would enhance NP invasive behaviour, and perhaps may have been adopted in GSCs during transformation from normal to malignant cells, or in transition from low grade to high grade tumours. Therefore, abrogation of the invading compartment of the assembloid assay may indicate intrinsic factors influencing the invasive potential of GSCs.

Alternatively, a CRISPR-screen assembloid assay could be developed to investigate the effect of the hCO compartment on the invading compartment behaviour. CRISPR screens involving PSCs prior to hCO differentiation may elucidate if there are extrinsic factors affecting GSC invasion.

The CRISPR screen-assembloid assay may indicate specific intrinsic and/or extrinsic factors which influence the invasive behaviour of GSCs, however for translation to clinic drugs must be identified which successfully abrogates this invasive behaviour. Again, in its current 96-well medium throughput form, with the establishment of automatic image analysis, the assembloid assay is suitable for a drug screening application. Drug treatments could be added to co-culture conditions to determine if there is an effect on invasion, this system is herein described as a drug screen-assembloid assay (Fig 1.10). These could be drugs that specifically target the previously identified invasion influencing factors or could be a repurposing screen of drugs. Additionally, it may be used for drugs at various stages of development, perhaps just the active structure before being packaged into a drug format.

Additionally, the advantage of using a multicompartmental system, with GSCs and normal hCOs, is it allows an indication of whether tested drugs or compounds affect the health of the hCO compartment. This gives initial indications of whether the drugs would cause significant side effects. The use of NP assembloids in the drug screens would also indicate the specificity of treatments. This also allows a drug screen-assembloid assay as a way to test drugs that not only affect specifically invasive behaviour, but also whether other drugs could specifically target GSCs. This has been exemplified with the use of KHS101, a compound which causes apoptotic exhaustion in specifically GSCs but not NPs [142]. Previous work within the group (data from Barbara da Silva not shown here) demonstrated the ability of KHS101 to be able to specifically target the GSC compartment of assembloids but does not affect either the NP compartment or the mCOs. Thus, a drug screen-assembloid system is amenable for the detection of specific drug targeting of GSCs.

The drug screen-assembloid assay provides a system for the preclinical testing of the effectiveness and selectivity of either new drugs or compounds or test the repurposing of approved drugs. This may reduce the number of animals in preclinical testing, in line with the NC3R principles of replacement, refinement and reduction of animals in clinical testing (https://www.nc3rs.org.uk). By having a multicompartmental system the specific effects against GSCs can be determined, as well as off target effects affecting the healthy hCO and NP cells. In turn better *in vitro* models will reduce the number of ineffective treatments going through to *in vivo* and clinical stages of drug development.

1.2.3 Interrogation of factors influencing invasive behaviour

The differentiation of hCOs have been previously described using both ESCs and iPSCs [256]. Therefore, we investigated the effect of ESC- and iPSC-derived hCOs within the standard-assembloid assay. Linkous et al previously showed there was no difference between the proliferation ability of GSCs within hCO derived from ESCs or iPSCs post infiltration [308], however, they did not consider whether infiltration behaviour was affected.

We initially observed growth differences between iPSC- and ESC-derived hCOs at days 2 and 4 of differentiation stage 1 (Fig 1.1A), however these differences were no longer evident at day 7 (Fig 1.8A). Initial size differences may be due to inherent variations between iPSCs and ESCs [404], however convergence to similar sizes by day 7 may be as a result of lack of growth factor availability. Advancement from stage 1 to stage 2 of differentiation (Fig 1.1A) is determined partly on the basis of diameter reaching ~500µM, whereby EBs are transferred to 24 well plates with neural differentiation factors. Therefore, the availability of growth factors in small volumes held in 96 well plate wells during differentiation stage 1 may be a growth limiting factor. This may explain why there is a transfer to 24 well plates, with an increase in media volume and therefore growth factor availability, once EBs reach this particular size to facilitate further growth. Advancement to the next differentiation stage based on size highlights the delicate balance of growth factors and timing required for successful hCO differentiation. Thus, we investigated if adaptations to the hCO differentiation timeline were required for the use of iPSC- or ESC-derived hCOs within the standard-assembloid assay.

Additionally, we considered the effect of conditions used for EB formation. Studies first described the use of knockout serum replacement based HSC media for EB plating and growth, however more recently methodology describes the maintained use of stem cell maintenance media mTeSR throughout the EB stage [302, 304]. We wanted to determine if this disparity affected invasion capability within the standard-assembloid assay.

Overall, we observed the different EB media did not make a significant difference in invasion capability of either GSCs or NPs within resulting assembloids (Fig 1.8D). In culture we observed less cell debris following plating of either iPSCs or ESCs with the use of routine culture mTeSR throughout EB plating and growth, resulting in higher quality EBs and resulting hCOs (images not shown). This may be due to less cellular shock by not switching media composition while cells are already experiencing physical shock through the transition from adherent to spheroid culture. Thus, for further experiments mTeSR was maintained throughout EB formation and growth.

With respect to investigation of the differentiation timeline for iPSC- and ESC-derived hCOs, prior to use within the assembloid assay, we did observe a consequential difference in invasive potential (Fig 1.8D). When comparing a timeline of early versus late advancement to stage 2 (Fig 1.8B), late timeline ESC-derived EBs resulted in hCOs which better demonstrated GSC infiltrative behaviour and contrasting NP non-invasive behaviour (Fig 1.8D). Overall iPSC-derived hCOs were able to achieve full invasion of GSC, whereas differences were more evident in detection of NP invasive behaviour. For iPSC-derived hCOs we observed the later timeline for advancement of EBs to stage 2 was more effective in differentiating invasive behaviour between GBM and NPs. This indicates the need for optimisation of differentiation timelines of hCOs depending on how they are derived, as successful differentiation is critical for the use of hCOs in the assembloid assay. This is further exemplified by ESC-derived hCOs in the early timeline resulting in obvious lack of proper hCO differentiation. The size of the ‘hCOs’ (Fig 1.8C top right, Fig A.1B) were much smaller than hCOs derived using any of the other conditions, with lack of any optical brightening, a marker of healthy neuroepithelium differentiation [256] (Fig 1.8C). Consequently, this resulted in no invasion of either GBM or NP. This further highlights the delicate balance of growth factor exposure within the optimum timeline for the proper differentiation of hCOs, especially for the use within the assembloid assay.

It should be made clear only one ESC and one iPSC line were used in this comparison, however there is known line-to-line variability between PSC lines [405, 406]. It is unclear how this line to line variation would influence the assembloid assay, but these results indicate there may need to be specific hCO differentiation timelines for specific lines. Often other studies describing hCO differentiation using various lines just indicate they used protocols originally developed [256], and therefore will advance through the differentiation stages based on EB/hCO size. However, without an exact indication of timelines, in terms of days, it means we can not comment on how other groups experience potential differentiation timeline differences as a result of line variability. Optimised differentiation timelines are required for the successful differentiation of hCO for use within the assembloid assay, as failure of proper differentiation resulted in the unsuccessful separation of

GBM invasive behaviour from NP non-invasive behaviour (Fig 1.8D: H9, early timeline, mTeSR). Exposure to growth factors in an improper timing fashion may have resulted in different resulting microenvironments. This indicates microenvironment may influence the invasive behaviour of invading compartments within the assay, proposing the potential of extrinsic factors influencing the invasive behaviour of cells, independent of inherent intrinsic factors. Observations of the level of successful hCO differentiation affecting invasive potential of invading compartments indicates the suitability of the assembloid assay to delineate these different intrinsic and extrinsic mechanisms.

To investigate how different microenvironments could influence invasive behaviour we wanted to control the microenvironment of the ‘invaded’ compartment of the assembloid assay. We did so by differentiating iPSC cells along different lineages (mesoderm, endoderm, ectoderm, neural) before forming spheroids and co-culturing with GSC and NP spheroids and observing consequential invasion behaviour. This system is henceforth described as a LB-assembloid assay (Fig 1.9C).

We altered the microenvironments by producing LBsphs with different germ layer identity: MESsph, ENDsph, ECTsph; also including neural identity spheroids: NEUsph. We chose three germ layer and neural differentiation spheroids as this would provide a defined and contrasting microenvironment for the invading compartment to be able to interrogate if this affected invasive behaviour. We performed initial PSCs differentiation in 2D before spheroid formation. This was performed to ensure a more homogeneous differentiation, avoiding a gradient of differentiation factors affecting lineage identity within different regions in a 3D spheroid differentiation [407]. This would have generated extra complexity if resulting regions affected invasion differently. Directed 2D differentiation of cells, followed by 3D assembly, has already been described to control and define the composition of multilineage hCOs [408], and thus we adopted for our LBsphs in a LB-assembloid assay (Fig 1.7C).

Additionally, performing initial 2D differentiation facilitated rapid confirmation of lineage identity, through marker expression, before use within the rest of the assay. Although the image resolution within this preliminary experiment was not the highest, expression of lineage specific markers was evident (Fig 1.7A). The development of a high content imaging pipeline would provide automation detection of marker expression. From this we could develop a threshold differentiation marker level which each lineage would be required to meet, before the subsequent LBsph could be used within the LB-assembloid assay. This would ensure similar levels of differentiation throughout different experiments.

At 48 hours post assembloid formation invading cells exhibited distinct invasion patterns (Fig 1.7D). In any of the LB-sph conditions, GSCs exhibited the capability of migration toward the assembloid core (see ‘deep’, ‘tidal’, ‘radial’, and ‘crescent’ GBM1 phenotypes). In contrast, the NP cells exclusively displayed peripheral localization patterns (see ‘vortex’, ‘spider, ‘marginal’, ‘none’ NP1 phenotypes).

This run of the LB-assembloid assay highlights its ability to differentiate GSCs and NP cells based on their invasion behaviour. GSCs can be identified based on depth of invasion, whereas the effect of microenvironment is clear with instinct invasion patterns depending on LBsph. This indicates the potential for the LB-assembloid assay to uncouple the intrinsic factors of malignant GSCs governing their ability to invade, from the influence of extrinsic factors from the microenvironment influencing invasive behaviour. Although GBM hCO systems have been able to show the microenvironment influences the transcriptional profile of GSC compartments [310], there has not yet been an uncovering of what the effect of microenvironment has on invasive behaviour within these systems.

Single cell sequencing of GSCs and NPs following co-culture with LBsphs will aid linking transcriptional profiles to resulting invasive phenotypes. Additionally, by sequencing at serial time points we may be able to uncouple transcriptional changes throughout the two, dynamic and static, phases of invasion. Differential gene expression between the different microenvironment LBsph conditions could uncouple intrinsic and extrinsic factors influencing invasion of invading GSC compartments. Aspects of transcriptional profiles which are common across all of the microenvironment would indicate factors intrinsic to GSC which govern its invasive behaviour. Comparison to intrinsic factors influencing NP invasion would allow identification of intrinsic factors specific to malignant GSCs. However, factors which are distinct to specific microenvironments would indicate these are extrinsically governed. With there being observable differences in invasion pattern between the microenvironments this may indicate which extrinsic factors influence specific invasion behaviour to result in distinct invasion patterns. Additionally, by comparing extrinsic factors within the trilineage LBsphs assembloids to the neural LBsph assembloids would initiate which neural specific extrinsic factors are influencing invasive behaviour of GSCs. Initial sequencing may reveal candidates for both intrinsic and extrinsic factors, which can be further tested to uncover their spatial expression. Spatial sequencing, using technology such as the Nanostring [409], could elucidate transcriptional changes between GSCs within the main core of the spheroid and disseminating cells while invading and producing patterns as previously seen. Additionally, highly multiplexed imaging mass cytometry, using technology such as the hyperion [410, 411], would allow for detection of where these markers are expressed in situ, indicating how invading cells may also be interacting with the hCO compartment.

The LB-assembloid assay however, is not the only way in which the assembloid assay can be used to identify extrinsic factors which may be influencing invasion. Through sampling of secreted factors in the culture medium following the culture of GSC and NP spheroids alone, hCOs alone and then throughout the invasion process in the assembloid assay may indicate which factors are influential in the invasion process. Due to non-invasive sampling of secreted factors the secretome could be collected and analysed throughout assembloid invasion, this process is henceforth referred to as a secretome-assembloid assay (Fig 1.10). Differential levels of particular factors may indicate whether the factors are likely to be secreted from invading spheroid components, or hCOs. This may also uncover factors that GSCs secrete to augment the hCO microenvironment to facilitate their own invasion. Paracrine signalling mechanisms of GBM tumours influencing the surrounding microenvironment is already known. The secretion of VEGF from GSCs VEGF promotes the growth of vasculature providing physical tracts for GSCs to migrate along, enabling further cellular invasion [113, 160, 161].

Therefore, detecting factors secreted during the invasion process may indicate ways in which the GSCs are augmenting the microenvironment to further promote their own invasion. The secretome-assembloid provides a system to test levels of particular factor candidates determined in transcriptional analysis following the LB-assembloid assay analysis. Alternatively, secretome mass spectrometry of culture medium could uncover novel candidate factors. CRISPR screens in hCOs could also reveal novel factors which influence the invasion of GSCs in a CRISPR screen-assembloid assay. This could involve nonspecific CRISPR screens in hCOs to identify novel extrinsic invasion factors, or more focused screens targeting testing candidates identified in other investigations.

It should also be highlighted that the current hCO differentiation methodology results in a more simple model of the human brain [412], lacking complex additional cell types. Therefore, the assembloid assay, using these more simple hCOs, currently does not model the extrinsic effect of these additional cell types on invasive GSC behaviour. By using hCO differentiation methodologies that combine and include additional cell types such as immune cells [413] and vasculature [301], invasive behaviour can be modelled in a more physiologically relevant system. The use of complex hCOs, with additional cell types and used within the assembloid assay for study of invasive behaviour is termed a complex-assembloid assay (Fig 1.10).

Another aspect required to be incorporated for a more physiologically relevant brain-like system would be the inclusion of flow, as a surrogate for a vascularised system which is lacking in the current 96 well assay format. The addition of flow can be achieved with the use of microfluidic systems and development of the assembloid assay for a smaller well format, which is herein described as a microfluidic-assembloid assay (Fig 1.10). By using microfluidic device technology that allows for the automation of formation and then fusion of two spheroid compartments, such as that described by Tomasi et al [414], would also allow an upscale of assay throughput. An increase in throughput, with the Tomasi et al suitable microfluidic device, would also allow the microfluidic-assembloid assay to aid in large scale drug screens with the testing of not only many different compounds but also drug gradients [414].

Here the assembloid assay has been shown to successfully detect differences in invasion capability between GSC models as well as between malignant and noncancerous noninvasive NP controls. Further advances to the assembloid system will allow further interrogation of invasion biology mechanisms uncovering intrinsic and extrinsic factors as well as observe invasive behaviour in more physiologically relevant assembloid systems (Fig 1.10).

1.2.4 Potential for assembloid assay clinical application

Advances in organoid technology have seen the use of cancer organoids to model and predict patient response to therapy. Vlachogiannis et al showed that the response of patient derived metastatic gastrointestinal organoids to current treatments accurately indicated patient treatment response [415]. The study found that in 100 percent of cases that if a drug didn’t work on a patient’s organoid, then it didn’t work in the patient. Conversely in nearly 90 percent of cases, if a drug successfully worked in the organoids, it successfully predicted it would work in the patient. Accordingly, we propose the assembloid assay for applications to not only indicate GSC response to experimental drugs but indicate patient response to current treatments.

Following resection surgery all patients receive radiation and TMZ treatments, so long as they are of good enough health to tolerate further treatment [416]. Despite this, combined radiochemotherapy has only been shown to only improve overall survival by 2.5 months, and progression free survival by 1.9 months on average [40, 42]. Unfortunately, not all patients benefit and experience increased survival but still experience the severe side effects such as nausea, fatigue as well as myelosuppression, which severely affects their quality of life [417, 418]. Although efforts to stratify patients based on tumour type to indicate their response to treatment have been investigated [55], often tumour subtype is not used as a prognostic marker within the clinical setting as it has not been shown to be a true indicator of patient treatment response due to high levels of intratumoural heterogeneity at the single cell level [79, 83]. Thus, if there was a way to personally indicate whether a particular patient would benefit from further treatment following surgery, and if not, could improve a particular patient's quality of life by advising against treatment that wouldn’t offer any extension to life.

Previously Linkous et al showed that GBM hCOs could be used to indicate response to TMZ and radiation [308]. This provides an indication of how patient derived GSCs respond to DNA-damaging agents used in clinics, in a hCO system. However, this has not yet been shown to test whether this predicts an individual patient's response to treatment.

We propose that the assembloid assay could provide a system to predict patients' treatment response, allowing personalisation of treatment plans, henceforth referred to as a clinical treatment-assembloid assay (Fig 1.10). Following surgical resection tumour samples are pathologically diagnosed which then indicates an individual's treatment plan. This process usually occurs within a window of ~2 weeks (personal communication with Leeds Teaching Hospital neuro-oncology team, Fig 1.11). Therefore, if the assembloid assay were to be developed for use as a clinical treatment indicator, it would need to be performed and provide conclusions within a two week period.

This immediately highlights the requirement for the replacement of established GSCs as the invading GBM compartment in the clinical treatment-assembloid assay. The isolation of GSC lines in culture from tumour specimens can often take many weeks to establish, and therefore would not be suitable for use within the two week clinical decision timeline. Also, extensive propagation of GSC lines can cause overselection, losing the vital heterogenous representation within the populations, which may be clinically relevant to treatment resistance [102]. Additionally, although GSCs are implicated as the most invasive population of cells within GBM tumours, few studies investigate complete tumour bulk components ex vivo. GBM tumours do not consist of pure GSC populations, but contain many other components such as immune cells, stroma and more differentiated neural populations [83, 419, 420]. As these other components may, as previously discussed, influence the invasive behaviour of GBM tumours we investigated whether freshly resected tumour specimen samples could replace GSCs in what will be henceforth described as a tissue-assembloid assay (Fig 1.10).

We were able to show the ability of freshly resected tumour tissue to infiltrate hCOs in a tissue-assembloid assay 24 hours post-surgery (Fig 1.7A). Tissue pieces consisted of gently dissociated tissue specimens, resulting in pieces of varying shapes but were selected by eye to be of similar size. The tissue pieces exhibited the ability to fuse with the hCOs and were almost fully infiltrated by 48 hours (Fig 1.7B). Although disseminated particles were shown to increase throughout the assay (Fig 1.7C), migration distance of the ‘spheroid leading edge’ and ‘single outermost cell’ parameters remained relatively stable between the period of 24 to 48 hours (Fig 1.7D). This indicated the two invasion phases (dynamic and static) are exhibited by not only GSCs but conserved with the use of tumour pieces. However, it should be highlighted behaviour may be affected by confinement by other components within a tumour matrix, compared to spheroids of one cell type. Thus, direct comparison to GSC and NP spheroids behaviour is of less value, but here they act as controls for infiltrative versus non-infiltrative behaviour. Therefore, treatment response comparison is of more value when considering plus/minus treatment on tumour pieces from the same patient.

The use of patient samples in a tissue-assembloid assay may not only be a way to test response to treatment but also allow observations of tumour behaviour. It would allow us to observe cells leaving tumour bulk, potentially across the hCO ‘brain’, as occurs within patients. This is currently only observed in xenograft models, with invasion into a murine microenvironment [421]. Here the tissue-assembloid assay would allow observation of this phenomenon in a microenvironment closer to a patient. Tissue pieces could even be adopted in a complex-assembloid assay allowing observation of invasion behaviour in an even more physiologically relevant system.

The use of patient samples within the assembloid assay may not only be a way to test response to treatment, but also model the way in which cells leave the tumour bulk to invade throughout the brain in patients, currently a phenomenon only able to be

It should be highlighted this tissue-assembloid assay has only been performed using one patient sample and therefore would need to be repeated to ensure most patient tumour samples would be suitable for use. Additionally, although we attempted to select tissue pieces of similar sizes to each other, and to GSC/NP 1000 cell number spheroids this was only done so by eye. Therefore, for further experimental runs a more accurate method of size selection should be used. Initially sieves may be used to dissociate tissue to similar size and shape pieces, and then selected for based on calculated area.

The successful infiltration, with exhibition of detectable invasive behaviour, indicates the suitable use of freshly resected tumour pieces in a tissue-assembloid assay. Tissue pieces could therefore be adopted into the clinical treatment-assembloid assay. Within 3 days post patient surgical resection GBM-tissue assembloid would be available for TMZ and radiation treatments. This allows sufficient time for the response of the GBM component of assembloids to treatment to be ascertained within the two week clinical decision window. Power calculations using Z’ principles would indicate the number of assembloids required to accurately determine response to treatment. This would allow assembloid treatment responses to be taken into account when deciding patient personalised treatment plans. This may result in the indication that treatment would not provide any benefit to the patient, therefore sparing debilitating side effects during most likely the last few months of life.

The use of a clinical treatment-assembloid assay may not only test current standard TMZ and radiotherapy treatments but is flexible to incorporate additional treatments that may become standard clinical practice in the future. Additionally, while determining assembloid response to the current treatments, the clinical treatment-assembloid assay may also be employed to determine eligibility for enrolment to clinical trials. This would indicate whether newer clinical trial treatments would provide any benefit to individual patients, with an additional safety testing step before patient exposure.

Here we propose to expose tissue-hCO assembloids, following infiltration, to standard treatment. This therefore extends the assay readouts to post 48 hours which is currently performed. As a result, a long term labelling dye would need to be used to ensure cells can be observed throughout the extended assay. We would want to ensure loss of signal be due to treatment induced cell death rather than efflux from still healthy cells.

We also need to be aware of the potential limitations of using resected tumour samples. Due to cellular intratumoural heterogeneity samples of tumour from different sites of the same resected piece may behave slightly differently [79, 80]. As a result, an increase in the number of tested assembloids would need to be increased from what was initially used in the tested tissue-assembloid assay above (Fig 1.7). This would ensure accurate indication of overall tumour response to treatments, irrespective of sampling region.

It also needs to be considered that the cells studied are from tumour bulk that is accessible enough to be removed from the brain. They therefore may not fully represent the cells which are inaccessible due to infiltration and intermingling within the normal brain, which inevitably cause the tumour recurrence. Previous efforts to indicate patient response based on patient-wide stratification however has been unsuccessful due to such high levels of patient intratumoural heterogeneity [55, 79, 83]. Here however, we propose the use of a personalised treatment response indication, through a tissue clinical treatment-assay, however, would be more likely to accurately predict an individual's treatment response.

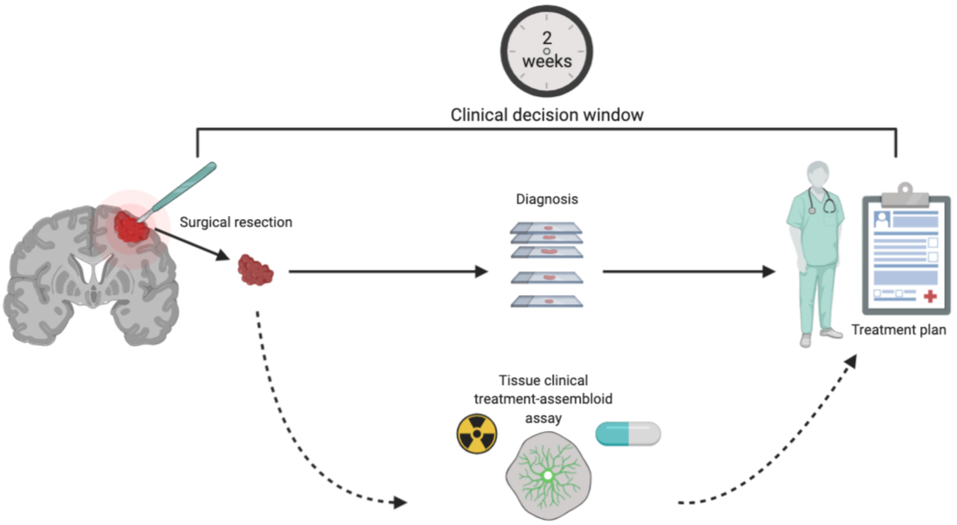

Figure 1.11 Two week clinical timeline for treatment plan following surgical resection of suspected GBM. The timeline of a clinical treatment-assembloid assay is suitable to be performed and provide personalised treatment recommendations within the two week clinical decision window. Created with BioRender.com

Here we have described the development of a system whereby the invasion of human GBM cells can be observed and detected within hCOs, termed the assembloid assay. In its simplest form the assay is able to detect differences in invasion between different GBM models, and able to differentiate invasive malignant GSC cells invasion compared to non-invasive non-malignant NP cells.

As described within this chapter, the assay is amenable to various developments allowing varying applications (Fig 1.10). The assembloid assay can be utilised to interrogate GBM biology with the investigation of factors influencing invasive behaviour, as well as provide a platform for clinical application with the resting of response to novel or standard clinical treatments. Although some of the developments of the assay, including ageing of hCOs or increase hCO complexity through the addition of various cellular compartments allows the study of invasion within a more physiologically relevant system, this will have an impact on throughput. Therefore, depending on the aspect being investigated the complexity versus throughput will have to be balanced. However, the development of the assembloid assay provides a system which through further understanding of GBM will allow a testing platform to support the clinical management of the disease.

Chapter 2

Novel cell population isolated from GBM tumour specimens using alternative Wnt based conditions

2.1 Results

2.1.1 NMP marker Brachyury (T) was absent in GBM cell lines and tissue sections

The presence of non-neuronal compartments within GBM, often subclassified as GS, indicate a highly aggressive form of tumour associated with a poor prognosis [75]. Both neural and sarcomatous compartments identified within these tumours can carry identical genetic abrogations suggesting a monoclonal cell of origin [66, 67, 71, 422, 423]. Chordomas, another CNS tumour, are also characterised by highly aggressive stemness which are attributed to amplified expression of T [351, 358, 359] and exhibit evidence of neuroepithelial and mesodermal cell types [424, 425]. We hypothesized that a bipotent NMP is giving rise to neural and non-neural cell lineages in brain tumours. NMPs are present in early embryonic development, contributing to both neural and mesodermal lineages such as posterior neuronal tracts and skeletal muscle of the paraxial mesoderm [313, 314]. NMPs are characterised by co-localisation of the transcription factors T and SOX2 [319]. To prospectively identify an NMP-like brain tumour stem cell population, we first investigated whether T expression in NMP-like cells is associated with aggressiveness in a subset of GBMs.

It has been previously found that T was detectable in 4% of GBM TCGA patient tissues as well as in a small number of patient-derived GBM cell lines [359, 426]. Accordingly, we investigated six GBM cell models (previously established: GBM1, GBM4, GBM11, GBM13, GBM20 [142] and newly established: SHF001N), and the NP1 line as well as three patient tumour specimens that were available as paraffin-embedded sections. T immunopositivity was negative in our range of tested GBM lines (Fig 2.1A) and in three GBM tissue specimens (Fig 2.1B).

Shah et al reported that elevated T expression was found in GBM lines that were grown in 3D spheroid conditions as compared to matched lines in adherent conditions [359]. However, utilizing qRT-PCR, we could not detect T mRNA within any of our GSC cell lines in both adherent and spheroid conditions (Fig 2.1C, left) The expression of the GSC marker NESTIN

[107, 108] did increase by ~40% in a single control experiment in four different GSC cell models (GBM1, GBM4, GBM20, SHF001N) spheroid conditions (Fig 2.1C, right), which was consistent with the study by Shah et al [359].

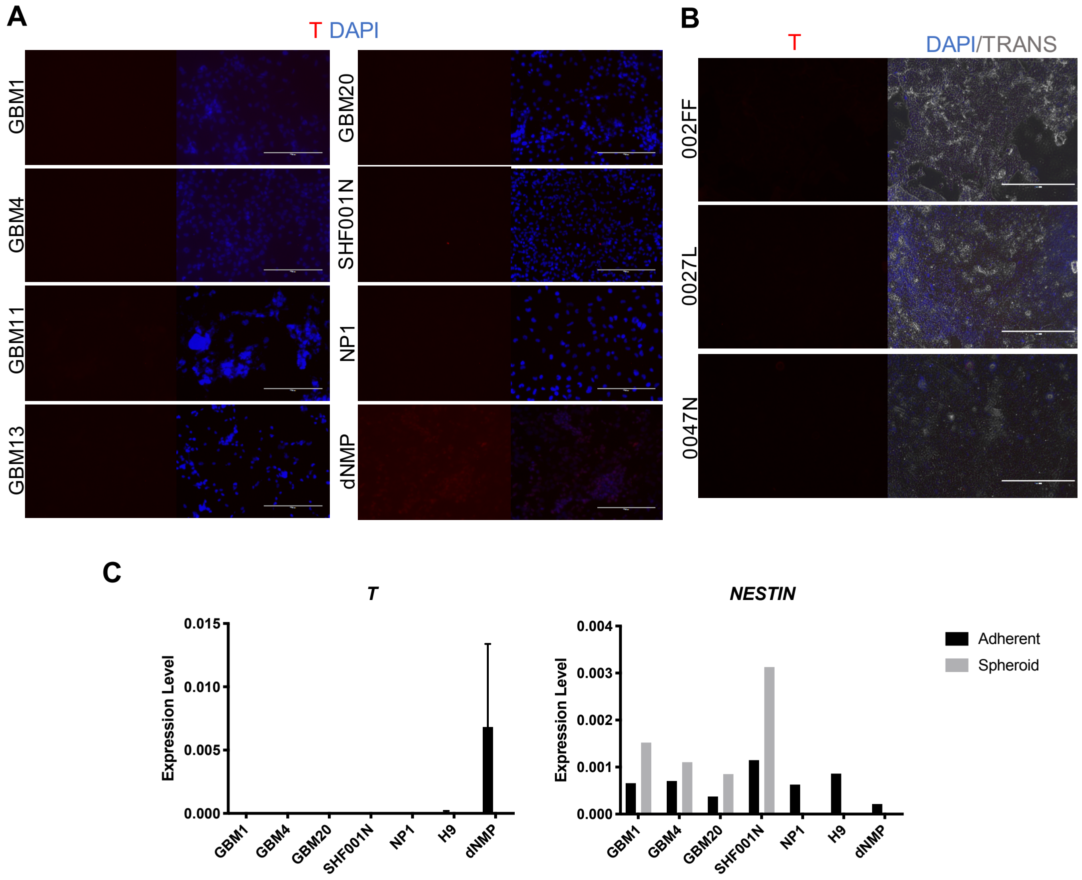

Figure 2.1 Brachyury is undetectable at the protein (T) and RNA level in GBM. (A) Representative images showing T expression shown in control differentiated NMP (dNMP), with lack of T expression in GBM1, GBM4, GBM11, GBM13, GBM20, SHF001N, and NP1 cell models as well as tumour sections from three GBM patients (**B**). Scale bar 400 µm. **(C)** mRNA expression levels of T and NESTIN in the indicated GBM, NP1, dNMP and ESC lines (H9). Data are the means of 3 biological replicates (T) or 3 technical replicates (NESTIN) per line. NP1, H9 and dNMP were only screened in adherent conditions.

2.1.2 Isolation of glioma stem-like cells in NMP based conditions

As gNSC conditions may select for exclusively NSC-like populations we sought to investigate whether alternative conditions could maintain other cell identities present within the tumour. By utilising conditions based on those used to derive NMPs *in vitro*, we hypothesised that Wnt activation, through GSK-3β-inhibitor (CHIR99021, Fig A.3) along with bFGF signalling would allow for the isolation and propagation of stem-like cells with bipotent neuromesodermal differentiation capability from freshly resected GBM tumours (Fig 2.2A). In parallel we also derived GSC lines using the classical gNSC conditions based on EGF and FGF from the same tumour specimens, throughout this chapter GSC lines derived in gNSC conditions are referred to as gNSC lines. Cells derived in CHIR99021 NMP conditions are named ending in -C, cells derived in Wnt3a NMP conditions are named ending in -W, with cells derived in gNSC conditions named ending in -N.

We observed morphological differences of primary tumour cells from the same specimen in NMP_CHIR99021 compared to gNSC culture conditions. NMP_CHIR99021-cultured cells showed a flatter cell body and larger cell body area (Fig 2.1B). However, while dissociated tumour tissue of patient ‘SHF001’ quickly expanded in gNSC medium, there was little observed growth of SHF001C cells in NMP_CHIR99021 conditions. Cellular confluency analysis of SHF001C cells was carried out after seven weeks by time lapse microscopy and assessed during a 96-hour observation period. SHF001C cells did not proliferate (Fig 2.1C).

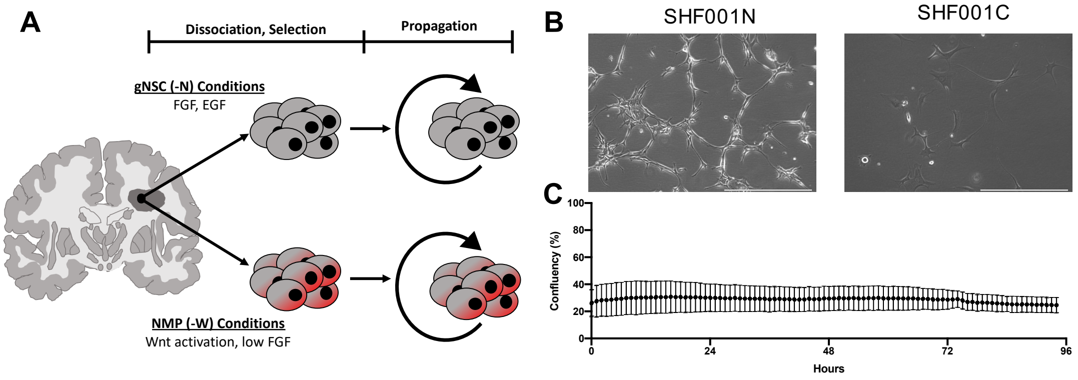

Figure 2.2 Isolation of GSCs in NMP_CHIR99021 conditions. (A) Schematic overview for the isolation of glioma stem cells and establishment of patient derived cell lines in gNSC and NMP conditions. **(B)** Isolation of phenotypically different cells from one tumour sample using gNSC and NMP_CHIR99021 conditions shown at seven weeks post isolation. Scale bar 400 µm. **(C)** Data are mean confluency (%) changes (± SD) of SHF001C, observed over a 96 hours period. Each dot represents the average of 3 technical replicates.

2.1.3 Wnt signalling activation by Wnt3A addition is sufficient to establish patient-derived glioma cell lines in NMP culture conditions

We hypothesized that establishing a patient-derived glioma stem cell-like line with neuromesodermal characteristics may require stimulation of Wnt signalling without the use of CHIR99021, as it not only inhibits GSK3β but also CDK2-Cyclin A, which has been shown to be required for cell cycle progression [427]. In contrast, cellular stimulation by Wnt3a has been previously shown to specifically promote T expression [428–430], leading to paraxial mesoderm formation [431, 432]. In mouse and zebrafish embryos, loss of the Wnt3a ligand results in formation of ectopic neural tissue and loss of posterior mesodermal structures [433–435], indicating its importance in the regulation of T expression and subsequent mesoderm formation. Additionally, Wnt3a has been shown to be upregulated in GBM patients [436, 437], indicating a contribution to the aberrant Wnt signalling niche that has been implicated in maintaining GSCs within tumours [149]. Thus, we investigated replacement of CHIR99021 with Wnt3a ligand.

From the tumour sample SHF003, cells were successfully isolated with observed proliferation and growth in both NMP_Wnt3a (SHF003W) and gNSC (SHF003N) conditions and therefore Wnt3a was continually adopted in NMP conditions for subsequent isolations. In total we successfully derived matched lines from nine specimens, five high grade tumours (SHF003, SHF005, BM002, BM004, BM005) and three low grade tumours (BM003, BM007 and BM008) in both NMP_Wnt3a (-W) and gNSC (-N) conditions (Fig 2.3A).

As seen previously in the NMP_CHIR99021 SHF001C cells, flatter and increased area cell bodies were observed in all nine NMP_Wnt3a derived lines compared to gNSC lines exemplified with lines derived from BM005, BM007 and BM009 tumour specimens (Fig 2.3B).

During the isolation of cells from SHF003, SHF005, BM002, BM003, BM004 tumour specimens, an increase in proliferation was observed in NMP_Wnt3a conditions compared to gNSC conditions irrespective of high- or low- grading of tumours. As a result, we quantified cell proliferation from the day of isolation of subsequent BM005, BM007, BM008, BM009 tumour specimens in both NMP_Wnt3a and gNSC conditions. Due to extensive cell debris during initial stages of cell isolation, the automation of cell confluency counts was not possible. Therefore, individual adherent cells were counted manually in fifteen fields from one day post tumour dissociation and cultured until one of the matched lines required passaging. In all cases there were a higher number of NMP_Wnt3a derived cells compared to gNSC cells (Fig 2.3C) indicating higher proliferation rates. Higher cell proliferation of NMP-Wnt3a cells was also irrespective of tumour grade. and the cause of measurements ending due to requiring passaging before gNSC cells.

Two of the matched lines were assessed for RNA expression of NMP markers, T and TBX6. However, although all lines exhibited expression of gNSC marker SOX2, there was no detectable expression of the tested NMP markers (Fig 2.3D).

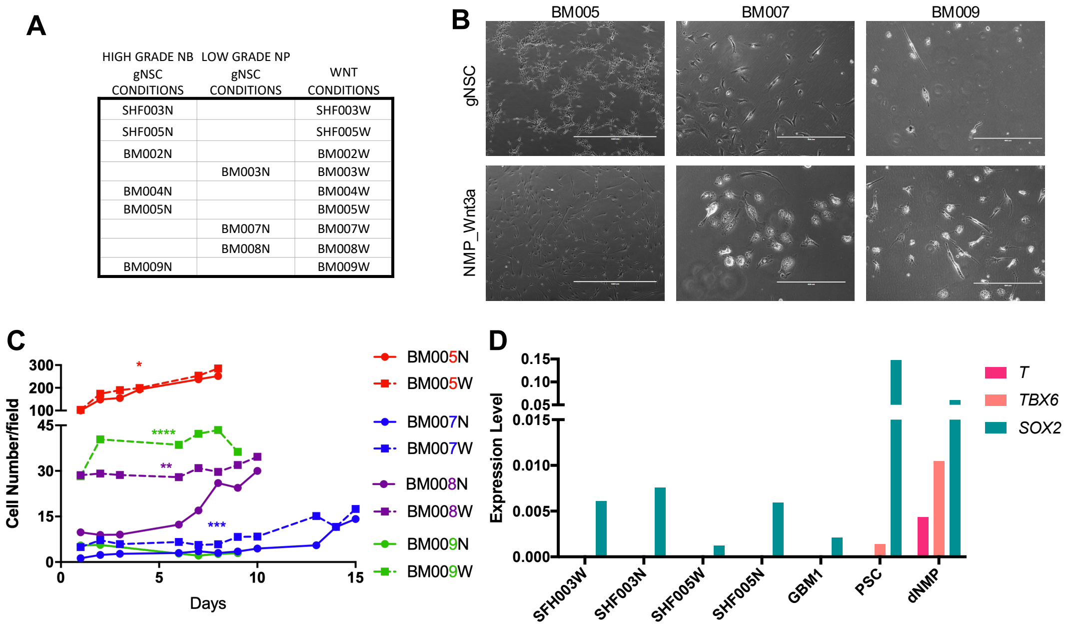

HIGH GRADE NB gNSC CONDITIONS	LOW GRADE NP gNSC CONDITIONS	WNT CONDITIONS
SHF003N		SHF003W
SHF005N		SHF005W
BM002N		BM002W
	BM003N	BM003W
BM004N		BM004W
BM005N		BM005W
	BM007N	BM007W
	BM008N	BM008W
BM009N		BM009W

Figure 2.3 Successful isolation of patient derived lines by Wnt3a ligand addition to NMP media. (A) Table shows nine gNSC and NMP_Wnt3a matched lines successfully isolated from both low and high grade tumours. Where -N indicates gNSC conditions and -W indicates NMP_Wnt3a conditions. **(B)** Representative images showing matched patient samples successfully derived in both gNSC and NMP_Wnt3a conditions. **(C)** Mean of cell numbers within 15 imaging fields assessing adhered cell numbers of matched gNSC- and NMP_Wnt3a-cultured primary cells following isolation from tumours. P-values are based on paired Student's t-tests and shown as *(<0.05), **(<0.005), ***(<0.0005), and ****(<0.0001). **(D)** Expression level of NMP markers in matched gNSC and NMP_Wnt3a GBM lines against PSC and dNMP.

2.1.4 An NMP signature is present in cells derived in NMP_Wnt3a conditions

Failure to detect characteristic NMP markers by staining and qRT-PCR led us to perform bulk RNA sequencing to determine whether NMP_Wnt3a derived cells displayed a non-conventional NMP signature. We performed mRNA sequencing on three matched gNSC and NMP_Wnt3a lines, from two high grade and one low grade glioma.

We used bulk mRNA sequencing to obtain the transcriptome of primary cells from the aforementioned BM005, BM007 and BM009 specimens comparing NMP_Wnt3a with gNSC conditions and a total of 17,797 mRNA transcripts were detected. Euclidean distance heat map and principle components analysis of this data indicated that NMP_Wnt3a conditions do not drastically alter the transcriptional landscape of

NMP_Wnt3a compared to gNSC cultured cells. The major transcriptional differences between samples resulted in separation with respect to tumour origin, which was expected due to intertumoural heterogeneity between patients (Fig 2.4A).

We then analysed differentially expressed genes across NMP_Wnt3a and gNSC conditions to determine which genes and pathways had altered expression between media conditions. Significant genes were determined using a cut off of a -log10 p-value of >2, which resulted in 477 differentially expressed genes in NMP_Wnt3a conditions compared to gNSC samples (Fig 2.4B).

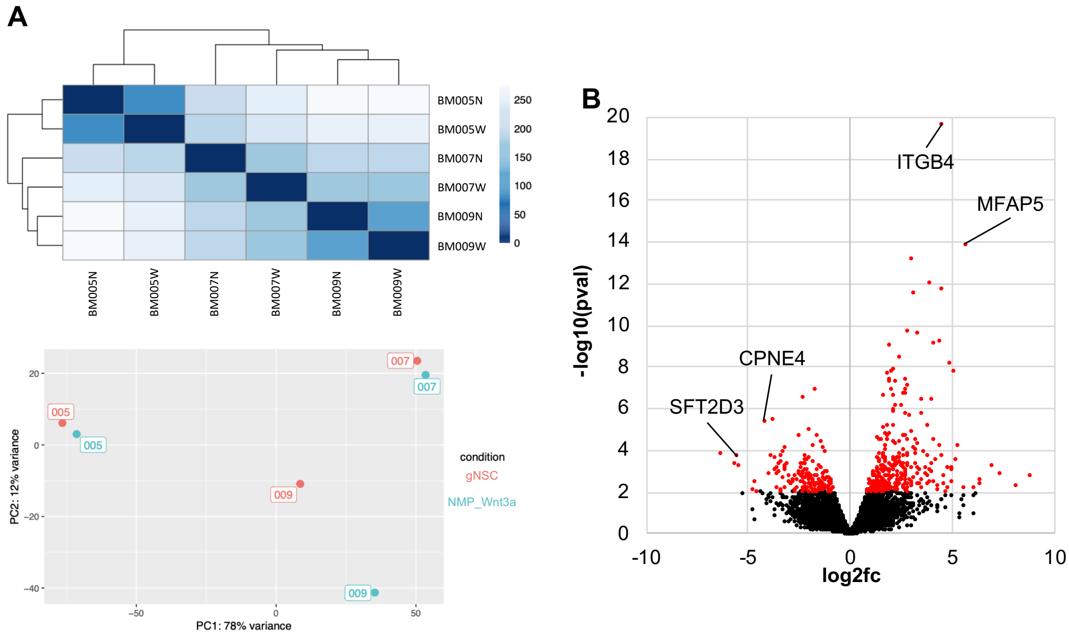

Figure 2.4 mRNA sequencing of 3 matched NMP_Wnt3a vs gNSC GBM lines. (A) Sample distances by heatmap (left) and principal components analysis (PCA) (right). **(B)** Volcano plot comparing transcriptional RNA-seq profiles of NMP_Wnt3a vs gNSC samples, with genes passing a -log10 p-value threshold of <0.01 indicated by red colour.

To detect an NMP signature within NMP_Wnt3a cultured BM005W, BM007W and BM009W cells, we compared genes that were differentially expressed between NMP_Wnt3a vs gNSC conditions with a previously identified *in vitro* dNMP gene set [438]. This revealed 145 shared genes, of which 101 genes were upregulated and 44 genes were down regulated in both datasets NMP_Wnt3a and dNMP datasets (Fig 2.5A).

The resulting 101 upregulated overlapping genes were combined as an upregulated_glioma_NMP signature and investigated for it's prognostic value in survival analysis. The upregulated_glioma_NMP signature was determined to be significantly associated with poor outcomes in a combined GBM and LGG dataset (Fig A.3B). Within GBM the signature was shown to be significantly associated with lower overall survival but not progression free survival (Fig 2.5B). Within LGG, specifically the astrocytoma subgroup, the upregulated_glioma_NMP signature was also shown to be significantly associated with lower overall and progression free survival (Fig 2.5B). However, the signature was shown not to be predictive of survival in the oligodendroglioma subtype of LGGs (Fig A.3B).

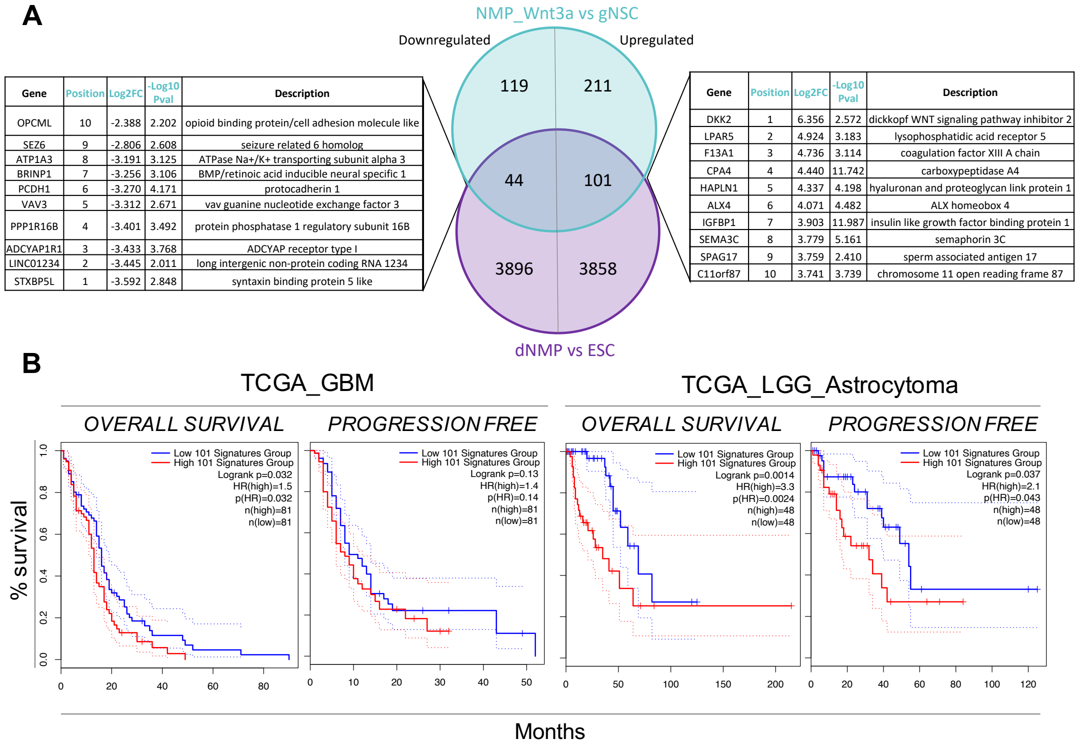

Gene	Position	Log2FC	-Log10 Pval	Description
OPCML	10	-2.388	2.202	opioid binding protein/cell adhesion molecule like
SEZ6	9	-2.806	2.608	seizure related 6 homolog
ATP1A3	8	-3.191	3.125	ATPase Na+/K+ transporting subunit alpha 3
BRINP1	7	-3.256	3.106	BMP/retinoic acid inducible neural specific 1
PCDH1	6	-3.270	4.171	protocadherin 1
VAV3	5	-3.312	2.671	vav guanine nucleotide exchange factor 3
PPP1R16B	4	-3.401	3.492	protein phosphatase 1 regulatory subunit 16B
ADCYAP1R1	3	-3.433	3.768	ADCYAP receptor type I
LINC01234	2	-3.445	2.011	long intergenic non-protein coding RNA 1234
STXBP5L	1	-3.592	2.848	syntaxin binding protein 5 like

Gene	Position	Log2FC	-Log10 Pval	Description
DKK2	1	6.356	2.572	dickkopf WNT signaling pathway inhibitor 2
LPAR5	2	4.924	3.183	lysophosphatidic acid receptor 5
F13A1	3	4.736	3.114	coagulation factor XIII A chain
CPA4	4	4.440	11.742	carboxypeptidase A4
HAPLN1	5	4.337	4.198	hyaluronan and proteoglycan link protein 1
ALX4	6	4.071	4.482	ALX homeobox 4
IGFBP1	7	3.903	11.987	insulin like growth factor binding protein 1
SEMA3C	8	3.779	5.161	semaphorin 3C
SPAG17	9	3.759	2.410	sperm associated antigen 17
C11orf87	10	3.741	3.739	chromosome 11 open reading frame 87

Figure 2.5 NMP signature in GBM and LGG shows poor prognosis. (A) Venn diagram comparing the number of up- and downregulated genes in dNMP vs ESC dataset with NMP_Wnt3a vs gNSC dataset. Top 10 most up- and downregulated genes shown for overlap genes in the NMP_Wnt3a dataset. **(B)** Overall and progression free survival for upregulated overlap genes in TCGA_GBM and TCGA_LGG_Astrocytoma datasets.

2.1.5 Cells derived in NMP_Wnt3a conditions are characterized by transcriptional upregulation of the EMT pathway

We next used GSEA to interrogate the characteristics of NMP_Wnt3a compared with gNSC-cultured populations. Unsupervised enrichment found the EMT pathway was significantly enriched in the NMP_Wnt3a glioma cell populations (Fig 2.6A). We further interrogated which members of the EMT pathway were attributed to this enrichment (Fig 2.6B). We found that members of the collagen family were significantly upregulated. Microfibril associated protein 5 (MFAP5) was the most significantly upregulated transcript within the EMT pathway network (Fig 2.6B) as well as in the initial NMP_Wnt3a vs gNSC differential gene expression (Fig 2.4B) indicating a large contribution to the transcriptional profile of NMP_Wnt3a cells. To determine if high expression of MFAP5 is prognostic within GBM and LGG, survival analysis using Cancer Genome Atlas (TCGA) and Chinese Cancer Genome Atlas (CCGA) datasets was conducted using GlioVis [374]. In both TCGA and CCGA data sets high expression of MFAP5 was shown to be significantly associated with poorer overall survival (Fig 2.6C).

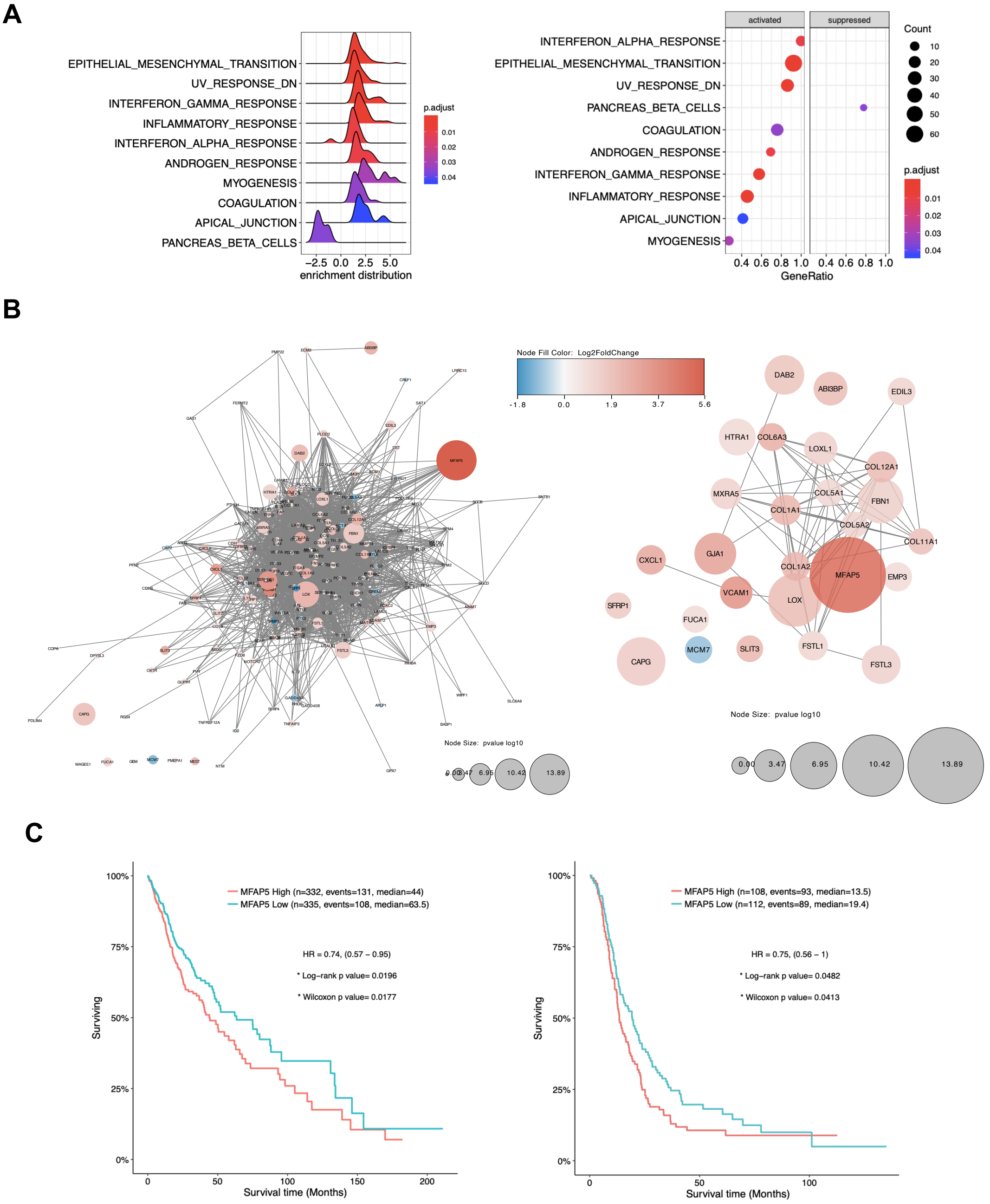

Figure 2.6 GSEA reveals upregulation of EMT pathway. (A) Ridgeplot (left) and dotplot (right) distribution pathway enrichment of NMP_Wnt3a vs gNSC samples, as determined by GSEA. (**B)** Entire EMT pathway protein interaction network (left) and members with log10 p-value significance above 2 (right). Colour indicates up- or down-regulation in NMP_Wnt3a vs gNSC samples and size indicates log10 p-value. **(C)** Kaplan Meier indicating survival in TCGA_GBM_LGG (left) and CCGA_GBM_LGG (right) datasets. Data interrogated and visualised using [374]**.**

2.2 Discussion

GBM is a highly aggressive disease due to difficulties in effectively treating tumours as a result of high levels of invasion and high level of cellular heterogeneity [55, 60, 79, 83]. Currently, for the *in vivo* modelling of GBM, GSC subpopulations, [93], are isolated from GBM tumours using EGF and FGF conditions as previously determined for normal NSC culture [102]. These conditions have been widely adopted in the glioma research community and have been shown to isolate and maintain NSC-like GSCs (gNSCs) from resected tumour specimens [102, 173, 174]. These resulting cultures exhibit different cell morphologies indicating a representation of some of the parental tumour's heterogeneity, as well as retain some histopathological features of human GBM tumours in murine xenograft models [102]. However, many other cellular subpopulations are lost when establishing gNSC lines through NSC-like selection via gNSC conditions. Although establishment of these models have allowed modelling and studies investigating the contribution of this particular gNSC fraction of cells within GBM tumour biology, the contribution and effects other subpopulations have not yet been fully modelled or considered.

Evidence of multilineage compartments within the same GBM tumour indicates both neural and mesodermal lineage cells have arisen from a monoclonal cell [66, 67, 71, 422, 423]. The presence of non-neuronal compartments within GBM indicate a highly aggressive tumour due to a poorer prognosis of ~9 months compared to the 12-15 months prognosis of more classical GBM [75].

Individual cells with populations of embryonic development NMPs give rise to neural and mesodermal cell types [313, 314]. We therefore hypothesised a NMP-like population within GBM sustains the presence of multilineage compartments and contributes to the aggressiveness, through increased invasive potential, of resulting tumours. Thus, we endeavoured to identify a novel NMP-like stem cell population within GBM. Specifically, this work focused on:

1. Isolation of an alternative stem cell population from GBM tumours
2. Isolation of glioma cells with an NMP signature independent of Brachyury
3. Upregulation of EMT pathway in novelly isolated GSCs

2.2.1 Isolation of an alternative stem cell population from GBM tumours

Previously determined conditions known to derive NMP populations *in vitro* [320, 360–365], based on FGF and Wnt activation, were adopted when isolating cell populations from resected GBM tumour specimens. As previously discussed, the use of appropriate controls in GBM research is imperative. Here the comparison of cell lines derived from the same tumour in both gNSC and NMP conditions indicates the effect of isolating cells in differing media, independent from the effects of different genetic or transcriptional profiles between patients (Fig 2.2A).

During the isolation of cells from the first patient specimen, the NMP_CHIR99021 medium used achieved Wnt activation via addition of GSK-3β inhibitor CHIR99021, as is done so in dNMP *in vitro* culturing [319]. Isolated cells were observed to have distinct morphologies with gNSC SHF001N cells exhibiting smaller, spindle-like cell bodies and NMP_CHIR99021 SHF001C cells flatter, larger cell bodies (Fig 2.2B). Such differences in morphology between mesenchymal and neural cells is commonly observed [439, 440], suggesting an alternative cell population had been isolated from the same tumour, indicating a more mesenchymal phenotype.

However, following seven weeks of culture SHF001C NMP_CHIR99021 media based cells did not exhibit evidence of growth, while the gNSC SHF001N cell underwent several passages. Subsequent confluency analysis showed SHF001C were not proliferating (Fig 2.2C), and eventually underwent cell death. We speculate the growth arrest observed in the SHF001C line may be due to the use of CHIR99021 as Wnt activator via GSK-3β inhibition. Despite its effective use in NMP *in vitro* derivation, in a kinase profiling inhibitor database CHIR99021 was found, at a concentration of 10 μM, to also inhibit PKCα, CDK-Cyclin A and MELK (Fig A.2), although a lower concentration of 3 μM was adopted in our NMP_CHIR99021 conditions. However, the sustained exposure to CHIR99021 may have affected the ability of SHF001C cells to enter the cell cycle and subsequently impaired division and growth. This may be due to the decreased activity of PKCα, CDK-Cyclin A and MELK which all have roles in cell cycle progression [441–443]. Additionally, derivation of NMPs *in vitro* requires exposure to CHIR99021 for only a period of 3 days and therefore any impact on cellular proliferation is unlikely to be detected or affect cell health. As a result, it was determined that Wnt activation via CHIR99021 GSK-3β inhibition was inapplicable for the isolation and long term culture of GSCs.

We then had to activate the Wnt pathway in an alternative way in the NMP conditions. Due to the implication of Wnt3a in activating Wnt signalling in developmental NMPs, specifically controlling paraxial formation through the promotion of T [428–432], we therefore adopted Wnt3a within our NMP glioma cell cultures. We successfully derived matched lines in gNSC and NMP_Wnt3a conditions from nine tumour specimens (Fig 2.3A). We observed similar morphological differences as previously seen with gNSC and NMP_CHIR99021 conditions (Fig 2.2B, 2.3B), strengthening the suggestion of FGF and Wnt activating conditions successfully isolating an alternative, more mesenchymal, cell population from tumours. The use of Wnt3a in the NMP cultures allowed the long term propagation of derived lines, indicating that stunted cell growth in SHF001C was due to the use of CHIR99021, rather than Wnt activation being unable to sustain glioma cells. In fact, the addition of Wnt3a to culture resulted in increased proliferation of cells in NMP_Wnt3a conditions compared to gNSC conditions from isolation (Fig 2.3C). This may indicate NMP_Wnt3a cells may represent an alternative cell fraction that is contributing to the aggressiveness of tumours perhaps fuelling tumour growth.

Culturing glioma cells in NMP_Wnt3a highlighted the efficiency of isolating and sustaining cells not only from high grade tumours, but also three low grade lines. LGG cells are difficult to grow *in vitro* [444–446], and despite the increased risk of drift from parental tumours with serum cultures [102], LGG cells are routinely isolated and sustained using NP conditions [142, 174, 307]. However, here we have shown the successful isolation and derivation of LGG lines using NMP_Wnt3a serum free conditions, indicating a new tool for use in LGG studies. Although the use of serum free conditions is shown to reduce drift from parental tumour features in gNSC conditions, cultures of both LGG and HGG NMP_Wnt3a would require subsequent transcriptional and genetic landscape analysis to ensure genotype and phenotype is preserved with long term propagation (Fig 2.7A).

Wnt3a has been previously implicated in tumour progression in GBM [436, 447], with some studies investigating the effect of Wnt3a in GSC culture [448]. However, although Rampazzo et al describes the effect of Wnt3a in patient derived GSC cell culture as promoting neuronal differentiation, these were performed under hypoxic conditions. Also, cells were exposed to Wnt3a for short term treatment courses rather than routine culture [448].

Additionally, the GSC cell lines used were isolated and maintained in gNSC conditions before Wnt3a treatment. Therefore, this study described the effect of Wnt3a on a gNSC isolated population and was not describing the use of Wnt3a as optimum isolation conditions for an alternative glioma cell population as we have described here. To our knowledge there are no studies describing the use of Wnt3a within isolation and routine culture conditions of cell populations from resected glioma tumour specimens.

The isolation and propagation of cells from glioma specimens using gNSC conditions are known to isolate a stem cell population [185]. Although NMP_Wnt3a conditions isolate self propagating populations, an important feature of normal and cancer stem cells [124], the stem cell properties of NMP_Wnt3a cells have yet to be explicitly demonstrated. Determination of GSC's stem cell potential requires characterisation of different stem cell behaviour (Fig 2.7B) [167, 449]. NMP_Wnt3a cells will need to be tested for their ability to form tumours upon intracranial injection into immunocompromised mice, and whether resulting tumours show pathological features of GBM tumours. Classical clonogenic assays will demonstrate true self renewal properties of cells. Additionally, cells should be tested for expression of classical GSC markers; such as SOX2 [105, 106], NESTIN [107, 108], OLIG2 [109] and VIM [110]. Additionally, the stem cell ability of the cells to differentiate will be tested using BMP4 treatment with an increase in expression of differentiation marker GFAP [450]. This will demonstrate whether the NMP_Wnt3a population is in the upper levels of the stem cell hierarchy with the ability to produce more differentiated populations.

Additionally, to ascertain if there has been isolation of a novel and separate stem cell population, potential plasticity of phenotype between gNSC and NMP_Wnt3a cells should be investigated. Currently gNSC cells are cultured on laminin coating and NMP_Wnt3a on vitronectin. It has been well documented the effect of different concentrations and composition of surface coatings on the morphology and behaviour of cells *in vitro* [451–454]. As a result, one concern may be that differing morphologies are simply as a result of differentiating coating material. The resulting effect on cell morphology, either maintenance of previously observed shape, or switch to the alternative morphology, may indicate if this is a consequence of culturing in particular media conditions or due to two distinct cell populations (Fig 2.7C). Therefore, it would be imperative to indicate the effects of the opposite coating on gNSC and NMP_Wnt3a populations.

We propose other stem cell fractions from GBM tumours cannot survive in gNSC medium, based on optimum medium condition isolation. As a result, a switch to the alternative medium may indicate whether gNSC and NMP_Wnt3a populations are distinct based on whether they survive or not in their non-optimum conditions (Fig 2.7C). Although, as glioma cells are known to be highly plastic, with the ability to switch between cell states [83], changes due to switching of medium conditions may allow the plasticity of GSCs to be observed.

Finally, although isolation of matched gNSC and NMP_Wnt3a lines from the same tumour specimen here has been demonstrated to be successful from nine patients, the derivation of matched lines from additional patients would ensure interpatient heterogeneity is represented using both gNSC and NMP_Wnt3a models (Fig 2.7A). Subsequent analysis of TCGA-subtype [55, 56] or NEFTEL-cell state [83] of parental tumours should be ascertained which would indicate if they are preserved within cells in either condition, or if NMP_Wnt3a cells represent a particular, separate subtype identity. If so, this would provide a tool to allow *in vitro* modelling of intratumoural heterogeneity. Although previously heterogeneity has been captured in *in vitro* modelling through the clonal expansion of different individual cells, these populations are maintained in gNSC based conditions therefore and may represent heterogeneity within the same cell fraction [455]. Here selection of a novel cell population from a different cell fraction of GBM tumours which could be used to interrogate the biology of intratumoural heterogeneity or determine differential treatment response of different cell fractions within the same tumour.

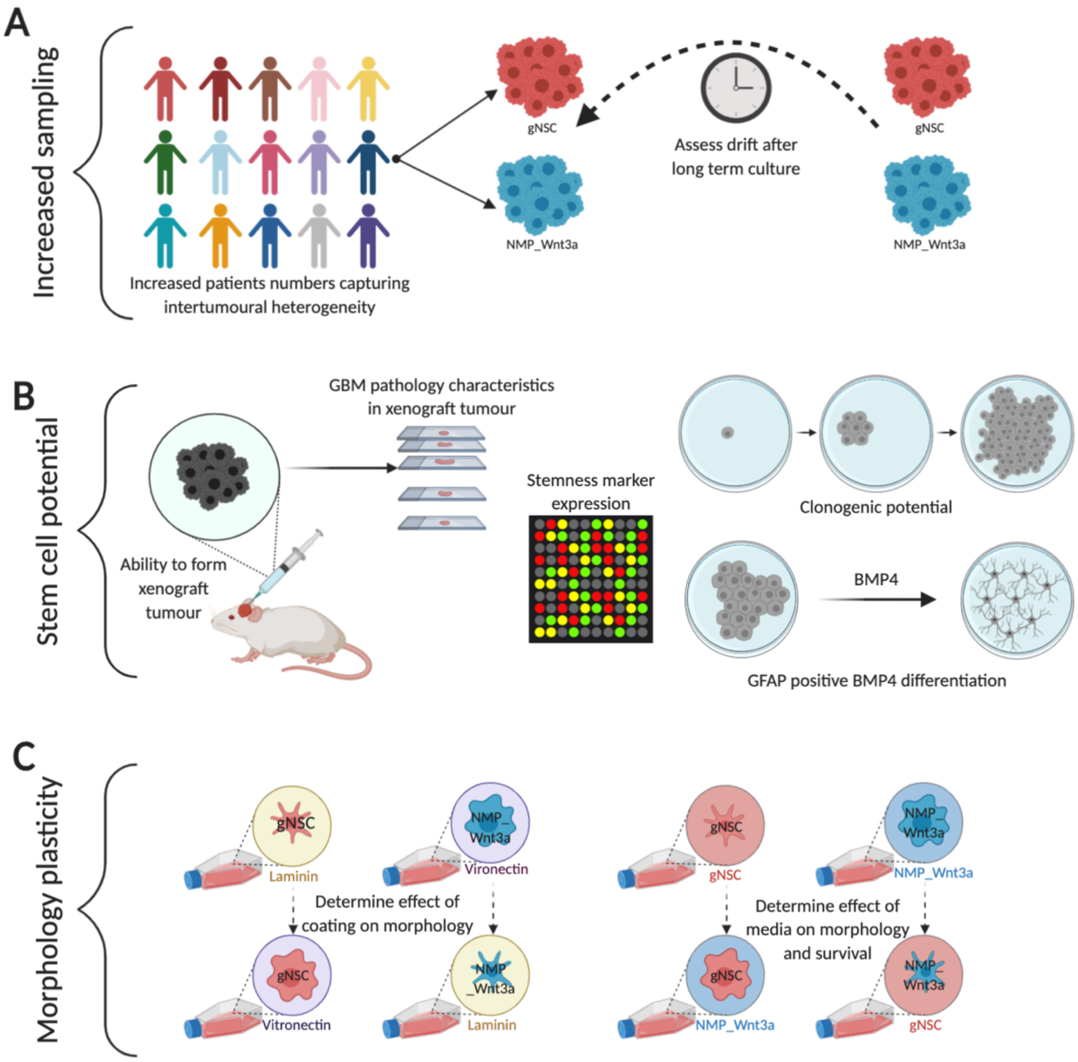

Figure 2.7 Validation of NMP_Wnt3a as a novel stem cell subpopulation within glioma. (A) Increased sampling will allow for inter-patient variation to be represented in downstream characterisation of gNSC vs NMP_Wnt3a lines. Genetic and phenotypic analysis should also be performed following long-term culture to determine drift from originally isolated populations. **(B)** GSC potential can be ascertained through the ability to form a xenograft tumour with GBM pathologic characteristics, expression of stemness markers, cologenic potential and increase in GFAP differentiation marker following BMP4 treatment. **(C)** Plasticity of distinct cell populations will be determined through morphological and survival analysis following switching of media or coating conditions. Created with BioRender.com

2.2.2 Isolation of glioma cells with an NMP signature independent of Brachyury

Due to our hypothesis that an NMP-like population may be driving an aggressive phenotype, with increased invasion and growth, within GBM we first determined if we could detect characteristic NMP markers within GSC patient-derived lines and patient specimens. NMP populations are characterised by the co-expression of neural marker SOX2 and mesodermal marker T [326], indicating its ability to give rise to both lineages. SOX2 is already highly implicated as a stemness marker in glioma [456, 457], and therefore could not be used as a marker to distinguish NMP populations from other GSC subpopulations. As a result, the mesodermal marker T was used as a marker of NMP-like identity within glioma. Additionally, the detection of T would have also indicated its role as a driver of aggressiveness in GBM tumours, similar to its implication in chordomas [351, 358, 359]. Its detection in the brain would further implicate it as a malignancy driver due to the normal absence of T post embryonic development, except within the testis and in some thyroid tissues [326, 333, 334].

Despite the indication of T expression in 4% of GBM patients and in a subset of GSC lines [359, 426], all our tested tumour specimens and gNSC patient derived lines were negative for T expression at the transcriptional and protein level (Fig 2.1). Despite lack of T expression detected across the six screened lines, which represented different subtypes (Table i.3), a significant increase in number of lines screened may be required to detect T expression.

Shah et al demonstrate spheroid culture was able to elevate the level of T expression, compared to adherent culture [359]. However, Shah et al demonstrated this elevation in a line which was already detected to have T expression, therefore it is perhaps not unexpected to find we could not replicate this finding as our lines which were found not to have baseline T expression (Fig 2.1C). If we identified a line with T expression, we may have been able to demonstrate elevated T expression, via spheroid culture, as we were able to show the elevation of stemness marker NESTIN in spheroid cultures compared to adherent culture (Fig 2.1C), as also demonstrated by Shah et al.

It should be noted that the inability to detect T expression at the protein or RNA level may be due to technical sensitivity. The immunopositive signal for T in dNMP controls was relatively weak (Fig 2.1A). While the signal was observably different to the tested lines, indicating negativity in those samples, this may not have been a sensitive enough antibody to detect weak expression. Additionally, at the time it was not possible to gain access to E8.5 mouse tissue samples which would have provided an additional suitable tissue screening control for T expression in endogenous NMPs [313, 314, 319]. Additionally, if a small number of cells were positive for T expression this may have not been detected in immunostainings with the current antibody. Also, due to qRT-PCR transcriptional profiles being conducted using bulk samples, which means it is unable to detect expression at a low level or on an individual cell basis.

On the other hand, the inability to detect T expression in our gNSC derived lines is perhaps to be expected. We hypothesize an NMP-like population has not been selected for using gNSC isolation conditions and represent another stem cell population within GBM tumours. As a result, expression of NMP marker T is less likely to be detected within gNSC lines. However, despite employing NMP conditions, which we hypothesised would support the isolation of an NMP-like population from tumours, our NMP_Wnt3a lines were also transcriptionally negative for T, as determined by qRT-PCR (Fig 2.3D). Again, this may have been due to technical sensitivity issues if T, as a transcription factor has a low expression, or is only expressed within a few single cells, and could not be detected by qRT-PCR methodology.

We therefore completed mRNA bulk sequencing to increase the sensitivity in transcriptional profiling, comparing the identity of three matched gNSC and NMP_Wnt3a lines. This corroborated the previous results with the expression of T undetectable. However, lack of T expression does not mean a non-NMP-like identity, as NMP populations have been shown to be characterised independent of T [458]. This led us to compare our NMP_Wnt3a dataset to a previously determined dNMP data set [438], which revealed a less conventional NMP gene signature with overlapping 101 up- and 44 down-regulated genes (Fig 2.5A). However, when you compare the position of these genes with respect to most up- or down regulated overlapping genes, the top 10 genes in the NMP_Wnt3a data set are not top candidates in the dNMP dataset (Fig A.3A). This indicates that while an NMP gene signature is present within NMP_Wnt3a cells, it is not the classical NMP gene signature but a malignant glioma specific NMP signature. However, there were detectable differences in the transcriptional profile of NMP_Wnt3a and gNSC samples (Fig 2.4), further indicating the isolation of an alternative stem cell population from the same glioma tumours.

Upregulation of the upregulated_glioma_NMP gene signature was found to be predictive of poor prognosis in GBM overall-survival as well as overall- and progression free-survival in LGG astrocytomas. Due to the upreguated_glioma_NMP signature not being predictive of survival in LGG oligodendrogliomas (Fig A.3B, right) this indicates its role in specifically glioma biology and prognosis. By identifying patients with this upregulated_glioma_signature we could potentially provide a more accurate prognosis, and perhaps treat accordingly with higher intensity treatment. The identification of this signature not only provides a basis for patient stratification, as well as providing new candidates for targeting cells contributing to the aggressive, highly infiltrative phenotype of GBM tumours.

Although a glioma_NMP signature has been determined independent of T, this does not eliminate the potential for T expression and contribution within these populations and GBM tumours. If T, as a transcription factor, was expressed at a low level, perhaps oscillating in a few individual cells, this is unlikely to have been detected using these methods [459]. Deep single cell sequencing of NMP_Wnt3a cells would be required to elucidate potential low or single cell T expression therefore it may still have a role within aggressive GBM tumour biology.

2.2.3 Upregulation of EMT pathway in novelly isolated GSCs

Pathway enrichment analysis indicated the upregulation of the EMT pathway within NMP_Wnt3a cells (Fig 2.6A). This indicates that while the classical NMP gene signature was not detected within NMP_Wnt3a cells, they exhibit some of the phenotypic features of developmental NMP [460]. These developmental NMP populations exhibit EMT as they migrate from the tail bud and mature to contribute to the developing paraxial mesoderm [460, 461]. Cells in a variety of cancers often undergo EMT during the metastasis process whereby cells dissociate from the primary tumour and form a secondary tumour at a distant site [462]. These mechanisms are thought to be adopted by GSCs as they disseminate from the tumour mass, invading and migrating across the brain, and thus implicated as a highly aggressive feature of GBMs [463–465].

Here, the upregulation of the EMT pathway within NMP_Wnt3a cells implicates this subpopulation could contribute to highly aggressive phenotype with cells more migratory. Being more invasive and highly motile increases the dissemination of GSCs throughout the brain, reducing the chance of maximal surgical resection as a larger proportion of unresectable cells remain allowing the formation of recurrent tumours. Although not having the classical NMP gene signature, adoption of its EMT characteristics implicates NMP_Wnt3a cells as contributing to a highly aggressive phenotype, with the prediction of poor prognosis with presence of upregulated_glioma_NMP signature in patients.

Although upregulation of the EMT pathway is detected transcriptionally, functional validation will be required to assess EMT behaviour phenotypically (Fig 2.8A). Scratch wound assays are typically used to indicate migration behaviour as a surrogate for EMT potential [210, 228-230, 466]. Detecting the time taken for cells to move and fill the scratch would indicate whether NMP_Wnt3a cells have a higher migratory phenotype compared to matched gNSC lines. The standard-assembloid assay could be employed to detect differences in invasive potential of the NMP_Wnt3a and gNSC populations.

On the other hand, if Wnt3a signalling is involved in sustaining a more aggressive cellular phenotype, as Wnt is known to be upregulated within GBM tumours [149], is this a potential extrinsic factor which affects the invasive potential of cells. Following the development of an inducible Wnt expressing PSC line, we could determine if Wnt expressing hCOs could increase the EMT phenotype in GSC cells in a Wnt-assembloid assay (Fig 2.8B). This may be through elevated Wnt stimulation increasing the invasion potential of NMP_Wnt3a cells, or alternatively would extrinsic Wnt stimulation cause an increase in invasion potential of gNSC populations.

Additionally, the assembloid assay could be developed to study the effect of two invading compartments competing for invasion of one hCO. This is henceforth referred to as a competing-assembloid assay (Fig 2.8B). Such a competing-assembloid assay could indicate whether NMP_Wnt3a or gNSC would preferentially invade, or if one does so quicker. If, or when, both invading compartments invade a hCO it would also indicate whether both can co-exist. Additionally, following on from the previous observation that NMP_Wnt3a cells have increased proliferation compared to gNSC cells, we may be able to detect whether this is conserved within assembloids.

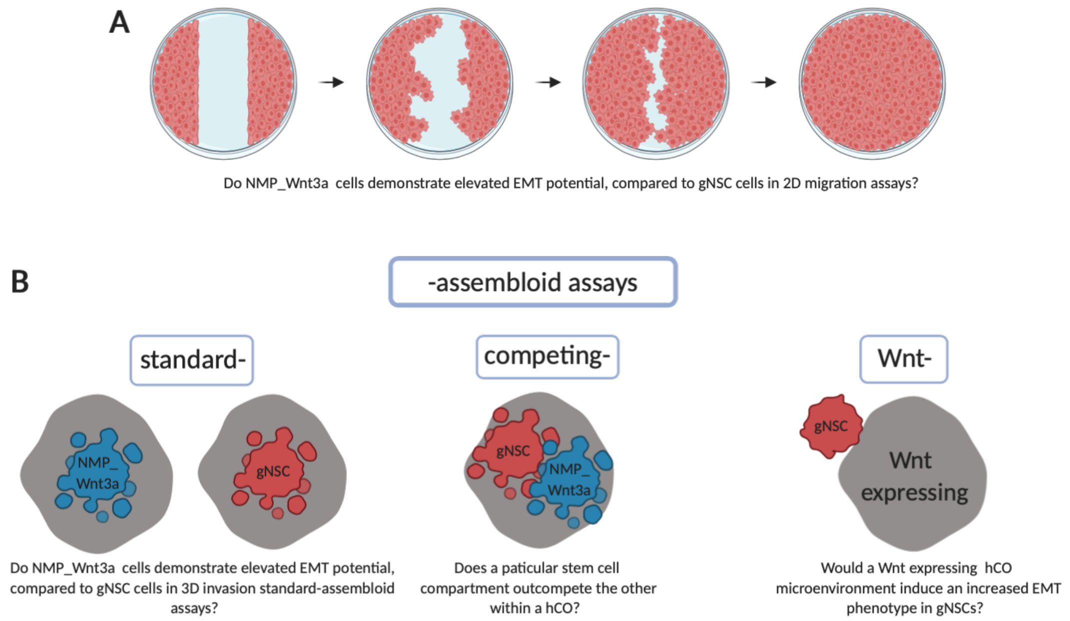

Do NMP_Wnt3a cells demonstrate elevated EMT potential, compared to gNSC cells in 2D migration assays?

Do NMP_Wnt3a cells demonstrate elevated EMT potential, compared to gNSC cells in 3D invasion standard-assembloid assays?

Does a paticular stem cell compartment outcompete the other within a hCO?

Would a Wnt expressing hCO microenvironment induce an increased EMT phenotype in gNSCs?

Figure 2.8 Assessment of EMT potential of NMP_Wnt3a and gNSC lines. (**A**) Traditional 2D scratch wound assays would indicate whether there is an increased migratory potential in NMP_Wnt3a cells compared to gNSC. (**B**) Developments of the assembloid assay allow the baseline invasive potential to be compared between NMP_Wnt3a and gNSC populations in the standard assembloid assay. The ability of either population has the ability to outcompeting the other, or able to co-exist within a single hCO in a competing assembloid assay. On the other hand, the effect of extrinsic Wnt on invasion can be determined using an inducible Wnt expression hCO and observing resulting invasion behaviour of GSC compartments in a Wnt-assembloid assay. Created with BioRender.com.

To further interrogate the enrichment of the EMT pathway in NMP_Wnt3a cells, compared to gNSCs. We sought to determine which of the EMT pathway members were specifically upregulated and contributing to the pathway enrichment. MFAP5 was determined to be the most upregulated member of the EMT pathway (Fig 2.6B). However, it was also found to be one of the most significantly differentially expressed genes when comparing the full transcriptional profile of NMP_Wnt3a cells versus gNSCs, indicating a pivotal role in NMP_Wnt3a cells (Fig 2.4B).

MFAP5 has known roles in elastic microfibril assembly and in regulation of endothelial cell behaviour and survival [467–470]. It is associated with increases in the EMT pathway with elevated migration and invasion in various cancers, such as: breast [471, 472], cervical [473] and head and neck squamous cell carcinoma [474]. Upregulation of MFAP5 has also been shown to be an unfavourable prognostic marker in urothelial, stomach, ovarian and prostate cancer [475–477]. It's implication as a poor prognostic marker in a variety of other cancers, thought to be as a consequence of elevated EMT and cellular invasion potential, further indicates a pivotal role of MFAP5 in NMP_Wnt3a cells. This indicates its contribution to a highly elevated phenotype of these cells within glioma, potentially resulting in poor prognosis with elevated expression in both GBM and LGG (Fig 2.6C).

Although elevation of MFAP5, and as a consequence upregulated EMT, has been indicated in NMP_Wnt3a cell transcriptionally we have yet to demonstrate and validate this phenotype behaviour. By using the previously described CRISPR-assembloid assay (Fig 1.10), following specific targeting of MFAP5 in either NMP_Wnt3a or gNSC, we could determine the influence of MFAP5 on invasive behaviour (Fig 2.9).

Due to MFAP5 being a secretory protein [472], levels could be detected, through serial medium sampling, during the different phases of invasion in a secretome-assembloid assay (Fig 1.10, 2.9). Previous reports of MFAP5 contribution to increased EMT and invasiveness is as a result of secretion from cancer associated stroma [478]. However, here the evidence of transcriptional upregulation within NMP_Wnt3a cells may indicate a self propagating mechanism of increased invasive behaviour through intrinsic derived paracrine signalling. Tracking secreted protein levels throughout the secretome assembloid-assay would allow us to uncouple if there is a specific stage of invasion MFAP5 contributes to invasion specifically (Fig 2.9). Additionally, if secretion is specific to NMP_Wnt3a cells we would be able to test whether the addition of medium from NMP_Wnt3a assembloids to the early stages of gNSC cell invasion in a different assembloid assay. This transfer of secretome containing medium from one assembloid to another is henceforth described as a secretome transfer-assembloid assay (Fig 2.9). This may indicate if specific factors, perhaps including MFAP5, from NMP_Wnt3a could be influencing the invasive behaviour of other cell populations within GBM tumours.

Additionally, by detecting levels between HGG and LGG NMP_Wnt3a may indicate whether there is a difference in expression level associated with aggressiveness of tumour grade. If LGG NMP_Wnt3a cells were indicated to have lower expression, the addition of recombinant MFAP5 to assembloid cultures could indicate whether this would increase the invasive behaviour of LGG cells in a recombinant protein-assembloid assay (Fig 2.9). If so MFAP5 may be implicated as a transforming factor as cells gain highly aggressive and invasive features transitioning from an LGG to a HGG.

Evidence of secretory MFAP5 influencing invasive behaviour would suggest it as a therapeutic target, whereby quenching of its activity may reduce promotion of invasion in GSCs. Immunotherapy blockade of MFAP5 has been previously shown to be effective in ovarian and pancreatic cancers, enhancing the chemosensitivity of cells and suppressed *in vivo* growth of tumours [479]. The effect of MFAP5 targeting therapies could be tested in a target focused drug screen-assembloid assay to indicate resulting effects on invasive behaviour (Fig 2.9). This may also indicate if therapeutic attenuation of MFAP5 activity would affect only the NMP_Wnt3a population or whether it would affect behaviour of other stem cell populations such as gNSC. If this does result in demonstration of only the NMP_Wnt3a populations being affected, then it further indicates that different cell fractions within GBM are governed by different mechanisms. This therefore indicates why broad spectrum or specifically gNSC targeting treatments have been ineffective due to the multiple cell types being present within glioma [79, 83]. This further highlights the potential need for multi-cell type targeting treatment regimens clinically.

Such therapeutic intervention could be adopted in glioma patients targeting the invasive behaviour of either NMP_Wnt3a alone or also other MFAP5 target cell populations potentially significantly reducing the aggressive migratory phenotype of GSC populations. As high expression of MFAP5 is associated with poor prognosis in both GBM and LGG (Fig 2.6C), and therefore activity attenuation, immunotherapeutically or using chemical blockade, may improve patient overall survival outcomes.

Alternatively, due to the determined role of Wnt in sustaining these alternative populations *in vitro*, therapeutic attenuation of Wnt signalling for the treatment of GBM tumours should be further explored. Current there are Wnt targeted drugs in GBM testing [149], as a result of Wnt niches being implicated in sustaining GSC populations. Although there are only a few being studied within GBM there are many more being investigated in other tumour types such as colorectal, breast, lung and melanoma cancer [149], therefore this provides a plethora of alternative targeting molecules and antibodies to be tested in a GBM context.

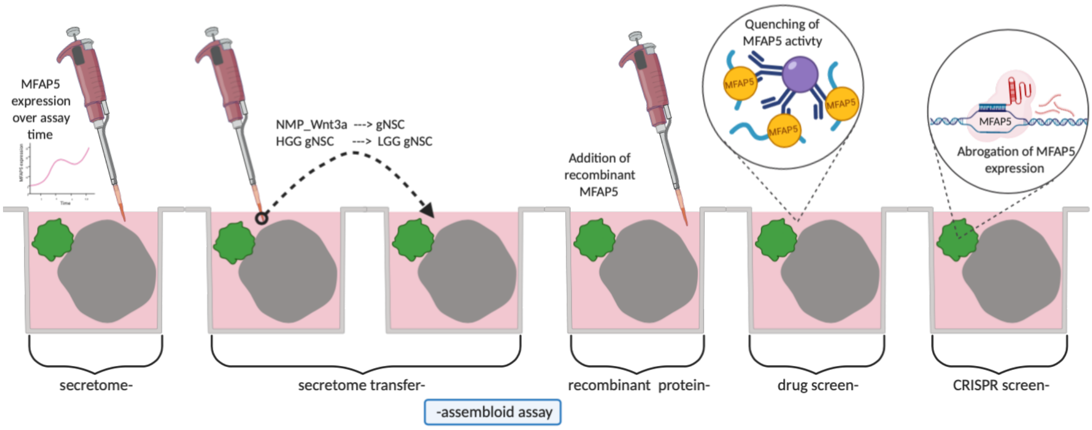

Figure 2.9 Adaptations to the assembloid assay to interrogate the role of MFAP5 in GSC invasion. Levels of secreted MFAP5 during the invasion process will be detected through multi sampling of media in a secretome-assembloid assay. To indicate whether secreted MFAP5 from one invading compartment could influence the invasive behaviour of another invading compartment through the transfer of media from one assembloid well to another assembloid well in a secretome transfer-assembloid assay. The addition of recombinant MFAP5 protein to assembloid medium would indicate the influence of the protein on in the invading compartment in a recombinant protein-assembloid assay. Effect of MFAP5 targeting drugs on invasion behaviour could be tested in a targeted drug screen-assembloid assay. The effect of abrogated MFAP5 expression could be determined through targeted CRISPR screen in invading cells followed by a CRISPR-assembloid assay. Created with BioRender.com.

Here we demonstrate the isolation and propagation of an alternative cellular population from GBM tumours using FGF and Wnt conditions based on those used to derive dNMP *in vitro*. This alternative NMP_Wnt3a population has not been detected to have a classical NMP transcriptional profile. However, we believe these cells demonstrate aspects of an NMP phenotype with more mesenchymal features than gNSCs, facilitating increased migratory and invasive potential.

2.2.4 Further validation of NMP_Wnt3a cells as a novel GSC subpopulation

Previously Wang et al has described the phenotype of GSCs to reside along a single axis of variation between proneural and mesenchymal [480]. When considering the differential proneural (*ASCL1, OLIG2*) and mesenchymal (*CD44, OLIG2*) genes used by Wang et al to differentiate the two most opposing phenotypes. However, our NMP_Wnt3a population did not show significant up- or down-regulation of these markers compared to matched gNSC cells. Therefore, they may reside at the apex of the axis with plasticity to contribute to proneural and mesenchymal phenotypes, demonstrating an NMP-like dual fate feature, or alternative may simply be a population which resides along the axis, rather than at either polar ends.

Irrespective of where the phenotype of NMP_Wnt3a cells may sit along this potential axis [480] we have demonstrated the successful isolation of an alternative glioma subpopulation. These cells with differential transcriptional profiles suggested an elevated invasive phenotype, to most commonly studied gNSC populations. However, here profiling was only performed on matched lines from 3 patients and overall only matched lines from nine patients were obtained. Therefore, to ensure we are able to model interpatient heterogeneity with both matched gNSC and NMP_Wnt3a lines with an increased number of patients would be required for sampling (Fig 2.10). High content screening of cellular morphology would ensure the observed morphological differences observed are conserved across an increased number of patient samples. Additionally, functional assays would confirm whether NMP_Wnt3a cells maintain the elevated EMT phenotype, further confirming an alternative highly migratory subpopulation. The increase of patient specimens and matched lines would increase the sample number for subsequent transcriptional profiling. This would allow further validation of the current glioma_NMP signature as determined here (Fig 2.5), or even refinement to a core signature network. This may provide more clear candidates to take forward for therapeutic intervention or provide a further refined prognostic signature. Additionally, if single cell sequencing was performed, we may be able to determine if there is a hierarchy with this subpopulation and perhaps the identity of a few T dependent single cells which may be driving the identity and aggressive phenotype within NMP_Wnt3a populations and glioma overall.

Validation of NMP_Wnt3a as a novel subpopulation, not yet studied or targeted, highlights the difficulties in treating highly heterogeneous glioma. However, the successful identification and characterisation of another GSC fraction may lead to specific targeting of the previously unknown population, reduction of invasive potential and a decrease in tumour aggressiveness, increasing overall patient outcomes.

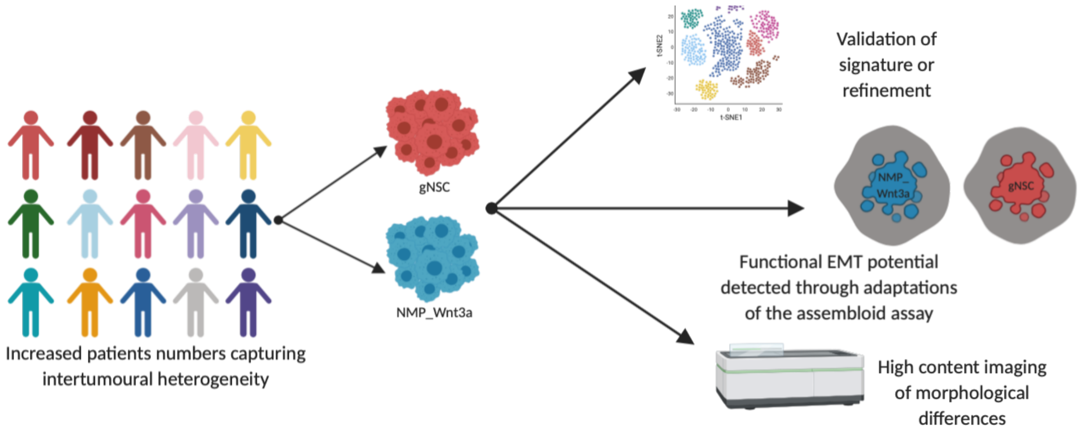

Figure 2.10 Future validation of NMP_Wnt3a populations. Morphological analysis detected through high content imaging will indicate if there are still morphological distinctions between NMP_Wnt3a and gNSC populations. Functional testing of elevated NMP_Wnt3a EMT potential, compared to gNSC cells, will be tested through previously described adaptations of the assembloid assay. Further sequencing of both populations will further validate the glioma_NMP signature or refine to a core signature. EMT= epithelial to mesenchymal transition. Created with BioRender.com.

Chapter 3

Glioma stem cells form functional networks following chemical inhibition of ROCK

3.1 Results

3.1.1 GBM GSCs are able to form ROCK inhibition (ROCKi) induced networks

The aggressive nature of GBM tumours have been attributed to the invasive behaviour of GSCs. Previous *in vivo* studies describe long GBM TMs with elongating cellular projections, at the invasive front of tumours and were suggested to be a means of tumour dissemination [216].

Previously da Silva et al demonstrated cellular networks are induced, with an increase in cellular projection length (CPL), in a number of GSC models following pan-inhibition of ROCK1/2 using chemical Y-27632 at a 20µM concentration [224]. ROCK inhibitor induced (ROCKi) cellular networks showed a decrease in cellular motility with no effect on proliferation or differentiation, and with phenotypic reversibility post ROCKi washout. ROCKi promoted 'networking' in patient derived models that led to cellular cooperation through the spreading of a calcium wave following single cell laser ablation. Networked cells also exhibited resistance to high levels of radiation. Additionally, more lysosomes and mitochondria were found within the CPLs of GBM1 cells compared to non-networked controls, suggestive of an increase in organelle trafficking. Following these discoveries key questions remained with regards to ROCKi GSC networks:

1. Were neurite extensions formed using existing neurofilaments?
2. Did Y-27632 successfully inhibit ROCK at the protein level?
3. Would activation of the RhoA pathway upstream of ROCK reverse the network phenotype?
4. Would inhibition of ROCK in other neural cell types replicate the cellular network phenotype?
5. How would the ROCKi network phenotype compare to other network inducer phenotypes?
6. Could trafficking of organelles in ROCKi networks be demonstrated?

We first sought to determine whether ROCKi-induced networks were formed using existing neurofilaments by determining protein levels of cytoskeleton markers. Following 24 hours of ROCKi (Y-27632, 20μM), GBM1 cells formed visible cellular networks (Fig 3.1A). These extended CPLs were immunopositive for neural specific cytoskeletal markers TuJ1 [481] and MAP2 [482] (Fig 3.1B) indicating an extension of neurofilaments in ROCKi networks. Level of TuJ1 and MAP2 protein was not altered throughout ROCKi network formation compared to the vehicle control, hence indicating a reuse and redistribution of existing neurofilaments rather than de novo formation.

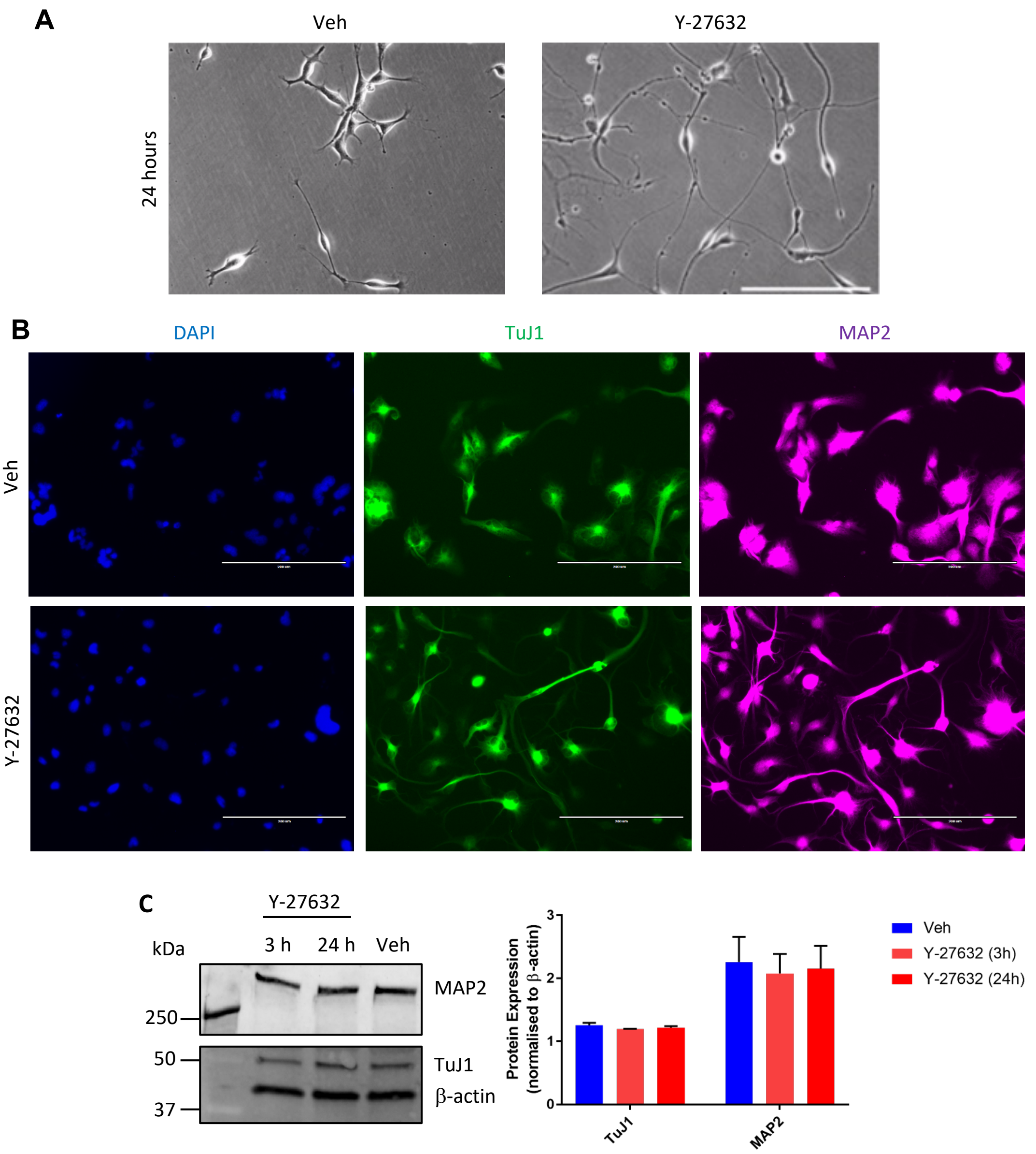

Figure 3.1 ROCK inhibition induces a cellular network with an extension of existing neurofilaments in GBM. (A) Representative phase contrast images of GBM1 cells following treatment with Y-27632 (20µM) or vehicle (H_2O). Scale bar 200µM. **(B)** Projections stain positive for TuJ1 and MAP2 in GBM1 cells treated with Y-27632 (20µM) or vehicle (H_2O). Scale bar 200 µm. **(C)** Immunoblot (left) showing total protein levels of MAP2 and TuJ1 in GBM1 cells following indicated length of treatment with Y-27632 (20µM) or Vehicle (H_2O) (left). Quantification (right) of expression levels of TuJ1 and MAP2 normalised to β-actin. Data are mean (± SD) of 3 biological repeats.

3.1.2 Y-27632 inhibits RhoA pathway via ROCKi even in presence of upstream activation

Da Silva et al previously demonstrated that inhibition of ROCK, via Y-27632, mimicked the increase in CPL phenotype following MLC inhibition [224]. However, an increase in CPL was not replicated via inhibition of LIMK suggesting that Y-27632 induced network formation through inhibition of actin depolymerase, via MLPT pathway arm (Fig 3.2A). We addressed the question whether Y-27632 could sufficiently inhibit the kinase activity of ROCK, even with upstream RhoA pathway activation.

Following stimulation of the RhoA/ROCK pathway by lysophosphatidic acid (LPA) in GBM1 cells, activation of MYTP1 (phosphorylation at Thr853 [483]) was found to be reduced at 0.5 and 4 hours compared to control (Fig 3.2B). RhoA pathway activation via LPA is known to cause neurite retraction in neuronal cells [484]. However, despite upstream activation Y-27632 is still able to induce network formation through the increase of CPL via ROCKi (Fig 3.2C).

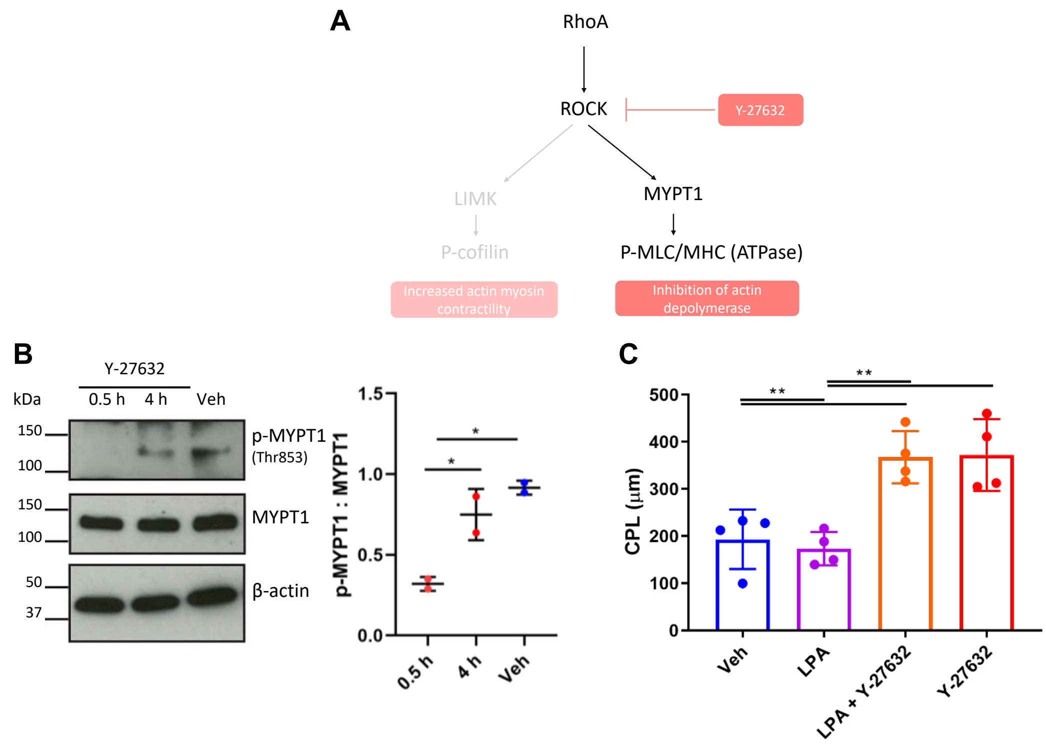

Figure 3.2 Y-27632 inhibits the ROCK pathway despite RhoA stimulation upstream. (A) Effect of Y-27632 inhibition of ROCK, in the RhoA pathway, on cell morphology. **(B)** Immunoblot (left) detecting phosphorylated and total MYPT1 protein in LPA-stimulated (1µM, overnight) GBM1 cells followed by Y-27632 (20µM) or vehicle (H_2O) treatments. Quantification (right) of phosphorylated MYPT1 (p-MYPT) levels. **(C)** CPL values of GBM1 cells pre-treated with Y-27632 (20µM) for 24 hours and subsequently for 8 hours with vehicle (H_2O), or LPA (1µM), or LPA (1µM)/Y-27632 (20µM), or Y-27632 (20µM). Data are mean (± SD) shown for biological repeats (dots). P-value is based on two-sided t-test (B) or one-way ANOVA (C) shown as *(< 0.05), **(<0.005), ***(<0.0005), and ****(<0.0001).

3.1.3 ROCKi induces network formation in NP cells

As stimulation of the pathway via LPA exposure previously demonstrated neurite retractions in neuronal cells [484], we investigated whether inhibition of the pathway, via ROCK, would result in a similar induced network phenotype as exhibited by GSCs.

Following 24 hours of exposure to Y-27632, NP1 cells formed visible cellular networks (Fig 3.4A) with a significant (>1.8 fold) increase in CPL compared to vehicle controls (Fig 3.4B). These cellular projections were also immunopositive for TuJ1 and MAP2 (Fig 3.4C), indicating a phenotype mimicking that seen in GSCs. The functionality of NP induced networks remains to be elucidated, especially in relation to whether it is similar or works in conjunction with GBM networks.

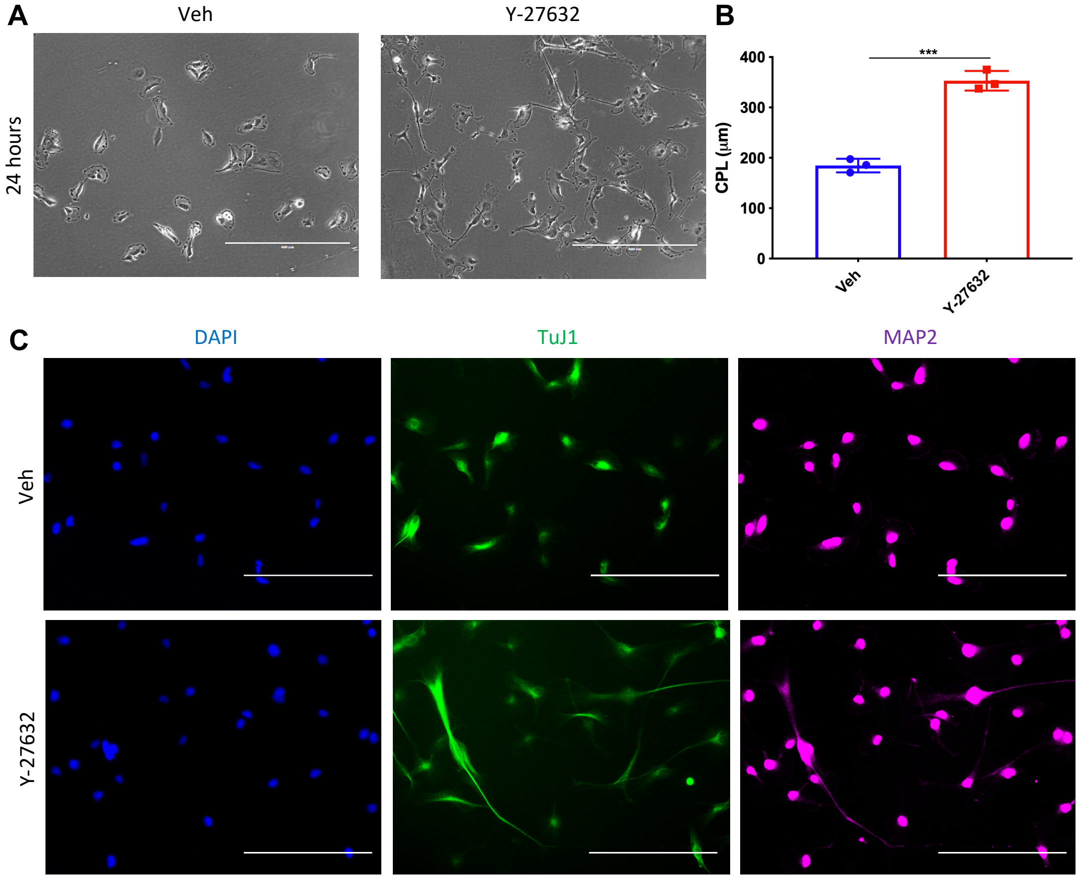

Figure 3.3 ROCK inhibition induces cellular networks in patient derived neural progenitors (NP). (A) Representative phase contrast images of NP1 cells following 24 hours treatment with Y-27632 (20µM) or vehicle (H_2O). Scale bar 200 µM. **(B)** TuJ1 positive CPL values of NP1 cells treated for 24 hours with Y-27632 (20µM) or vehicle (H_2O). Data are mean (± SD) shown for biological repeats (dots). P-value is based on unpaired t-test shown as *(<0.05), **(<0.005), ***(<0.0005), and ****(<0.0001). **(C)** Projections stain positive for TuJ1 and MAP2 in NP1 cells treated with Y-27632 (20µM) or vehicle (H_2O). Scale bar 200µM.

3.1.4 ROCKi induced network phenotype was equal or additive with dual treatment with other network inducers

Inhibition of ROCK is not the only methodology known to induce cellular networks and therefore we investigated the phenotypic effect other network inducers would have in conjunction with ROCKi.

Previously it has been shown Matrigel can promote tube formation in cell lines [227]. Following 24 hours of culture within Matrigel droplets, GBM1 cells showed a further extension of CPLs with Y-27632 treatment (~1.8 fold) compared to vehicle (Fig 3.4A). This demonstrated an additive effect of Matrigel and Y-27632 dual treatment with an increase in GBM1 CPL (~1.5 fold) compared to Y-27632 alone previously shown (Fig 2.3C).

Low concentrations of TGFβ (10ng/ml) have also been previously shown to induce network formation in GBM cells (Daubon et al unpublished data). In normal coating conditions an increase in CPL was observed in both GBM1 and NP1 cells, with a similar phenotype seen with dual Y-27632/TGFβ treatment as with Y-27632 alone (Fig 3.4B). However, in Matrigel coated conditions control cells had similar CPL to dual Y-27632/TGFβ treatment.

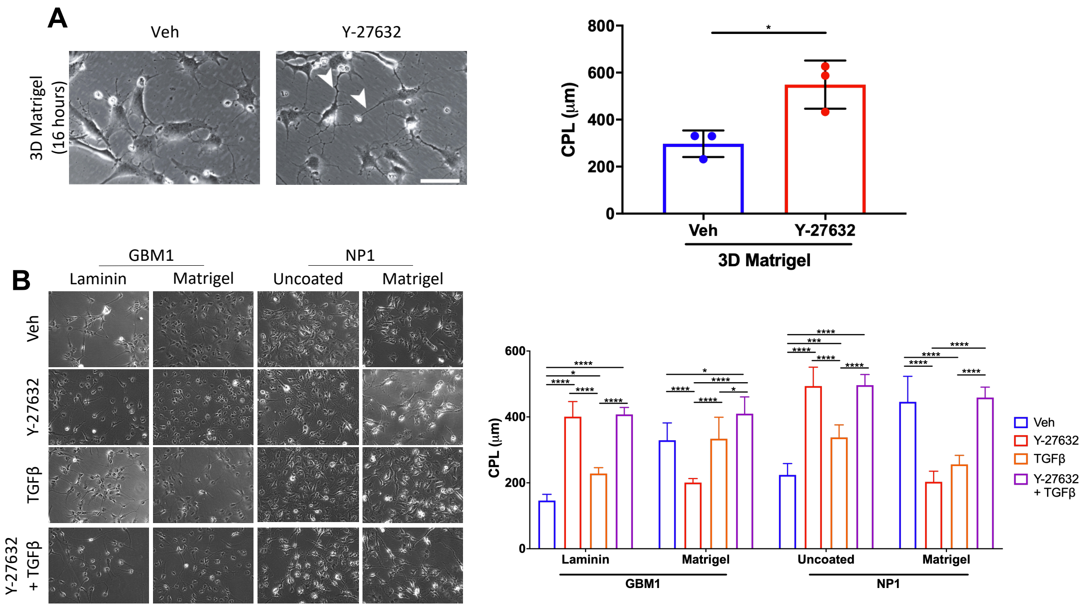

Figure 3.4 In combination with other network inducers the ROCK inhibition phenotype was equal or additive. Representative images (left) of GBM1 cells following a 16-hour period in 3D Matrigel droplet with vehicle (H2O) or Y-27632 (20µM). Arrowheads depict neurite-like outgrowth. Scale bar 20µM. CPL values (right) of vehicle and Y-27632 treatment. Data are mean (± SD) shown for biological replicates (dots). **(B)** Representative images (left) with mean CPL values (right) of GBM1 and NP1 cells plated on Matrigel and normal coating conditions (laminin and uncoated respectively), following 72 hours of treatment with vehicle (H2O), or Y-27632 (20µM), or TGFβ (10ng/ml), or TGFβ (10ng/ml)/Y-27632 (20µM). Mean (± SD) shown for 5 image fields per condition. P-values is based on unpaired t-test (A) or two-way ANOVA and shown as *(< 0.05), **(<0.005), ***(<0.0005), and ****(<0.0001).

3.1.5 Mitochondria intercellular transfer in ROCKi induced networks

Following exposure to radiation da Silva et al showed that ROCKi induced networks of GBM cells exhibited an increase in cell viability, less cell damage with lower percentage of fragmented nuclei and an increase in oxygen consumption rate when compared to control cells. This suggested the network phenotype promoted radioresistance and therefore survival in GBM cells through cellular cooperation [224]. Cells also showed an increase of mitochondria in cellular projections, an observation also described in *in vivo* GBM networked cells [216]. Previously it has been described the ability of cellular uptake of healthy mitochondria can rescue mitochondrial respiration defects in recipient cells [485]. Thus, we investigated whether the increase in the number of mitochondria in cellular projections is an indication of mitochondria transferring intracellularly and if transfer is cancer cell dependent or if there is cooperation between other cell types.

ROCKi networks have been shown to promote radioresistance and therefore survival in GBM cells, as well as an increase of mitochondria in cellular projections [486]. Evidence of mitochondria in cellular projections has also been described in *in vivo* GBM networked cells [216]. As the ability of cells with mitochondrial respiration defects to uptake healthy mitochondria, by a means of intracellular transfer, has been previously described [485], we investigated evidence for this within GBM1 ROCKi induced networks.

We investigated mitochondrial transfer using a co-culture system with MitoTrackerRed-labelled ‘donor’ cells and GFP-expressing ‘recipient’ cells. Transfer of mitochondria from the ‘donor’ population would be indicated by detection of MitoTrackerRed label within ‘recipient’ GFP population.

Following 24 hours of co-culture, detection of transferred mitochondria in ‘recipient’ GFP-GBM1 from ‘donor’ GBM1 cells was significantly increased (≥ 2-fold) in network cells compared to controls (Fig 3.A, B). We found this to be density dependent, with physical connections within the network required for direct transfer (Fig 3.A). We also observed the ability of mitochondrial transfer from ‘donor’ NP1 cells to ‘recipient’ GFP-NP1 (Fig 3.4C) as well as ‘recipient’ GFP-GBM1 with fold changes of ≥ 3.

The ability of transfer of mitochondria may indicate a mechanism by which GBM promotes survival, by restoring mitochondrial function by intercellular transfer from other GBM cells or from other healthy surrounding cells.

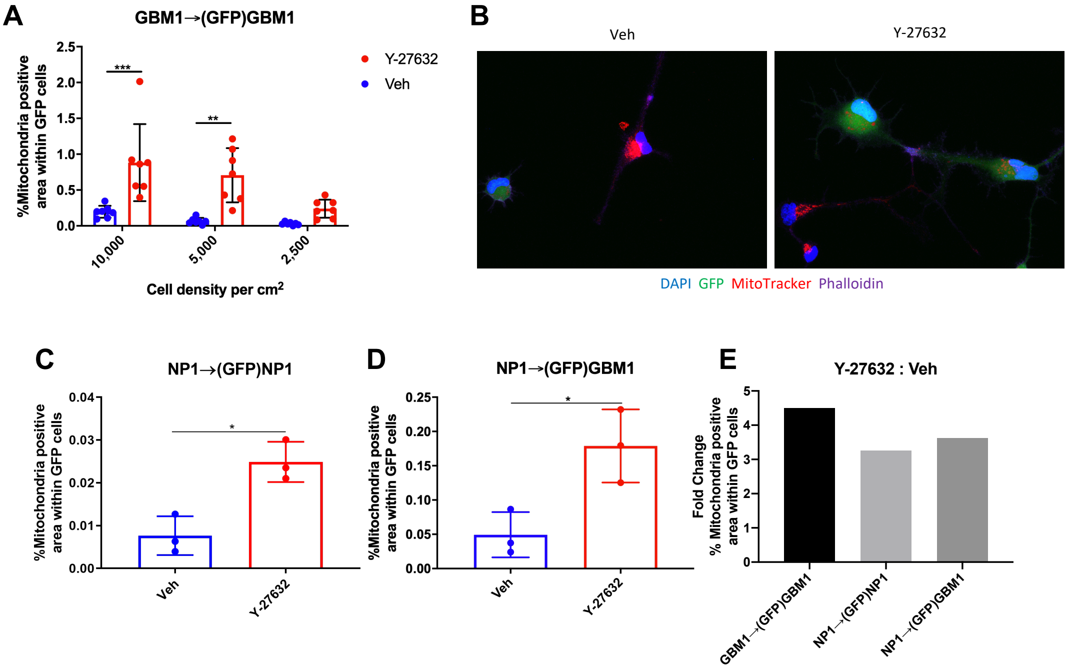

Figure 3.5 ROCK inhibition induced network phenotype promotes cell-cell transfer of mitochondria. (A) Mean percentages assessing MitoTracker-positive signal within GFP-expressing 'recipient' GBM1 cells following 24 hours treatment with Y-27632 (20μM) or vehicle (H_2O), at the indicated densities. **(B)** Confocal microscopy image of 'donor' (GBM1) and 'recipient' (GBM1 GFP-positive) cells after 24 hours of treatment with Y-27632 (20μM) or vehicle (H_2O). Mean percentages assessing MitoTracker-positive signal from 'donor' NP1 cells within GFP-expressing 'recipient' NP1 **(C)** and GBM1 **(D)** cells following 24 hours treatment with Y-27632 (20μM) or vehicle (H_2O). **(E)** Fold change of percentage MitoTracker positive signal area within recipient cells following treatment with Y-27632 (20μM) versus vehicle (H_2O). Mean (± SD) shown for biological repeats (dots), where p-value is shown as *(< 0.05), **(<0.005), ***(<0.0005), and ****(<0.0001).

3.2 Discussion

Extension of glioma cell neurites, forming cellular networks, are proposed to promote radioresistance as well as be a form of tumour dissemination. Previously da Silva et al described the *in vitro* formation cellular networks with extension of cell projections, via inhibition of ROCK [224].

Following these discoveries key questions remained with regards to ROCKi GSC networks:

1. Were neurite extensions formed using existing neurofilaments?
2. Did Y-27632 successfully inhibit ROCK at the protein level?
3. Would activation of the RhoA pathway upstream of ROCK reverse the network phenotype?
4. Would inhibition of ROCK in other neural cell types replicate the cellular network phenotype?
5. How would the ROCKi network phenotype compare to other network inducer phenotypes?
6. Could trafficking of organelles in ROCKi networks be demonstrated?

3.2.1 Inhibition of ROCK pathway in GSCs induces a cellular network phenotype through the extension of neurofilaments

The increase in CPL following ROCKi was previously observed [224]. Here we were able to determine expression levels of neurite specific cytoskeletal markers TuJ1 [481] and MAP2 [482] remained unaltered (Fig 3.1B), indicating redistribution of cell body neurofilaments into the elongating projections. Overexpression of some neurofilament components have been implicated in disease with interruption axonal transport functionality [487]. Therefore, redistribution of neurofilaments following ROCKi ensures a GSC neurite network could be formed and remain functional.

Gritsenko et al also demonstrated extension of GSC neurites following Y-27632 inhibition of ROCK but in spheroid cultures [217]. This indicates ROCKi networks, via Y-27632, are not specific to 2D cultures. Gritsenko et al suggested that it was specifically inhibition of actin myosin contractility inducing the increase in neurite length phenotype. However, da Silva, through the use of inhibitors targeting different components of the RhoA pathway, and observing the resulting phenotypes, inferred the Y-27632 ROCKi phenotype was governed by inhibition actin depolymerase ((Fig 1.A of [224]), (Fig 3.2A). Here we were able to demonstrate the decrease of MYPT1 activation with use of Y-27632 after 30 minutes (Fig 3.2B). This indicates the ability of Y-27632 inhibited ROCK to affect activation of proteins in that arm of the RhoA pathway.

The Thr835 phosphorylation mark was selected due evidence of it being more specifically following inhibition of ROCK than the Thr696 site, which is also often used as a mark of activation [483, 488, 489]. However, we were not able to demonstrate the sustained decrease in Thr853 activation mark (Fig 3.2B). Evidence of MYPT1 activity returning slightly by 4 hours, although still decreased compared to vehicle controls, may be due to redundancy of the myosin phosphatase regulatory pathway [488, 490]. Many kinases are described to phosphorylate MYPT1, including ROCK, ZIPK and p21 [491], and therefore long term significant diminishment of MYPT1 phosphatase activity perhaps was not to be expected. However, the sustainment of the ROCKi network phenotype for up to 5 days, as well as a similar phenotype observed following the use of inhibitors of other components of this specific arm of the RhoA pathway ((Fig 4, 1.A of [224]) indicates downstream ROCK inhibition is sufficient via Y-27632.

The inhibition of ROCK via Y-27632 is also shown to be sufficient to maintain a cellular network phenotype despite upstream RhoA activation. LPA has been shown to activate the RhoA pathway, and cause neurite retraction [484], however Y-27632 inhibition of ROCK maintained increased neurite elongation (Fig 3.2). This demonstrates that Y-27632 is sufficient to reduce levels of ROCK enough to decrease downstream signalling enough to promote the network phenotype observed.

3.2.2 Cellular networks in other cell types and induced via other mechanisms

3.2.2.1 Network phenotype is replicated in human NPs via Y-27632 inhibition of ROCK

It has previously been shown that NPs can organise into cellular networks with other NPs which promotes cell proliferation [492], and as with GBM networks [216]. It has also been previously demonstrated that Y-27632 is able to promote neurite growth in murine NPs *in vitro* [493], we sought to determine if our human NPs would replicate this finding. We observed that, following Y-27632 treatment, our human NPs exhibited a cellular network phenotype, similar to that observed in ROCKi GSCs, with increased CPL with immunopositivity for neurite specific markers TuJ1 and MAP2 (Fig 3.3).

Although a similar ROCKi phenotype has been observed in NPs as with GSCs funcional validation has yet to be performed. In depth analysis of functional cellular cooperation within NP networks would be required to determine if the specific cooperative functions of GSC networks are maintained within NP networks. There is however suggestion of calcium trafficking in previously described NP networks, indicating there may be some similar functionality [492]. However, further investigation of whether this cellular coordination, and calcium signalling conferred radioresistance would need to be tested to determine if this is cancer specific coordination, or common to neural cell types.

3.2.2.2 Alternative inducers of cellular networks

Matrigel has been previously shown to promote branching and the organization of microvessels into a network during *in vitro* angiogenesis [494]. Such branching phenotypes have also been observed following the plating of various tumour cells onto Matrigel matrix [495], as well as specifically in a GBM cell line [227]. These branching phenotypes have been proposed as a common mechanism of invasion between tumour and growth factor-activated endothelial cells [494]. Here we showed although there was some evidence of slight CPL increase in GSCs within Matrigel droplets, the presence of Matrigel was unable to phenocopy the ROCKi networks (Fig 3.4A), indicating separate mechanisms of network formation. However, the combination of Matrigel and ROCKi resulted in CPLs increasing above the normal ROCKi alone phenotype, indicating an additive effect. This may indicate how extracellular matrix components within the brain may facilitate cellular branching and networking. GSCs are known to remodel their extracellular matrix microenvironment [194, 496], and this may indicate how this remodelling helps provide a survival advantage through promotion of cellular networking.

Alternatively, TGFβ has been previously implicated in regulating neurite outgrowths in neuronal [497], retinal [498], and more recently in GSCs cells (group collaboration, unpublished data). Within our system, in our GBM1 model (Table i.3), in normal cell coating conditions, TGFβ was able to, although what seemed subtly, significantly increase CPLs of both GSCs and NPs (Fig 3.4B). However, co-treatments of TGFβ and Y-27632 did not elevate CPL beyond those detected in Y-27632 conditions alone indicating ROCKi network mechanisms may dominate.

We also wanted to use Matrigel coating conditions as was done when the TGFβ system was developed. On the other hand, in Matrigel conditions, used for the initial effect of TGFβ on neurite length (group collaboration, unpublished data). While dual TGFβ and Y-27632 treatment resulted again in the most pronounced CPLs, the effect of Y-27632 alone was lost and in fact vehicle cells exhibited an elevated CPL, in both GSCs and NP cells. It should be highlighted that this is only one repeat, with technical replicates, and therefore further biological repeats would reveal the true effects of each treatment condition on CPL length. Additionally, Matrigel is known to contain many growth factors, one of which is TGFβ, with only information regarding an approximate range of concentration level provided. Therefore, the exact total concentration of TGFβ cells were exposed to could not be determined. To uncouple the effects of the desired concentration of TGFβ from the potential effects of additional unknown levels of TGFβ within Matrigel, in future the use of growth factor reduced Matrigel should be adopted.

Although TGFβ has a longstanding implication in many aspects of glioma biology [499], it has not yet been shown to promote cellular networks. Although this is an *in vitro* system and may only provide a model system for cellular networks, we are not commenting on whether this is a mechanism by which networks are promoted *in vivo*.

3.2.3 ROCKi networks facilitate intercellular transfer of organelles

The evidence of increased mitochondria numbers within the projections of GSCs, with increased migration speeds, is suggestive of the transfer of mitochondria between cells [224]. However, this was not previously tested or quantified. Here we developed a mitochondrial transfer system and were able to show the transfer of MitoRed labelled mitochondria from one cell population to another cell population (Fig 3.5B). We were able to indicate that in addition to GSCs being able to transfer mitochondria between themselves, they were able to accept mitochondria transferred from NP cells (Fig 3.5A, C, E). This provides an insight into how GSCs may be able to protect themselves from radiation induced damage, enlisting network coordination between GSC populations and perhaps between normal cells within the brain for the transfer and acceptance of healthy mitochondria.

There is a plethora of evidence of mitochondrial transfer between healthy to damaged cells, in compromised aerobic and trauma conditions, protecting cells from apoptosis [485, 500–503]. Previously da Silva et al demonstrated an increased oxygen consumption rate of ROCKi networked GSCs with increased survival following radiation exposure [224]. Alongside this and our evidence of transfer of mitochondria between GSCs and between NPs, leads us to propose that mitochondrial transfer from healthy to radiation damaged GSCs is providing protection from radiation induced cell death.

To try and observe if the radioprotective effects could be attributed to mitochondrial transfer we wanted to test if blocking of mitochondrial movement through increase of intracellular-free-Zn^{2+} [504], would sensitise the networks to radiation. However, using methodology described by Malaiyandi et al, Zn^{2+} perfusing conditions resulted in visible deterioration of the GBM cells, with the appearance of stress fibres and cell rounding (data not shown). This is consistent with other reports indicating elevated levels of intracellular-Zn^{2+} is cytotoxic to neurons [505]. As a result, we could not determine if mitochondrial transfer was responsible for the radioprotective effects of ROCKi networks using this methodology, but the evidence of increased oxygen consumption following radiation in ROCKi GSC networks suggests this may be a mechanism of radioprotection.

Here we have addressed key remaining questions regarding the ROCKi modelling of cellular networks. The work shown significantly supplemented the da Silva et al report [224] resulting in the revised da Silva et al article [486].

3.2.4 Modelling cellular networks in glioma

Cellular networks have been implicated in radioresistance and an invasive phenotype within GBM *in vivo* [216]. These direct cell to cell contacts were proposed to be tumour microtubes (TMs), malignant forms of normally occurring tunnelling nanotubes (TNTs) required for cell to cell communication [506, 507]. TNTs are elongated cellular protrusions, first described in Drosophila development [508], which facilitate long range intercellular communication and play a role in the transport of organelles and proteins

[509, 510], spreading of infectious particles [511], stem cell signalling [512] and functional cell-cell coupling [513–515].

The presence and extension of TNTs in cancer are thought to be induced by cellular stress to enhance cell survival. They have been observed in response to reactive oxygen species [516–520], hypoxia [521], chemotherapy [522], UV irradiation [523] and serum deprivation [518].

GBM TNTs were first described in *in vitro* systems [524], and since have been observed *in vitro* in human [525–528], mouse [529] and rat [517] derived GBM cell lines. However, it wasn't until advances in *in vivo* microscopy techniques facilitated the observation of TMs in glioma [216]. The observation of TNTs in glioma up until now were focused on connections between a small number of cells, whereas *in vivo* observations revealed a widespread network of cells indicating multicellular functional coordination not yet described. This has been corroborated with further *in vivo* studies [220]. Such long and widespread connections between multiple cells were henceforth termed TMs [216]. The existence of TMs has been specifically attributed to higher grade astrocytomas, as they have not been detected within oligodendroglioma [216]. This implicates the existence of TMs in the facilitation of the growth, and a hallmark feature, of more specifically aggressive, treatment resistant and highly infiltrative glioma tumours. Within GBM there has been suggested to be the existence of two subtypes of TMs, an interconnecting: facilitating treatment resistance, and an invasive: as a mechanism of cell dissemination from a tumour mass [216, 220]. While TMs of both subtypes have been shown to have similar physical features, such as length, diameter and lifetime, they are thought to differ with the number of connections to other cells. Invasive TMs are thought to connect with 1-2 connections per cell, whereas interconnecting TMs are observed to have ≥4 per cell, this further indicates the use of interconnecting TMs to facilitate multicellular communication, whereas invasive TMs promote dissemination [530]. However, it is expensive to observe networks in vivo, requiring specialised equipment and difficult to mechanistically study.

As a result, this *in vitro* system using ROCK inhibition, via chemical Y-27632 treatment, has been developed and shown to induce multicellular networks in patient derived GSCs [217, 486]. The structures of classical TMs have been shown to have a high actin content [516]. This indicated how inhibition of ROCK, leading to the inhibition of actin depolymerase (Fig 3.2A), results in extension of neurites into a cellular network phenotype in GSCs, similar to TMs.

Here we do not propose for ROCK inhibition to be the sole mechanism for TM extension *in vivo* or that ROCKi cellular projections directly represent them. Previously gap junction connections between TMs have been shown to be connexin 43 dependent [216], however previously ROCKi network connections were shown to be connexin 43 negative (data by Barbara da Silva not shown). This indicates ROCKi cellular connections are not simply of a TM identity *in vitro*. Screening of the expression of additional connexins may implicate the role of others governing cellular connections in ROCKi networks as many connexins are implicated in cancer [531]. However, our observations do not suggest a gap junction between cellular connections and instead fusion with a continuous connection between cells (data not shown). However higher resolution microscopy including electron microscopy may reveal gap junctions are present at cellular extension connections and just have not yet been observed. Here instead we present the use of ROCK inhibition for an easily accessible model system to understand the functionality and mechanisms involved in GSC networks *in vitro*.

The 2D system has been shown to demonstrate similar functionality as has been determined in *in vivo* networks [216]. As well as demonstrating an interconnected network morphology, with extension of cellular projections, cells exhibited a radioprotective phenotype with calcium wave propagation, decreased fragmented nuclei, alongside increased cell viability and basal oxygen consumption rate following high doses of radiation [486]. Additionally, the increased number organelles within cellular projection, previously described by Osswald et al [216], were also able to be demonstrated in ROCKi networks. We have also been able to further functionally investigate this and demonstrate the ability of mitochondria to transfer directly from one cell to another. It has been previously been shown that the transfer of mitochondria between healthy and cells at risk of apoptosis following exposure to radiation [523], our work indicates we have been able to demonstrate a mitochondrial transfer mechanism by which networked GSCs are able to be protected from the effects of radiation. Therefore, we propose to have developed an *in vitro* system that accurately models not only the functionality of networks observed *in vivo*, but also provides a system to further understand GSC mechanisms of radioprotection.

The ROCKi network system could be used to further investigate mitochondrial dynamics in GSCs and uncover further mechanisms by which they contribute to a radioprotective phenotype. Mitochondria dysfunction, with dysregulated fission and fusion, is already implicated in GBM pathophysiology and specifically implicated in treatment resistance [532-536]. Here the ROCKi system could be used for more in depth investigation of fission and fusion mitochondrial processes, and how these may differ between interconnected versus unconnected cells. Additionally, following the evidence of mitochondria transfer between NPs and GSCs (Fig 3.5D), it would help uncover the process of normal to malignant cell organelle transfer.

To further interrogate this, we could adapt the assembloid assay to indicate how ROCKi GSCs interact with cells in a brain hCO microenvironment. In previous hCO studies of GBM the existence of microtubes have been detected [308, 393], which means it is possible study the intercellular connections of GSCs with normal cells, as well as show the dynamics of networks in 3D. Additionally we could detect transfer of mitochondria from cells within the hCO, labelled with MitoRed mitochondrial tracker to GSCs in an adapted assembloid assay termed an organelle transfer-assembloid assay. (Fig 3.6B). Using high resolution imaging or FACs analysis we could quantify the amount of transfer throughout the different stages of invasion to understand how the dynamics may differ throughout the invasion process.

Additionally, we could investigate how mitochondrial transfer from normal hCO cells to GSC is affected following whole assembloid radiation. This would model how the mechanism may act clinically when both the normal brain and tumour of patients are exposed to radiation in whole brain radiation regimes [537]. Additionally, single cell lasering could model the effects of more targeted stereotactic radiation regimes to understand how mitochondria transfer mediated radioprotection differs with targeted versus whole brain radiation [538].

Using the ROCKi system we will be able to further investigate the role of mitochondria in GSC pathophysiology and its contribution to a radioprotective phenotype. Targeting of mitochondrial components have also been able to specifically target GBM cells for apoptosis [142], therefore further understanding mitochondrial dynamics may reveal further therapeutic targets.

Although due to it’s in the radioprotective phenotype of networked GSCs we could detect the transfer of specifically mitochondria, but the organelle transfer-assembloid assay could also be employed to detect transfer of other organelles as the transfer of lysosomes has also been previously implicated [224].

The da Silva et al ROCKi system has been shown to induce networks in a panel of GSC models [486], representing different GBM TCGA-subtypes, indicating this may be a GBM wide mechanism. Although the formation of the network phenotype is morphologically observed in the other models, only GBM1 was fully functionally characterised and therefore validation of network functionality in the other models would be required to further indicate GBM wide behaviour.

The da Silva et al study also demonstrated that when more cells were involved in the network there was a decrease in cell movement [486]. This, alongside the evidence of radioprotective properties attributed to multicellular coordination, indicate 2D Y-27632 ROCKi networks represent an interconnected phenotype. However, the use of Y-27632 in embedded GBM spheroids indicated cells remain networked as they migrated from the spheroid core [217], perhaps indicating an invasive network phenotype. This indicates the ability of ROCKi to model the two phenotypes of cellular networks. It is still not yet known if cells exhibiting one network phenotype are able to switch to the other, but the ability of Y-27632 treatments to produce both subtypes indicates the model is suitable to investigate mechanisms of functionality in each subtype.

By using the standard-assembloid assay we could determine whether spheroids of ROCKi networked GSCs exhibit an invasive advantage compared to non-networked cells (Fig 3.6B). By establishing an interconnected network phenotype in 2D and then maintaining exposure to Y-27632 while networked spheroids are formed before placing within the assembloid assay may indicate a switch to an invasive network phenotype. Hence, we may be able to exemplify the ability of the same network population to switch between the two phenotypes, perhaps influenced by invasive cues. This would further implicate the microenvironment’s role in GBM’s invasive behaviour.

Thus, the use of ROCKi networks in GBM allows for multicellular interconnected networks to be modelled *in vitro*, allowing for further interrogation of network formation and functional mechanisms of cellular cooperation, in addition to perhaps uncovering new potential therapeutic targets.

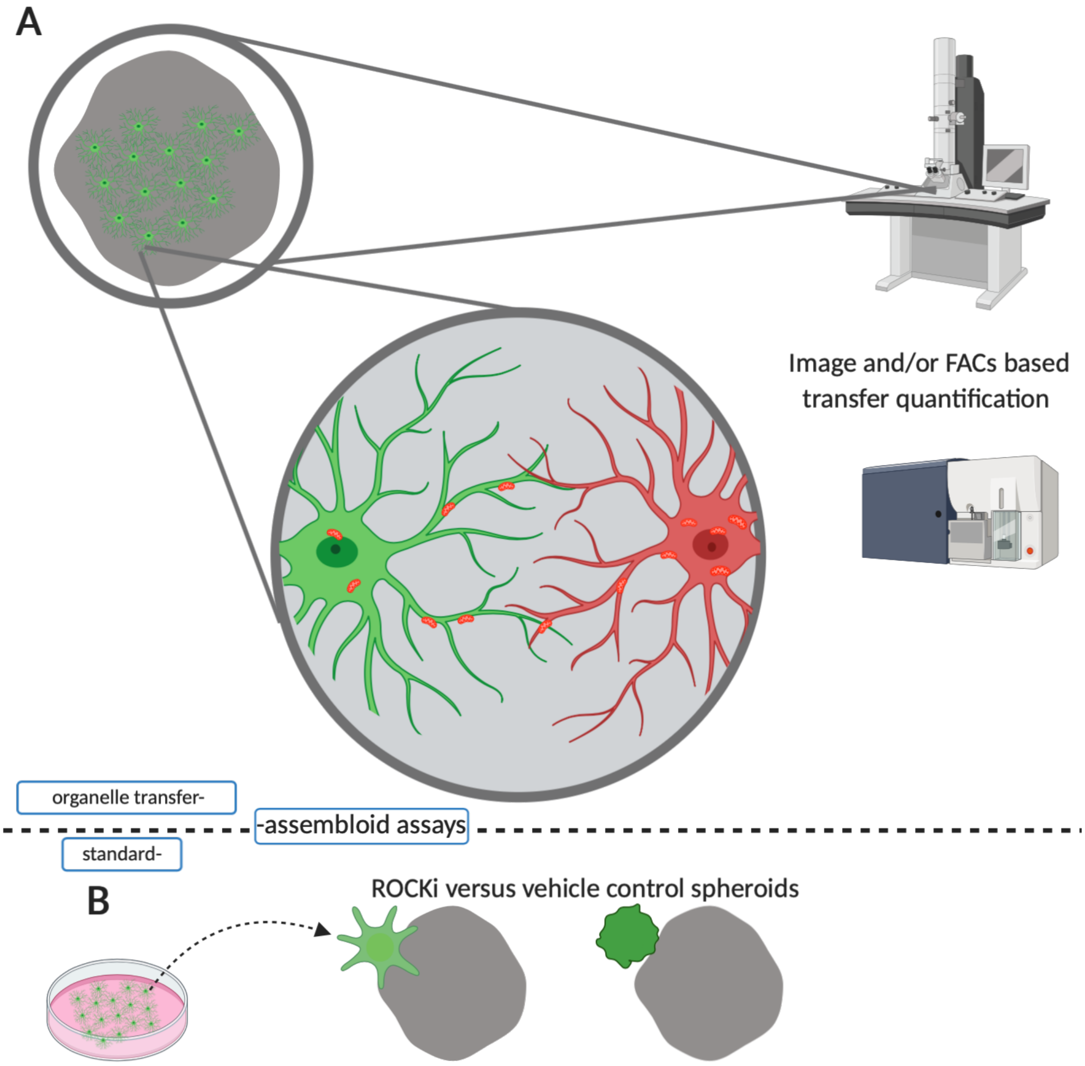

Figure 3.6 Use of the assembloid assay to investigate ROCKi networks in a 3D system. (A) An organelle transfer-assembloid assay would allow the visualization of intracellular organelle transfer between cells within the hCO and GSCs. Donor cell (red) mitochondria labelled with MitoRedTracker showing transfer to recipient cell (green). Transfer could be determined by either FACs or image based quantification. Investigation of organelle dynamics could be determined though high resolution electron microscopy. **(B)** The standard-assembloid assay could uncover invasive potential differences between ROCKi networked cells and non-networked controls. Created with BioRender.com.

Conclusion

In the presented study we investigated different aspects of GBM biology with a focus on phenotype plasticity of glioma stem cells (GSC), specifically invasion, migration, transcriptional EMT upregulation and formation of cellular networks through developing three glioma *in vitro* approaches. These included the development of a human-human assembloid system, developing alternative isolation conditions for GSC populations and validation of the use of ROCK inhibitor treatments.

We further developed our previously established assembloid assay using human pluripotent stem cell-derived cerebral organoids (hCOs). We observed the spontaneous attachment, fusion of spheroids and patient derived GSCs with hCOs, followed by infiltration of cells throughout the hCO. We further investigated the ability of this assay to quantify the invasion capability of several different GSC models. This allowed us to identify two phases of GSC-assembloid invasion. An initial dynamic phase, whereby cells intrinsic invasion behaviour affects the rate and invasion of spheroids into the hCO allowing differences between cell models to be uncovered with significant changes in invasion parameters. Followed by a more static phase, whereby majority of spheroid invasion into the hCO has occurred with little change in invasion parameters. This dynamic and highly infiltrative phase followed by a static, more migratory phase was also demonstrated with the use of freshly resected tumour specimens. This allowed us to investigate and demonstrate the invasion and migratory potential of GSCs providing a system to allow the furth study of spatiotemporal invasion mechanisms. However, the assembloid assay also has the potential to be used drug testing for the discovery of new effective drugs, as well as testing of routine clinical treatments to personalise treatment plans for patients.

Via the use of alternative isolation conditions, based on Wnt signalling, a previously unidentified cell population has been isolated from patient samples. This cell fraction exhibits transcriptional upregulation of the EMT pathway, perhaps representing a population which is preparing for invasion into peripheral tissue showing the observed mesenchymal morphological features (such as large and flat cell bodies). This can shed light on the processes that cells are undergoing during tissue invasion, as well as how these alternative cellular populations may differentially respond to treatment compared to classically isolated GSCs.

Physical cellular networking has been implicated as a means of invasive GSCs dissemination. Here we have demonstrated that a 2D chemically-inducible is able to recapitulate the cellular network phenotype observed *in vivo*. We have been able to observe cells within these ROCK inhibitor induced (ROCKi) network are able to transfer mitochondria intercellularly. We propose that this mechanism of intercellular mitochondrial transfer may be, in part, responsible for the previously identified radioprotective phenotype of connected cells. Although we have currently shown this in a 2D system, we are yet to demonstrate this in 3D. However, with the use of adapted assembloid assays we may be able to use the ROCKi system to uncover the plastic switch between invasive and interconnected phenotypes within GBM, which are currently a barrier to effective (DNA-damaging) treatment.

Following surgical resection, cells that have disseminated from the tumour bulk remain within the margin zone. The invasion and migration of these cell populations are thought to undergo transition to a more mesenchymal phenotype to aid their dissemination as well as forming communicating physical cellular co-operation networks. As a result, we believe the development of the assembloid assay allows for the integration of GSC phenotypes, with the upregulation of EMT and cellular networks as cells invade and migrate, modelling the process by which cells disseminate from tumour bulk within patients. By using a one model, integrative approach, we will be able to more closely model the phenotypic plasticity cells are undergoing within the margin zone. A better understanding of the behaviour of cells within this zone will lead to new ways to target these populations in the hope to reduce the likelihood of tumour recurrence, ultimately leading to better outcomes for patients who are diagnosed with a fatal brain tumour.

List of Abbreviations

5-ALA	5-aminolevulinic acid
aSCs	Adult stem cells
bFGF	Basic fibroblast growth factor
CCGA	Chinese Cancer Genome Atlas
CLE	Caudal lateral epiblast
CNS	Central nervous system
COs	Cerebral organoids
CPL	Cellular projection length
CSC	Cancer stem cells
dNMPs	Differentiated NMPs
EBs	Embryoid bodies
ECM	Extracellular matrix
ECTsph	Ectodermal spheroid
EDTA	Ethylenediaminetetraacetic acid
EGF	Epidermal growth factor
EMT	Epithelial to mesenchymal transition
ENDsph	Endodermal spheroid
ESC	Embryonic stem cells
FBS	Fetal bovine serum
GBM	Glioblastoma multiforme
gNSC	Glioma neural stem cell
GS	Gliosarcoma
GSC	Glioma stem cell
hCO	Human cerebral organoid
HGG	High grade glioma
IDH	Isocitrate dehydrogenase
iPSC	Induced pluripotent stem cells
iPSCsph	iPSC spheroid
LBsphs	Lineage biased spheroids
LGG	Low grade glioma
mCO	Mouse cerebral organoid
MEM-NEAA	Minimum essential medium non-essential amino acids
MESsph	Mesodermal spheroid
MFAP5	Microfibril associated protein 5

MGMT	O-6-methylguanine-DNA methyltransferase
MMR	Mismatch repair
MRI	Magnetic resource imaging
mTeSR	Modified Tenneille special recipe
NMPs	Neuromesodermal progenitors
NOS	Not otherwise specified
NPs	Neural progenitors
NSB	Node streak border
NSC	Neural stem cell
OCT	Optimum cutting temperature
PET	Positron emission tomography
PFA	Paraformaldehyde
PS	Primitive streak
PSCs	Pluripotent stem cells
ROCK	RHO-associated serine/threonine kinase
ROCKi	ROCK induced
scRNA-seq	Single cell RNA-sequencing
SOX2	Sex determining region Y-box 2
SVZ	Subventricular zone
T	Brachyury
TCGA	The Cancer Genome Atlas
TMs	Tumour microtubles
TMZ	Temozolomide
TNC	Tenascin C
TNTs	Tunnelling nanotubes
ULA	Ultra low attachment
VEGF	Vascular endothelial growth factor
VIM	Vimentin
WHO	World Health Organisation

Appendix A

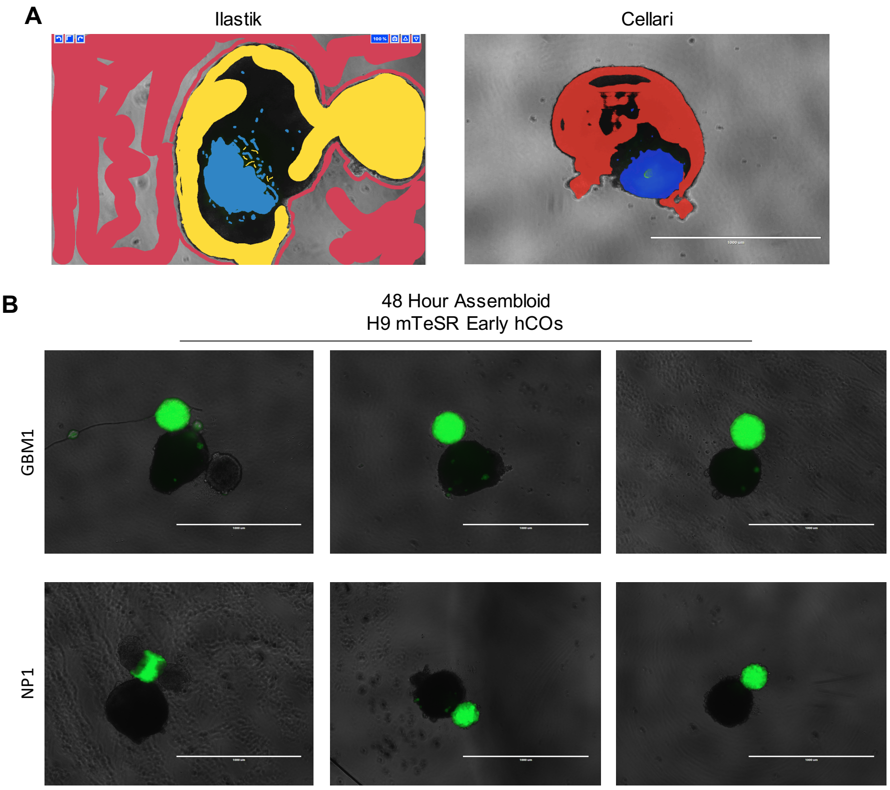

Figure A.1 Detection of invading spheroid behaviour within assembloids. (A) Separation of invading GFP spheroids and hCOs using manual segmentation training programmes Ilastik (left) and Cellari (right) was not effective. **(B)** Deriving H9 hCOs using mTeSR during stage 1 with early advancement to stage 2 results in improper differentiation with hCOs exhibiting a small area and lack of optical brightening. At 48 hours resulting assembloids do not show invasion of GBM or NP spheroids.

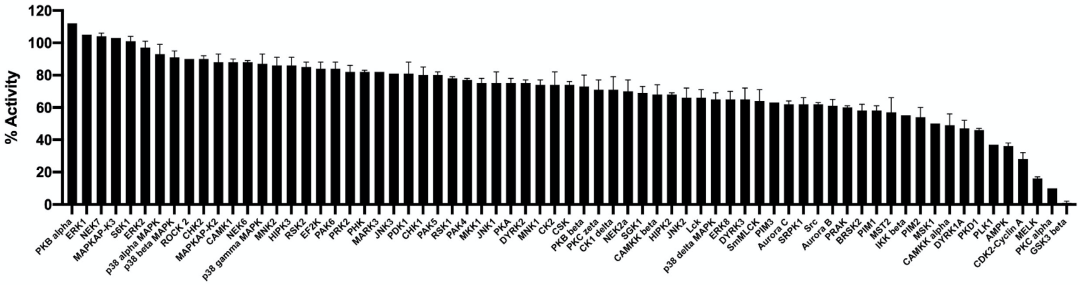

Figure A.2 Percentage of kinase activity following treatment with 10 µM CHIR99021. Data obtained from: http://www.kinase-screen.mrc.ac.uk/screening-compounds/341051

A

Gene	NMP_Wnt3a vs gNSC			dNMP vs ESC			Description
	Position	Log2FC	-Log10 Pval	Position	Log2FC	-Log10 Pval	
Upregulated							
DKK2	1	6.356	2.572	272	3.810	28.102	dickkopf WNT signaling pathway inhibitor 2
LPAR5	2	4.924	3.183	1201	1.572	3.336	lysophosphatidic acid receptor 5
F13A1	3	4.736	3.114	834	2.086	16.403	coagulation factor XIII A chain
CPA4	4	4.440	11.742	843	2.066	2.681	carboxypeptidase A4
HAPLN1	5	4.337	4.198	275	3.792	35.207	hyaluronan and proteoglycan link protein 1
ALX4	6	4.071	4.482	215	4.270	10.211	ALX homeobox 4
IGFBP1	7	3.903	11.987	638	2.463	3.381	insulin like growth factor binding protein 1
SEMA3C	8	3.779	5.161	274	3.797	65.703	semaphorin 3C
SPAG17	9	3.759	2.410	1186	1.600	5.832	sperm associated antigen 17
C11orf87	10	3.741	3.739	119	5.260	26.406	chromosome 11 open reading frame 87
Downregulated							
OPCML	10	-2.388	2.202	448	-2.762	24.566	opioid binding protein/cell adhesion molecule like
SEZ6	9	-2.806	2.608	114	-4.317	30.493	seizure related 6 homolog
ATP1A3	8	-3.191	3.125	1678	-1.089	17.765	ATPase Na+/K+ transporting subunit alpha 3
BRINP1	7	-3.256	3.106	115	-4.307	105.804	BMP/retinoic acid inducible neural specific 1
PCDH1	6	-3.270	4.171	362	-3.022	28.419	protocadherin 1
VAV3	5	-3.312	2.671	1874	-0.951	11.642	vav guanine nucleotide exchange factor 3
PPP1R16B	4	-3.401	3.492	312	-3.211	24.896	protein phosphatase 1 regulatory subunit 16B
ADCYAP1R1	3	-3.433	3.768	1231	-1.529	41.139	ADCYAP receptor type I
LINC01234	2	-3.445	2.011	1417	-1.330	9.529	long intergenic non-protein coding RNA 1234
STXBP5L	1	-3.592	2.848	1911	-0.929	12.010	syntaxin binding protein 5 like

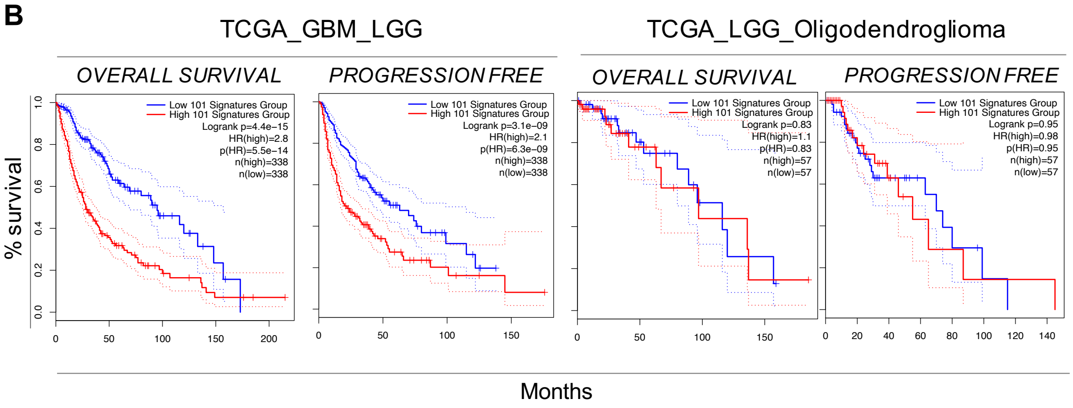

Figure A.3 Prognosis of glioma_NMP signature. (A) Top 10 most up- and downregulated genes in NMP_Wnt3a dataset, compared to position of genes in dNMP dataset. (**B**) Overall and progression free survival for upregulated overlap genes in TCGA_GBM_LGG and TCGA_LGG_Oligodendroglioma datasets.

Bibliography

1. Ferlay, J., Soerjomataram, I., Dikshit, R., Eser, S., Mathers, C., Rebelo, M., Parkin, D. M., Forman, D., and Bray, F. (2015). Cancer incidence and mortality worldwide: sources, methods and major patterns in GLOBOCAN 2012. Int. J. Cancer *136*, E359-86.
2. Louis, D. N., Perry, A., Reifenberger, G., von Deimling, A., Figarella-Branger, D., Cavenee, W. K., Ohgaki, H., Wiestler, O. D., Kleihues, P., and Ellison, D. W. (2016). The 2016 World Health Organization Classification of Tumors of the Central Nervous System: a summary. Acta Neuropathol. *131*, 803–820.
3. Tamimi, A. F., and Juweid, M. (2017). Epidemiology and outcome of glioblastoma. In Glioblastoma, S. De Vleeschouwer, ed. (Brisbane (AU): Codon Publications).
4. Ohgaki, H., and Kleihues, P. (2005). Population-based studies on incidence, survival rates, and genetic alterations in astrocytic and oligodendroglial gliomas. J. Neuropathol. Exp. Neurol. *64*, 479–489.
5. Brodbelt, A., Greenberg, D., Winters, T., Williams, M., Vernon, S., Collins, V. P., and (UK) National Cancer Information Network Brain Tumour Group (2015). Glioblastoma in England: 2007-2011. Eur. J. Cancer *51*, 533–542.
6. Chamberlain, M. C., and Kormanik, P. A. (1998). Practical guidelines for the treatment of malignant gliomas. West J Med *168*, 114–120.
7. Chang, S. M., Parney, I. F., Huang, W., Anderson, F. A., Asher, A. L., Bernstein, M., Lillehei, K. O., Brem, H., Berger, M. S., Laws, E. R., et al. (2005). Patterns of care for adults with newly diagnosed malignant glioma. JAMA *293*, 557–564.
8. Ostrom, Q. T., Cioffi, G., Gittleman, H., Patil, N., Waite, K., Kruchko, C., and Barnholtz-Sloan, J. S. (2019). CBTRUS Statistical Report: Primary Brain and Other Central Nervous System Tumors Diagnosed in the United States in 2012-2016. Neuro. Oncol. *21*, v1–v100.
9. Ly, K. I., Wen, P. Y., and Huang, R. Y. (2020). Imaging of central nervous system tumors based on the 2016 world health organization classification. Neurol. Clin. *38*, 95–113.
10. Hu, L. S., Eschbacher, J. M., Dueck, A. C., Heiserman, J. E., Liu, S., Karis, J. P., Smith, K. A., Shapiro, W. R., Pinnaduwage, D. S., Coons, S. W., et al. (2012). Correlations between perfusion MR imaging cerebral blood volume, microvessel quantification, and clinical outcome using stereotactic analysis in recurrent high-grade glioma. AJNR Am. J. Neuroradiol. *33*, 69–76.
11. Sadeghi, N., D’Haene, N., Decaestecker, C., Levivier, M., Metens, T., Maris, C., Wikler, D., Baleriaux, D., Salmon, I., and Goldman, S. (2008). Apparent diffusion coefficient and cerebral blood volume in brain gliomas: relation to tumor cell density and tumor microvessel density based on stereotactic biopsies. AJNR Am. J. Neuroradiol. *29*, 476–482.
12. Wesseling, P., van der Laak, J. A., de Leeuw, H., Ruiter, D. J., and

Burger, P. C. (1994). Quantitative immunohistological analysis of the microvasculature in untreated human glioblastoma multiforme. Computer-assisted image analysis of whole-tumor sections. J. Neurosurg. *81*, 902–909.

13. Cohen, A. L., Holmen, S. L., and Colman, H. (2013). IDH1 and IDH2 mutations in gliomas. Curr Neurol Neurosci Rep *13*, 345.
14. Horbinski, C. (2013). What do we know about IDH1/2 mutations so far, and how do we use it? Acta Neuropathol. *125*, 621–636.
15. Ohgaki, H., and Kleihues, P. (2007). Genetic pathways to primary and secondary glioblastoma. Am. J. Pathol. *170*, 1445–1453.
16. Ohgaki, H., and Kleihues, P. (2013). The definition of primary and secondary glioblastoma. Clin. Cancer Res. *19*, 764–772.
17. Ohka, F., Natsume, A., and Wakabayashi, T. (2012). Current trends in targeted therapies for glioblastoma multiforme. Neurol Res Int *2012*, 878425.
18. Thakkar, J. P., Dolecek, T. A., Horbinski, C., Ostrom, Q. T., Lightner, D. D., Barnholtz-Sloan, J. S., and Villano, J. L. (2014). Epidemiologic and molecular prognostic review of glioblastoma. Cancer Epidemiol. Biomarkers Prev. *23*, 1985–1996.
19. Bush, N. A. O., Chang, S. M., and Berger, M. S. (2017). Current and future strategies for treatment of glioma. Neurosurg. Rev *40*, 1–14.
20. Lacroix, M., Abi-Said, D., Fourney, D. R., Gokaslan, Z. L., Shi, W., DeMonte, F., Lang, F. F., McCutcheon, I. E., Hassenbusch, S. J., Holland, E., et al. (2001). A multivariate analysis of 416 patients with glioblastoma multiforme: prognosis, extent of resection, and survival. J. Neurosurg. *95*, 190–198.
21. McGirt, M. J., Chaichana, K. L., Gathinji, M., Attenello, F. J., Than, K., Olivi, A., Weingart, J. D., Brem, H., and Quiñones-Hinojosa, A. R. (2009). Independent association of extent of resection with survival in patients with malignant brain astrocytoma. J. Neurosurg. *110*, 156–162.
22. Grossman, S. A., and Batara, J. F. (2004). Current management of glioblastoma multiforme. Semin. Oncol. *31*, 635–644.
23. Sahm, F., Capper, D., Jeibmann, A., Habel, A., Paulus, W., Troost, D., and von Deimling, A. (2012). Addressing diffuse glioma as a systemic brain disease with single-cell analysis. Arch. Neurol. *69*, 523–526.
24. Stummer, W., Pichlmeier, U., Meinel, T., Wiestler, O. D., Zanella, F., Reulen, H.-J., and ALA-Glioma Study Group (2006). Fluorescence-guided surgery with 5-aminolevulinic acid for resection of malignant glioma: a randomised controlled multicentre phase III trial. Lancet Oncol. *7*, 392–401.
25. Sanai, N., Polley, M.-Y., McDermott, M. W., Parsa, A. T., and Berger, M. S. (2011). An extent of resection threshold for newly diagnosed glioblastomas. J. Neurosurg. *115*, 3–8.
26. Kreth, F. W., Thon, N., Simon, M., Westphal, M., Schackert, G., Nikkhah, G., Hentschel, B., Reifenberger, G., Pietsch, T., Weller, M., et

al. (2013). Gross total but not incomplete resection of glioblastoma prolongs survival in the era of radiochemotherapy. Ann. Oncol. *24*, 3117–3123.

27. Grabowski, M. M., Recinos, P. F., Nowacki, A. S., Schroeder, J. L., Angelov, L., Barnett, G. H., and Vogelbaum, M. A. (2014). Residual tumor volume versus extent of resection: predictors of survival after surgery for glioblastoma. J. Neurosurg. *121*, 1115–1123.
28. Marko, N. F., Weil, R. J., Schroeder, J. L., Lang, F. F., Suki, D., and Sawaya, R. E. (2014). Extent of resection of glioblastoma revisited: personalized survival modeling facilitates more accurate survival prediction and supports a maximum-safe-resection approach to surgery. J. Clin. Oncol. *32*, 774–782.
29. Brown, T. J., Brennan, M. C., Li, M., Church, E. W., Brandmeir, N. J., Rakszawski, K. L., Patel, A. S., Rizk, E. B., Suki, D., Sawaya, R., et al. (2016). Association of the Extent of Resection With Survival in Glioblastoma: A Systematic Review and Meta-analysis. JAMA Oncol. *2*, 1460–1469.
30. Ringel, F., Pape, H., Sabel, M., Krex, D., Bock, H. C., Misch, M., Weyerbrock, A., Westermaier, T., Senft, C., Schucht, P., et al. (2016). Clinical benefit from resection of recurrent glioblastomas: results of a multicenter study including 503 patients with recurrent glioblastomas undergoing surgical resection. Neuro. Oncol. *18*, 96–104.
31. Suchorska, B., Weller, M., Tabatabai, G., Senft, C., Hau, P., Sabel, M. C., Herrlinger, U., Ketter, R., Schlegel, U., Marosi, C., et al. (2016). Complete resection of contrast-enhancing tumor volume is associated with improved survival in recurrent glioblastoma-results from the DIRECTOR trial. Neuro. Oncol. *18*, 549–556.
32. Ellingson, B. M., Abrey, L. E., Nelson, S. J., Kaufmann, T. J., Garcia, J., Chinot, O., Saran, F., Nishikawa, R., Henriksson, R., Mason, W. P., et al. (2018). Validation of postoperative residual contrast-enhancing tumor volume as an independent prognostic factor for overall survival in newly diagnosed glioblastoma. Neuro. Oncol. *20*, 1240–1250.
33. Stummer, W., Tonn, J.-C., Mehdorn, H. M., Nestler, U., Franz, K., Goetz, C., Bink, A., Pichlmeier, U., and ALA-Glioma Study Group (2011). Counterbalancing risks and gains from extended resections in malignant glioma surgery: a supplemental analysis from the randomized 5-aminolevulinic acid glioma resection study. Clinical article. J. Neurosurg. *114*, 613–623.
34. Gulati, S., Jakola, A. S., Nerland, U. S., Weber, C., and Solheim, O. (2011). The risk of getting worse: surgically acquired deficits, perioperative complications, and functional outcomes after primary resection of glioblastoma. World Neurosurg. *76*, 572–579.
35. Chaichana, K. L., Jusue-Torres, I., Navarro-Ramirez, R., Raza, S. M., Pascual-Gallego, M., Ibrahim, A., Hernandez-Hermann, M., Gomez, L., Ye, X., Weingart, J. D., et al. (2014). Establishing percent resection and residual volume thresholds affecting survival and recurrence for patients with newly diagnosed intracranial glioblastoma. Neuro. Oncol. *16*, 113–

122.

36. Albert, N. L., Weller, M., Suchorska, B., Galldiks, N., Soffietti, R., Kim, M. M., la Fougère, C., Pope, W., Law, I., Arbizu, J., et al. (2016). Response Assessment in Neuro-Oncology working group and European Association for Neuro-Oncology recommendations for the clinical use of PET imaging in gliomas. Neuro. Oncol. *18*, 1199–1208.

37. Suchorska, B., Albert, N. L., Bauer, E. K., Tonn, J.-C., and Galldiks, N. (2018). The role of amino-acid PET in the light of the new WHO classification 2016 for brain tumors. Q. J. Nucl. Med. Mol. Imaging *62*, 267–271.

38. De Witt Hamer, P. C., Robles, S. G., Zwinderman, A. H., Duffau, H., and Berger, M. S. (2012). Impact of intraoperative stimulation brain mapping on glioma surgery outcome: a meta-analysis. J. Clin. Oncol. *30*, 2559–2565.

39. Jenkinson, M. D., Barone, D. G., Bryant, A., Vale, L., Bulbeck, H., Lawrie, T. A., Hart, M. G., and Watts, C. (2018). Intraoperative imaging technology to maximise extent of resection for glioma. Cochrane Database Syst. Rev. *1*, CD012788.

40. Stupp, R., Mason, W. P., van den Bent, M. J., Weller, M., Fisher, B., Taphoorn, M. J. B., Belanger, K., Brandes, A. A., Marosi, C., Bogdahn, U., et al. (2005). Radiotherapy plus concomitant and adjuvant temozolomide for glioblastoma. N. Engl. J. Med. *352*, 987–996.

41. Stupp, R., Hegi, M. E., Mason, W. P., van den Bent, M. J., Taphoorn, M. J. B., Janzer, R. C., Ludwin, S. K., Allgeier, A., Fisher, B., Belanger, K., et al. (2009). Effects of radiotherapy with concomitant and adjuvant temozolomide versus radiotherapy alone on survival in glioblastoma in a randomised phase III study: 5-year analysis of the EORTC-NCIC trial. Lancet Oncol. *10*, 459–466.

42. Messali, A., Villacorta, R., and Hay, J. W. (2014). A review of the economic burden of glioblastoma and the cost effectiveness of pharmacologic treatments. Pharmacoeconomics *32*, 1201–1212.

43. Brem, S. S., Bierman, P. J., Black, P., Blumenthal, D. T., Brem, H., Chamberlain, M. C., Chiocca, E. A., DeAngelis, L. M., Fenstermaker, R. A., Fine, H. A., et al. (2005). Central nervous system cancers: Clinical Practice Guidelines in Oncology. J Natl Compr Canc Netw *3*, 644–690.

44. Friedman, H. S., Kerby, T., and Calvert, H. (2000). Temozolomide and treatment of malignant glioma. Clin. Cancer Res. *6*, 2585–2597.

45. Carlsson, S. K., Brothers, S. P., and Wahlestedt, C. (2014). Emerging treatment strategies for glioblastoma multiforme. EMBO Mol. Med. *6*, 1359–1370.

46. Gerber, D. E., Grossman, S. A., and Streiff, M. B. (2006). Management of venous thromboembolism in patients with primary and metastatic brain tumors. J. Clin. Oncol. *24*, 1310–1318.

47. Lamborn, K. R., Yung, W. K. A., Chang, S. M., Wen, P. Y., Cloughesy, T. F., DeAngelis, L. M., Robins, H. I., Lieberman, F. S., Fine, H. A., Fink, K. L., et al. (2008). Progression-free survival: an important end point in

evaluating therapy for recurrent high-grade gliomas. Neuro. Oncol. *10*, 162–170.

48. Wu, W., Lamborn, K. R., Buckner, J. C., Novotny, P. J., Chang, S. M., O'Fallon, J. R., Jaeckle, K. A., and Prados, M. D. (2010). Joint NCCTG and NABTC prognostic factors analysis for high-grade recurrent glioma. Neuro. Oncol. *12*, 164–172.
49. Clarke, J. L., Ennis, M. M., Yung, W. K. A., Chang, S. M., Wen, P. Y., Cloughesy, T. F., Deangelis, L. M., Robins, H. I., Lieberman, F. S., Fine, H. A., et al. (2011). Is surgery at progression a prognostic marker for improved 6-month progression-free survival or overall survival for patients with recurrent glioblastoma? Neuro. Oncol. *13*, 1118–1124.
50. Gilbert, M. R. (2011). Recurrent glioblastoma: a fresh look at current therapies and emerging novel approaches. Semin. Oncol. *38 Suppl 4*, S21-33.
51. Wen, P. Y., Weller, M., Lee, E. Q., Alexander, B. A., Barnholtz-Sloan, J. S., Barthel, F. P., Batchelor, T. T., Bindra, R. S., Chang, S. M., Chiocca, E. A., et al. (2020). Glioblastoma in Adults: A Society for Neuro-Oncology (SNO) and European Society of Neuro-Oncology (EANO) Consensus Review on Current Management and Future Directions. Neuro. Oncol.
52. Gilbert, M. R., Dignam, J. J., Armstrong, T. S., Wefel, J. S., Blumenthal, D. T., Vogelbaum, M. A., Colman, H., Chakravarti, A., Pugh, S., Won, M., et al. (2014). A randomized trial of bevacizumab for newly diagnosed glioblastoma. N. Engl. J. Med. *370*, 699–708.
53. Chinot, O. L., Wick, W., Mason, W., Henriksson, R., Saran, F., Nishikawa, R., Carpentier, A. F., Hoang-Xuan, K., Kavan, P., Cernea, D., et al. (2014). Bevacizumab plus radiotherapy-temozolomide for newly diagnosed glioblastoma. N. Engl. J. Med. *370*, 709–722.
54. Wick, W., Gorlia, T., Bendszus, M., Taphoorn, M., Sahm, F., Harting, I., Brandes, A. A., Taal, W., Domont, J., Idbaih, A., et al. (2017). Lomustine and bevacizumab in progressive glioblastoma. N. Engl. J. Med. *377*, 1954–1963.
55. Verhaak, R. G. W., Hoadley, K. A., Purdom, E., Wang, V., Qi, Y., Wilkerson, M. D., Miller, C. R., Ding, L., Golub, T., Mesirov, J. P., et al. (2010). Integrated genomic analysis identifies clinically relevant subtypes of glioblastoma characterized by abnormalities in PDGFRA, IDH1, EGFR, and NF1. Cancer Cell *17*, 98–110.
56. Wang, Q., Hu, B., Hu, X., Kim, H., Squatrito, M., Scarpace, L., deCarvalho, A. C., Lyu, S., Li, P., Li, Y., et al. (2017). Tumor Evolution of Glioma-Intrinsic Gene Expression Subtypes Associates with Immunological Changes in the Microenvironment. Cancer Cell *32*, 42–56.e6.
57. Teo, W.-Y., Sekar, K., Seshachalam, P., Shen, J., Chow, W.-Y., Lau, C. C., Yang, H., Park, J., Kang, S.-G., Li, X., et al. (2019). Relevance of a TCGA-derived Glioblastoma Subtype Gene-Classifier among Patient Populations. Sci. Rep. *9*, 7442.

58. Gill, B. J., Pisapia, D. J., Malone, H. R., Goldstein, H., Lei, L., Sonabend, A., Yun, J., Samanamud, J., Sims, J. S., Banu, M., et al. (2014). MRI-localized biopsies reveal subtype-specific differences in molecular and cellular composition at the margins of glioblastoma. Proc. Natl. Acad. Sci. USA *111*, 12550–12555.

59. Sturm, D., Witt, H., Hovestadt, V., Khuong-Quang, D.-A., Jones, D. T. W., Konermann, C., Pfaff, E., Tönjes, M., Sill, M., Bender, S., et al. (2012). Hotspot mutations in H3F3A and IDH1 define distinct epigenetic and biological subgroups of glioblastoma. Cancer Cell *22*, 425–437.

60. Brennan, C. W., Verhaak, R. G. W., McKenna, A., Campos, B., Noushmehr, H., Salama, S. R., Zheng, S., Chakravarty, D., Sanborn, J. Z., Berman, S. H., et al. (2013). The somatic genomic landscape of glioblastoma. Cell *155*, 462–477.

61. Li, J., Lu, Y., Akbani, R., Ju, Z., Roebuck, P. L., Liu, W., Yang, J.-Y., Broom, B. M., Verhaak, R. G. W., Kane, D. W., et al. (2013). TCPA: a resource for cancer functional proteomics data. Nat. Methods *10*, 1046–1047.

62. Louis, D. N., Ohgaki, H., Wiestler, O. D., Cavenee, W. K., Burger, P. C., Jouvet, A., Scheithauer, B. W., and Kleihues, P. (2007). The 2007 WHO classification of tumours of the central nervous system. Acta Neuropathol. *114*, 97–109.

63. Feigin, I. H., and Gross, S. W. (1955). Sarcoma arising in glioblastoma of the brain. Am. J. Pathol. *31*, 633–653.

64. Boerman, R. H., Anderl, K., Herath, J., Borell, T., Johnson, N., Schaeffer-Klein, J., Kirchhof, A., Raap, A. K., Scheithauer, B. W., and Jenkins, R. B. (1996). The glial and mesenchymal elements of gliosarcomas share similar genetic alterations. J. Neuropathol. Exp. Neurol. *55*, 973–981.

65. Biernat, W., Aguzzi, A., Sure, U., Grant, J. W., Kleihues, P., and Hegi, M. E. (1995). Identical mutations of the p53 tumor suppressor gene in the gliomatous and the sarcomatous components of gliosarcomas suggest a common origin from glial cells. J. Neuropathol. Exp. Neurol. *54*, 651–656.

66. Reis, R. M., Könü-Lebleblicioglu, D., Lopes, J. M., Kleihues, P., and Ohgaki, H. (2000). Genetic profile of gliosarcomas. Am. J. Pathol. *156*, 425–432.

67. Charfi, S., Ayadi, L., Khabir, A., Daoud, E., Kallel, R., Kharrat, O., Mnif, Z., Boudawara, Z., Makni, S., and Boudawara, T. (2009). Gliosarcoma with osteosarcomatous features: a short illustrated review. Acta Neurochir. (Wien) *151*, 809–13; discussion 813.

68. deCarvalho, A. C., Nelson, K., Lemke, N., Lehman, N. L., Arbab, A. S., Kalkanis, S., and Mikkelsen, T. (2010). Gliosarcoma stem cells undergo glial and mesenchymal differentiation in vivo. Stem Cells *28*, 181–190.

69. Lee, D., Kang, S. Y., Suh, Y.-L., Jeong, J. Y., Lee, J.-I., and Nam, D.-H. (2012). Clinicopathologic and genomic features of gliosarcomas. J. Neurooncol. *107*, 643–650.

70. Nagaishi, M., Paulus, W., Brokinkel, B., Vital, A., Tanaka, Y., Nakazato, Y., Giangaspero, F., and Ohgaki, H. (2012). Transcriptional factors for epithelial-mesenchymal transition are associated with mesenchymal differentiation in gliosarcoma. Brain Pathol. *22*, 670–676.

71. Forshew, T., Lewis, P., Waldman, A., Peterson, D., Glaser, M., Brock, C., Sheer, D., and Mulholland, P. J. (2013). Three different brain tumours evolving from a common origin. Oncogenesis *2*, e41.

72. Damodaran, O., van Heerden, J., Nowak, A. K., Bynevelt, M., McDonald, K., Marsh, J., and Lee, G. (2014). Clinical management and survival outcomes of gliosarcomas in the era of multimodality therapy. J. Clin. Neurosci. *21*, 478–481.

73. Cachia, D., Kamiya-Matsuoka, C., Mandel, J. J., Olar, A., Cykowski, M. D., Armstrong, T. S., Fuller, G. N., Gilbert, M. R., and De Groot, J. F. (2015). Primary and secondary gliosarcomas: clinical, molecular and survival characteristics. J. Neurooncol. *125*, 401–410.

74. Schwetye, K. E., Joseph, N. M., Al-Kateb, H., Rich, K. M., Schmidt, R. E., Perry, A., Gutmann, D. H., and Dahiya, S. (2016). Gliosarcomas lack BRAFV600E mutation, but a subset exhibit β-catenin nuclear localization. Neuropathology *36*, 448–455.

75. Smith, D. R., Wu, C.-C., Saadatmand, H. J., Isaacson, S. R., Cheng, S. K., Sisti, M. B., Bruce, J. N., Sheth, S. A., Lassman, A. B., Iwamoto, F. M., et al. (2018). Clinical and molecular characteristics of gliosarcoma and modern prognostic significance relative to conventional glioblastoma. J. Neurooncol. *137*, 303–311.

76. Galanis, E., Buckner, J. C., Dinapoli, R. P., Scheithauer, B. W., Jenkins, R. B., Wang, C. H., O'Fallon, J. R., and Farr, G. (1998). Clinical outcome of gliosarcoma compared with glioblastoma multiforme: North Central Cancer Treatment Group results. J. Neurosurg. *89*, 425–430.

77. Rodriguez, F. J., Scheithauer, B. W., Giannini, C., Bryant, S. C., and Jenkins, R. B. (2008). Epithelial and pseudoepithelial differentiation in glioblastoma and gliosarcoma: a comparative morphologic and molecular genetic study. Cancer *113*, 2779–2789.

78. Kozak, K. R., Mahadevan, A., and Moody, J. S. (2009). Adult gliosarcoma: epidemiology, natural history, and factors associated with outcome. Neuro. Oncol. *11*, 183–191.

79. Patel, A. P., Tirosh, I., Trombetta, J. J., Shalek, A. K., Gillespie, S. M., Wakimoto, H., Cahill, D. P., Nahed, B. V., Curry, W. T., Martuza, R. L., et al. (2014). Single-cell RNA-seq highlights intratumoral heterogeneity in primary glioblastoma. Science *344*, 1396–1401.

80. Couturier, C. P., Ayyadhury, S., Le, P. U., Nadaf, J., Monlong, J., Riva, G., Allache, R., Baig, S., Yan, X., Bourgey, M., et al. (2020). Single-cell RNA-seq reveals that glioblastoma recapitulates a normal neurodevelopmental hierarchy. Nat. Commun. *11*, 3406.

81. Sottoriva, A., Spiteri, I., Piccirillo, S. G. M., Touloumis, A., Collins, V. P., Marioni, J. C., Curtis, C., Watts, C., and Tavaré, S. (2013). Intratumor heterogeneity in human glioblastoma reflects cancer evolutionary

dynamics. Proc. Natl. Acad. Sci. USA *110*, 4009–4014.

82. Darmanis, S., Sloan, S. A., Croote, D., Mignardi, M., Chernikova, S., Samghababi, P., Zhang, Y., Neff, N., Kowarsky, M., Caneda, C., et al. (2017). Single-Cell RNA-Seq Analysis of Infiltrating Neoplastic Cells at the Migrating Front of Human Glioblastoma. Cell Rep. *21*, 1399–1410.

83. Neftel, C., Laffy, J., Filbin, M. G., Hara, T., Shore, M. E., Rahme, G. J., Richman, A. R., Silverbush, D., Shaw, M. L., Hebert, C. M., et al. (2019). An integrative model of cellular states, plasticity, and genetics for glioblastoma. Cell *178*, 835–849.e21.

84. Yu, Z., Pestell, T. G., Lisanti, M. P., and Pestell, R. G. (2012). Cancer stem cells. Int. J. Biochem. Cell Biol. *44*, 2144–2151.

85. Furth, J., Khan, M. C., and Breedis, C. (1937). The Transmission of Leukemia of Mice with a Single Cell. Am. J. Cancer *31*, 276–282.

86. Lapidot, T., Sirard, C., Vormoor, J., Murdoch, B., Hoang, T., Caceres-Cortes, J., Minden, M., Paterson, B., Caligiuri, M. A., and Dick, J. E. (1994). A cell initiating human acute myeloid leukaemia after transplantation into SCID mice. Nature *367*, 645–648.

87. Bonnet, D., and Dick, J. E. (1997). Human acute myeloid leukemia is organized as a hierarchy that originates from a primitive hematopoietic cell. Nat. Med. *3*, 730–737.

88. Al-Hajj, M., Wicha, M. S., Benito-Hernandez, A., Morrison, S. J., and Clarke, M. F. (2003). Prospective identification of tumorigenic breast cancer cells. Proc. Natl. Acad. Sci. USA *100*, 3983–3988.

89. Collins, A. T., Berry, P. A., Hyde, C., Stower, M. J., and Maitland, N. J. (2005). Prospective identification of tumorigenic prostate cancer stem cells. Cancer Res. *65*, 10946–10951.

90. O'Brien, C. A., Pollett, A., Gallinger, S., and Dick, J. E. (2007). A human colon cancer cell capable of initiating tumour growth in immunodeficient mice. Nature *445*, 106–110.

91. Ricci-Vitiani, L., Lombardi, D. G., Pilozzi, E., Biffoni, M., Todaro, M., Peschle, C., and De Maria, R. (2007). Identification and expansion of human colon-cancer-initiating cells. Nature *445*, 111–115.

92. Li, C., Heidt, D. G., Dalerba, P., Burant, C. F., Zhang, L., Adsay, V., Wicha, M., Clarke, M. F., and Simeone, D. M. (2007). Identification of pancreatic cancer stem cells. Cancer Res. *67*, 1030–1037.

93. Gimple, R. C., Bhargava, S., Dixit, D., and Rich, J. N. (2019). Glioblastoma stem cells: lessons from the tumor hierarchy in a lethal cancer. Genes Dev. *33*, 591–609.

94. Bachoo, R. M., Maher, E. A., Ligon, K. L., Sharpless, N. E., Chan, S. S., You, M. J., Tang, Y., DeFrances, J., Stover, E., Weissleder, R., et al. (2002). Epidermal growth factor receptor and Ink4a/Arf: convergent mechanisms governing terminal differentiation and transformation along the neural stem cell to astrocyte axis. Cancer Cell *1*, 269–277.

95. Holland, E. C., Celestino, J., Dai, C., Schaefer, L., Sawaya, R. E., and Fuller, G. N. (2000). Combined activation of Ras and Akt in neural

progenitors induces glioblastoma formation in mice. Nat. Genet. *25*, 55–57.

96. Zhu, Y., Guignard, F., Zhao, D., Liu, L., Burns, D. K., Mason, R. P., Messing, A., and Parada, L. F. (2005). Early inactivation of p53 tumor suppressor gene cooperating with NF1 loss induces malignant astrocytoma. Cancer Cell *8*, 119–130.

97. Alcantara Llaguno, S., Chen, J., Kwon, C.-H., Jackson, E. L., Li, Y., Burns, D. K., Alvarez-Buylla, A., and Parada, L. F. (2009). Malignant astrocytomas originate from neural stem/progenitor cells in a somatic tumor suppressor mouse model. Cancer Cell *15*, 45–56.

98. Lee, J. H., Lee, J. E., Kahng, J. Y., Kim, S. H., Park, J. S., Yoon, S. J., Um, J.-Y., Kim, W. K., Lee, J.-K., Park, J., et al. (2018). Human glioblastoma arises from subventricular zone cells with low-level driver mutations. Nature *560*, 243–247.

99. Pollen, A. A., Nowakowski, T. J., Chen, J., Retallack, H., Sandoval-Espinosa, C., Nicholas, C. R., Shuga, J., Liu, S. J., Oldham, M. C., Diaz, A., et al. (2015). Molecular identity of human outer radial glia during cortical development. Cell *163*, 55–67.

100. Bardella, C., Al-Dalahmah, O., Krell, D., Brazauskas, P., Al-Qahtani, K., Tomkova, M., Adam, J., Serres, S., Lockstone, H., Freeman-Mills, L., et al. (2016). Expression of idh1r132h in the murine subventricular zone stem cell niche recapitulates features of early gliomagenesis. Cancer Cell *30*, 578–594.

101. Singh, S. K., Hawkins, C., Clarke, I. D., Squire, J. A., Bayani, J., Hide, T., Henkelman, R. M., Cusimano, M. D., and Dirks, P. B. (2004). Identification of human brain tumour initiating cells. Nature *432*, 396–401.

102. Lee, J., Kotliarova, S., Kotliarov, Y., Li, A., Su, Q., Donin, N. M., Pastorino, S., Purow, B. W., Christopher, N., Zhang, W., et al. (2006). Tumor stem cells derived from glioblastomas cultured in bFGF and EGF more closely mirror the phenotype and genotype of primary tumors than do serum-cultured cell lines. Cancer Cell *9*, 391–403.

103. Singh, S. K., Clarke, I. D., Terasaki, M., Bonn, V. E., Hawkins, C., Squire, J., and Dirks, P. B. (2003). Identification of a cancer stem cell in human brain tumors. Cancer Res. *63*, 5821–5828.

104. Phillips, H. S., Kharbanda, S., Chen, R., Forrest, W. F., Soriano, R. H., Wu, T. D., Misra, A., Nigro, J. M., Colman, H., Soroceanu, L., et al. (2006). Molecular subclasses of high-grade glioma predict prognosis, delineate a pattern of disease progression, and resemble stages in neurogenesis. Cancer Cell *9*, 157–173.

105. Hemmati, H. D., Nakano, I., Lazareff, J. A., Masterman-Smith, M., Geschwind, D. H., Bronner-Fraser, M., and Kornblum, H. I. (2003). Cancerous stem cells can arise from pediatric brain tumors. Proc. Natl. Acad. Sci. USA *100*, 15178–15183.

106. Annovazzi, L., Mellai, M., Caldera, V., Valente, G., and Schiffer, D. (2011). SOX2 expression and amplification in gliomas and glioma cell

lines. Cancer Genomics Proteomics *8*, 139–147.

107. Tunici, P., Bissola, L., Lualdi, E., Pollo, B., Cajola, L., Broggi, G., Sozzi, G., and Finocchiaro, G. (2004). Genetic alterations and in vivo tumorigenicity of neurospheres derived from an adult glioblastoma. Mol. Cancer *3*, 25.

108. Jin, X., Jin, X., Jung, J.-E., Beck, S., and Kim, H. (2013). Cell surface Nestin is a biomarker for glioma stem cells. Biochem. Biophys. Res. Commun. *433*, 496–501.

109. Ligon, K. L., Huillard, E., Mehta, S., Kesari, S., Liu, H., Alberta, J. A., Bachoo, R. M., Kane, M., Louis, D. N., Depinho, R. A., et al. (2007). Olig2-regulated lineage-restricted pathway controls replication competence in neural stem cells and malignant glioma. Neuron *53*, 503–517.

110. Jan, H.-J., Lee, C.-C., Shih, Y.-L., Hueng, D.-Y., Ma, H.-I., Lai, J.-H., Wei, H.-W., and Lee, H.-M. (2010). Osteopontin regulates human glioma cell invasiveness and tumor growth in mice. Neuro. Oncol. *12*, 58–70.

111. Kim, J., Woo, A. J., Chu, J., Snow, J. W., Fujiwara, Y., Kim, C. G., Cantor, A. B., and Orkin, S. H. (2010). A Myc network accounts for similarities between embryonic stem and cancer cell transcription programs. Cell *143*, 313–324.

112. Wakimoto, H., Kesari, S., Farrell, C. J., Curry, W. T., Zaupa, C., Aghi, M., Kuroda, T., Stemmer-Rachamimov, A., Shah, K., Liu, T.-C., et al. (2009). Human glioblastoma-derived cancer stem cells: establishment of invasive glioma models and treatment with oncolytic herpes simplex virus vectors. Cancer Res. *69*, 3472–3481.

113. Bao, S., Wu, Q., Sathornsumetee, S., Hao, Y., Li, Z., Hjelmeland, A. B., Shi, Q., McLendon, R. E., Bigner, D. D., and Rich, J. N. (2006). Stem cell-like glioma cells promote tumor angiogenesis through vascular endothelial growth factor. Cancer Res. *66*, 7843–7848.

114. Bao, S., Wu, Q., McLendon, R. E., Hao, Y., Shi, Q., Hjelmeland, A. B., Dewhirst, M. W., Bigner, D. D., and Rich, J. N. (2006). Glioma stem cells promote radioresistance by preferential activation of the DNA damage response. Nature *444*, 756–760.

115. Liu, G., Yuan, X., Zeng, Z., Tunici, P., Ng, H., Abdulkadir, I. R., Lu, L., Irvin, D., Black, K. L., and Yu, J. S. (2006). Analysis of gene expression and chemoresistance of CD133+ cancer stem cells in glioblastoma. Mol. Cancer *5*, 67.

116. Chen, J., Li, Y., Yu, T.-S., McKay, R. M., Burns, D. K., Kernie, S. G., and Parada, L. F. (2012). A restricted cell population propagates glioblastoma growth after chemotherapy. Nature *488*, 522–526.

117. Hunter, C., Smith, R., Cahill, D. P., Stephens, P., Stevens, C., Teague, J., Greenman, C., Edkins, S., Bignell, G., Davies, H., et al. (2006). A hypermutation phenotype and somatic MSH6 mutations in recurrent human malignant gliomas after alkylator chemotherapy. Cancer Res. *66*, 3987–3991.

118. Cancer Genome Atlas Research Network (2008). Comprehensive genomic characterization defines human glioblastoma genes and core pathways. Nature *455*, 1061–1068.

119. Johnson, B. E., Mazor, T., Hong, C., Barnes, M., Aihara, K., McLean, C. Y., Fouse, S. D., Yamamoto, S., Ueda, H., Tatsuno, K., et al. (2014). Mutational analysis reveals the origin and therapy-driven evolution of recurrent glioma. Science *343*, 189–193.

120. Wang, J., Cazzato, E., Ladewig, E., Frattini, V., Rosenbloom, D. I. S., Zairis, S., Abate, F., Liu, Z., Elliott, O., Shin, Y.-J., et al. (2016). Clonal evolution of glioblastoma under therapy. Nat. Genet. *48*, 768–776.

121. Barthel, F. P., Johnson, K. C., Varn, F. S., Moskalik, A. D., Tanner, G., Kocakavuk, E., Anderson, K. J., Abiola, O., Aldape, K., Alfaro, K. D., et al. (2019). Longitudinal molecular trajectories of diffuse glioma in adults. Nature *576*, 112–120.

122. Touat, M., Li, Y. Y., Boynton, A. N., Spurr, L. F., Iorgulescu, J. B., Bohrson, C. L., Cortes-Ciriano, I., Birzu, C., Geduldig, J. E., Pelton, K., et al. (2020). Mechanisms and therapeutic implications of hypermutation in gliomas. Nature *580*, 517–523.

123. Cahill, D. P., Levine, K. K., Betensky, R. A., Codd, P. J., Romany, C. A., Reavie, L. B., Batchelor, T. T., Futreal, P. A., Stratton, M. R., Curry, W. T., et al. (2007). Loss of the mismatch repair protein MSH6 in human glioblastomas is associated with tumor progression during temozolomide treatment. Clin. Cancer Res. *13*, 2038–2045.

124. Lathia, J. D., Mack, S. C., Mulkearns-Hubert, E. E., Valentim, C. L. L., and Rich, J. N. (2015). Cancer stem cells in glioblastoma. Genes Dev. *29*, 1203–1217.

125. Suvà, M. L., Rheinbay, E., Gillespie, S. M., Patel, A. P., Wakimoto, H., Rabkin, S. D., Riggi, N., Chi, A. S., Cahill, D. P., Nahed, B. V., et al. (2014). Reconstructing and reprogramming the tumor-propagating potential of glioblastoma stem-like cells. Cell *157*, 580–594.

126. Sherry, M. M., Reeves, A., Wu, J. K., and Cochran, B. H. (2009). STAT3 is required for proliferation and maintenance of multipotency in glioblastoma stem cells. Stem Cells *27*, 2383–2392.

127. Verginelli, F., Perin, A., Dali, R., Fung, K. H., Lo, R., Longatti, P., Guiot, M.-C., Del Maestro, R. F., Rossi, S., di Porzio, U., et al. (2013). Transcription factors FOXG1 and Groucho/TLE promote glioblastoma growth. Nat. Commun. *4*, 2956.

128. Clement, V., Sanchez, P., de Tribolet, N., Radovanovic, I., and Ruiz i Altaba, A. (2007). HEDGEHOG-GLI1 signaling regulates human glioma growth, cancer stem cell self-renewal, and tumorigenicity. Curr. Biol. *17*, 165–172.

129. Rheinbay, E., Suvà, M. L., Gillespie, S. M., Wakimoto, H., Patel, A. P., Shahid, M., Oksuz, O., Rabkin, S. D., Martuza, R. L., Rivera, M. N., et al. (2013). An aberrant transcription factor network essential for Wnt signaling and stem cell maintenance in glioblastoma. Cell Rep. *3*, 1567–1579.

130. Fang, X., Huang, Z., Zhou, W., Wu, Q., Sloan, A. E., Ouyang, G., McLendon, R. E., Yu, J. S., Rich, J. N., and Bao, S. (2014). The zinc finger transcription factor ZFX is required for maintaining the tumorigenic potential of glioblastoma stem cells. Stem Cells *32*, 2033–2047.

131. Zbinden, M., Duquet, A., Lorente-Trigos, A., Ngwabyt, S.-N., Borges, I., and Ruiz i Altaba, A. (2010). NANOG regulates glioma stem cells and is essential in vivo acting in a cross-functional network with GLI1 and p53. EMBO J. *29*, 2659–2674.

132. Chudnovsky, Y., Kim, D., Zheng, S., Whyte, W. A., Bansal, M., Bray, M.-A., Gopal, S., Theisen, M. A., Bilodeau, S., Thiru, P., et al. (2014). ZFHX4 interacts with the NuRD core member CHD4 and regulates the glioblastoma tumor-initiating cell state. Cell Rep. *6*, 313–324.

133. Hegi, M. E., Diserens, A.-C., Gorlia, T., Hamou, M.-F., de Tribolet, N., Weller, M., Kros, J. M., Hainfellner, J. A., Mason, W., Mariani, L., et al. (2005). MGMT gene silencing and benefit from temozolomide in glioblastoma. N. Engl. J. Med. *352*, 997–1003.

134. Hegi, M. E., and Stupp, R. (2015). Withholding temozolomide in glioblastoma patients with unmethylated MGMT promoter--still a dilemma? Neuro. Oncol. *17*, 1425–1427.

135. Park, C.-K., Kim, J. E., Kim, J. Y., Song, S. W., Kim, J. W., Choi, S. H., Kim, T. M., Lee, S.-H., Kim, I. H., and Park, S.-H. (2012). The Changes in MGMT Promoter Methylation Status in Initial and Recurrent Glioblastomas. Transl Oncol *5*, 393–397.

136. Osuka, S., and Van Meir, E. G. (2017). Overcoming therapeutic resistance in glioblastoma: the way forward. J. Clin. Invest. *127*, 415–426.

137. Weinhouse, S., Warburg, O., Burk, D., and Schade, A. L. (1956). On respiratory impairment in cancer cells. Science *124*, 269–270.

138. Li, Z., Bao, S., Wu, Q., Wang, H., Eyler, C., Sathornsumetee, S., Shi, Q., Cao, Y., Lathia, J., McLendon, R. E., et al. (2009). Hypoxia-inducible factors regulate tumorigenic capacity of glioma stem cells. Cancer Cell *15*, 501–513.

139. Flavahan, W. A., Wu, Q., Hitomi, M., Rahim, N., Kim, Y., Sloan, A. E., Weil, R. J., Nakano, I., Sarkaria, J. N., Stringer, B. W., et al. (2013). Brain tumor initiating cells adapt to restricted nutrition through preferential glucose uptake. Nat. Neurosci. *16*, 1373–1382.

140. Eyler, C. E., Wu, Q., Yan, K., MacSwords, J. M., Chandler-Militello, D., Misuraca, K. L., Lathia, J. D., Forrester, M. T., Lee, J., Stamler, J. S., et al. (2011). Glioma stem cell proliferation and tumor growth are promoted by nitric oxide synthase-2. Cell *146*, 53–66.

141. Lu, C., Ward, P. S., Kapoor, G. S., Rohle, D., Turcan, S., Abdel-Wahab, O., Edwards, C. R., Khanin, R., Figueroa, M. E., Melnick, A., et al. (2012). IDH mutation impairs histone demethylation and results in a block to cell differentiation. Nature *483*, 474–478.

142. Polson, E. S., Kuchler, V. B., Abbosh, C., Ross, E. M., Mathew, R. K.,

Beard, H. A., da Silva, B., Holding, A. N., Ballereau, S., Chuntharpursat-Bon, E., et al. (2018). KHS101 disrupts energy metabolism in human glioblastoma cells and reduces tumor growth in mice. Sci. Transl. Med. *10*.

143. Li, Z., Wang, H., Eyler, C. E., Hjelmeland, A. B., and Rich, J. N. (2009). Turning cancer stem cells inside out: an exploration of glioma stem cell signaling pathways. J. Biol. Chem. *284*, 16705–16709.

144. Day, B. W., Stringer, B. W., Al-Ejeh, F., Ting, M. J., Wilson, J., Ensbey, K. S., Jamieson, P. R., Bruce, Z. C., Lim, Y. C., Offenhäuser, C., et al. (2013). EphA3 maintains tumorigenicity and is a therapeutic target in glioblastoma multiforme. Cancer Cell *23*, 238–248.

145. Yan, K., Wu, Q., Yan, D. H., Lee, C. H., Rahim, N., Tritschler, I., DeVecchio, J., Kalady, M. F., Hjelmeland, A. B., and Rich, J. N. (2014). Glioma cancer stem cells secrete Gremlin1 to promote their maintenance within the tumor hierarchy. Genes Dev. *28*, 1085–1100.

146. Korinek, V., Barker, N., Moerer, P., van Donselaar, E., Huls, G., Peters, P. J., and Clevers, H. (1998). Depletion of epithelial stem-cell compartments in the small intestine of mice lacking Tcf-4. Nat. Genet. *19*, 379–383.

147. Huelsken, J., Vogel, R., Erdmann, B., Cotsarelis, G., and Birchmeier, W. (2001). beta-Catenin controls hair follicle morphogenesis and stem cell differentiation in the skin. Cell *105*, 533–545.

148. Clevers, H., Loh, K. M., and Nusse, R. (2014). Stem cell signaling. An integral program for tissue renewal and regeneration: Wnt signaling and stem cell control. Science *346*, 1248012.

149. McCord, M., Mukouyama, Y.-S., Gilbert, M. R., and Jackson, S. (2017). Targeting WNT signaling for multifaceted glioblastoma therapy. Front. Cell Neurosci. *11*, 318.

150. Lee, Y., Lee, J.-K., Ahn, S. H., Lee, J., and Nam, D.-H. (2016). WNT signaling in glioblastoma and therapeutic opportunities. Lab. Invest. *96*, 137–150.

151. Zheng, H., Ying, H., Wiedemeyer, R., Yan, H., Quayle, S. N., Ivanova, E. V., Paik, J.-H., Zhang, H., Xiao, Y., Perry, S. R., et al. (2010). PLAGL2 regulates Wnt signaling to impede differentiation in neural stem cells and gliomas. Cancer Cell *17*, 497–509.

152. Hanahan, D., and Weinberg, R. A. (2011). Hallmarks of cancer: the next generation. Cell *144*, 646–674.

153. Ransohoff, R. M., and Engelhardt, B. (2012). The anatomical and cellular basis of immune surveillance in the central nervous system. Nat. Rev. Immunol. *12*, 623–635.

154. Platten, M., Wick, W., and Weller, M. (2001). Malignant glioma biology: role for TGF-beta in growth, motility, angiogenesis, and immune escape. Microsc. Res. Tech. *52*, 401–410.

155. Ricklefs, F. L., Alayo, Q., Krenzlin, H., Mahmoud, A. B., Speranza, M. C., Nakashima, H., Hayes, J. L., Lee, K., Balaj, L., Passaro, C., et al.

(2018). Immune evasion mediated by PD-L1 on glioblastoma-derived extracellular vesicles. Sci. Adv. *4*, eaar2766.

156. Wu, A., Wei, J., Kong, L.-Y., Wang, Y., Priebe, W., Qiao, W., Sawaya, R., and Heimberger, A. B. (2010). Glioma cancer stem cells induce immunosuppressive macrophages/microglia. Neuro. Oncol. *12*, 1113–1125.

157. Prosniak, M., Harshyne, L. A., Andrews, D. W., Kenyon, L. C., Bedelbaeva, K., Apanasovich, T. V., Heber-Katz, E., Curtis, M. T., Cotzia, P., and Hooper, D. C. (2013). Glioma grade is associated with the accumulation and activity of cells bearing M2 monocyte markers. Clin. Cancer Res. *19*, 3776–3786.

158. Harshyne, L. A., Nasca, B. J., Kenyon, L. C., Andrews, D. W., and Hooper, D. C. (2016). Serum exosomes and cytokines promote a T-helper cell type 2 environment in the peripheral blood of glioblastoma patients. Neuro. Oncol. *18*, 206–215.

159. Griveau, A., Seano, G., Shelton, S. J., Kupp, R., Jahangiri, A., Obernier, K., Krishnan, S., Lindberg, O. R., Yuen, T. J., Tien, A.-C., et al. (2018). A Glial Signature and Wnt7 Signaling Regulate Glioma-Vascular Interactions and Tumor Microenvironment. Cancer Cell *33*, 874–889.e7.

160. Holash, J., Maisonpierre, P. C., Compton, D., Boland, P., Alexander, C. R., Zagzag, D., Yancopoulos, G. D., and Wiegand, S. J. (1999). Vessel cooption, regression, and growth in tumors mediated by angiopoietins and VEGF. Science *284*, 1994–1998.

161. Batchelor, T. T., Sorensen, A. G., di Tomaso, E., Zhang, W.-T., Duda, D. G., Cohen, K. S., Kozak, K. R., Cahill, D. P., Chen, P.-J., Zhu, M., et al. (2007). AZD2171, a pan-VEGF receptor tyrosine kinase inhibitor, normalizes tumor vasculature and alleviates edema in glioblastoma patients. Cancer Cell *11*, 83–95.

162. Miroshnikova, Y. A., Mouw, J. K., Barnes, J. M., Pickup, M. W., Lakins, J. N., Kim, Y., Lobo, K., Persson, A. I., Reis, G. F., McKnight, T. R., et al. (2016). Tissue mechanics promote IDH1-dependent HIF1α-tenascin C feedback to regulate glioblastoma aggression. Nat. Cell Biol. *18*, 1336–1345.

163. Haas, T. L., Sciuto, M. R., Brunetto, L., Valvo, C., Signore, M., Fiori, M. E., di Martino, S., Giannetti, S., Morgante, L., Boe, A., et al. (2017). Integrin α7 is a functional marker and potential therapeutic target in glioblastoma. Cell Stem Cell *21*, 35–50.e9.

164. Barnes, J. M., Kaushik, S., Bainer, R. O., Sa, J. K., Woods, E. C., Kai, F., Przybyla, L., Lee, M., Lee, H. W., Tung, J. C., et al. (2018). A tension-mediated glycocalyx-integrin feedback loop promotes mesenchymal-like glioblastoma. Nat. Cell Biol. *20*, 1203–1214.

165. Calabrese, C., Poppleton, H., Kocak, M., Hogg, T. L., Fuller, C., Hamner, B., Oh, E. Y., Gaber, M. W., Finklestein, D., Allen, M., et al. (2007). A perivascular niche for brain tumor stem cells. Cancer Cell *11*, 69–82.

166. Zhu, T. S., Costello, M. A., Talsma, C. E., Flack, C. G., Crowley, J. G.,

Hamm, L. L., He, X., Hervey-Jumper, S. L., Heth, J. A., Muraszko, K. M., et al. (2011). Endothelial cells create a stem cell niche in glioblastoma by providing NOTCH ligands that nurture self-renewal of cancer stem-like cells. Cancer Res. *71*, 6061–6072.

167. Galli, R., Binda, E., Orfanelli, U., Cipelletti, B., Gritti, A., De Vitis, S., Fiocco, R., Foroni, C., Dimeco, F., and Vescovi, A. (2004). Isolation and characterization of tumorigenic, stem-like neural precursors from human glioblastoma. Cancer Res. *64*, 7011–7021.

168. Bidlingmaier, S., Zhu, X., and Liu, B. (2008). The utility and limitations of glycosylated human CD133 epitopes in defining cancer stem cells. J. Mol. Med. *86*, 1025–1032.

169. Gilbert, C. A., and Ross, A. H. (2009). Cancer stem cells: cell culture, markers, and targets for new therapies. J. Cell Biochem. *108*, 1031–1038.

170. Son, M. J., Woolard, K., Nam, D.-H., Lee, J., and Fine, H. A. (2009). SSEA-1 is an enrichment marker for tumor-initiating cells in human glioblastoma. Cell Stem Cell *4*, 440–452.

171. Wan, F., Zhang, S., Xie, R., Gao, B., Campos, B., Herold-Mende, C., and Lei, T. (2010). The utility and limitations of neurosphere assay, CD133 immunophenotyping and side population assay in glioma stem cell research. Brain Pathol. *20*, 877–889.

172. Pastrana, E., Silva-Vargas, V., and Doetsch, F. (2011). Eyes wide open: a critical review of sphere-formation as an assay for stem cells. Cell Stem Cell *8*, 486–498.

173. Pollard, S. M., Yoshikawa, K., Clarke, I. D., Danovi, D., Stricker, S., Russell, R., Bayani, J., Head, R., Lee, M., Bernstein, M., et al. (2009). Glioma stem cell lines expanded in adherent culture have tumor-specific phenotypes and are suitable for chemical and genetic screens. Cell Stem Cell *4*, 568–580.

174. Wurdak, H., Zhu, S., Romero, A., Lorger, M., Watson, J., Chiang, C.-Y., Zhang, J., Natu, V. S., Lairson, L. L., Walker, J. R., et al. (2010). An RNAi screen identifies TRRAP as a regulator of brain tumor-initiating cell differentiation. Cell Stem Cell *6*, 37–47.

175. Hubert, C. G., Rivera, M., Spangler, L. C., Wu, Q., Mack, S. C., Prager, B. C., Couce, M., McLendon, R. E., Sloan, A. E., and Rich, J. N. (2016). A Three-Dimensional Organoid Culture System Derived from Human Glioblastomas Recapitulates the Hypoxic Gradients and Cancer Stem Cell Heterogeneity of Tumors Found In Vivo. Cancer Res. *76*, 2465–2477.

176. Bian, S., Repic, M., Guo, Z., Kavirayani, A., Burkard, T., Bagley, J. A., Krauditsch, C., and Knoblich, J. A. (2018). Genetically engineered cerebral organoids model brain tumor formation. Nat. Methods *15*, 631–639.

177. Ogawa, J., Pao, G. M., Shokhirev, M. N., and Verma, I. M. (2018). Glioblastoma model using human cerebral organoids. Cell Rep. *23*, 1220–1229.

178. Langer, E. M., Allen-Petersen, B. L., King, S. M., Kendsersky, N. D., Turnidge, M. A., Kuziel, G. M., Riggers, R., Samatham, R., Amery, T. S., Jacques, S. L., et al. (2019). Modeling Tumor Phenotypes In Vitro with Three-Dimensional Bioprinting. Cell Rep. *26*, 608–623.e6.

179. Miyai, M., Tomita, H., Soeda, A., Yano, H., Iwama, T., and Hara, A. (2017). Current trends in mouse models of glioblastoma. J. Neurooncol. *135*, 423–432.

180. Oldrini, B., Curiel-García, Á., Marques, C., Matia, V., Uluçkan, Ö., Graña-Castro, O., Torres-Ruiz, R., Rodriguez-Perales, S., Huse, J. T., and Squatrito, M. (2018). Somatic genome editing with the RCAS-TVA-CRISPR-Cas9 system for precision tumor modeling. Nat. Commun. *9*, 1466.

181. Hambardzumyan, D., Amankulor, N. M., Helmy, K. Y., Becher, O. J., and Holland, E. C. (2009). Modeling Adult Gliomas Using RCAS/t-va Technology. Transl Oncol *2*, 89–95.

182. Hidalgo, M., Amant, F., Biankin, A. V., Budinská, E., Byrne, A. T., Caldas, C., Clarke, R. B., de Jong, S., Jonkers, J., Mælandsmo, G. M., et al. (2014). Patient-derived xenograft models: an emerging platform for translational cancer research. Cancer Discov. *4*, 998–1013.

183. Ben-David, U., Ha, G., Tseng, Y.-Y., Greenwald, N. F., Oh, C., Shih, J., McFarland, J. M., Wong, B., Boehm, J. S., Beroukhim, R., et al. (2017). Patient-derived xenografts undergo mouse-specific tumor evolution. Nat. Genet. *49*, 1567–1575.

184. Jung, J., Seol, H. S., and Chang, S. (2018). The Generation and Application of Patient-Derived Xenograft Model for Cancer Research. Cancer Res. Treat. *50*, 1–10.

185. Joo, K. M., Kim, J., Jin, J., Kim, M., Seol, H. J., Muradov, J., Yang, H., Choi, Y.-L., Park, W.-Y., Kong, D.-S., et al. (2013). Patient-specific orthotopic glioblastoma xenograft models recapitulate the histopathology and biology of human glioblastomas in situ. Cell Rep. *3*, 260–273.

186. Cheng, L., Wu, Q., Guryanova, O. A., Huang, Z., Huang, Q., Rich, J. N., and Bao, S. (2011). Elevated invasive potential of glioblastoma stem cells. Biochem. Biophys. Res. Commun. *406*, 643–648.

187. Prados, M. D., Byron, S. A., Tran, N. L., Phillips, J. J., Molinaro, A. M., Ligon, K. L., Wen, P. Y., Kuhn, J. G., Mellinghoff, I. K., de Groot, J. F., et al. (2015). Toward precision medicine in glioblastoma: the promise and the challenges. Neuro. Oncol. *17*, 1051–1063.

188. Kallenberg, K., Goldmann, T., Menke, J., Strik, H., Bock, H. C., Stockhammer, F., Buhk, J. H., Frahm, J., Dechent, P., and Knauth, M. (2013). Glioma infiltration of the corpus callosum: early signs detected by DTI. J. Neurooncol. *112*, 217–222.

189. Milano, M. T., Okunieff, P., Donatello, R. S., Mohile, N. A., Sul, J., Walter, K. A., and Korones, D. N. (2010). Patterns and timing of recurrence after temozolomide-based chemoradiation for glioblastoma. Int. J. Radiat. Oncol. Biol. Phys. *78*, 1147–1155.

190. Lun, M., Lok, E., Gautam, S., Wu, E., and Wong, E. T. (2011). The natural history of extracranial metastasis from glioblastoma multiforme. J. Neurooncol. *105*, 261–273.

191. Beauchesne, P. (2011). Extra-neural metastases of malignant gliomas: myth or reality? Cancers (Basel) *3*, 461–477.

192. Hamilton, J. D., Rapp, M., Schneiderhan, T., Sabel, M., Hayman, A., Scherer, A., Kröpil, P., Budach, W., Gerber, P., Kretschmar, U., et al. (2014). Glioblastoma multiforme metastasis outside the CNS: three case reports and possible mechanisms of escape. J. Clin. Oncol. *32*, e80-4.

193. Friedl, P., and Alexander, S. (2011). Cancer invasion and the microenvironment: plasticity and reciprocity. Cell *147*, 992–1009.

194. Bellail, A. C., Hunter, S. B., Brat, D. J., Tan, C., and Van Meir, E. G. (2004). Microregional extracellular matrix heterogeneity in brain modulates glioma cell invasion. Int. J. Biochem. Cell Biol. *36*, 1046–1069.

195. Zhong, J., Paul, A., Kellie, S. J., and O'Neill, G. M. (2010). Mesenchymal migration as a therapeutic target in glioblastoma. J Oncol *2010*, 430142.

196. Cha, J., Kang, S.-G., and Kim, P. (2016). Strategies of Mesenchymal Invasion of Patient-derived Brain Tumors: Microenvironmental Adaptation. Sci. Rep. *6*, 24912.

197. Wolf, K., Wu, Y. I., Liu, Y., Geiger, J., Tam, E., Overall, C., Stack, M. S., and Friedl, P. (2007). Multi-step pericellular proteolysis controls the transition from individual to collective cancer cell invasion. Nat. Cell Biol. *9*, 893–904.

198. Sahai, E., and Marshall, C. J. (2003). Differing modes of tumour cell invasion have distinct requirements for Rho/ROCK signalling and extracellular proteolysis. Nat. Cell Biol. *5*, 711–719.

199. Tamariz, E., and Grinnell, F. (2002). Modulation of fibroblast morphology and adhesion during collagen matrix remodeling. Mol. Biol. Cell *13*, 3915–3929.

200. Ballestrem, C., Hinz, B., Imhof, B. A., and Wehrle-Haller, B. (2001). Marching at the front and dragging behind: differential alphaVbeta3-integrin turnover regulates focal adhesion behavior. J. Cell Biol. *155*, 1319–1332.

201. Hagemann, C., Anacker, J., Ernestus, R.-I., and Vince, G. H. (2012). A complete compilation of matrix metalloproteinase expression in human malignant gliomas. World J. Clin. Oncol. *3*, 67–79.

202. Cuddapah, V. A., Robel, S., Watkins, S., and Sontheimer, H. (2014). A neurocentric perspective on glioma invasion. Nat. Rev. Neurosci. *15*, 455–465.

203. Rao, J. S. (2003). Molecular mechanisms of glioma invasiveness: the role of proteases. Nat. Rev. Cancer *3*, 489–501.

204. Scherer, H. J. (1938). Structural Development in Gliomas. Am. J. Cancer *34*, 333–351.

205. Montana, V., and Sontheimer, H. (2011). Bradykinin promotes the chemotactic invasion of primary brain tumors. J. Neurosci. *31*, 4858–4867.

206. Pedersen, P. H., Edvardsen, K., Garcia-Cabrera, I., Mahesparan, R., Thorsen, J., Mathisen, B., Rosenblum, M. L., and Bjerkvig, R. (1995). Migratory patterns of lac-z transfected human glioma cells in the rat brain. Int. J. Cancer *62*, 767–771.

207. Farin, A., Suzuki, S. O., Weiker, M., Goldman, J. E., Bruce, J. N., and Canoll, P. (2006). Transplanted glioma cells migrate and proliferate on host brain vasculature: a dynamic analysis. Glia *53*, 799–808.

208. Esmaeili, M., Stensjøen, A. L., Berntsen, E. M., Solheim, O., and Reinertsen, I. (2018). The direction of tumour growth in glioblastoma patients. Sci. Rep. *8*, 1199.

209. Azevedo, F. A. C., Carvalho, L. R. B., Grinberg, L. T., Farfel, J. M., Ferretti, R. E. L., Leite, R. E. P., Jacob Filho, W., Lent, R., and Herculano-Houzel, S. (2009). Equal numbers of neuronal and nonneuronal cells make the human brain an isometrically scaled-up primate brain. J. Comp. Neurol. *513*, 532–541.

210. Gritsenko, P. G., Ilina, O., and Friedl, P. (2012). Interstitial guidance of cancer invasion. J. Pathol. *226*, 185–199.

211. Zhang, H., Kelly, G., Zerillo, C., Jaworski, D. M., and Hockfield, S. (1998). Expression of a cleaved brain-specific extracellular matrix protein mediates glioma cell invasion In vivo. J. Neurosci. *18*, 2370–2376.

212. Xia, S., Lal, B., Tung, B., Wang, S., Goodwin, C. R., and Laterra, J. (2016). Tumor microenvironment tenascin-C promotes glioblastoma invasion and negatively regulates tumor proliferation. Neuro. Oncol. *18*, 507–517.

213. de Gooijer, M. C., Guillén Navarro, M., Bernards, R., Wurdinger, T., and van Tellingen, O. (2018). An experimenter's guide to glioblastoma invasion pathways. Trends Mol. Med. *24*, 763–780.

214. Pencheva, N., de Gooijer, M. C., Vis, D. J., Wessels, L. F. A., Würdinger, T., van Tellingen, O., and Bernards, R. (2017). Identification of a druggable pathway controlling glioblastoma invasiveness. Cell Rep. *20*, 48–60.

215. Zimmermann, D. R., and Dours-Zimmermann, M. T. (2008). Extracellular matrix of the central nervous system: from neglect to challenge. Histochem. Cell Biol. *130*, 635–653.

216. Osswald, M., Jung, E., Sahm, F., Solecki, G., Venkataramani, V., Blaes, J., Weil, S., Horstmann, H., Wiestler, B., Syed, M., et al. (2015). Brain tumour cells interconnect to a functional and resistant network. Nature *528*, 93–98.

217. Gritsenko, P. G., Atlasy, N., Dieteren, C. E. J., Navis, A. C., Venhuizen, J.-H., Veelken, C., Schubert, D., Acker-Palmer, A., Westerman, B. A., Wurdinger, T., et al. (2020). p120-catenin-dependent collective brain infiltration by glioma cell networks. Nat. Cell Biol. *22*, 97–107.

218. Zhu, Z., Khan, M. A., Weiler, M., Blaes, J., Jestaedt, L., Geibert, M., Zou, P., Gronych, J., Bernhardt, O., Korshunov, A., et al. (2014). Targeting self-renewal in high-grade brain tumors leads to loss of brain tumor stem cells and prolonged survival. Cell Stem Cell *15*, 185–198.

219. Lowery, L. A., and Van Vactor, D. (2009). The trip of the tip: understanding the growth cone machinery. Nat. Rev. Mol. Cell Biol. *10*, 332–343.

220. Jung, E., Osswald, M., Blaes, J., Wiestler, B., Sahm, F., Schmenger, T., Solecki, G., Deumelandt, K., Kurz, F. T., Xie, R., et al. (2017). Tweety-Homolog 1 Drives Brain Colonization of Gliomas. J. Neurosci. *37*, 6837–6850.

221. Fletcher, D. A., and Mullins, R. D. (2010). Cell mechanics and the cytoskeleton. Nature *463*, 485–492.

222. Maekawa, M., Ishizaki, T., Boku, S., Watanabe, N., Fujita, A., Iwamatsu, A., Obinata, T., Ohashi, K., Mizuno, K., and Narumiya, S. (1999). Signaling from Rho to the actin cytoskeleton through protein kinases ROCK and LIM-kinase. Science *285*, 895–898.

223. Sanz-Moreno, V., Gaggioli, C., Yeo, M., Albrengues, J., Wallberg, F., Viros, A., Hooper, S., Mitter, R., Féral, C. C., Cook, M., et al. (2011). ROCK and JAK1 signaling cooperate to control actomyosin contractility in tumor cells and stroma. Cancer Cell *20*, 229–245.

224. da Silva, B., Polson, E. S., Droop, A., Mathew, R. K., Stead, L. F., Williams, J., Short, S. C., Scarcia, M., Mavria, G., and Wurdak, H. (2018). Chemically-induced Neurite-like Outgrowth Reveals Multicellular Network Function in Patient-derived Glioblastoma Cells. BioRxiv.

225. Pataskar, A., Jung, J., Smialowski, P., Noack, F., Calegari, F., Straub, T., and Tiwari, V. K. (2016). NeuroD1 reprograms chromatin and transcription factor landscapes to induce the neuronal program. EMBO J. *35*, 24–45.

226. Schäck, L., Budde, S., Lenarz, T., Krettek, C., Gross, G., Windhagen, H., Hoffmann, A., and Warnecke, A. (2016). Induction of neuronal-like phenotype in human mesenchymal stem cells by overexpression of Neurogenin1 and treatment with neurotrophins. Tissue Cell *48*, 524–532.

227. Francescone, R. A., Faibish, M., and Shao, R. (2011). A Matrigel-based tube formation assay to assess the vasculogenic activity of tumor cells. J. Vis. Exp.

228. Valster, A., Tran, N. L., Nakada, M., Berens, M. E., Chan, A. Y., and Symons, M. (2005). Cell migration and invasion assays. Methods *37*, 208–215.

229. Justus, C. R., Leffler, N., Ruiz-Echevarria, M., and Yang, L. V. (2014). In vitro cell migration and invasion assays. J. Vis. Exp.

230. Rao, S. S., Lannutti, J. J., Viapiano, M. S., Sarkar, A., and Winter, J. O. (2014). Toward 3D biomimetic models to understand the behavior of glioblastoma multiforme cells. Tissue Eng. Part B Rev. *20*, 314–327.

231. Friedl, P., Sahai, E., Weiss, S., and Yamada, K. M. (2012). New dimensions in cell migration. Nat. Rev. Mol. Cell Biol. *13*, 743–747.

232. Levin, V. A., Panchabhai, S., Shen, L., and Baggerly, K. A. (2012). Protein and phosphoprotein levels in glioma and adenocarcinoma cell lines grown in normoxia and hypoxia in monolayer and three-dimensional cultures. Proteome Sci *10*, 5.

233. Heffernan, J. M., Overstreet, D. J., Le, L. D., Vernon, B. L., and Sirianni, R. W. (2015). Bioengineered scaffolds for 3D analysis of glioblastoma proliferation and invasion. Ann. Biomed. Eng. *43*, 1965–1977.

234. Ulrich, T. A., de Juan Pardo, E. M., and Kumar, S. (2009). The mechanical rigidity of the extracellular matrix regulates the structure, motility, and proliferation of glioma cells. Cancer Res. *69*, 4167–4174.

235. Thomas, T. W., and DiMilla, P. A. (2000). Spreading and motility of human glioblastoma cells on sheets of silicone rubber depend on substratum compliance. Med Biol Eng Comput *38*, 360–370.

236. Rao, S. S., Dejesus, J., Short, A. R., Otero, J. J., Sarkar, A., and Winter, J. O. (2013). Glioblastoma behaviors in three-dimensional collagen-hyaluronan composite hydrogels. ACS Appl. Mater. Interfaces *5*, 9276–9284.

237. Yang, Y., Sun, C., Wilhelm, M. E., Fox, L. J., Zhu, J., and Kaufman, L. J. (2011). Influence of chondroitin sulfate and hyaluronic acid on structure, mechanical properties, and glioma invasion of collagen I gels. Biomaterials *32*, 7932–7940.

238. Chonan, Y., Taki, S., Sampetrean, O., Saya, H., and Sudo, R. (2017). Endothelium-induced three-dimensional invasion of heterogeneous glioma initiating cells in a microfluidic coculture platform. Integr Biol (Camb) *9*, 762–773.

239. Fernandes, J. T. S., Chutna, O., Chu, V., Conde, J. P., and Outeiro, T. F. (2016). A Novel Microfluidic Cell Co-culture Platform for the Study of the Molecular Mechanisms of Parkinson's Disease and Other Synucleinopathies. Front. Neurosci. *10*, 511.

240. Gao, Y., Majumdar, D., Jovanovic, B., Shaifer, C., Lin, P. C., Zijlstra, A., Webb, D. J., and Li, D. (2011). A versatile valve-enabled microfluidic cell co-culture platform and demonstration of its applications to neurobiology and cancer biology. Biomed Microdevices *13*, 539–548.

241. Jung, S., Kim, H.-W., Lee, J.-H., Kang, S.-S., Rhu, H.-H., Jeong, Y.-I., Yang, S.-Y., Chung, H.-Y., Bae, C.-S., Choi, C., et al. (2002). Brain tumor invasion model system using organotypic brain-slice culture as an alternative to in vivo model. J. Cancer Res. Clin. Oncol. *128*, 469–476.

242. Jung, S., Ackerley, C., Ivanchuk, S., Mondal, S., Becker, L. E., and Rutka, J. T. (2001). Tracking the invasiveness of human astrocytoma cells by using green fluorescent protein in an organotypical brain slice model. J. Neurosurg. *94*, 80–89.

243. Yoshida, D., Watanabe, K., Noha, M., Takahashi, H., Teramoto, A., and Sugisaki, Y. (2002). Tracking cell invasion of human glioma cells and

suppression by anti-matrix metalloproteinase agent in rodent brain-slice model. Brain Tumor Pathol. *19*, 69–76.

244. Ohnishi, T., Matsumura, H., Izumoto, S., Hiraga, S., and Hayakawa, T. (1998). A novel model of glioma cell invasion using organotypic brain slice culture. Cancer Res. *58*, 2935–2940.

245. Holtkamp, N., Afanasieva, A., Elstner, A., van Landeghem, F. K. H., Könneker, M., Kuhn, S. A., Kettenmann, H., and von Deimling, A. (2005). Brain slice invasion model reveals genes differentially regulated in glioma invasion. Biochem. Biophys. Res. Commun. *336*, 1227–1233.

246. Yamada, K. M., and Cukierman, E. (2007). Modeling tissue morphogenesis and cancer in 3D. Cell *130*, 601–610.

247. Krusche, B., Ottone, C., Clements, M. P., Johnstone, E. R., Goetsch, K., Lieven, H., Mota, S. G., Singh, P., Khadayate, S., Ashraf, A., et al. (2016). EphrinB2 drives perivascular invasion and proliferation of glioblastoma stem-like cells. Elife *5*.

248. Guillamo, J. S., Lisovoski, F., Christov, C., Le Guérinel, C., Defer, G. L., Peschanski, M., and Lefrançois, T. (2001). Migration pathways of human glioblastoma cells xenografted into the immunosuppressed rat brain. J. Neurooncol. *52*, 205–215.

249. Yoshida, D., Takahashi, H., and Teramoto, A. (2004). Inhibition of glioma angiogenesis and invasion by SI-27, an anti-matrix metalloproteinase agent in a rat brain tumor model. Neurosurgery *54*, 1213–20; discussion 1220.

250. Sampetrean, O., Saga, I., Nakanishi, M., Sugihara, E., Fukaya, R., Onishi, N., Osuka, S., Akahata, M., Kai, K., Sugimoto, H., et al. (2011). Invasion precedes tumor mass formation in a malignant brain tumor model of genetically modified neural stem cells. Neoplasia *13*, 784–791.

251. Jensen, S. S., Meyer, M., Petterson, S. A., Halle, B., Rosager, A. M., Aaberg-Jessen, C., Thomassen, M., Burton, M., Kruse, T. A., and Kristensen, B. W. (2016). Establishment and Characterization of a Tumor Stem Cell-Based Glioblastoma Invasion Model. PLoS One *11*, e0159746.

252. Zhang, F., Xie, J., Liu, G., He, Y., Lu, G., and Chen, X. (2011). In vivo MRI tracking of cell invasion and migration in a rat glioma model. Mol. Imaging Biol. *13*, 695–701.

253. Ricard, C., and Debarbieux, F. C. (2014). Six-color intravital two-photon imaging of brain tumors and their dynamic microenvironment. Front. Cell Neurosci. *8*, 57.

254. Pittet, M. J., and Weissleder, R. (2011). Intravital imaging. Cell *147*, 983–991.

255. Eiraku, M., and Sasai, Y. (2012). Self-formation of layered neural structures in three-dimensional culture of ES cells. Curr. Opin. Neurobiol. *22*, 768–777.

256. Lancaster, M. A., and Knoblich, J. A. (2014). Generation of cerebral organoids from human pluripotent stem cells. Nat. Protoc. *9*, 2329–

2340.

257. Clevers, H. (2016). Modeling Development and Disease with Organoids. Cell *165*, 1586–1597.

258. Wilson, H. V. (1907). A NEW METHOD BY WHICH SPONGES MAY BE ARTIFICIALLY REARED. Science *25*, 912–915.

259. Moscona, A. (1961). Rotation-mediated histogenetic aggregation of dissociated cells. A quantifiable approach to cell interactions in vitro. Exp. Cell Res. *22*, 455–475.

260. Holtfeter, J. (1944). Experimental studies on the development of the pronephros. Rev. Can. Biol. *3*, 220–250.

261. Weiss, P., and Taylor, A. C. (1960). Reconstitution of complete organs from single-cell suspensions of chick embryos in advanced stages of differentiation. Proc. Natl. Acad. Sci. USA *46*, 1177–1185.

262. Rookmaaker, M. B., Schutgens, F., Verhaar, M. C., and Clevers, H. (2015). Development and application of human adult stem or progenitor cell organoids. Nat. Rev. Nephrol. *11*, 546–554.

263. Schutgens, F., and Clevers, H. (2020). Human organoids: tools for understanding biology and treating diseases. Annu. Rev. Pathol. *15*, 211–234.

264. Drost, J., van Boxtel, R., Blokzijl, F., Mizutani, T., Sasaki, N., Sasselli, V., de Ligt, J., Behjati, S., Grolleman, J. E., van Wezel, T., et al. (2017). Use of CRISPR-modified human stem cell organoids to study the origin of mutational signatures in cancer. Science *358*, 234–238.

265. Qian, X., Nguyen, H. N., Song, M. M., Hadiono, C., Ogden, S. C., Hammack, C., Yao, B., Hamersky, G. R., Jacob, F., Zhong, C., et al. (2016). Brain-Region-Specific Organoids Using Mini-bioreactors for Modeling ZIKV Exposure. Cell *165*, 1238–1254.

266. Garcez, P. P., Loiola, E. C., Madeiro da Costa, R., Higa, L. M., Trindade, P., Delvecchio, R., Nascimento, J. M., Brindeiro, R., Tanuri, A., and Rehen, S. K. (2016). Zika virus impairs growth in human neurospheres and brain organoids. Science *352*, 816–818.

267. Dang, J., Tiwari, S. K., Lichinchi, G., Qin, Y., Patil, V. S., Eroshkin, A. M., and Rana, T. M. (2016). Zika Virus Depletes Neural Progenitors in Human Cerebral Organoids through Activation of the Innate Immune Receptor TLR3. Cell Stem Cell *19*, 258–265.

268. Watanabe, M., Buth, J. E., Vishlaghi, N., de la Torre-Ubieta, L., Taxidis, J., Khakh, B. S., Coppola, G., Pearson, C. A., Yamauchi, K., Gong, D., et al. (2017). Self-Organized Cerebral Organoids with Human-Specific Features Predict Effective Drugs to Combat Zika Virus Infection. Cell Rep. *21*, 517–532.

269. Eiraku, M., Watanabe, K., Matsuo-Takasaki, M., Kawada, M., Yonemura, S., Matsumura, M., Wataya, T., Nishiyama, A., Muguruma, K., and Sasai, Y. (2008). Self-organized formation of polarized cortical tissues from ESCs and its active manipulation by extrinsic signals. Cell Stem Cell *3*, 519–532.

270. McCracken, K. W., Catá, E. M., Crawford, C. M., Sinagoga, K. L., Schumacher, M., Rockich, B. E., Tsai, Y.-H., Mayhew, C. N., Spence, J. R., Zavros, Y., et al. (2014). Modelling human development and disease in pluripotent stem-cell-derived gastric organoids. Nature *516*, 400–404.

271. Takebe, T., Sekine, K., Enomura, M., Koike, H., Kimura, M., Ogaeri, T., Zhang, R.-R., Ueno, Y., Zheng, Y.-W., Koike, N., et al. (2013). Vascularized and functional human liver from an iPSC-derived organ bud transplant. Nature *499*, 481–484.

272. McCracken, K. W., Howell, J. C., Wells, J. M., and Spence, J. R. (2011). Generating human intestinal tissue from pluripotent stem cells in vitro. Nat. Protoc. *6*, 1920–1928.

273. Chen, Y.-W., Huang, S. X., de Carvalho, A. L. R. T., Ho, S.-H., Islam, M. N., Volpi, S., Notarangelo, L. D., Ciancanelli, M., Casanova, J.-L., Bhattacharya, J., et al. (2017). A three-dimensional model of human lung development and disease from pluripotent stem cells. Nat. Cell Biol. *19*, 542–549.

274. Takasato, M., Er, P. X., Chiu, H. S., Maier, B., Baillie, G. J., Ferguson, C., Parton, R. G., Wolvetang, E. J., Roost, M. S., Chuva de Sousa Lopes, S. M., et al. (2015). Kidney organoids from human iPS cells contain multiple lineages and model human nephrogenesis. Nature *526*, 564–568.

275. Iakobachvili, N., and Peters, P. J. (2017). Humans in a dish: the potential of organoids in modeling immunity and infectious diseases. Front. Microbiol. *8*, 2402.

276. Sato, T., Stange, D. E., Ferrante, M., Vries, R. G. J., Van Es, J. H., Van den Brink, S., Van Houdt, W. J., Pronk, A., Van Gorp, J., Siersema, P. D., et al. (2011). Long-term expansion of epithelial organoids from human colon, adenoma, adenocarcinoma, and Barrett's epithelium. Gastroenterology *141*, 1762–1772.

277. Bartfeld, S., Bayram, T., van de Wetering, M., Huch, M., Begthel, H., Kujala, P., Vries, R., Peters, P. J., and Clevers, H. (2015). In vitro expansion of human gastric epithelial stem cells and their responses to bacterial infection. Gastroenterology *148*, 126–136.e6.

278. Boj, S. F., Hwang, C.-I., Baker, L. A., Chio, I. I. C., Engle, D. D., Corbo, V., Jager, M., Ponz-Sarvise, M., Tiriac, H., Spector, M. S., et al. (2015). Organoid models of human and mouse ductal pancreatic cancer. Cell *160*, 324–338.

279. Huch, M., Gehart, H., van Boxtel, R., Hamer, K., Blokzijl, F., Verstegen, M. M. A., Ellis, E., van Wenum, M., Fuchs, S. A., de Ligt, J., et al. (2015). Long-term culture of genome-stable bipotent stem cells from adult human liver. Cell *160*, 299–312.

280. Dekkers, J. F., Berkers, G., Kruisselbrink, E., Vonk, A., de Jonge, H. R., Janssens, H. M., Bronsveld, I., van de Graaf, E. A., Nieuwenhuis, E. E. S., Houwen, R. H. J., et al. (2016). Characterizing responses to CFTR-modulating drugs using rectal organoids derived from subjects with cystic fibrosis. Sci. Transl. Med. *8*, 344ra84.

281. van de Wetering, M., Francies, H. E., Francis, J. M., Bounova, G., Iorio, F., Pronk, A., van Houdt, W., van Gorp, J., Taylor-Weiner, A., Kester, L., et al. (2015). Prospective derivation of a living organoid biobank of colorectal cancer patients. Cell *161*, 933–945.

282. Sato, T., Vries, R. G., Snippert, H. J., van de Wetering, M., Barker, N., Stange, D. E., van Es, J. H., Abo, A., Kujala, P., Peters, P. J., et al. (2009). Single Lgr5 stem cells build crypt-villus structures in vitro without a mesenchymal niche. Nature *459*, 262–265.

283. Nanduri, L. S. Y., Baanstra, M., Faber, H., Rocchi, C., Zwart, E., de Haan, G., van Os, R., and Coppes, R. P. (2014). Purification and ex vivo expansion of fully functional salivary gland stem cells. Stem Cell Rep. *3*, 957–964.

284. Kessler, M., Hoffmann, K., Brinkmann, V., Thieck, O., Jackisch, S., Toelle, B., Berger, H., Mollenkopf, H.-J., Mangler, M., Sehouli, J., et al. (2015). The Notch and Wnt pathways regulate stemness and differentiation in human fallopian tube organoids. Nat. Commun. *6*, 8989.

285. Hill, S. J., Decker, B., Roberts, E. A., Horowitz, N. S., Muto, M. G., Worley, M. J., Feltmate, C. M., Nucci, M. R., Swisher, E. M., Nguyen, H., et al. (2018). Prediction of DNA Repair Inhibitor Response in Short-Term Patient-Derived Ovarian Cancer Organoids. Cancer Discov. *8*, 1404–1421.

286. Broutier, L., Mastrogiovanni, G., Verstegen, M. M., Francies, H. E., Gavarró, L. M., Bradshaw, C. R., Allen, G. E., Arnes-Benito, R., Sidorova, O., Gaspersz, M. P., et al. (2017). Human primary liver cancer-derived organoid cultures for disease modeling and drug screening. Nat. Med. *23*, 1424–1435.

287. Hu, H., Gehart, H., Artegiani, B., LÖpez-Iglesias, C., Dekkers, F., Basak, O., van Es, J., Chuva de Sousa Lopes, S. M., Begthel, H., Korving, J., et al. (2018). Long-Term Expansion of Functional Mouse and Human Hepatocytes as 3D Organoids. Cell *175*, 1591–1606.e19.

288. Karthaus, W. R., Iaquinta, P. J., Drost, J., Gracanin, A., van Boxtel, R., Wongvipat, J., Dowling, C. M., Gao, D., Begthel, H., Sachs, N., et al. (2014). Identification of multipotent luminal progenitor cells in human prostate organoid cultures. Cell *159*, 163–175.

289. Sachs, N., de Ligt, J., Kopper, O., Gogola, E., Bounova, G., Weeber, F., Balgobind, A. V., Wind, K., Gracanin, A., Begthel, H., et al. (2018). A living biobank of breast cancer organoids captures disease heterogeneity. Cell *172*, 373–386.e10.

290. Sachs, N., Papaspyropoulos, A., Zomer-van Ommen, D. D., Heo, I., Böttinger, L., Klay, D., Weeber, F., Huelsz-Prince, G., Iakobachvili, N., Amatngalim, G. D., et al. (2019). Long-term expanding human airway organoids for disease modeling. EMBO J. *38*.

291. Ren, W., Lewandowski, B. C., Watson, J., Aihara, E., Iwatsuki, K., Bachmanov, A. A., Margolskee, R. F., and Jiang, P. (2014). Single Lgr5- or Lgr6-expressing taste stem/progenitor cells generate taste bud cells ex vivo. Proc. Natl. Acad. Sci. USA *111*, 16401–16406.

292. Turco, M. Y., Gardner, L., Hughes, J., Cindrova-Davies, T., Gomez, M. J., Farrell, L., Hollinshead, M., Marsh, S. G. E., Brosens, J. J., Critchley, H. O., et al. (2017). Long-term, hormone-responsive organoid cultures of human endometrium in a chemically defined medium. Nat. Cell Biol. *19*, 568–577.

293. Schutgens, F., Rookmaaker, M. B., Margaritis, T., Rios, A., Ammerlaan, C., Jansen, J., Gijzen, L., Vormann, M., Vonk, A., Viveen, M., et al. (2019). Tubuloids derived from human adult kidney and urine for personalized disease modeling. Nat. Biotechnol. *37*, 303–313.

294. Lancaster, M. A., Renner, M., Martin, C.-A., Wenzel, D., Bicknell, L. S., Hurles, M. E., Homfray, T., Penninger, J. M., Jackson, A. P., and Knoblich, J. A. (2013). Cerebral organoids model human brain development and microcephaly. Nature *501*, 373–379.

295. Xia, X., and Zhang, S.-C. (2009). Differentiation of neuroepithelia from human embryonic stem cells. Methods Mol. Biol. *549*, 51–58.

296. Quadrato, G., Nguyen, T., Macosko, E. Z., Sherwood, J. L., Min Yang, S., Berger, D. R., Maria, N., Scholvin, J., Goldman, M., Kinney, J. P., et al. (2017). Cell diversity and network dynamics in photosensitive human brain organoids. Nature *545*, 48–53.

297. Jo, J., Xiao, Y., Sun, A. X., Cukuroglu, E., Tran, H.-D., Göke, J., Tan, Z. Y., Saw, T. Y., Tan, C.-P., Lokman, H., et al. (2016). Midbrain-like Organoids from Human Pluripotent Stem Cells Contain Functional Dopaminergic and Neuromelanin-Producing Neurons. Cell Stem Cell *19*, 248–257.

298. Xiang, Y., Tanaka, Y., Patterson, B., Kang, Y.-J., Govindaiah, G., Roselaar, N., Cakir, B., Kim, K.-Y., Lombroso, A. P., Hwang, S.-M., et al. (2017). Fusion of Regionally Specified hPSC-Derived Organoids Models Human Brain Development and Interneuron Migration. Cell Stem Cell *21*, 383–398.e7.

299. Birey, F., Andersen, J., Makinson, C. D., Islam, S., Wei, W., Huber, N., Fan, H. C., Metzler, K. R. C., Panagiotakos, G., Thom, N., et al. (2017). Assembly of functionally integrated human forebrain spheroids. Nature *545*, 54–59.

300. Bhatia, S. N., and Ingber, D. E. (2014). Microfluidic organs-on-chips. Nat. Biotechnol. *32*, 760–772.

301. Mansour, A. A., Gonçalves, J. T., Bloyd, C. W., Li, H., Fernandes, S., Quang, D., Johnston, S., Parylak, S. L., Jin, X., and Gage, F. H. (2018). An in vivo model of functional and vascularized human brain organoids. Nat. Biotechnol. *36*, 432–441.

302. Camp, J. G., Badsha, F., Florio, M., Kanton, S., Gerber, T., Wilsch-Bräuninger, M., Lewitus, E., Sykes, A., Hevers, W., Lancaster, M., et al. (2015). Human cerebral organoids recapitulate gene expression programs of fetal neocortex development. Proc. Natl. Acad. Sci. USA *112*, 15672–15677.

303. Tanaka, Y., Cakir, B., Xiang, Y., Sullivan, G. J., and Park, I.-H. (2020). Synthetic Analyses of Single-Cell Transcriptomes from Multiple Brain

Organoids and Fetal Brain. Cell Rep. *30*, 1682–1689.e3.

304. Kanton, S., Boyle, M. J., He, Z., Santel, M., Weigert, A., Sanchís-Calleja, F., Guijarro, P., Sidow, L., Fleck, J. S., Han, D., et al. (2019). Organoid single-cell genomic atlas uncovers human-specific features of brain development. Nature *574*, 418–422.

305. Mariani, J., Coppola, G., Zhang, P., Abyzov, A., Provini, L., Tomasini, L., Amenduni, M., Szekely, A., Palejev, D., Wilson, M., et al. (2015). FOXG1-Dependent Dysregulation of GABA/Glutamate Neuron Differentiation in Autism Spectrum Disorders. Cell *162*, 375–390.

306. Jacob, F., Salinas, R. D., Zhang, D. Y., Nguyen, P. T. T., Schnoll, J. G., Wong, S. Z. H., Thokala, R., Sheikh, S., Saxena, D., Prokop, S., et al. (2020). A Patient-Derived Glioblastoma Organoid Model and Biobank Recapitulates Inter- and Intra-tumoral Heterogeneity. Cell *180*, 188–204.e22.

307. da Silva, B., Mathew, R. K., Polson, E. S., Williams, J., and Wurdak, H. (2018). Spontaneous Glioblastoma Spheroid Infiltration of Early-Stage Cerebral Organoids Models Brain Tumor Invasion. SLAS Discov. *23*, 862–868.

308. Linkous, A., Balamatsias, D., Snuderl, M., Edwards, L., Miyaguchi, K., Milner, T., Reich, B., Cohen-Gould, L., Storaska, A., Nakayama, Y., et al. (2019). Modeling Patient-Derived Glioblastoma with Cerebral Organoids. Cell Rep. *26*, 3203–3211.e5.

309. Bhaduri, A., Di Lullo, E., Jung, D., Müller, S., Crouch, E. E., Espinosa, C. S., Ozawa, T., Alvarado, B., Spatazza, J., Cadwell, C. R., et al. (2020). Outer Radial Glia-like Cancer Stem Cells Contribute to Heterogeneity of Glioblastoma. Cell Stem Cell *26*, 48–63.e6.

310. Pine, A. R., Cirigliano, S. M., Nicholson, J. G., Hu, Y., Linkous, A., Miyaguchi, K., Edwards, L., Singhania, R., Schwartz, T. H., Ramakrishna, R., et al. (2020). Tumor microenvironment is critical for the maintenance of cellular states found in primary glioblastomas. Cancer Discov. *10*, 964–979.

311. Krieger, T. G., Tirier, S. M., Park, J., Jechow, K., Eisemann, T., Peterziel, H., Angel, P., Eils, R., and Conrad, C. (2020). Modeling glioblastoma invasion using human brain organoids and single-cell transcriptomics. Neuro. Oncol.

312. von Kölliker, A. (1884). Die embryonalen Keimblätter und die Gewebe. Wilhelm Engelmann *40*, 179–213.

313. Cambray, N., and Wilson, V. (2002). Axial progenitors with extensive potency are localised to the mouse chordoneural hinge. Development *129*, 4855–4866.

314. Cambray, N., and Wilson, V. (2007). Two distinct sources for a population of maturing axial progenitors. Development *134*, 2829–2840.

315. Brown, J. M., and Storey, K. G. (2000). A region of the vertebrate neural plate in which neighbouring cells can adopt neural or epidermal fates. Curr. Biol. *10*, 869–872.

316. Iimura, T., and Pourquié, O. (2006). Collinear activation of Hoxb genes during gastrulation is linked to mesoderm cell ingression. Nature *442*, 568–571.

317. McGrew, M. J., Sherman, A., Lillico, S. G., Ellard, F. M., Radcliffe, P. A., Gilhooley, H. J., Mitrophanous, K. A., Cambray, N., Wilson, V., and Sang, H. (2008). Localised axial progenitor cell populations in the avian tail bud are not committed to a posterior Hox identity. Development *135*, 2289–2299.

318. Olivera-Martinez, I., Harada, H., Halley, P. A., and Storey, K. G. (2012). Loss of FGF-dependent mesoderm identity and rise of endogenous retinoid signalling determine cessation of body axis elongation. PLoS Biol. *10*, e1001415.

319. Henrique, D., Abranches, E., Verrier, L., and Storey, K. G. (2015). Neuromesodermal progenitors and the making of the spinal cord. Development *142*, 2864–2875.

320. Tsakiridis, A., Huang, Y., Blin, G., Skylaki, S., Wymeersch, F., Osorno, R., Economou, C., Karagianni, E., Zhao, S., Lowell, S., et al. (2014). Distinct Wnt-driven primitive streak-like populations reflect in vivo lineage precursors. Development *141*, 1209–1221.

321. Gubbay, J., Collignon, J., Koopman, P., Capel, B., Economou, A., Münsterberg, A., Vivian, N., Goodfellow, P., and Lovell-Badge, R. (1990). A gene mapping to the sex-determining region of the mouse Y chromosome is a member of a novel family of embryonically expressed genes. Nature *346*, 245–250.

322. Sinclair, A. H., Berta, P., Palmer, M. S., Hawkins, J. R., Griffiths, B. L., Smith, M. J., Foster, J. W., Frischauf, A. M., Lovell-Badge, R., and Goodfellow, P. N. (1990). A gene from the human sex-determining region encodes a protein with homology to a conserved DNA-binding motif. Nature *346*, 240–244.

323. Collignon, J., Sockanathan, S., Hacker, A., Cohen-Tannoudji, M., Norris, D., Rastan, S., Stevanovic, M., Goodfellow, P. N., and Lovell-Badge, R. (1996). A comparison of the properties of Sox-3 with Sry and two related genes, Sox-1 and Sox-2. Development *122*, 509–520.

324. Pevny, L. H., and Lovell-Badge, R. (1997). Sox genes find their feet. Curr. Opin. Genet. Dev. *7*, 338–344.

325. Avilion, A. A., Nicolis, S. K., Pevny, L. H., Perez, L., Vivian, N., and Lovell-Badge, R. (2003). Multipotent cell lineages in early mouse development depend on SOX2 function. Genes Dev. *17*, 126–140.

326. Wilkinson, D. G., Bhatt, S., and Herrmann, B. G. (1990). Expression pattern of the mouse T gene and its role in mesoderm formation. Nature *343*, 657–659.

327. Dobrovolskaia-Zavadskaia, N. (1927). Sur la mortification spontanee de la queuw chez la spuris nouveau et sur l'existence d'un caractere (facteur) hereditaire non viable. Compr. Soc. Biol *97*, 114–119.

328. Chesley, P. (1935). Development of the short-tailed mutant in the house mouse. J. Exp. Zool. *70*, 429–459.

329. Gluecksohn-Schoenheimer, S. (1938). The development of two tailless mutants in the house mouse. Genetics *23*, 573–584.

330. Gruneberg, H. (1958). Genetical studies on the skeleton of the mouse. XXIII. The development of brachyury and anury. J Embryol Exp Morphol *6*, 424–443.

331. Fujimoto, H., and Yanagisawa, K. O. (1983). Defects in the archenteron of mouse embryos homozygous for the T-mutation. Differentiation. *25*, 44–47.

332. Yanagisawa, K. O., Fujimoto, H., and Urushihara, H. (1981). Effects of the brachyury (T) mutation on morphogenetic movement in the mouse embryo. Dev. Biol. *87*, 242–248.

333. Edwards, Y. H., Putt, W., Lekoape, K. M., Stott, D., Fox, M., Hopkinson, D. A., and Sowden, J. (1996). The human homolog T of the mouse T(Brachyury) gene; gene structure, cDNA sequence, and assignment to chromosome 6q27. Genome Res. *6*, 226–233.

334. Hamilton, D. H., Fernando, R. I., Schlom, J., and Palena, C. (2015). Aberrant expression of the embryonic transcription factor brachyury in human tumors detected with a novel rabbit monoclonal antibody. Oncotarget *6*, 4853–4862.

335. Park, J. C., Chae, Y. K., Son, C. H., Kim, M. S., Lee, J., Ostrow, K., Sidransky, D., Hoque, M. O., and Moon, C. (2008). Epigenetic silencing of human T (brachyury homologue) gene in non-small-cell lung cancer. Biochem. Biophys. Res. Commun. *365*, 221–226.

336. Fernando, R. I., Litzinger, M., Trono, P., Hamilton, D. H., Schlom, J., and Palena, C. (2010). The T-box transcription factor Brachyury promotes epithelial-mesenchymal transition in human tumor cells. J. Clin. Invest. *120*, 533–544.

337. Kilic, N., Feldhaus, S., Kilic, E., Tennstedt, P., Wicklein, D., Wasielewski, R. von, Viebahn, C., Kreipe, H., and Schumacher, U. (2011). Brachyury expression predicts poor prognosis at early stages of colorectal cancer. Eur. J. Cancer *47*, 1080–1085.

338. Imajyo, I., Sugiura, T., Kobayashi, Y., Shimoda, M., Ishii, K., Akimoto, N., Yoshihama, N., Kobayashi, I., and Mori, Y. (2012). T-box transcription factor Brachyury expression is correlated with epithelial-mesenchymal transition and lymph node metastasis in oral squamous cell carcinoma. Int. J. Oncol. *41*, 1985–1995.

339. Roselli, M., Fernando, R. I., Guadagni, F., Spila, A., Alessandroni, J., Palmirotta, R., Costarelli, L., Litzinger, M., Hamilton, D., Huang, B., et al. (2012). Brachyury, a driver of the epithelial-mesenchymal transition, is overexpressed in human lung tumors: an opportunity for novel interventions against lung cancer. Clin. Cancer Res. *18*, 3868–3879.

340. Sarkar, D., Shields, B., Davies, M. L., Müller, J., and Wakeman, J. A. (2012). BRACHYURY confers cancer stem cell characteristics on colorectal cancer cells. Int. J. Cancer *130*, 328–337.

341. Shimoda, M., Sugiura, T., Imajyo, I., Ishii, K., Chigita, S., Seki, K., Kobayashi, Y., and Shirasuna, K. (2012). The T-box transcription factor

Brachyury regulates epithelial-mesenchymal transition in association with cancer stem-like cells in adenoid cystic carcinoma cells. BMC Cancer *12*, 377.

342. Haro, A., Yano, T., Kohno, M., Yoshida, T., Koga, T., Okamoto, T., Takenoyama, M., and Maehara, Y. (2013). Expression of Brachyury gene is a significant prognostic factor for primary lung carcinoma. Ann. Surg. Oncol. *20 Suppl 3*, S509-16.

343. Huang, B., Cohen, J. R., Fernando, R. I., Hamilton, D. H., Litzinger, M. T., Hodge, J. W., and Palena, C. (2013). The embryonic transcription factor Brachyury blocks cell cycle progression and mediates tumor resistance to conventional antitumor therapies. Cell Death Dis. *4*, e682.

344. Larocca, C., Cohen, J. R., Fernando, R. I., Huang, B., Hamilton, D. H., and Palena, C. (2013). An autocrine loop between TGF-β1 and the transcription factor brachyury controls the transition of human carcinoma cells into a mesenchymal phenotype. Mol. Cancer Ther. *12*, 1805–1815.

345. Kobayashi, Y., Sugiura, T., Imajyo, I., Shimoda, M., Ishii, K., Akimoto, N., Yoshihama, N., and Mori, Y. (2014). Knockdown of the T-box transcription factor Brachyury increases sensitivity of adenoid cystic carcinoma cells to chemotherapy and radiation in vitro: implications for a new therapeutic principle. Int. J. Oncol. *44*, 1107–1117.

346. Palena, C., Roselli, M., Litzinger, M. T., Ferroni, P., Costarelli, L., Spila, A., Cavaliere, F., Huang, B., Fernando, R. I., Hamilton, D. H., et al. (2014). Overexpression of the EMT driver brachyury in breast carcinomas: association with poor prognosis. J. Natl. Cancer Inst. *106*.

347. Pinto, F., Pértega-Gomes, N., Pereira, M. S., Vizcaíno, J. R., Monteiro, P., Henrique, R. M., Baltazar, F., Andrade, R. P., and Reis, R. M. (2014). T-box transcription factor brachyury is associated with prostate cancer progression and aggressiveness. Clin. Cancer Res. *20*, 4949–4961.

348. Pinto, F., Campanella, N. C., Abrahão-Machado, L. F., Scapulatempo-Neto, C., de Oliveira, A. T., Brito, M. J., Andrade, R. P., Guimarães, D. P., and Reis, R. M. (2016). The embryonic Brachyury transcription factor is a novel biomarker of GIST aggressiveness and poor survival. Gastric Cancer *19*, 651–659.

349. Pires, M. M., and Aaronson, S. A. (2014). Brachyury: a new player in promoting breast cancer aggressiveness. J. Natl. Cancer Inst. *106*.

350. Du, R., Wu, S., Lv, X., Fang, H., Wu, S., and Kang, J. (2014). Overexpression of brachyury contributes to tumor metastasis by inducing epithelial-mesenchymal transition in hepatocellular carcinoma. J Exp Clin Cancer Res *33*, 105.

351. Miettinen, M., Wang, Z., Lasota, J., Heery, C., Schlom, J., and Palena, C. (2015). Nuclear brachyury expression is consistent in chordoma, common in germ cell tumors and small cell carcinomas, and rare in other carcinomas and sarcomas: an immunohistochemical study of 5229 cases. Am. J. Surg. Pathol. *39*, 1305–1312.

352. Shao, C., Zhang, J., Fu, J., and Ling, F. (2015). The potential role of

Brachyury in inducing epithelial-to-mesenchymal transition (EMT) and HIF-1α expression in breast cancer cells. Biochem. Biophys. Res. Commun. *467*, 1083–1089.

353. Xu, K., Liu, B., and Liu, Y. (2015). Impact of Brachyury on epithelial-mesenchymal transitions and chemosensitivity in non-small cell lung cancer. Mol. Med. Rep. *12*, 995–1001.

354. Jezkova, J., Williams, J. S., Pinto, F., Sammut, S. J., Williams, G. T., Gollins, S., McFarlane, R. J., Reis, R. M., and Wakeman, J. A. (2016). Brachyury identifies a class of enteroendocrine cells in normal human intestinal crypts and colorectal cancer. Oncotarget *7*, 11478–11486.

355. Li, K., Ying, M., Feng, D., Chen, Y., Wang, J., and Wang, Y. (2016). SMC1 promotes epithelial-mesenchymal transition in triple-negative breast cancer through upregulating Brachyury. Oncol. Rep. *35*, 2405–2412.

356. Yoshihama, R., Yamaguchi, K., Imajyo, I., Mine, M., Hiyake, N., Akimoto, N., Kobayashi, Y., Chigita, S., Kumamaru, W., Kiyoshima, T., et al. (2016). Expression levels of SOX2, KLF4 and brachyury transcription factors are associated with metastasis and poor prognosis in oral squamous cell carcinoma. Oncol. Lett. *11*, 1435–1446.

357. Lee, K. H., Kim, E. Y., Yun, J. S., Park, Y. L., Do, S.-I., Chae, S. W., and Park, C. H. (2018). Prognostic significance of expression of epithelial-mesenchymal transition driver brachyury in breast cancer and its association with subtype and characteristics. Oncol. Lett. *15*, 1037–1045.

358. Vujovic, S., Henderson, S., Presneau, N., Odell, E., Jacques, T. S., Tirabosco, R., Boshoff, C., and Flanagan, A. M. (2006). Brachyury, a crucial regulator of notochordal development, is a novel biomarker for chordomas. J. Pathol. *209*, 157–165.

359. Shah, S. R., David, J. M., Tippens, N. D., Mohyeldin, A., Martinez-Gutierrez, J. C., Ganaha, S., Schiapparelli, P., Hamilton, D. H., Palena, C., Levchenko, A., et al. (2017). Brachyury-YAP Regulatory Axis Drives Stemness and Growth in Cancer. Cell Rep. *21*, 495–507.

360. Gouti, M., Tsakiridis, A., Wymeersch, F. J., Huang, Y., Kleinjung, J., Wilson, V., and Briscoe, J. (2014). In vitro generation of neuromesodermal progenitors reveals distinct roles for wnt signalling in the specification of spinal cord and paraxial mesoderm identity. PLoS Biol. *12*, e1001937.

361. Turner, D. A., Hayward, P. C., Baillie-Johnson, P., Rué, P., Broome, R., Faunes, F., and Martinez Arias, A. (2014). Wnt/β-catenin and FGF signalling direct the specification and maintenance of a neuromesodermal axial progenitor in ensembles of mouse embryonic stem cells. Development *141*, 4243–4253.

362. Lippmann, E. S., Williams, C. E., Ruhl, D. A., Estevez-Silva, M. C., Chapman, E. R., Coon, J. J., and Ashton, R. S. (2015). Deterministic HOX patterning in human pluripotent stem cell-derived neuroectoderm. Stem Cell Rep. *4*, 632–644.

363. Denham, M., Hasegawa, K., Menheniott, T., Rollo, B., Zhang, D., Hough, S., Alshawaf, A., Febbraro, F., Ighaniyan, S., Leung, J., et al. (2015). Multipotent caudal neural progenitors derived from human pluripotent stem cells that give rise to lineages of the central and peripheral nervous system. Stem Cells *33*, 1759–1770.

364. Cunningham, T. J., Colas, A., and Duester, G. (2016). Early molecular events during retinoic acid induced differentiation of neuromesodermal progenitors. Biol. Open *5*, 1821–1833.

365. Gouti, M., Delile, J., Stamataki, D., Wymeersch, F. J., Huang, Y., Kleinjung, J., Wilson, V., and Briscoe, J. (2017). A Gene Regulatory Network Balances Neural and Mesoderm Specification during Vertebrate Trunk Development. Dev. Cell *41*, 243–261.e7.

366. Tsakiridis, A., and Wilson, V. (2015). Assessing the bipotency of in vitro-derived neuromesodermal progenitors. [version 2; peer review: 2 approved, 1 approved with reservations]. F1000Res. *4*, 100.

367. Koch, F., Scholze, M., Wittler, L., Schifferl, D., Sudheer, S., Grote, P., Timmermann, B., Macura, K., and Herrmann, B. G. (2017). Antagonistic Activities of Sox2 and Brachyury Control the Fate Choice of Neuro-Mesodermal Progenitors. Dev. Cell *42*, 514–526.e7.

368. Frith, T. J. R., Gogolou, A., Hackland, J. O. S., Hewitt, Z. A., Moore, H. D., Barbaric, I., Thapar, N., Burns, A. J., Andrews, P. W., Tsakiridis, A., et al. (2020). Retinoic Acid Accelerates the Specification of Enteric Neural Progenitors from In-Vitro-Derived Neural Crest. Stem Cell Rep.

369. Patro, R., Duggal, G., Love, M. I., Irizarry, R. A., and Kingsford, C. (2017). Salmon provides fast and bias-aware quantification of transcript expression. Nat. Methods *14*, 417–419.

370. Subramanian, A., Tamayo, P., Mootha, V. K., Mukherjee, S., Ebert, B. L., Gillette, M. A., Paulovich, A., Pomeroy, S. L., Golub, T. R., Lander, E. S., et al. (2005). Gene set enrichment analysis: a knowledge-based approach for interpreting genome-wide expression profiles. Proc. Natl. Acad. Sci. USA *102*, 15545–15550.

371. Liberzon, A., Subramanian, A., Pinchback, R., Thorvaldsdóttir, H., Tamayo, P., and Mesirov, J. P. (2011). Molecular signatures database (MSigDB) 3.0. Bioinformatics *27*, 1739–1740.

372. Liberzon, A., Birger, C., Thorvaldsdóttir, H., Ghandi, M., Mesirov, J. P., and Tamayo, P. (2015). The Molecular Signatures Database (MSigDB) hallmark gene set collection. Cell Syst. *1*, 417–425.

373. Tang, Z., Kang, B., Li, C., Chen, T., and Zhang, Z. (2019). GEPIA2: an enhanced web server for large-scale expression profiling and interactive analysis. Nucleic Acids Res. *47*, W556–W560.

374. Bowman, R. L., Wang, Q., Carro, A., Verhaak, R. G. W., and Squatrito, M. (2017). GlioVis data portal for visualization and analysis of brain tumor expression datasets. Neuro. Oncol. *19*, 139–141.

375. Zhao, Z., Meng, F., Wang, W., Wang, Z., Zhang, C., and Jiang, T. (2017). Comprehensive RNA-seq transcriptomic profiling in the malignant progression of gliomas. Sci. Data *4*, 170024.

376. Schindelin, J., Arganda-Carreras, I., Frise, E., Kaynig, V., Longair, M., Pietzsch, T., Preibisch, S., Rueden, C., Saalfeld, S., Schmid, B., et al. (2012). Fiji: an open-source platform for biological-image analysis. Nat. Methods *9*, 676–682.

377. Carpenter, A. E., Jones, T. R., Lamprecht, M. R., Clarke, C., Kang, I. H., Friman, O., Guertin, D. A., Chang, J. H., Lindquist, R. A., Moffat, J., et al. (2006). CellProfiler: image analysis software for identifying and quantifying cell phenotypes. Genome Biol. *7*, R100.

378. Szklarczyk, D., Gable, A. L., Lyon, D., Junge, A., Wyder, S., Huerta-Cepas, J., Simonovic, M., Doncheva, N. T., Morris, J. H., Bork, P., et al. (2019). STRING v11: protein-protein association networks with increased coverage, supporting functional discovery in genome-wide experimental datasets. Nucleic Acids Res. *47*, D607–D613.

379. Shannon, P., Markiel, A., Ozier, O., Baliga, N. S., Wang, J. T., Ramage, D., Amin, N., Schwikowski, B., and Ideker, T. (2003). Cytoscape: a software environment for integrated models of biomolecular interaction networks. Genome Res. *13*, 2498–2504.

380. Pool, M., Thiemann, J., Bar-Or, A., and Fournier, A. E. (2008). NeuriteTracer: a novel ImageJ plugin for automated quantification of neurite outgrowth. J. Neurosci. Methods *168*, 134–139.

381. Chen, H. I., Song, H., and Ming, G.-L. (2019). Applications of human brain organoids to clinical problems. Dev. Dyn. *248*, 53–64.

382. Lenting, K., Verhaak, R., Ter Laan, M., Wesseling, P., and Leenders, W. (2017). Glioma: experimental models and reality. Acta Neuropathol. *133*, 263–282.

383. Medvedev, S. P., Shevchenko, A. I., Mazurok, N. A., and Zakiian, S. M. (2008). [OCT4 and NANOG are the key genes in the system of pluripotency maintenance in mammalian cells]. Genetika *44*, 1589–1608.

384. Sansom, S. N., Griffiths, D. S., Faedo, A., Kleinjan, D.-J., Ruan, Y., Smith, J., van Heyningen, V., Rubenstein, J. L., and Livesey, F. J. (2009). The level of the transcription factor Pax6 is essential for controlling the balance between neural stem cell self-renewal and neurogenesis. PLoS Genet. *5*, e1000511.

385. Giudicelli, F., Taillebourg, E., Charnay, P., and Gilardi-Hebenstreit, P. (2001). Krox-20 patterns the hindbrain through both cell-autonomous and non cell-autonomous mechanisms. Genes Dev. *15*, 567–580.

386. Berg, S., Kutra, D., Kroeger, T., Straehle, C. N., Kausler, B. X., Haubold, C., Schiegg, M., Ales, J., Beier, T., Rudy, M., et al. (2019). ilastik: interactive machine learning for (bio)image analysis. Nat. Methods *16*, 1226–1232.

387. Quail, D. F., and Joyce, J. A. (2013). Microenvironmental regulation of tumor progression and metastasis. Nat. Med. *19*, 1423–1437.

388. Iacob, G., and Dinca, E. B. (2009). Current data and strategy in glioblastoma multiforme. J. Med. Life 2, 386–393.

389. Hide, T., Makino, K., Nakamura, H., Yano, S., Anai, S., Takezaki, T., Kuroda, J., Shinojima, N., Ueda, Y., and Kuratsu, J. (2013). New treatment strategies to eradicate cancer stem cells and niches in glioblastoma. Neurol Med Chir (Tokyo) *53*, 764–772.

390. Aldape, K., Brindle, K. M., Chesler, L., Chopra, R., Gajjar, A., Gilbert, M. R., Gottardo, N., Gutmann, D. H., Hargrave, D., Holland, E. C., et al. (2019). Challenges to curing primary brain tumours. Nat. Rev. Clin. Oncol. *16*, 509–520.

391. Ginis, I., Luo, Y., Miura, T., Thies, S., Brandenberger, R., Gerecht-Nir, S., Amit, M., Hoke, A., Carpenter, M. K., Itskovitz-Eldor, J., et al. (2004). Differences between human and mouse embryonic stem cells. Dev. Biol. *269*, 360–380.

392. Gabdoulline, R., Kaisers, W., Gaspar, A., Meganathan, K., Doss, M. X., Jagtap, S., Hescheler, J., Sachinidis, A., and Schwender, H. (2015). Differences in the early development of human and mouse embryonic stem cells. PLoS One *10*, e0140803.

393. Goranci-Buzhala, G., Mariappan, A., Gabriel, E., Ramani, A., Ricci-Vitiani, L., Buccarelli, M., D'Alessandris, Q. G., Pallini, R., and Gopalakrishnan, J. (2020). Rapid and efficient invasion assay of glioblastoma in human brain organoids. Cell Rep. *31*, 107738.

394. Vera, E., Bosco, N., and Studer, L. (2016). Generating Late-Onset Human iPSC-Based Disease Models by Inducing Neuronal Age-Related Phenotypes through Telomerase Manipulation. Cell Rep. *17*, 1184–1192.

395. Miller, J. D., Ganat, Y. M., Kishinevsky, S., Bowman, R. L., Liu, B., Tu, E. Y., Mandal, P. K., Vera, E., Shim, J., Kriks, S., et al. (2013). Human iPSC-based modeling of late-onset disease via progerin-induced aging. Cell Stem Cell *13*, 691–705.

396. Benson, E. K., Lee, S. W., and Aaronson, S. A. (2010). Role of progerin-induced telomere dysfunction in HGPS premature cellular senescence. J. Cell Sci. *123*, 2605–2612.

397. Hu, J. L., Todhunter, M. E., LaBarge, M. A., and Gartner, Z. J. (2018). Opportunities for organoids as new models of aging. J. Cell Biol. *217*, 39–50.

398. Lemée, J.-M., Com, E., Clavreul, A., Avril, T., Quillien, V., de Tayrac, M., Pineau, C., and Menei, P. (2013). Proteomic analysis of glioblastomas: what is the best brain control sample? J. Proteomics *85*, 165–173.

399. Walton, N. M., Sutter, B. M., Chen, H.-X., Chang, L.-J., Roper, S. N., Scheffler, B., and Steindler, D. A. (2006). Derivation and large-scale expansion of multipotent astroglial neural progenitors from adult human brain. Development *133*, 3671–3681.

400. Soroceanu, L., Matlaf, L., Bezrookove, V., Harkins, L., Martinez, R., Greene, M., Soteropoulos, P., and Cobbs, C. S. (2011). Human cytomegalovirus US28 found in glioblastoma promotes an invasive and angiogenic phenotype. Cancer Res. *71*, 6643–6653.

401. Floyd, D. H., Zhang, Y., Dey, B. K., Kefas, B., Breit, H., Marks, K., Dutta, A., Herold-Mende, C., Synowitz, M., Glass, R., et al. (2014). Novel anti-apoptotic microRNAs 582-5p and 363 promote human glioblastoma stem cell survival via direct inhibition of caspase 3, caspase 9, and Bim. PLoS One *9*, e96239.

402. Giuliano, K. A. (1997). High-Content Screening: A New Approach to Easing Key Bottlenecks in the Drug Discovery Process. J. Biomol. Screen. *2*, 249–259.

403. Carpenter, A. E. (2007). Image-based chemical screening. Nat. Chem. Biol. *3*, 461–465.

404. Chin, M. H., Mason, M. J., Xie, W., Volinia, S., Singer, M., Peterson, C., Ambartsumyan, G., Aimiuwu, O., Richter, L., Zhang, J., et al. (2009). Induced pluripotent stem cells and embryonic stem cells are distinguished by gene expression signatures. Cell Stem Cell *5*, 111–123.

405. Allegrucci, C., and Young, L. E. (2007). Differences between human embryonic stem cell lines. Hum. Reprod. Update *13*, 103–120.

406. Volpato, V., and Webber, C. (2020). Addressing variability in iPSC-derived models of human disease: guidelines to promote reproducibility. Dis. Model. Mech. *13*.

407. McMurtrey, R. J. (2017). Roles of Diffusion Dynamics in Stem Cell Signaling and Three-Dimensional Tissue Development. Stem Cells Dev. *26*, 1293–1303.

408. Paşca, S. P. (2019). Assembling human brain organoids. Science *363*, 126–127.

409. Price, A. E., Shamardani, K., Lugo, K. A., Deguine, J., Roberts, A. W., Lee, B. L., and Barton, G. M. (2018). A Map of Toll-like Receptor Expression in the Intestinal Epithelium Reveals Distinct Spatial, Cell Type-Specific, and Temporal Patterns. Immunity *49*, 560–575.e6.

410. Gerdtsson, E., Pore, M., Thiele, J.-A., Gerdtsson, A. S., Malihi, P. D., Nevarez, R., Kolatkar, A., Velasco, C. R., Wix, S., Singh, M., et al. (2018). Multiplex protein detection on circulating tumor cells from liquid biopsies using imaging mass cytometry. Converg. Sci. Phys. Oncol. *4*.

411. Wang, Y. J., Traum, D., Schug, J., Gao, L., Liu, C., HPAP Consortium, Atkinson, M. A., Powers, A. C., Feldman, M. D., Naji, A., et al. (2019). Multiplexed in situ imaging mass cytometry analysis of the human endocrine pancreas and immune system in type 1 diabetes. Cell Metab. *29*, 769–783.e4.

412. Bhaduri, A., Andrews, M. G., Mancia Leon, W., Jung, D., Shin, D., Allen, D., Jung, D., Schmunk, G., Haeussler, M., Salma, J., et al. (2020). Cell stress in cortical organoids impairs molecular subtype specification. Nature *578*, 142–148.

413. Ormel, P. R., Vieira de Sá, R., van Bodegraven, E. J., Karst, H., Harschnitz, O., Sneeboer, M. A. M., Johansen, L. E., van Dijk, R. E., Scheefhals, N., Berdenis van Berlekom, A., et al. (2018). Microglia innately develop within cerebral organoids. Nat. Commun. *9*, 4167.

414. Tomasi, R. F.-X., Sart, S., Champetier, T., and Baroud, C. N. (2020). Individual Control and Quantification of 3D Spheroids in a High-Density Microfluidic Droplet Array. Cell Rep. *31*, 107670.

415. Vlachogiannis, G., Hedayat, S., Vatsiou, A., Jamin, Y., Fernández-Mateos, J., Khan, K., Lampis, A., Eason, K., Huntingford, I., Burke, R., et al. (2018). Patient-derived organoids model treatment response of metastatic gastrointestinal cancers. Science *359*, 920–926.

416. Morgan, E. R., Norman, A., Laing, K., and Seal, M. D. (2017). Treatment and outcomes for glioblastoma in elderly compared with non-elderly patients: a population-based study. Curr. Oncol. *24*, e92–e98.

417. Garside, R., Pitt, M., Anderson, R., Rogers, G., Dyer, M., Mealing, S., Somerville, M., Price, A., and Stein, K. (2007). The effectiveness and cost-effectiveness of carmustine implants and temozolomide for the treatment of newly diagnosed high-grade glioma: a systematic review and economic evaluation. Health Technol. Assess. *11*, iii–iv, ix.

418. Sijben, A. E., McIntyre, J. B., Roldán, G. B., Easaw, J. C., Yan, E., Forsyth, P. A., Parney, I. F., Magliocco, A. M., Bernsen, H., and Cairncross, J. G. (2008). Toxicity from chemoradiotherapy in older patients with glioblastoma multiforme. J. Neurooncol. *89*, 97–103.

419. Pombo Antunes, A. R., Scheyltjens, I., Duerinck, J., Neyns, B., Movahedi, K., and Van Ginderachter, J. A. (2020). Understanding the glioblastoma immune microenvironment as basis for the development of new immunotherapeutic strategies. Elife *9*.

420. Wang, X., Prager, B. C., Wu, Q., Kim, L. J. Y., Gimple, R. C., Shi, Y., Yang, K., Morton, A. R., Zhou, W., Zhu, Z., et al. (2018). Reciprocal Signaling between Glioblastoma Stem Cells and Differentiated Tumor Cells Promotes Malignant Progression. Cell Stem Cell *22*, 514–528.e5.

421. Zhao, Y., Xiao, A., diPierro, C. G., Carpenter, J. E., Abdel-Fattah, R., Redpath, G. T., Lopes, M.-B. S., and Hussaini, I. M. (2010). An extensive invasive intracranial human glioblastoma xenograft model: role of high level matrix metalloproteinase 9. Am. J. Pathol. *176*, 3032–3049.

422. Smith, T. W., and Davidson, R. I. (1984). Medullomyoblastoma. A histologic, immunohistochemical, and ultrastructural study. Cancer *54*, 323–332.

423. Majumdar, K., Tyagi, I., Saran, R. K., Sakhuja, P., and Sharma, A. (2013). Medulloblastoma with focal divergent/teratoid differentiation. Brain Tumor Pathol. *30*, 50–56.

424. Safari, M., and Khoshnevisan, A. (2014). An overview of the role of cancer stem cells in spine tumors with a special focus on chordoma. World J. Stem Cells *6*, 53–64.

425. Sun, X., Hornicek, F., and Schwab, J. H. (2015). Chordoma: an update on the pathophysiology and molecular mechanisms. Curr Rev Musculoskelet Med *8*, 344–352.

426. Holmberg, J., He, X., Peredo, I., Orrego, A., Hesselager, G., Ericsson, C., Hovatta, O., Oba-Shinjo, S. M., Marie, S. K. N., Nistér, M., et al.

(2011). Activation of neural and pluripotent stem cell signatures correlates with increased malignancy in human glioma. PLoS One *6*, e18454.

427. Mitra, J., and Enders, G. H. (2004). Cyclin A/Cdk2 complexes regulate activation of Cdk1 and Cdc25 phosphatases in human cells. Oncogene *23*, 3361–3367.

428. Yamaguchi, T. P., Takada, S., Yoshikawa, Y., Wu, N., and McMahon, A. P. (1999). T (Brachyury) is a direct target of Wnt3a during paraxial mesoderm specification. Genes Dev. *13*, 3185–3190.

429. Martin, B. L., and Kimelman, D. (2008). Regulation of canonical Wnt signaling by Brachyury is essential for posterior mesoderm formation. Dev. Cell *15*, 121–133.

430. Savory, J. G. A., Bouchard, N., Pierre, V., Rijli, F. M., De Repentigny, Y., Kothary, R., and Lohnes, D. (2009). Cdx2 regulation of posterior development through non-Hox targets. Development *136*, 4099–4110.

431. Nowotschin, S., Ferrer-Vaquer, A., Concepcion, D., Papaioannou, V. E., and Hadjantonakis, A.-K. (2012). Interaction of Wnt3a, Msgn1 and Tbx6 in neural versus paraxial mesoderm lineage commitment and paraxial mesoderm differentiation in the mouse embryo. Dev. Biol. *367*, 1–14.

432. Chalamalasetty, R. B., Garriock, R. J., Dunty, W. C., Kennedy, M. W., Jailwala, P., Si, H., and Yamaguchi, T. P. (2014). Mesogenin 1 is a master regulator of paraxial presomitic mesoderm differentiation. Development *141*, 4285–4297.

433. Takada, S., Stark, K. L., Shea, M. J., Vassileva, G., McMahon, J. A., and McMahon, A. P. (1994). Wnt-3a regulates somite and tailbud formation in the mouse embryo. Genes Dev. *8*, 174–189.

434. Yoshikawa, Y., Fujimori, T., McMahon, A. P., and Takada, S. (1997). Evidence that absence of Wnt-3a signaling promotes neuralization instead of paraxial mesoderm development in the mouse. Dev. Biol. *183*, 234–242.

435. Martin, B. L., and Kimelman, D. (2012). Canonical Wnt signaling dynamically controls multiple stem cell fate decisions during vertebrate body formation. Dev. Cell *22*, 223–232.

436. Kaur, N., Chettiar, S., Rathod, S., Rath, P., Muzumdar, D., Shaikh, M. L., and Shiras, A. (2013). Wnt3a mediated activation of Wnt/β-catenin signaling promotes tumor progression in glioblastoma. Mol. Cell. Neurosci. *54*, 44–57.

437. Zhang, H., Qi, Y., Geng, D., Shi, Y., Wang, X., Yu, R., and Zhou, X. (2018). Expression profile and clinical significance of Wnt signaling in human gliomas. Oncol. Lett. *15*, 610–617.

438. Frith, T. J., Granata, I., Wind, M., Stout, E., Thompson, O., Neumann, K., Stavish, D., Heath, P. R., Ortmann, D., Hackland, J. O., et al. (2018). Human axial progenitors generate trunk neural crest cells in vitro. Elife *7*.

439. Bertani, N., Malatesta, P., Volpi, G., Sonego, P., and Perris, R. (2005).

Neurogenic potential of human mesenchymal stem cells revisited: analysis by immunostaining, time-lapse video and microarray. J. Cell Sci. *118*, 3925–3936.

440. Urrutia, D. N., Caviedes, P., Mardones, R., Minguell, J. J., Vega-Letter, A. M., and Jofre, C. M. (2019). Comparative study of the neural differentiation capacity of mesenchymal stromal cells from different tissue sources: An approach for their use in neural regeneration therapies. PLoS One *14*, e0213032.

441. Poli, A., Mongiorgi, S., Cocco, L., and Follo, M. Y. (2014). Protein kinase C involvement in cell cycle modulation. Biochem. Soc. Trans. *42*, 1471–1476.

442. Satyanarayana, A., and Kaldis, P. (2009). Mammalian cell-cycle regulation: several Cdks, numerous cyclins and diverse compensatory mechanisms. Oncogene *28*, 2925–2939.

443. Ganguly, R., Mohyeldin, A., Thiel, J., Kornblum, H. I., Beullens, M., and Nakano, I. (2015). MELK-a conserved kinase: functions, signaling, cancer, and controversy. Clin. Transl. Med. *4*, 11.

444. Le Mercier, M., Fortin, S., Mathieu, V., Roland, I., Spiegl-Kreinecker, S., Haibe-Kains, B., Bontempi, G., Decaestecker, C., Berger, W., Lefranc, F., et al. (2009). Galectin 1 proangiogenic and promigratory effects in the Hs683 oligodendroglioma model are partly mediated through the control of BEX2 expression. Neoplasia *11*, 485–496.

445. Klink, B., Miletic, H., Stieber, D., Huszthy, P. C., Campos Valenzuela, J. A., Balss, J., Wang, J., Schubert, M., Sakariassen, P. Ø., Sundstrøm, T., et al. (2013). A novel, diffusely infiltrative xenograft model of human anaplastic oligodendroglioma with mutations in FUBP1, CIC, and IDH1. PLoS One *8*, e59773.

446. Navis, A. C., Niclou, S. P., Fack, F., Stieber, D., van Lith, S., Verrijp, K., Wright, A., Stauber, J., Tops, B., Otte-Holler, I., et al. (2013). Increased mitochondrial activity in a novel IDH1-R132H mutant human oligodendroglioma xenograft model: in situ detection of 2-HG and α-KG. Acta Neuropathol. Commun. *1*, 18.

447. Denysenko, T., Annovazzi, L., Cassoni, P., Melcarne, A., Mellai, M., and Schiffer, D. (2016). WNT/β-catenin Signaling Pathway and Downstream Modulators in Low- and High-grade Glioma. Cancer Genomics Proteomics *13*, 31–45.

448. Rampazzo, E., Persano, L., Pistollato, F., Moro, E., Frasson, C., Porazzi, P., Della Puppa, A., Bresolin, S., Battilana, G., Indraccolo, S., et al. (2013). Wnt activation promotes neuronal differentiation of glioblastoma. Cell Death Dis. *4*, e500.

449. Qiang, L., Yang, Y., Ma, Y.-J., Chen, F.-H., Zhang, L.-B., Liu, W., Qi, Q., Lu, N., Tao, L., Wang, X.-T., et al. (2009). Isolation and characterization of cancer stem like cells in human glioblastoma cell lines. Cancer Lett. *279*, 13–21.

450. Piccirillo, S. G. M., Reynolds, B. A., Zanetti, N., Lamorte, G., Binda, E., Broggi, G., Brem, H., Olivi, A., Dimeco, F., and Vescovi, A. L. (2006).

Bone morphogenetic proteins inhibit the tumorigenic potential of human brain tumour-initiating cells. Nature *444*, 761–765.

451. Leha, A., Moens, N., Meleckyte, R., Culley, O. J., Gervasio, M. K., Kerz, M., Reimer, A., Cain, S. A., Streeter, I., Folarin, A., et al. (2016). A high-content platform to characterise human induced pluripotent stem cell lines. Methods *96*, 85–96.

452. Vigilante, A., Laddach, A., Moens, N., Meleckyte, R., Leha, A., Ghahramani, A., Culley, O. J., Kathuria, A., Hurling, C., Vickers, A., et al. (2019). Identifying Extrinsic versus Intrinsic Drivers of Variation in Cell Behavior in Human iPSC Lines from Healthy Donors. Cell Rep. *26*, 2078–2087.e3.

453. Yeung, T., Georges, P. C., Flanagan, L. A., Marg, B., Ortiz, M., Funaki, M., Zahir, N., Ming, W., Weaver, V., and Janmey, P. A. (2005). Effects of substrate stiffness on cell morphology, cytoskeletal structure, and adhesion. Cell Motil. Cytoskeleton *60*, 24–34.

454. Liberio, M. S., Sadowski, M. C., Soekmadji, C., Davis, R. A., and Nelson, C. C. (2014). Differential effects of tissue culture coating substrates on prostate cancer cell adherence, morphology and behavior. PLoS One *9*, e112122.

455. Meyer, M., Reimand, J., Lan, X., Head, R., Zhu, X., Kushida, M., Bayani, J., Pressey, J. C., Lionel, A. C., Clarke, I. D., et al. (2015). Single cell-derived clonal analysis of human glioblastoma links functional and genomic heterogeneity. Proc. Natl. Acad. Sci. USA *112*, 851–856.

456. Schmitz, M., Temme, A., Senner, V., Ebner, R., Schwind, S., Stevanovic, S., Wehner, R., Schackert, G., Schackert, H. K., Fussel, M., et al. (2007). Identification of SOX2 as a novel glioma-associated antigen and potential target for T cell-based immunotherapy. Br. J. Cancer *96*, 1293–1301.

457. Gangemi, R. M. R., Griffero, F., Marubbi, D., Perera, M., Capra, M. C., Malatesta, P., Ravetti, G. L., Zona, G. L., Daga, A., and Corte, G. (2009). SOX2 silencing in glioblastoma tumor-initiating cells causes stop of proliferation and loss of tumorigenicity. Stem Cells *27*, 40–48.

458. Javali, A., Misra, A., Leonavicius, K., Acharyya, D., Vyas, B., and Sambasivan, R. (2017). Co-expression of Tbx6 and Sox2 identifies a novel transient neuromesoderm progenitor cell state. Development *144*, 4522–4529.

459. Martin, E. W., and Sung, M.-H. (2018). Challenges of decoding transcription factor dynamics in terms of gene regulation. Cells *7*.

460. Goto, H., Kimmey, S. C., Row, R. H., Matus, D. Q., and Martin, B. L. (2017). FGF and canonical Wnt signaling cooperate to induce paraxial mesoderm from tailbud neuromesodermal progenitors through regulation of a two-step epithelial to mesenchymal transition. Development *144*, 1412–1424.

461. Lawton, A. K., Nandi, A., Stulberg, M. J., Dray, N., Sneddon, M. W., Pontius, W., Emonet, T., and Holley, S. A. (2013). Regulated tissue fluidity steers zebrafish body elongation. Development *140*, 573–582.

462. Pastushenko, I., and Blanpain, C. (2019). EMT Transition States during Tumor Progression and Metastasis. Trends Cell Biol. *29*, 212–226.

463. Mao, P., Joshi, K., Li, J., Kim, S.-H., Li, P., Santana-Santos, L., Luthra, S., Chandran, U. R., Benos, P. V., Smith, L., et al. (2013). Mesenchymal glioma stem cells are maintained by activated glycolytic metabolism involving aldehyde dehydrogenase 1A3. Proc. Natl. Acad. Sci. USA *110*, 8644–8649.

464. Nakano, I. (2015). Stem cell signature in glioblastoma: therapeutic development for a moving target. J. Neurosurg. *122*, 324–330.

465. Iwadate, Y. (2016). Epithelial-mesenchymal transition in glioblastoma progression. Oncol. Lett. *11*, 1615–1620.

466. Yan, C., Grimm, W. A., Garner, W. L., Qin, L., Travis, T., Tan, N., and Han, Y.-P. (2010). Epithelial to mesenchymal transition in human skin wound healing is induced by tumor necrosis factor-alpha through bone morphogenic protein-2. Am. J. Pathol. *176*, 2247–2258.

467. Lemaire, R., Bayle, J., Mecham, R. P., and Lafyatis, R. (2007). Microfibril-associated MAGP-2 stimulates elastic fiber assembly. J. Biol. Chem. *282*, 800–808.

468. Kielty, C. M., Sherratt, M. J., and Shuttleworth, C. A. (2002). Elastic fibres. J. Cell Sci. *115*, 2817–2828.

469. Spivey, K. A., and Banyard, J. (2010). A prognostic gene signature in advanced ovarian cancer reveals a microfibril-associated protein (MAGP2) as a promoter of tumor cell survival and angiogenesis. Cell Adh Migr *4*, 169–171.

470. Albig, A. R., Becenti, D. J., Roy, T. G., and Schiemann, W. P. (2008). Microfibril-associate glycoprotein-2 (MAGP-2) promotes angiogenic cell sprouting by blocking notch signaling in endothelial cells. Microvasc. Res. *76*, 7–14.

471. Wu, Z., Wang, T., Fang, M., Huang, W., Sun, Z., Xiao, J., and Yan, W. (2018). MFAP5 promotes tumor progression and bone metastasis by regulating ERK/MMP signaling pathways in breast cancer. Biochem. Biophys. Res. Commun. *498*, 495–501.

472. Wu, Y., Wu, P., Zhang, Q., Chen, W., Liu, X., and Zheng, W. (2019). MFAP5 promotes basal-like breast cancer progression by activating the EMT program. Cell Biosci. *9*, 24.

473. Li, Q., Zhang, Y., and Jiang, Q. (2018). MFAP5 suppression inhibits migration/invasion, regulates cell cycle and induces apoptosis via promoting ROS production in cervical cancer. Biochem. Biophys. Res. Commun. *507*, 51–58.

474. Xu, Q., Chang, H., Tian, X., Lou, C., Ma, H., and Yang, X. (2020). Hypoxia-induced MFAP5 Promotes Tumor Migration and Invasion via AKT Pathway in Head and Neck Squamous Cell Carcinoma. J. Cancer *11*, 1596–1605.

475. Uhlén, M., Fagerberg, L., Hallström, B. M., Lindskog, C., Oksvold, P., Mardinoglu, A., Sivertsson, Å., Kampf, C., Sjöstedt, E., Asplund, A., et

al. (2015). Proteomics. Tissue-based map of the human proteome. Science *347*, 1260419.

476. Leung, C. S., Yeung, T.-L., Yip, K.-P., Pradeep, S., Balasubramanian, L., Liu, J., Wong, K.-K., Mangala, L. S., Armaiz-Pena, G. N., Lopez-Berestein, G., et al. (2014). Calcium-dependent FAK/CREB/TNNC1 signalling mediates the effect of stromal MFAP5 on ovarian cancer metastatic potential. Nat. Commun. *5*, 5092.

477. Jia, Z., Wang, Y., Sawyers, A., Yao, H., Rahmatpanah, F., Xia, X.-Q., Xu, Q., Pio, R., Turan, T., Koziol, J. A., et al. (2011). Diagnosis of prostate cancer using differentially expressed genes in stroma. Cancer Res. *71*, 2476–2487.

478. Principe, S., Mejia-Guerrero, S., Ignatchenko, V., Sinha, A., Ignatchenko, A., Shi, W., Pereira, K., Su, S., Huang, S. H., O'Sullivan, B., et al. (2018). Proteomic Analysis of Cancer-Associated Fibroblasts Reveals a Paracrine Role for MFAP5 in Human Oral Tongue Squamous Cell Carcinoma. J. Proteome Res. *17*, 2045–2059.

479. Yeung, T.-L., Leung, C. S., Yip, K.-P., Sheng, J., Vien, L., Bover, L. C., Birrer, M. J., Wong, S. T. C., and Mok, S. C. (2019). Anticancer immunotherapy by MFAP5 blockade inhibits fibrosis and enhances chemosensitivity in ovarian and pancreatic cancer. Clin. Cancer Res. *25*, 6417–6428.

480. Wang, L., Babikir, H., Müller, S., Yagnik, G., Shamardani, K., Catalan, F., Kohanbash, G., Alvarado, B., Di Lullo, E., Kriegstein, A., et al. (2019). The phenotypes of proliferating glioblastoma cells reside on a single axis of variation. Cancer Discov. *9*, 1708–1719.

481. Memberg, S. P., and Hall, A. K. (1995). Dividing neuron precursors express neuron-specific tubulin. J. Neurobiol. *27*, 26–43.

482. Cassimeris, L., and Spittle, C. (2001). Regulation of microtubule-associated proteins. Int Rev Cytol *210*, 163–226.

483. Garton, A. J., Castaldo, L., and Pachter, J. A. (2008). Quantitative high-throughput cell-based assays for inhibitors of ROCK kinases. In Small gtpases in disease, part B Methods in Enzymology. (Elsevier), pp. 491–500.

484. Kranenburg, O., Poland, M., van Horck, F. P., Drechsel, D., Hall, A., and Moolenaar, W. H. (1999). Activation of RhoA by lysophosphatidic acid and Galpha12/13 subunits in neuronal cells: induction of neurite retraction. Mol. Biol. Cell *10*, 1851–1857.

485. Spees, J. L., Olson, S. D., Whitney, M. J., and Prockop, D. J. (2006). Mitochondrial transfer between cells can rescue aerobic respiration. Proc. Natl. Acad. Sci. USA *103*, 1283–1288.

486. da Silva, B., Irving, B. K., Polson, E. S., Droop, A., Griffiths, H. B. S., Mathew, R. K., Stead, L. F., Marrison, J., Williams, C., Williams, J., et al. (2019). Chemically induced neurite-like outgrowth reveals a multicellular network function in patient-derived glioblastoma cells. J. Cell Sci. *132*.

487. Gafson, A. R., Barthélemy, N. R., Bomont, P., Carare, R. O., Durham,

H. D., Julien, J.-P., Kuhle, J., Leppert, D., Nixon, R. A., Weller, R. O., et al. (2020). Neurofilaments: neurobiological foundations for biomarker applications. Brain *143*, 1975–1998.

488. Dimopoulos, G. J., Semba, S., Kitazawa, K., Eto, M., and Kitazawa, T. (2007). Ca2+-dependent rapid Ca2+ sensitization of contraction in arterial smooth muscle. Circ. Res. *100*, 121–129.

489. Qiao, Y.-N., He, W.-Q., Chen, C.-P., Zhang, C.-H., Zhao, W., Wang, P., Zhang, L., Wu, Y.-Z., Yang, X., Peng, Y.-J., et al. (2014). Myosin phosphatase target subunit 1 (MYPT1) regulates the contraction and relaxation of vascular smooth muscle and maintains blood pressure. J. Biol. Chem. *289*, 22512–22523.

490. Lincoln, T. M. (2007). Myosin phosphatase regulatory pathways: different functions or redundant functions? Circ. Res. *100*, 10–12.

491. Chu, J., Miller, C. T., Kislitsyna, K., Laine, G. A., Stewart, R. H., Cox, C. S., and Uray, K. S. (2012). Decreased myosin phosphatase target subunit 1(MYPT1) phosphorylation via attenuated rho kinase and zipper-interacting kinase activities in edematous intestinal smooth muscle. Neurogastroenterol. Motil. *24*, 257–66, e109.

492. Malmersjö, S., Rebellato, P., Smedler, E., Planert, H., Kanatani, S., Liste, I., Nanou, E., Sunner, H., Abdelhady, S., Zhang, S., et al. (2013). Neural progenitors organize in small-world networks to promote cell proliferation. Proc. Natl. Acad. Sci. USA *110*, E1524-32.

493. Jia, X.-F., Ye, F., Wang, Y.-B., and Feng, D.-X. (2016). ROCK inhibition enhances neurite outgrowth in neural stem cells by upregulating YAP expression in vitro. Neural Regen. Res. *11*, 983–987.

494. Benelli, R., and Albini, A. (1999). In vitro models of angiogenesis: the use of Matrigel. Int. J. Biol. Markers *14*, 243–246.

495. Liotta, L. A., Steeg, P. S., and Stetler-Stevenson, W. G. (1991). Cancer metastasis and angiogenesis: an imbalance of positive and negative regulation. Cell *64*, 327–336.

496. Yoo, K.-C., Suh, Y., An, Y., Lee, H.-J., Jeong, Y. J., Uddin, N., Cui, Y.-H., Roh, T.-H., Shim, J.-K., Chang, J. H., et al. (2018). Proinvasive extracellular matrix remodeling in tumor microenvironment in response to radiation. Oncogene *37*, 3317–3328.

497. Knöferle, J., Ramljak, S., Koch, J. C., Tönges, L., Asif, A. R., Michel, U., Wouters, F. S., Heermann, S., Krieglstein, K., Zerr, I., et al. (2010). TGF-beta 1 enhances neurite outgrowth via regulation of proteasome function and EFABP. Neurobiol. Dis. *38*, 395–404.

498. Au, E., Richter, M. W., Vincent, A. J., Tetzlaff, W., Aebersold, R., Sage, E. H., and Roskams, A. J. (2007). SPARC from olfactory ensheathing cells stimulates Schwann cells to promote neurite outgrowth and enhances spinal cord repair. J. Neurosci. *27*, 7208–7221.

499. Han, J., Alvarez-Breckenridge, C. A., Wang, Q.-E., and Yu, J. (2015). TGF-β signaling and its targeting for glioma treatment. Am. J. Cancer Res. *5*, 945–955.

500. Liu, K., Ji, K., Guo, L., Wu, W., Lu, H., Shan, P., and Yan, C. (2014). Mesenchymal stem cells rescue injured endothelial cells in an in vitro ischemia-reperfusion model via tunneling nanotube like structure-mediated mitochondrial transfer. Microvasc. Res. *92*, 10–18.

501. Torralba, D., Baixauli, F., and Sánchez-Madrid, F. (2016). Mitochondria know no boundaries: mechanisms and functions of intercellular mitochondrial transfer. Front. Cell Dev. Biol. *4*, 107.

502. Han, H., Hu, J., Yan, Q., Zhu, J., Zhu, Z., Chen, Y., Sun, J., and Zhang, R. (2016). Bone marrow-derived mesenchymal stem cells rescue injured H9c2 cells via transferring intact mitochondria through tunneling nanotubes in an in vitro simulated ischemia/reperfusion model. Mol. Med. Rep. *13*, 1517–1524.

503. Mahrouf-Yorgov, M., Augeul, L., Da Silva, C. C., Jourdan, M., Rigolet, M., Manin, S., Ferrera, R., Ovize, M., Henry, A., Guguin, A., et al. (2017). Mesenchymal stem cells sense mitochondria released from damaged cells as danger signals to activate their rescue properties. Cell Death Differ. *24*, 1224–1238.

504. Malaiyandi, L. M., Honick, A. S., Rintoul, G. L., Wang, Q. J., and Reynolds, I. J. (2005). Zn2+ inhibits mitochondrial movement in neurons by phosphatidylinositol 3-kinase activation. J. Neurosci. *25*, 9507–9514.

505. Dineley, K. E., Scanlon, J. M., Kress, G. J., Stout, A. K., and Reynolds, I. J. (2000). Astrocytes are more resistant than neurons to the cytotoxic effects of increased [Zn(2+)](i). Neurobiol. Dis. *7*, 310–320.

506. Teddy, J. M., and Kulesa, P. M. (2004). In vivo evidence for short- and long-range cell communication in cranial neural crest cells. Development *131*, 6141–6151.

507. Baker, M. (2017). How the Internet of cells has biologists buzzing. Nature *549*, 322–324.

508. Ramírez-Weber, F. A., and Kornberg, T. B. (1999). Cytonemes: cellular processes that project to the principal signaling center in Drosophila imaginal discs. Cell *97*, 599–607.

509. Rustom, A., Saffrich, R., Markovic, I., Walther, P., and Gerdes, H.-H. (2004). Nanotubular highways for intercellular organelle transport. Science *303*, 1007–1010.

510. Lou, E., Fujisawa, S., Morozov, A., Barlas, A., Romin, Y., Dogan, Y., Gholami, S., Moreira, A. L., Manova-Todorova, K., and Moore, M. A. S. (2012). Tunneling nanotubes provide a unique conduit for intercellular transfer of cellular contents in human malignant pleural mesothelioma. PLoS One *7*, e33093.

511. Sowinski, S., Jolly, C., Berninghausen, O., Purbhoo, M. A., Chauveau, A., Köhler, K., Oddos, S., Eissmann, P., Brodsky, F. M., Hopkins, C., et al. (2008). Membrane nanotubes physically connect T cells over long distances presenting a novel route for HIV-1 transmission. Nat. Cell Biol. *10*, 211–219.

512. Inaba, M., Buszczak, M., and Yamashita, Y. M. (2015). Nanotubes mediate niche-stem-cell signalling in the Drosophila testis. Nature *523*,

329–332.

513. Hsiung, F., Ramirez-Weber, F.-A., Iwaki, D. D., and Kornberg, T. B. (2005). Dependence of Drosophila wing imaginal disc cytonemes on Decapentaplegic. Nature *437*, 560–563.

514. Smith, I. F., Shuai, J., and Parker, I. (2011). Active generation and propagation of Ca2+ signals within tunneling membrane nanotubes. Biophys. J. *100*, L37-9.

515. Wang, X., Veruki, M. L., Bukoreshtliev, N. V., Hartveit, E., and Gerdes, H.-H. (2010). Animal cells connected by nanotubes can be electrically coupled through interposed gap-junction channels. Proc. Natl. Acad. Sci. USA *107*, 17194–17199.

516. Rustom, A. (2016). The missing link: does tunnelling nanotube-based supercellularity provide a new understanding of chronic and lifestyle diseases? Open Biol *6*.

517. Zhang, L., and Zhang, Y. (2015). Tunneling nanotubes between rat primary astrocytes and C6 glioma cells alter proliferation potential of glioma cells. Neurosci. Bull. *31*, 371–378.

518. Wang, Y., Cui, J., Sun, X., and Zhang, Y. (2011). Tunneling-nanotube development in astrocytes depends on p53 activation. Cell Death Differ. *18*, 732–742.

519. Liang, D. (2018). A Salutary Role of Reactive Oxygen Species in Intercellular Tunnel-Mediated Communication. Front. Cell Dev. Biol. *6*, 2.

520. Zhu, D., Tan, K. S., Zhang, X., Sun, A. Y., Sun, G. Y., and Lee, J. C.-M. (2005). Hydrogen peroxide alters membrane and cytoskeleton properties and increases intercellular connections in astrocytes. J. Cell Sci. *118*, 3695–3703.

521. Desir, S., Dickson, E. L., Vogel, R. I., Thayanithy, V., Wong, P., Teoh, D., Geller, M. A., Steer, C. J., Subramanian, S., and Lou, E. (2016). Tunneling nanotube formation is stimulated by hypoxia in ovarian cancer cells. Oncotarget *7*, 43150–43161.

522. Desir, S., O’Hare, P., Vogel, R. I., Sperduto, W., Sarkari, A., Dickson, E. L., Wong, P., Nelson, A. C., Fong, Y., Steer, C. J., et al. (2018). Chemotherapy-Induced Tunneling Nanotubes Mediate Intercellular Drug Efflux in Pancreatic Cancer. Sci. Rep. *8*, 9484.

523. Wang, X., and Gerdes, H. H. (2015). Transfer of mitochondria via tunneling nanotubes rescues apoptotic PC12 cells. Cell Death Differ. *22*, 1181–1191.

524. Sato, M., and Kornberg, T. B. (2002). FGF is an essential mitogen and chemoattractant for the air sacs of the drosophila tracheal system. Dev. Cell *3*, 195–207.

525. Venkataramani, V., Tanev, D. I., Strahle, C., Studier-Fischer, A., Fankhauser, L., Kessler, T., Körber, C., Kardorff, M., Ratliff, M., Xie, R., et al. (2019). Glutamatergic synaptic input to glioma cells drives brain tumour progression. Nature *573*, 532–538.

526. Weil, S., Osswald, M., Solecki, G., Grosch, J., Jung, E., Lemke, D., Ratliff, M., Hänggi, D., Wick, W., and Winkler, F. (2017). Tumor microtubes convey resistance to surgical lesions and chemotherapy in gliomas. Neuro. Oncol. *19*, 1316–1326.

527. Pontes, B., Viana, N. B., Campanati, L., Farina, M., Neto, V. M., and Nussenzveig, H. M. (2008). Structure and elastic properties of tunneling nanotubes. Eur Biophys J *37*, 121–129.

528. Carone, C., Genedani, S., Leo, G., Filaferro, M., Fuxe, K., and Agnati, L. F. (2015). In vitro effects of cocaine on tunneling nanotube formation and extracellular vesicle release in glioblastoma cell cultures. J. Mol. Neurosci. *55*, 42–50.

529. Reindl, J., Shevtsov, M., Dollinger, G., Stangl, S., and Multhoff, G. (2019). Membrane Hsp70-supported cell-to-cell connections via tunneling nanotubes revealed by live-cell STED nanoscopy. Cell Stress Chaperones *24*, 213–221.

530. Osswald, M., Jung, E., Wick, W., and Winkler, F. (2019). Tunneling nanotube-like structures in brain tumors. Cancer Rep.

531. Wu, J.-I., and Wang, L.-H. (2019). Emerging roles of gap junction proteins connexins in cancer metastasis, chemoresistance and clinical application. J Biomed Sci *26*, 8.

532. Ordys, B. B., Launay, S., Deighton, R. F., McCulloch, J., and Whittle, I. R. (2010). The role of mitochondria in glioma pathophysiology. Mol. Neurobiol. *42*, 64–75.

533. Xie, Q., Wu, Q., Horbinski, C. M., Flavahan, W. A., Yang, K., Zhou, W., Dombrowski, S. M., Huang, Z., Fang, X., Shi, Y., et al. (2015). Mitochondrial control by DRP1 in brain tumor initiating cells. Nat. Neurosci. *18*, 501–510.

534. Chen, H., and Chan, D. C. (2017). Mitochondrial dynamics in regulating the unique phenotypes of cancer and stem cells. Cell Metab. *26*, 39–48.

535. Kriel, J., Müller-Nedebock, K., Maarman, G., Mbizana, S., Ojuka, E., Klumperman, B., and Loos, B. (2018). Coordinated autophagy modulation overcomes glioblastoma chemoresistance through disruption of mitochondrial bioenergetics. Sci. Rep. *8*, 10348.

536. Lu, C., Chen, X., Wang, Q., Xu, X., and Xu, B. (2018). TNFα promotes glioblastoma A172 cell mitochondrial apoptosis via augmenting mitochondrial fission and repression of MAPK-ERK-YAP signaling pathways. Onco. Targets. Ther. *11*, 7213–7227.

537. Lahmi, L., Idbaih, A., Rivin Del Campo, E., Hoang-Xuan, K., Mokhtari, K., Sanson, M., Canova, C. H., Carpentier, A., Jacob, J., Maingon, P., et al. (2019). Whole brain radiotherapy with concurrent temozolomide in multifocal and/or multicentric newly diagnosed glioblastoma. J. Clin. Neurosci. *68*, 39–44.

538. Shah, J. L., Li, G., Shaffer, J. L., Azoulay, M. I., Gibbs, I. C., Nagpal, S., and Soltys, S. G. (2018). Stereotactic radiosurgery and hypofractionated radiotherapy for glioblastoma. Neurosurgery *82*, 24-34

539. Marshall, J.J. and Mason, J.O., 2019. Mouse vs man: Organoid models of brain development & disease. Brain Research, 1724, p.146427.